

Modelling and Design of Earthquake Resistant Low-Rise Concentrically
Braced Frames with Dissipative Single-Pin Connections

Cristina Caprarelli

A Thesis
in
The Department of
Building, Civil & Environmental Engineering

Presented in Partial Fulfillment of the Requirements
for the Degree of Master of Applied Science (Civil Engineering) at
Concordia University
Montreal, Quebec Canada

August 2012

© Cristina Caprarelli, 2012

CONCORDIA UNIVERSITY
School of Graduate Studies

This is to certify that the thesis prepared

By: Cristina Caprarelli

Entitled: Modelling and Design of Earthquake Resistant Concentrically Braced Frames with Dissipative Single-Pin Connections

and submitted in partial fulfillment of the requirements for the degree of

MASc Civil Engineering

complies with the regulations of the University and meets the accepted standards with respect to originality and quality.

Signed by the final examining committee:

Dr. Ashutosh Bagchi Chair

Dr. Khaled Galal Examiner

Dr. Muthukumaran Packirisamy Examiner

Dr. Lucia Tirca Supervisor

Approved by _____
Chair of Department or Graduate Program Director

Dean of Faculty

Date _____

ABSTRACT

Modelling and Design of Earthquake Resistant Low-Rise Concentrically Braced Frames with Dissipative Single-Pin Connections

Cristina Caprarelli

Low and middle-rise concentrically braced frames (CBFs) possess large stiffness and low ductility and are the most common systems used to resist seismic loads in Canada. In general, the system behaves in a non-symmetric way after braces have buckled and lost their compressive strength, while the deformation is concentrated within a single floor.

In this light, the aim of this research is to improve the behaviour of earthquake resistant CBF systems in terms of ductility and structure stability by mitigating the tendency of soft storey mechanism formation. Thus, by concentrating the input energy at the level of brace-to-frame connections, braces are able to behave elastically, the ductility is improved and in turn the ability of the structure to dissipate energy is enhanced.

The CBF system with dissipative brace-to-frame connections was proposed and mainly studied through experimental test by European researchers in the frame of the INERD project and several experimental tests were conducted. The connection device is composed of two outer plates, two inner plates and a pin running through all four plates. The energy is dissipated by the pin while it deforms in bending. However, in order to investigate the seismic response of CBF structures with single-pin devices, numerical models of the pin devices as well as braced frames equipped with pin devices are required.

The main objective of this thesis is to investigate, through non-linear numerical modelling, the seismic response of CBF systems with X-bracing configuration and single-pin brace to frame connections by using the OpenSees software (Open System for Earthquake Engineering Simulation). First, the numerical model was validated against experimental test results at the level of the single-pin connection. Then, the numerical model of the single-storey CBF equipped with dissipative connections was verified against experimental test results obtained under quasi-static displacement loading. All experimental test results were obtained from researchers involved in the INERD project. In addition, the experimental results were used to devise a design method for dissipative single-pin connections. The results of the numerical models were compared to the proposed theoretical design model.

Finally, to investigate the behaviour of CBFs with dissipative devices versus a conventional CBF system, a comparative study was conducted for single- and two-storey CBF buildings, designed according to S16-2009 in conjunction with NBCC 2010 provisions. The two braced frames, with and without dissipative connections, were designed for Victoria, BC and were subjected to three ensembles of ground motions: crustal, subduction and near-field.

It was concluded that forces induced into the structure were reduced due to an increase in building period and the ductility of CBFs equipped with dissipative connections. Also, the amount of energy dissipated by pin devices increased significantly. Meanwhile, by lowering the forces triggered in CBF columns, the cost of their foundation reduces as well. However, further experimental tests are required for a better understanding of the behaviour of the pin in a frame environment. During this research,

some limitations regarding pin size and structure height are recommended. To overcome the force limit of a single-pin connection, further research is proposed to develop double-pin and multi-pin dissipative connections.

ACKNOWLEDGEMENTS

I would like to begin by expressing my greatest thanks to my mentor and professor, Dr. Lucia Tirca. Without her endless help and support none of this would be possible. I am very grateful for all the time and effort she offered in helping me complete this great chapter in my life. I have learned so much through her enlightening lectures and vast knowledge in this field.

Thank you to Concordia University and its wonderful team of professors who have made my years in university some that I will never forget. Also, a special thanks to Dr. Luis Calado from Instituto Superior Técnico, Lisbon, Portugal and Dr. Carlo Castiglioni from Politecnico di Milano, Italy, for providing experimental test results. In addition, a special thanks to Dr. Andre Plumier from Université de Liège, Belgium and Dr. Ioannis Vayas from National Technical University of Athens, for providing theoretical results on their findings for the studied connection.

Mom, Dad, Stefano, and Anthony, you are my foundation. I will forever be indebted to you for your endless love and support. Your words of wisdom and love were always the ones to keep me going. Thank you for being so optimistic when it just didn't seem possible. I love you and I hope to inspire you as much as you have me.

To my wonderful extended family, I am finished! I know it took me a while, but I have finally made it and I could not have done it without you! I have held all your words of encouragement near and dear to my heart. Without them I would not have made it this far. Thank you and I love you.

To my best friend, Saby, who has been there with me before this whole process began, thank you for putting up with me through all of this. All I can ever hope for is that I am to you as much of a sister as you have been to me. Thank you Luf!

Last, but not at all least, Nicolae, Zhi, Juan David, Leon, it's been quite a journey! I know that some of you have finished and moved on to bigger and better things, and I wish you all the best of luck in your life endeavors, but I would also like to thank you for making my years as a graduate student some unforgettable ones. I hope our paths will cross again in the future!

TABLE OF CONTENTS

LIST OF FIGURES	xi
LIST OF TABLES	xxi
LIST OF EQUATIONS.....	xxii
Chapter 1. Introduction	1
1.1 General.....	1
1.2 Objectives and Scope.....	3
1.3 Description and Methodology	3
1.4 Thesis Organization.....	5
Chapter 2. Literature Review.....	7
2.1 General Overview	7
2.2 Ring Fuses	8
2.3 HSS Brace Fuse.....	9
2.4 Cut-Out Ductile Fuses for Angle Braces.....	10
2.5 Dissipative Single-Pin Connection Device.....	12
2.5.1 European Experimental Testing of Pin-Connection Behaviour.....	13
2.5.2 European Experimental Testing of an X-Braced Frame Equipped with Pin-Connections.....	15
2.5.3 Previous Modelling of Dissipative Pin Connections	16
2.5.3.1 FE Model.....	16
2.5.3.2 Previous Development of the Beam Model	18
2.5.4 Previous Theoretical Beam Model.....	19
2.6 Yielding Brace System (YBS).....	21
Chapter 3. Modelling and Design of Dissipative Single-Pin Connections.....	22
3.1 Experimental Test Results Used to Design and Calibrate the OpenSees Model of Dissipative Single-Pin Connections	24

3.2 Theoretical Study of the Dissipative Single-Pin Connection; Simple Beam Model	30
3.3 OpenSees Beam Model	35
3.4 Numerical Modelling of Dissipative Single-Pin Connections	41
3.4.1 Integrative Model for Use in Braced Frame Analysis	41
3.4.2 Calibration of the Integrative Model.....	44
3.5 Experimental Testing of a CBF Equipped with Dissipative Single-Pin Connections	47
3.6 Numerical Modelling of the Experimentally Tested Braced Frame Equipped with Single-Pin Connections Using OpenSees.....	49
Chapter 4. Seismic Analysis of Low-Rise Concentrically Braced Frames with Traditional Gusset Plate Connections Using OpenSees	58
4.1 Design of One-Storey and Two-Storey Concentrically Braced Frames	58
4.1.1 Building Description and Load Definitions.....	58
4.1.2 SFRS Brace Selection.....	62
4.1.3 SFRS Beam and Column Design.....	63
4.2 Modelling of the Single- and Two-Storey CBF Buildings in OpenSees.....	65
4.2.1 The OpenSees Framework.....	65
4.2.2 Modelling of Beams and Columns	66
4.2.3 Modelling of Braces.....	70
4.2.4 Tridimensional Modelling of Gusset Plates.....	71
4.2.5 Dynamic Analysis in OpenSees.....	73
4.3 Selection and Scaling of Ground Motions.....	74
4.3.1 Selection of Ground Motions.....	74
4.3.2 Scaling of Ground Motions.....	75
4.3.2.1 Ground Motion Scaling for the Single-Storey Building	76
4.3.2.2 Ground Motion Scaling for the Two-Storey Building	80
4.4 Seismic Response of Studied CBFs	81
4.4.1 Single-Storey CBF building.....	81

4.4.2 Two-Storey CBF Building.....	88
Chapter 5. Seismic Analysis of Low-Rise Structures Equipped with Dissipative Single- Pin Connections Using OpenSees.....	96
5.1 Design of the Dissipative Single-Pin Connections.....	96
5.1.1 Design of the Connection for the Single-Storey Structure	96
5.1.2 Design of the Connections for the Two-Storey Structure.....	99
5.2 Scaling and Simulation of Ground Motions.....	103
5.2.1 Scaling of Ground Motions for the Single-Storey Structure with Dissipative Single-Pin Connections.....	104
5.2.2 Scaling of Ground Motions for the Two-Storey Structure with Dissipative Single- Pin Connections.....	106
5.3 Seismic Response of Studied CBFs with Single-Pin Connections	108
5.3.1 Single-Storey CBF Building with Single-Pin Connections.....	108
5.3.2 Two-Storey CBF Building with Single-Pin Connections.....	120
5.3.3 Residual Deformations.....	135
5.4 Limitations of the Dissipative Single Pin Connection	137
5.4.1 Limitations with Respect to Pin Size.....	137
5.4.2 Limitations with Respect to Wind Loads.....	141
Chapter 6. Conclusion and Future Work	143
6.1 Conclusion.....	143
6.2 Future Work.....	146
REFERENCES.....	148
APPENDIX A - Selected Records.....	154

LIST OF FIGURES

Figure 2.1: Ring fuse in its original and deformed state (Tremblay et al., 2011).....	9
Figure 2.2: Configuration of a HSS brace fuse (Rezai et al., 2000)	11
Figure 2.3: Configuration of a cut-out ductile fuse (Desjardins and Légeron, 2010).....	11
Figure 2.4: Pin connection configuration (Vayas and Thanopoulos, 2005)	13
Figure 2.5: Failed rounded pin after being subjected to ECCS loading protocol (Calado, 2010)	14
Figure 2.6: Global frame test set-up (Castiglioni, 2010)	15
Figure 2.7: Finite element model of the quarter connection (Vayas and Thanopoulos, 2005)	17
Figure 2.8: SOFISTIK beam model (Plumier et al., 2004).....	18
Figure 2.9: Configuration of a Yielding Brace System (YBS) (Gray et al., 2010)	21
Figure 3.1: Geometrical properties of the dissipative single-pin connection	25
Figure 3.2: Pin Geometries used in experimental testing (Calado, 2010)	26
Figure 3.3: Loading protocols used in the experimental testing of the dissipative single- pin connections (Calado, 2010).....	27
Figure 3.4: a) Failed specimen P-A9, b) Failed specimen P-3, c) Failed specimen P-A6, d) Failed specimen P-2, (Calado, 2010).....	28
Figure 3.5: Hysteresis loops of single-pin connection responses obtained during the experimental tests under the ECCS displacement loading protocol (Calado, 2010) ...	29
Figure 3.6: Energy dissipation comparison between specimens P-A6 and P-A9.....	30
Figure 3.7: Proposed behaviour of the pin in a dissipative single-pin connection	31

Figure 3.8: Tri-linear curve.....	32
Figure 3.9: Dissipative single-pin connection configuration.....	35
Figure 3.10: Tri-linear curve of the 40x60mm dissipative single-pin connection.....	35
Figure 3.11: OpenSees beam model	36
Figure 3.12: Deformation of the dissipative single-pin connection during experimental testing (Calado, 2010)	37
Figure 3.13: Effective length of the outer plate	38
Figure 3.14: Comparison between the simple beam model and OpenSees tri-linear curves for the P-A9 sample	39
Figure 3.15: a) Strain diagram of OpenSees beam model replicating the P-A9 device, b) Stress diagram of OpenSees beam model at pin’s mid-length replicating the P-A9 device behaviour	40
Figure 3.16: Pinching4 material definition	42
Figure 3.17: Integrative OpenSees model.....	43
Figure 3.18: Hysteresis loops recorded from the OpenSees model vs. experimental test results: a) P- A9, b) P- 3.....	45
Figure 3.19: Energy dissipated per cycle for specimens P-A9 and P-3	46
Figure 3.20: Cumulative energy dissipated for specimens P-A9 and P-3	46
Figure 3.21: Milano experimental frame set-up (Plumier et al., 2004)	47
Figure 3.22: Brace equipped with connection and subjected to tensile forces	48
Figure 3.23: The OpenSees model of the experimentally tested CBF with single-pin connection devices	50
Figure 3.24: Loading protocols used for testing of the OpenSees braced frame models .	51

Figure 3.25: Deformation of dissipative single-pin connection when the brace is subjected to tensile and compressive forces.....	53
Figure 3.26: a) OpenSees frame response vs. experimental frame response (ECCS), b) OpenSees pin response vs. experimental pin response (ECCS)	53
Figure 3.27: a) OpenSees frame response vs. experimental frame response (AISC), b) OpenSees pin response vs. experimental pin response (AISC)	54
Figure 3.28: Comparison of cumulated energy dissipated during the experimental test using ECCS loading, the replicated computer model under the ECCS and AISC loading.....	55
Figure 3.29: Time series of the base shear response of the modelled CBF with and without single-pin connections using OpenSees	56
Figure 3.30: a) Bottom pin behaviour of tension brace (CBF with pins, ECCS), b) Top pin behaviour of tension brace (CBF with pins, ECCS), c) Tensile brace behaviour (CBF with pins, ECCS).....	57
Figure 3.31: a) Braced Frame displacement, CBF (ECCS), b) Tension and compression brace displacement (ECCS)	57
Figure 4.1: a) Plan view of studied buildings , b) CBF elevation of one-storey building model, c) CBF elevation of 2-storey building model.....	60
Figure 4.2: UHS for Victoria, B.C.....	61
Figure 4.3: Overview of the OpenSees Framework (Mazzoni et al., 2007)	66
Figure 4.4: Response of the OpenSees Steel02 material (Mazzoni et al., 2007)	67
Figure 4.5: OpenSees beam with hinges elements (Mazzoni et al., 2007)	68
Figure 4.6: Discretization of the beam and column cross sections in OpenSees.....	68

Figure 4.7: OpenSees model of the single- and two-storey structures	69
Figure 4.8: Discretization of the HSS brace cross-section	70
Figure 4.9: Sizing of the gusset plates (adapted from Izvernari, 2007).....	72
Figure 4.10: Victoria’s UHS.....	78
Figure 4.11: Scaled spectral acceleration for single-storey building - a) Crustal, b) Subduction, c) Near-Field	79
Figure 4.12: Scaled spectral acceleration for two-storey building - a) Crustal, b) Subduction, c) Near-Field	81
Figure 4.13: Time history response for C2 record - a) Accelerogram, b) Base shear, c) Response of brace from joint #1 to #3 (Figure 4.7), d) Single-storey frame response	82
Figure 4.14: Time history response for C4 record - a) Accelerogram, b) Base shear, c) Response of brace from joint #1 to #3 (Figure 4.7), d) Single-storey frame response	83
Figure 4.15: Time history response for S1 record - a) Accelerogram, b) Base shear, c) Response of brace from joint #1 to #3 (Figure 4.7), d) Single-storey frame response	84
Figure 4.16: Time history response for S3 record - a) Accelerogram, b) Base shear, c) Response of brace from joint #1 to #3 (Figure 4.7), d) Single-storey frame response	85
Figure 4.17: Time history response for N1 record - a) Accelerogram, b) Base shear, c) Response of brace from joint #1 to #3 (Figure 4.7), d) Single-storey frame response	86
Figure 4.18: Time history response for N3 record - a) Accelerogram, b) Base shear, c) Response of brace from joint #1 to #3 (Figure 4.7), d) Single-storey frame response	87
Figure 4.19: Interstorey drift - Crustal ground motions.....	87
Figure 4.20: Time history response for C2 record - a) Accelerogram, b) Base shear	89

Figure 4.21: Hysteretic response for C2 record - a) Two-storey ground floor response, b) Two-storey second floor response	89
Figure 4.22: Hysteretic response for C2 record - a) Response of brace from joint #1 to #5 (Figure 4.7), b) Response of brace from joint #2 to #4 (Figure 4.7).....	90
Figure 4.23: Time history response for C4 record - a) Accelerogram, b) Base shear	91
Figure 4.24: Hysteretic response for C4 record - a) Two-storey ground floor response, b) Two-storey second floor response record	91
Figure 4.25: Hysteretic response for C4 record - a) Response of brace from joint #1 to #5 (Figure 4.7), b) Response of brace from joint #2 to #4 (Figure 4.7).....	92
Figure 4.26: Time history response for S1 record - a) Accelerogram, b) Base shear.....	93
Figure 4.27: Hysteretic response for S1 record - a) Two-storey ground floor response, b) Two-storey second floor response	93
Figure 4.28: Hysteretic response for S1 record - a) Response of brace from joint #1 to #5 (Figure 4.7), b) Response of brace from joint #2 to #4 (Figure 4.7).....	94
Figure 4.29: Time history response for S3 record - a) Accelerogram, b) Base shear.....	94
Figure 4.30: Hysteretic response for S3 record - a) Two-storey ground floor response, b) Two-storey second floor response	95
Figure 4.31: Hysteretic response for S3 record - a) Response of brace from joint #1 to #5 (Figure 4.7), b) Response of brace from joint #2 to #4 (Figure 4.7).....	95
Figure 4.32: Interstorey drift - Crustal ground motions.....	95
Figure 5.1: Design of the inner and outer plates.....	97
Figure 5.2: Pin design for the single-storey CBF- a) Theoretical tri-linear curve of the 35x50mm pin , b) OpenSees tri-linear curve comparison.....	98

Figure 5.3: a) Strain curve along the height of the cross-section of the 35x50mm pin connection, b) Stress curve along the height of the cross-section of the 35x50mm pin connection	99
Figure 5.4: Characteristics of the dissipative single-pin connection for the single-storey frame	99
Figure 5.5: Pin design for the two-storey CBF: a) Theoretical tri-linear curve of pin 30x55mm pin, b) OpenSees tri-linear curve comparison for 30x55mm pin, c) Theoretical tri-linear curve of pin 45x60mm pin, d) OpenSees tri-linear curve comparison of 45x60mm.....	101
Figure 5.6: a) Strain curve along the height of the cross-section (45x60), b) Stress curve along the height of the cross-section (45x60), c) Strain curve along the height of the cross-section (30x55), d) Stress curve along the height of the cross-section (30x55)	102
Figure 5.7: a) Pin geometry for the 45x60mm pin connection, b) Pin geometry for the 30x55mm pin connection.....	103
Figure 5.8: Scaled spectral acceleration for single-storey building - a) Crustal, b) Subduction, c) Near-Field	105
Figure 5.9: Scaled spectral acceleration for two-storey building - a) Crustal, b) Subduction, c) Near-Field	107
Figure 5.10: Time history response for C2 record - a) Accelerogram, b) Base shear	109
Figure 5.11: Single-storey frame response for C2 record.....	110
Figure 5.12: Hysteretic response of pin devices belonging to brace from joint #1 to #3 (Figure 4.7) for C2 record	110
Figure 5.13: Time history response for C4 record - a) Accelerogram, b) Base shear	111

Figure 5.14: Single-storey frame response for C4 record.....	111
Figure 5.15: Hysteretic response of pin devices belonging to brace from joint #1 to #3 (Figure 4.7) for C4 record	112
Figure 5.16: Time history response for S1 record - a) Accelerogram, b) Base shear.....	113
Figure 5.17: Single-storey frame response for S1 record	114
Figure 5.18: Hysteretic response of pin devices belonging to brace from joint #1 to #3 (Figure 4.7) for S1 record.....	114
Figure 5.19: Time history response for S3 record - a) Accelerogram, b) Base shear.....	115
Figure 5.20: Single-storey frame response for S3 record	115
Figure 5.21: Hysteretic response of pin devices belonging to brace from joint #1 to #3 (Figure 4.7) for S3 record.....	116
Figure 5.22: Time history response for N1 record - a) Accelerogram, b) Base shear	117
Figure 5.23: Single-storey frame response for N1 record.....	117
Figure 5.24: Hysteretic response of pin devices belonging to brace from joint #1 to #3 (Figure 4.7) for N1 record.....	118
Figure 5.25: Time history response for N3 record - a) Accelerogram, b) Base shear	118
Figure 5.26: Single-storey frame response for N3 record.....	119
Figure 5.27: Hysteretic response of pin devices belonging to brace from joint #1 to #3 (Figure 4.7) for N3 record.....	119
Figure 5.28: Interstorey drift - Crustal ground motions.....	119
Figure 5.29: Displacement ductility comparisons for single-storey CBF with and without dissipative single-pin connection under crustal ground motions	120

Figure 5.30: Two-storey CBF with pin devices: a) Accelerogram C2, b) Base shear time history response for C2 record	121
Figure 5.31: Two-storey CBF with pin devices: CBF response of ground floor for C2 record.....	122
Figure 5.32: Two-storey CBF with pin devices: Hysteretic response of pin devices located at ground floor and belonging to brace from joint #1 to #5 (Figure 4.7) for C2 record.....	123
Figure 5.33: Two-storey CBF with pin devices: CBF response of second floor for C2 record.....	123
Figure 5.34: Two-storey CBF with pin devices: Hysteretic response of pin devices located at the 2 nd floor and belonging to brace from joint #2 to #4 (Figure 4.7) for C2 record.....	124
Figure 5.35: Two-storey CBF with pin devices: a) Accelerogram C4, b) Base shear time history response for C4 record	124
Figure 5.36: Two-storey CBF with pin devices: CBF response of ground floor for C4 record.....	125
Figure 5.37: Two-storey CBF with pin devices: Hysteretic response of pin devices located at ground floor and belonging to brace from joint #1 to #5 (Figure 4.7) for C4 record.....	125
Figure 5.38: Two-storey CBF with pin devices: CBF response of 2 nd floor for C4 record	126
Figure 5.39: Two-storey CBF with pin devices Hysteretic response of pin devices located at 2 nd floor and belonging to brace from joint #2 to #4 (Figure 4.7) for C4 record ...	126

Figure 5.40: Two-storey CBF with pin devices: a) Accelerogram S1, b) Base shear time history response for S1 record.....	127
Figure 5.41: Two-storey CBF with pin devices: CBF response of ground floor for S1 record.....	128
Figure 5.42: Two-storey CBF with pin devices: Hysteretic response of pin devices located at ground floor and belonging to brace from joint #1 to #5 (Figure 4.7) for S1 record.....	128
Figure 5.43: Two-storey CBF with pin devices: CBF response of 2 nd for S1 record....	129
Figure 5.44: Two-storey CBF with pin devices: Hysteretic response of pin devices located at 2 nd floor and belonging to brace from joint #2 to #4 (Figure 4.7) for S1 record.....	129
Figure 5.45: Two-storey CBF with pin devices: a) Accelerogram S3, b) Base shear time history response for S3 record.....	130
Figure 5.46: Two-storey CBF with pin devices: Two-storey frame response of ground floor for S3 record.....	130
Figure 5.47: Two-storey CBF with pin devices: Hysteretic response of pin devices located at ground floor and belonging to brace from joint #1 to #5 (Figure 4.7) for S3 record.....	131
Figure 5.48: Two-storey CBF with pin devices: CBF response of 2 nd floor for S3 record	131
Figure 5.49: Two-storey CBF with pin devices: Hysteretic response of pin devices located at 2 nd floor and belonging to brace from joint #2 to #4 (Figure 4.7) for S3 record.....	132

Figure 5.50: Acceleration time history for N1 record.....	132
Figure 5.51: Time history responses for N1 record - a) Acceleration, b) Base shear, c) Interstorey drift.....	133
Figure 5.52: Acceleration time history for N1 record.....	133
Figure 5.53: Time history responses for N3 record - a) Acceleration, b) Base shear, c) Interstorey drift.....	134
Figure 5.54: Interstorey drift - Crustal ground motions.....	134
Figure 5.55: Displacement ductility comparisons of two-storey frame with and without dissipative single-pin connection	135
Figure 5.56: Single-storey CBF with pin devices: a) Interstorey residual deformation under the studies ground motions, b) Maximum interstorey drift under the studies ground motions, c) Ratio of the interstorey residual deformation to the maximum interstorey drift.....	136
Figure 5.57: Two-storey structure - a) Interstorey residual deformation under the studies ground motions, b) Maximum interstorey drift under the studies ground motions, c) Ratio of the interstorey residual deformation to the maximum interstorey drift	137
Figure 5.58: Montreal and Victoria region storey shear for a 4-, and 8-storey structure with respect to storey shear limitation for single and double pin dissipative connections.....	140

LIST OF TABLES

Table 2.1: Design steps in determining pin geometries and the tri-linear curve (Plumier et al., 2004).....	20
Table 4.1: Seismic design data for Victoria, B.C., Canada as per Appendix C, NBCC 2010.....	61
Table 4.2: Load summary for 1-storey and 2-storey buildings.....	62
Table 4.3: Members selected for the single-storey CBF.....	65
Table 4.4: Members selected for the two-storey CBF.....	65
Table 4.5: Seismic design and building characteristics for the CBF with gusset plate connections.....	73
Table 4.6: Ground motion characteristics.....	77
Table 4.7: Ground motions and their respective scale factors for the single-storey structure with gusset plate connections.....	79
Table 4.8: Ground motions and their respective scale factors for the two-storey structure with gusset plate connections.....	80
Table 5.1: Seismic design and building characteristics for the CBF equipped with single-pin connections.....	104
Table 5.2: Ground motions and their respective scale factors for the single-storey structure with single-pin connections.....	105
Table 5.3: Ground motions and their respective scale factors for the two-storey structure with single-pin connections.....	106
Table 5.4: Pin design for 4- and 8-storey structures in Montreal and Victoria regions..	139
Table 5.5: Alternative design for the 4- and 8-storey structure in the Victoria region...	140

LIST OF EQUATIONS

Equation 3.1	32
Equation 3.2	33
Equation 3.3	33
Equation 3.4	34
Equation 3.5	34
Equation 3.6	34
Equation 3.7	34
Equation 3.8	41
Equation 4.1	58
Equation 4.2	59
Equation 4.3	59
Equation 4.4	59
Equation 4.5	61
Equation 4.6	62
Equation 4.7	62
Equation 4.8	62
Equation 4.9	63
Equation 4.10	63
Equation 4.11	63
Equation 4.12	64
Equation 4.13	64
Equation 4.14	64
Equation 4.15	71
Equation 4.16	71
Equation 4.17	71
Equation 4.18	72
Equation 4.19	72
Equation 4.20	72
Equation 4.21	76

Equation 4.22	76
Equation 5.1	141
Equation 5.2	141
Equation 5.3	141

Chapter 1. Introduction

1.1 General

An efficient seismic force resisting system should possess enough strength (member forces are lower than the factored resistance), supply adequate stiffness to limit the system's deformation, and exhibit sufficient ductility. Thus, concentrically braced frames are characterized by a high stiffness-to-weight ratio and limited ductility. The dissipative zones of the traditional CBF systems are located in the brace members, which are designed to yield in tension and buckle in compression. However, during the hysteresis response, braces on the verge of buckling lose their buckling strength, which causes deterioration in storey shear resistance. Also, the degradation of the buckling strength causes an asymmetrical frame response when subjected to lateral loads.

To overcome this deficiency, a solution could be to relocate the dissipative region of the concentrically braced frame from the braces to their connections. For example, in Eurocode 8, it is suggested that the location of dissipative zones may be placed "either in the structural members or in the connections". Also, it states that "the overstrength condition for connections need not apply if the connections are designed to contribute significantly to the energy dissipation capability" of the system. Therefore, the main purpose of this research is to analyze the behaviour of low-rise concentrically braced frames equipped with dissipative single-pin connections, by means of numerical models using OpenSees (Open System for Earthquake Engineering Simulation). This finite element software is an open source framework developed for earthquake engineering applications (McKenna et al., 2004).

Initially, the single-pin connection device was proposed and experimentally tested during the European INERD (Innovations for Earthquake Resistant Desing) project (Plumier et al., 2005). In addition, in the frame of the aforementioned research project, experimental tests were carried out for a single-storey, full scale braced frame in X-bracing configuration, equipped with single-pin devices, and it was subjected to quasi-static displacement loading. The single-pin connection consists of two outer plates connected to the column, two inner plates connected to the brace member and a pin passing through the plates. In this type of configuration, the pin transfers the axial forces developed in the attached brace to the adjacent column. For the pin member, designed to behave in bending, it was suggested to use a rectangular cross-section with rounded corners. Thus, the dissipative zone of the connection device is located in the pin, which yields in bending, while the remaining connection components are designed to respond in elastic range. When subjected to earthquake loads, CBFs equipped with dissipative single-pin connections allow braces to develop 60 to 80% of their compressive strength, while buckling is prevented. Nevertheless, when dissipative zones are located in the connections and yielding is expected to occur in the pin, adjacent members shall be designed with sufficient overstrength.

The main advantage of this dissipative connection is its ability to reduce the cost and the replacement duration of a failed brace connection system due to seismic activity. To maintain the brace response in elastic range, the capacity at yield of the dissipative connection is designed to be 60 to 80% of the brace compressive strength. Also, dissipative connections have the ability to reduce forces induced into a structure, due to their increased ductility factor. For cost-efficiency demand, this connection can be

designed to satisfy the code requirements in terms of interstorey drift limitations, while increasing the ductility of the structure.

1.2 Objectives and Scope

The objectives of this research are as follows:

- ❖ Develop a numerical model that is validated against experimental test results, as well as propose an analytical method for preliminary design of the single-pin device. The outcome of this objective is to gain an overall knowledge of the behaviour of dissipative single-pin connection devices.
- ❖ Develop a numerical model for the single-storey X-braced frame system, equipped with single-pin devices using OpenSees, and validate it against experimental test results. The main outcome of this objective is to obtain an accurate computer model able to provide confident results under cyclic loading.
- ❖ To analyze the behaviour of low-rise concentrically braced frames (CBFs), equipped with dissipative single-pin connections, under earthquake loads. A comparative behavioural study between conventional CBFs and CBFs with dissipative connections is carried out. Herein, the main outcome is to quantify the ability of the CBF system, equipped with dissipative single-pin connections, to resist earthquake loads.

1.3 Description and Methodology

In order to attain the abovementioned objectives the following methodology is employed:

- ❖ Study the behaviour of pin members through the analogy of a 4 point loaded beam, under incremental loading, until failure is reached. The complexity of its behaviour

from elastic to plastic is to simulate the changes that occur at the support level, while evolving from a simple to a fixed support. The tri-linear force displacement curve, built analytically with the purpose of simulating the pin's behaviour, is validated with the computer model developed in OpenSees. In this phase, a preliminary calibration of the *Pinching4* material, defined in OpenSees and selected to simulate the changes in the restraint degree at the support level, is performed. Then, the numerical model of the connection device is validated against experimental test results obtained in the European testing under quasi-static displacement loading.

- ❖ During the second step, the accuracy of the computer model is validated. Thus, the single-storey frame, subjected to experimental tests under quasi-static displacement loading in Europe, is simulated in OpenSees. The brace-to-column dissipative connections are defined by using the knowledge developed above. Thus, the numerical model of the single-storey X-braced frame equipped with dissipative connections is validated with the European experimental test results.
- ❖ To analyze the seismic behaviour of low-rise braced frames equipped with dissipative devices and located in Victoria, BC, three ensembles of 7 ground motions each, representing the crustal, subduction and near-field group, are selected and scaled in agreement with the ASCE/ SEI 2007 procedure in order to fit the uniform hazard spectrum (UHS) for Victoria. Although the near-field ground motions with forward directivity and distinctive velocity-pulses are not characteristic for the Victoria region, they are chosen to analyze their effect on the seismic response of the studied system.

- ❖ To emphasize the system behaviour, a comparison of the system response with and without dissipative single-pin connections is carried out. The limitations of using the dissipative single-pin connection are also studied.

1.4 Thesis Organization

The following research is devised into six chapters starting with a brief introduction. A general overview of the objectives and scope of the research is presented. A brief description and methodologies employed are also described in this introductory chapter.

Chapter two is an overview of past studies that have been used in the advancement of the research in this thesis. Different types of dissipative systems composed of braces and the adjacent brace to beam/column connections are described. In addition, a general overview of experimental tests performed on the dissipative single-pin connection during the INERD project is reviewed.

The third chapter explains the behaviour of the single-pin connection device as well as the process of validating the numerical models built using OpenSees and calibrated against the INERD project experimental tests results. From the simulated pin model, a modified analytical method for preliminary design of the pin member is deduced. Using this preliminary design method, a numerical model of the connection is devised and validated against the experimental test results. Finally, a numerical model replicating the experimental test of a full scale single-storey X-braced frame equipped with dissipative single-pin connections, carried out in Milano, Italy, is built and the seismic response under a displacement loading protocol is validated using experimental test results.

In the fourth chapter, a single- and two-storey concentrically braced frame with gusset plate connections are designed using CSA/S16-2009 and NBCC 2010 provisions and are modelled in OpenSees. Also, sets of ground motions are chosen and scaled with respect to methods described in FEMA356 and ASCE/SEI-2007 provisions. The frames are then both subjected to crustal, subduction and near-field ground motions for the Victoria, B.C., region. Parameters such as strength, deformation and ductility are then studied.

The next step, found in Chapter five, is to equip the same frames tested in Chapter four with dissipative single-pin connections and subject them to the same set of ground motions. The connections are designed with the method devised in Chapter three. The results of the numerical models, being subjected to the seismic activity, are then compared to the results of a conventional concentrically braced frame (CBF) in order to analyze the effects of the connection on the frame response.

Finally, conclusions are given in Chapter six, as well as recommendations for future work.

Chapter 2. Literature Review

2.1 General Overview

Concentrically braced frames are widely used in Canada as seismic force resisting systems. The design philosophy behind this type of structure is to design braces to dissipate the seismic input energy through yielding or buckling, while all other members of the structure behave in elastic range. This braced frame system provides high lateral stiffness, adequate strength and low ductility. The main drawbacks of this seismic force resisting system are:

- CBFs are prone to asymmetrical behaviour after braces have buckled and their buckling strength is consumed;
- CBFs exhibit concentration of deformation within a floor that causes the storey mechanism formation;
- Due to their large stiffness, the system is subjected to large base shear demand;
- Replacement of braces after buckling has occurred is a costly and time consuming task.

In order to avoid the aforementioned drawbacks, during the last decades, several researchers (Plumier et al., 2006; Tremblay et al., 2011; Gray et al., 2010; Desjardins and Légeron, 2010; Kassis and Tremblay, 2008; Constantinou and Symans, 1993; Vayas and Thanopoulos, 2005; Rezai et al., 2000) have proposed innovative earthquake resistant braced frame systems that incorporate different types of devices at the level of the braces or at the level of the brace connections.

In this light, the main concept is to prevent the buckling of braces by adding different types of fuses, either at the brace level or at the level of their connections. By applying these techniques, braces are enforced to respond in elastic range. These devices, better known as fuses, prove to minimize tension/compression ratios and to diminish the asymmetrical response of the structure. The fuses also generate higher energy dissipation and reduce the base shear induced into the structure by lateral forces. Another advantage of fuse brace connections is that they limit structural damage in the connections, a smaller region of the structure, therefore improving the cost effectiveness of the replacement of damaged structural components.

In the following sections, different types of fuse devices, that can be employed either at the level of braces or at their connections, are presented. In addition, these fuses can be incorporated in both new and existing CBF systems. Fuses that are added at the level of the braces are as follows: ring fuses; HSS brace fuses; cut-out ductile fuses for angle braces, buckling restrained braces and others, while fuses acting at a brace-to-frame connection level are: single-pin connection device; double-pin connection device; yielding brace system and others.

2.2 Ring Fuses

Among the research conducted at McGill University, a ring fuse was added at the mid-span of the brace in order to avoid buckling of braces. This ring fuse consists of a steel ring placed to yield in tension, as shown in Figure 2.1. The fuse provides the frame with ductility and limits the forces transferred to other members of the structure, including the braces. The fuse was originally studied in New Zealand, in the 1980's, and its configuration was different from the one shown in Figure 2.1. The pushover test in

tension concluded that with this type of fuse, a more gradual yielding at lower force levels as well as consistent strain hardening is inhibited. There was a significant increase in deformation capacity and the fuse proved to be an affordable solution for the seismic upgrade of low rise buildings. Tests are still ongoing for this type of fuse system, with hopes of improving the system's behaviour.

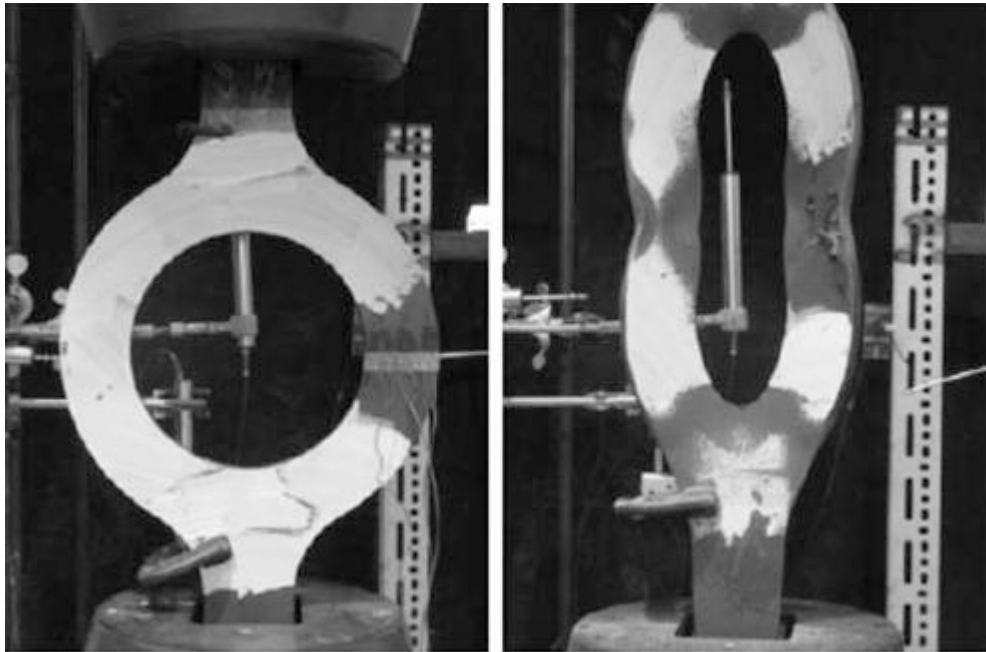


Figure 2.1: Ring fuse in its original and deformed state (Tremblay et al., 2011)

2.3 HSS Brace Fuse

In 2000, a fuse, fit for square and rectangular tubular braces, which performs with a higher compressive resistance, was studied and tested at École Polytechnique de Montréal (Rezai et al., 2000; Kassis and Tremblay, 2008; Tremblay et al. 2011). The fuse consisted of a HSS brace cut along its mid span. The cut starts at a short distance from the brace ends and is held by four angles, welded onto either side of the tube. These angles transferred the loads between the two end brace segments split by the cut. The legs

of the angle were trimmed in order to achieve the desired brace tensile resistance. The length over which the angles were trimmed was designed to allow deformations without exhibiting any fractures in the angles. The inward and outward buckling of the brace, at the area of the cut, was avoided by the built up box consisting of the angles and the internal support of the tubular brace, as illustrated in Figure 2.2.

Full scale quasi-static and dynamic testing was performed on a single diagonal brace and various fuse designs. There were many advantages observed during the testing process. Firstly, the fuse reached the design ductility prior to its fracture in tension and the peak forces and strain hardening were easily predicted. One of the downfalls of the fuse was that the yield resistance was greater than the compressive resistance, therefore the braces buckled in compression while the fuse yielded in tension. It was found that in order to minimize this effect, more attention had to be paid to the width-to-thickness ratios of the brace cross-sections. This would in effect eliminate the low-cycle fatigue failure from local buckling at brace plastic hinge locations.

A numerical model was also built, exhibiting a new structure subjected to a non-linear seismic analysis. This study proved that the ductility demand of the structure was increased and therefore underwent larger lateral deformations.

2.4 Cut-Out Ductile Fuses for Angle Braces

Approximately ten years after the study of a HSS brace fuse at École Polytechnique, researchers, at the University of Sherbrooke, devised a fuse called the Cut-out Ductile fuse for angle braces. This fuse consists of locally reducing the cross section of a brace by creating a transition zone, as shown in Figure 2.3. This zone is created by machine cutting circular sections at the fuse ends. This type of fuse can be

used in existing, tension only, concentrically braced frames by ensuring that the tensile resistance of the fuse does not exceed the tensile resistance of the brace connection. Also, minimum ductility is achieved by limiting the strain in the fuse to 5%.

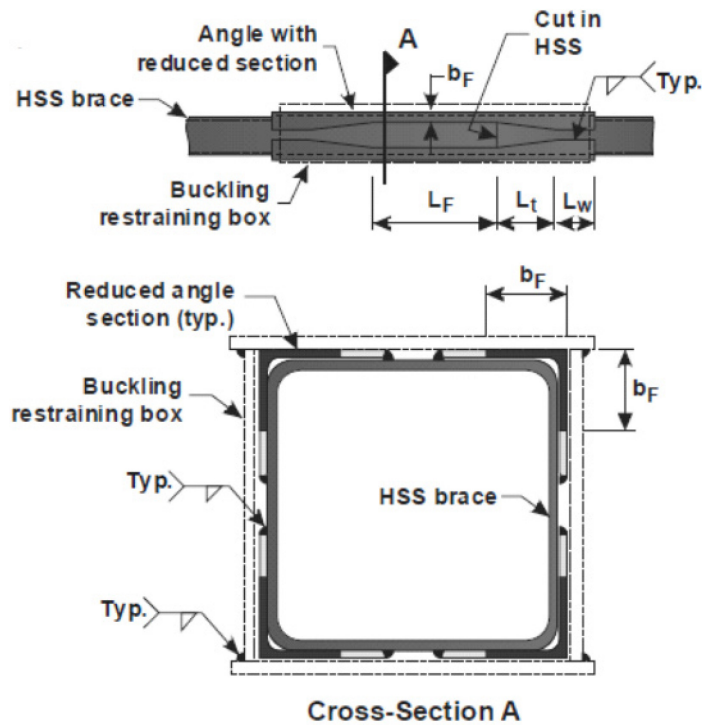


Figure 2.2: Configuration of a HSS brace fuse (Rezai et al., 2000)



Figure 2.3: Configuration of a cut-out ductile fuse (Desjardins and Légeron, 2010)

Large scale testing was performed with respect to different design assumptions such as fuse geometries and locating the fuses on different areas of the brace. Results from testing proved that the fuses lowered axial force in the braces and increased the ductility of the structure by significant amounts. The cycles endured by the structure, with and without the fuses, were the same and stable and gradual strain hardening was observed despite the loss of compression capacity in the brace.

The loss of compressive resistance is one of the downfalls of a concentrically braced frame, and in order to improve the response of the fuse, four shorter fuses along the brace length were tested. This reduced the loss of compressive resistance, but at the same time caused the structure to fail after a lower number of cycles due to a lower ductility. It also caused an unbalance in forces between the two braces due to excessive curvature demand.

While these type of fuses are not designed to reach equal resistance in tension and compression, their storey shear resistance was greater than the design storey shear resistance and the higher axial loads, which developed in the tension brace, compensated for the loss of compressive resistance. Further testing is required in order to have a clear understanding of this fuse connection.

2.5 Dissipative Single-Pin Connection Device

In order to enhance the behaviour of CBF systems, while braces respond in elastic range, an innovative dissipative connection was proposed in the frame of the European INERD project. The connection consists of two outer plates bolted or welded to the column, two inner plates welded to the braces, and a pin running through the four plates, as shown in Figure 2.4. As is illustrated, the pin has a rectangular cross-section. To

ensure that the buckling of the pin occurs in plane, the pin is subjected to bending on the weak axis of its cross-section.

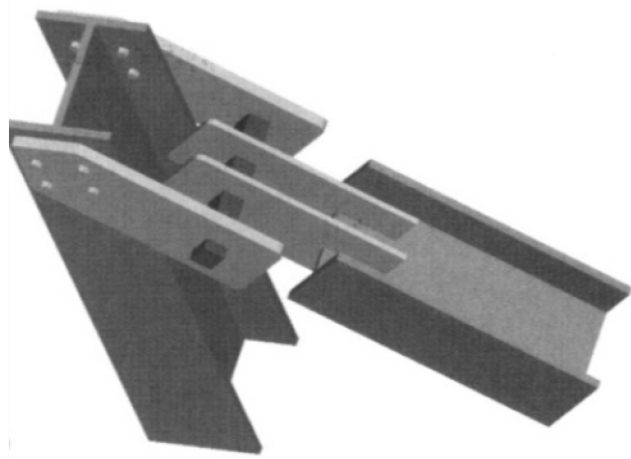


Figure 2.4: Pin connection configuration (Vayas and Thanopoulos, 2005)

Regarding pin devices, several experimental tests were conducted at Instituto Superior Tecnico, in Portugal (Calado, 2010), with the aim to exhibit the pins' behaviour under cyclic loading and to determine how certain geometrical properties influence the behaviour of the connection. Further on, experimental testing of the pin behaviour, in the full scale CBF frame, was conducted at the Politecnico di Milano (Castiglioni, 2010). In order to provide a simple design method for the pin connections, numerical modelling and finite element assessments of the connection device, using Abaqus, were conducted in Athens, Greece (Vayas and Thanopoulos, 2004).

2.5.1 European Experimental Testing of Pin-Connection Behaviour

Experimental tests were conducted, within the frame of the INERD project, in order to determine the behaviour of the connection under quasi-static cyclic displacement loading and the effects of different geometrical properties of connection members

(Plumier et al., 2004). Both rectangular, 60mmx40mm, and rounded pins, with a diameter of 50mm, were tested with different distances between the inner plates, namely 50mm and 70mm. The energy dissipation and the number of cycles exhibited before rupture were used to compare the effectiveness of the connections, built up with the aforementioned pins. All specimens were subjected to quasi-static displacement loading that complies with the ECCS loading protocol (ECCS, 1986). In Figure 2.5, two failed pins are shown (Calado, 2010). Two failure location points were observed during the testing period. When the distance between the outer plate and the inner plate is larger than the distance between the inner plates, the failure occurs in the longer pin segment at the external face of the inner plate (Figure 2.5). When the distance between the inner plates is larger, the failure occurs in the middle segment at the internal face of the inner plate (Figure 2.5).

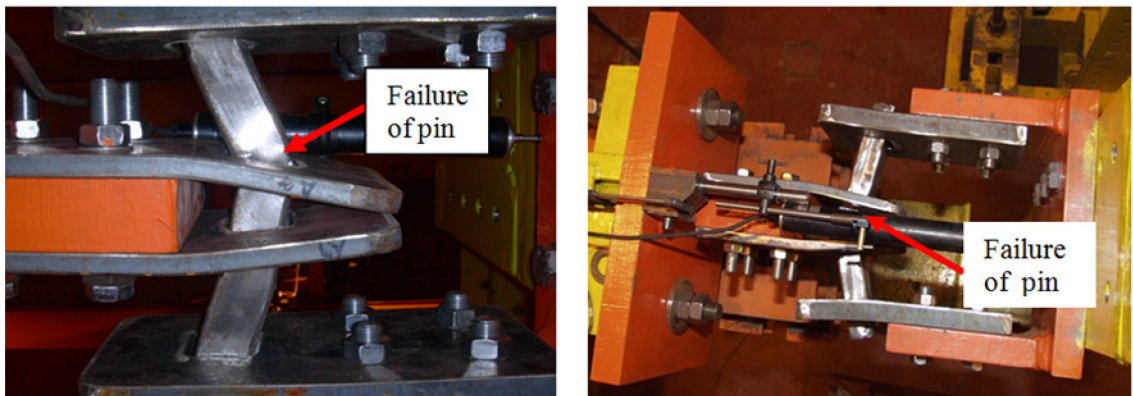


Figure 2.5: Failed rounded pin after being subjected to ECCS loading protocol (Calado, 2010)

It was concluded that dissipative connection behaviour improves with increasing distance of the inner plates and the failure mechanism is changed as well. On the other hand, the behaviour of the rectangular pin proved better than for the rounded pins when

subjected to the ECCS loading protocol, although the circular pin has equal moment of inertia on both axes.

2.5.2 European Experimental Testing of an X-Braced Frame Equipped with Pin-Connections

Cyclic quasi-static tests were performed on a large scale concentrically braced frame with X-bracing configuration and dissipative pin connections attached at both braces ends, as shown in Figure 2.6. The geometric properties of the pin were the same as above, rectangular (60mmx40mm) and rounded (50mm diameter) pins with 50mm and 70mm distances between the outer plates. The frames were subjected to the ECCS loading protocol as well as a ground motion and the tests were carried out in displacement control mode. The main objectives of the large scale testing of the frame were to determine the yield force, yield displacement, elastic stiffness and the dissipated energy of the frame.



Figure 2.6: Global frame test set-up (Castiglioni, 2010)

The members of the frame were selected from the ARBED tables (ARBED, 1982). The columns used were HE240B, beams were HE200B and the braces selected

were HE160B. The properties of the steel used for the rectangular 60mmx40mm pin were, $F_y=396MPa$, $F_u=558MPa$, and for the rounded 50mm diameter pin they were, $F_y=331MPa$, $F_u=559MPa$.

The conclusions attained, after various testing, were that the rounded pin was able to resist larger amplitude forces due to lower torsional effects, while for smaller cycles the rectangular pin performed better. It was also found that the rounded pin dissipated more energy, due to its ability to perform better under larger amplitude cycles. These results are opposite of the results obtained when the connection was tested on its own, as described in section 2.5.1. It can be concluded that more experimental tests are needed in order to determine the best geometrical configuration required for an efficient performance.

2.5.3 Previous Modelling of Dissipative Pin Connections

2.5.3.1 FE Model

To simulate the behaviour of the pin connection, a finite element model was built using ABAQUS (Vayas and Thanopoulos, 2005). Due to the symmetry of the connection, the modelling of one quarter of the connection was sufficient. The model was then subjected to monotonic and cyclic loads, and the stress developed was observed. This series of testing shed light on the different components of the connection and how they affect its behaviour. The main factors were the inner and outer plates connecting the pin to the column/beam and the brace. A depiction of the stress distribution in the quarter connection can be seen in Figure 2.7.

Pinching was observed due to the enlargement of the holes in the outer plates. This deformation of the holes was caused by large bearing stresses formed from the

contact of the pin and the outer plate when the pin deformed. While the yielding of the pin depends on its geometrical and material properties, it was found that the thickness of the outer plates also plays a role in the deformation properties of the pin. A thicker outer plate increases the clamping effect caused by the bearing stress, but it also increases the connection strength in its inelastic region. It was found that when the thickness of the outer plate is 75% that of the pin, the strength of the connection is maximized and the compressive and tensile resistance of the connection are almost equal. Any increase in thickness of the outer plate above 75% of the pin thickness does not improve the strength of the connection by any relevance.

Also, an important design factor was observed, namely in order to minimize the out of plane bending of the outer plates up to 90%, the minimal thickness of the outer plates should be 50% of the thickness of the pin. It is noted that when the brace behaves in tension, the outer plates act in compression and they tend to deform towards the exterior, while when the brace behaves in compression, the outer plates act in tension and they deform towards the interior.

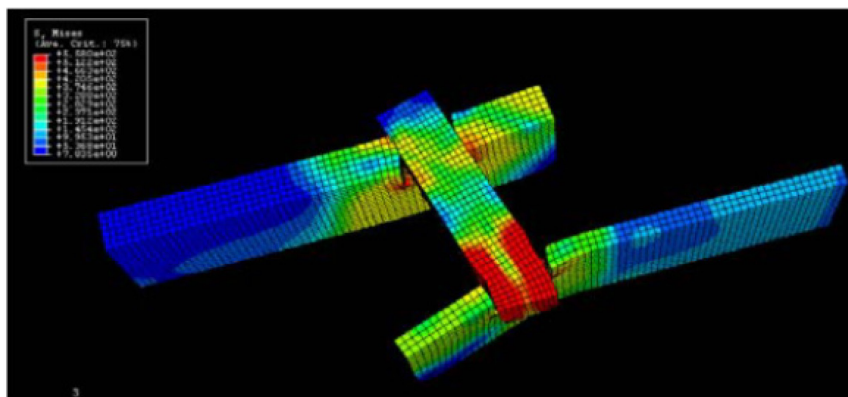


Figure 2.7: Finite element model of the quarter connection (Vayas and Thanopoulos, 2005)

2.5.3.2 Previous Development of the Beam Model

Another type of numerical modelling of the connection was performed in the frame of the INERD project (Plumier et. al, 2004). The SOFISTIK software (Sofistik, 2011), was used to model the connection as a simply supported beam that has rotational spring at its ends, which aim to simulate the outer plate reactions. The material used in the model was defined by a stress-strain diagram and the beam was divided into 10 elements. This provided a continual reading of stiffness at each loading step. Strain hardening of the material was approximated and was activated after the attainment of the yield stress. The overall span of the beam was taken as the free length of the pin, including half the thickness of the outer plate on each side. The loads on the beam were considered to be at the location of the inner plates, where the force is transferred from the brace to the connection, and the load was uniformly distributed along the thickness of the inner plate, as shown in Figure 2.8. The axial force developed in the brace is transferred through the inner plates to the pin member. It is proposed that the inner plate force acts as uniformly distributed load over its thickness.

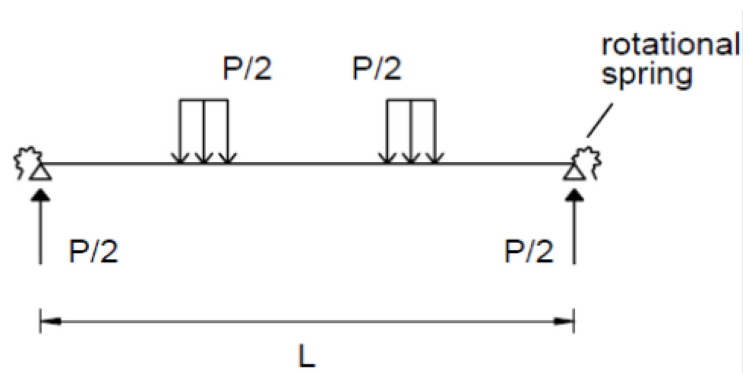


Figure 2.8: SOFISTIK beam model (Plumier et al., 2004)

Initially the beam behaved as simply supported beam because its stiffness was higher than the stiffness in the rotational springs. The rotational springs attracted no moment until yielding began in the sections under the applied loading. As the beam stiffness decreased because of yielding, the stiffness in the springs gradually increased. This behaviour occurred until yielding began near the end supports, followed by a significant increase in stiffness, while the moment in the springs increased at a slower rate. It was observed that the final maximum moments in the middle and at the ends of the beam, at ultimate states, were between the values of the full plastic moments when considering F_y and F_u as ultimate stresses.

It was concluded that for practical applications a theoretical beam model was required.

2.5.4 Previous Theoretical Beam Model

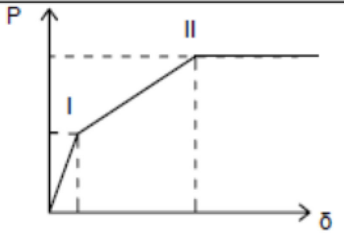
As the studies of the connection furthered and through the results of the beam model, devised using the SOFISTIK program, a simple theoretical design method was adopted for sizing the connection. The preliminary design method helps to size the pin member and to build the tri-linear curve capacity in terms of force-deformation.

The four point loaded beam was devised into two systems that follow each other. The first one was a simply supported beam until attainment of plastic moment at its ends, which at that point became a clamped beam.

A set of formulae were devised in order to build the tri-linear response of the connection and were dependant on the geometrical properties of the pin. These formulae are summarized in Table 2.1 and a more detailed explanation will follow in Chapter 3.

The European studies concluded that a dissipative pin connection will provide more ductility to the structure, without surpassing the code limitations of drift, in turn reducing the force induced into the structure. The energy dissipation from buckling or yielding is experienced by the single-pin connection and the brace behaves as all the other members would, in elastic range. Also, the response of the structure becomes symmetrical due to the equal amount of compressive and tensile resistances of the connection. Another advantage of the single-pin dissipative connection is the simplified installation process, time efficiency, and cost effectiveness of its replacement once the failure of the connection occurs.

Table 2.1: Design steps in determining pin geometries and the tri-linear curve (Plumier et al., 2004)

	Force P	Deformations δ
Point I "yielding y"	$P_y = \frac{2 \cdot M_p}{a}$	$\delta_y = 1,5 \cdot \frac{M_p}{EI} \cdot l^2 \cdot \frac{\alpha}{6} \cdot (3 - 4\alpha)$
Point II "ultimate u"	$P_u = \frac{4 \cdot M_u}{a}$	$\delta_{II} = 0,2 \cdot a$
Deformation capacity		$\delta_{lim} = 0,4 \cdot a$
$M_p = W_{pl} \cdot f_y$, $M_u = W_{pl} \cdot f_u$, $W_{pl} = b \cdot h^2 / 4$ (for rectangular pins) $l =$ pin length, $h =$ pin height, $b =$ pin width $a =$ axial distance between internal and external eye-bars $\alpha = a/l$ $f_y =$ yield stress of pin $f_u =$ tensile strength of pin		

2.6 Yielding Brace System (YBS)

Recently, a new type of fuse named the Yielding Brace System (YBS) was proposed and studied by researchers at the University of Toronto (Gray et al, 2010). This fuse is a result of creating a simple and straightforward connection in order to provide a structure with an amplified seismic functioning.

The connection consists of two steel casting members, welded to the ends of a wide flanged brace and connected to a middle yielding gusset system, specially designed for this type of connection. The yielding gusset system is composed of several yielding “fingers”, as illustrated in Figure 2.9. The main purpose of “finger” elements, which are triangular shaped plates, is to dissipate energy through yielding while acting in bending. The size and quantity of these fingers also controls the elastic stiffness of the connection. They possess a post-yield stiffness, which allows their deformation to increase as the deformation of the brace increases. Another advantage of this type of connection is its ability to reduce the risk of the soft story mechanism in a structure by maintaining all brace members in elastic range.

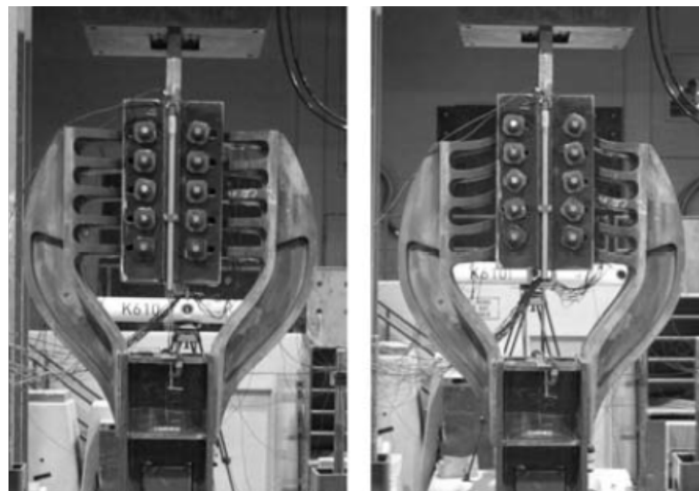


Figure 2.9: Configuration of a Yielding Brace System (YBS) (Gray et al., 2010)

Chapter 3. Modelling and Design of Dissipative Single-Pin Connections

Dissipative single-pin connections play a significant role in the improvement of the behaviour of concentrically braced frames. As mentioned in the previous chapters, the purpose of this study is to investigate the dissipative single-pin connection's behaviour through computer modelling and to propose simple design guidelines. In order to develop numerical simulation models, experimental test results are required. The first experimental testing of pin connections has been conducted in the frame of the INERD project (Plumier et al., 2004) at Instituto Superior Tecnico, Lisbon. In the frame of this project, the so-called pin connection is composed of a single-pin member, whose capacity in flexure depends on its geometry (length and cross-section). To extend the applicability of the proposed dissipative pin connection to multi-storey building applications the following configurations were proposed: single-pin, double-pin and multi-pin. Thus, in this study, the pin connection proposed in the frame of the INERD project is labeled the single-pin connection.

Regarding the study in this chapter, two papers were published under the supervision of Dr. Tirca. The first paper, "Behaviour of a Low-Rise Concentrically Braced Frame Building with and without Dissipative Pin Connections" (Tirca et al., 2011), consisted of a combined effort between all the authors. Works included developing Matlab algorithms to facilitate data processing and the study and development of loading protocols used in the research work as well as building and testing a model of the dissipative single-pin connection, in and out of the frame environment by using OpenSees. For the second paper, "Modelling and Design of Dissipative Connections for Brace-to-Column Joints" (Tirca et al., 05/2005), Dr. Calado, of Instituto Superior

Tecnico, emphasized on fatigue behaviour of the single-pin connection samples, while research conducted on dissipative single- and double-pin connections was conducted by the other authors.

In this research, four samples tested in 2003-2004 at Instituto Superior Tecnico, Lisbon, Portugal (Calado, 2010), are selected for computer model validation and to investigate the behaviour of single-pin connections in an X-braced frame environment. In addition, the results obtained by testing the single-storey braced frame, equipped with 60mmx40mm dissipative single-pin connections were carried out at Politecnico di Milano, are retained (Castiglioni, 2010). The braced frame, tested under quasi-static displacement cyclic loading, is a full scale single-storey braced frame in X-bracing configuration and is equipped with single-pin connections at both ends of the braces.

The purpose of incorporating single-pin connections in CBFs is to concentrate the dissipative energy in the brace-to-frame connections, while enabling braces to behave elastically, during which the CBF behaves in the non-linear range. Meanwhile, a CBF equipped with single-pin connections shows higher ductility than a traditional moderately ductile CBF.

In order to validate the design method applied to size the members of single-pin connections, three approaches are employed in this research: the simple (theoretical) beam model to size the pin device, the OpenSees beam model to validate the size of the pin device and the OpenSees model for the single-pin connection.

First, the simple beam model approach, proposed during the INERD project (Plumier et al. 2005; Vayas and Thanopoulos, 2005), is considered in this study. The

proposed equations are slightly modified in order to obtain a better match with the experimental test results.

Second, the simple beam model is replicated in OpenSees and incrementally loaded until failure occurs. This method is used to size the single-pin connection members, to validate it with the theoretical approach and to approximate the behaviour of the pin in non-linear range.

Third, the OpenSees model of the single-pin connection, cyclically loaded under a quasi-static displacement loading protocol, is validated against experimental test results.

Finally, the experimental braced frame, tested at Politecnico di Milano, is replicated in the OpenSees framework and the numerical results are compared to the experimental test results.

3.1 Experimental Test Results Used to Design and Calibrate the OpenSees Model of Dissipative Single-Pin Connections

In this study, the experimental test results of four single-pin connection samples that were carried out at Instituto Superior Tecnico, Lisbon (Calado, 2010), are selected. The purpose of the testing program, conducted on the behaviour of single-pin connections, was to decipher how certain geometrical properties of the connection, shown in Figure 3.1, influence their behaviour. Researchers have concluded that the most contributing parameters to the connection's behaviour are: the distance between the inner and outer plates, namely the parameter "a", and the geometrical shape and size of the pin member.

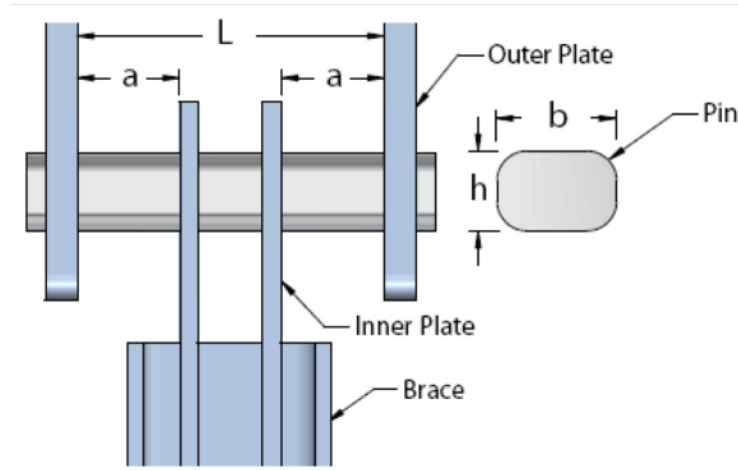


Figure 3.1: Geometrical properties of the dissipative single-pin connection

The four specimens, selected among others, are illustrated in Figure 3.2. Specimens P-3 and P-A9 consist of a rectangular 60mmx40mm pin with rounded corners. The difference between specimens P-3 and P-A9 is the distance between the inner plates, which is 70mm for P-3 and 50mm for P-A9. The other two specimens, P-2 and P-A6 exhibit a 50mmx40mm pin with two circular faces, as shown in Figure 3.2. The distance between the inner plates for specimen P-2 is 70mm and for the specimen P-A6 it is 50mm. The thickness of the inner plates is 15mm and the thickness of the outer plates is 30mm.

These four specimens were mounted on a box stand (Figure 3.4) and were subjected to quasi-static cyclic loading under displacement controls, developed in agreement with the ECCS loading protocols (ECCS,1986). The time-history protocol series consist of three successive cycles of equal displacement that are incrementally increased and repeated until failure is reached. The increment is a multiple of displacement at yield, Δ_y , while the duration is dependent on the rate of loading. The illustrated ECCS displacement loading protocols exhibit the same time series

displacement pattern with a maximum value close to 40 mm on both sides. However, the rate of loading was higher for specimens P-2 and P-3 than for P-A6 and P-A9, as explained further in section 3.4. The main failure mode observed in all cases was the rupture of the pin at the inner plate location. As shown in Figure 3.4, if the distance between the outer plate and inner plate is larger than that between the inner plates, the rupture of the pin occurs at the external face of the inner plate (see P-A9 and P-A6). When the distance between inner plates is larger (see P-2 and P-3), the rupture of the pin occurs at the internal face of the inner plate. However, this conclusion must be confirmed with further experimental tests.

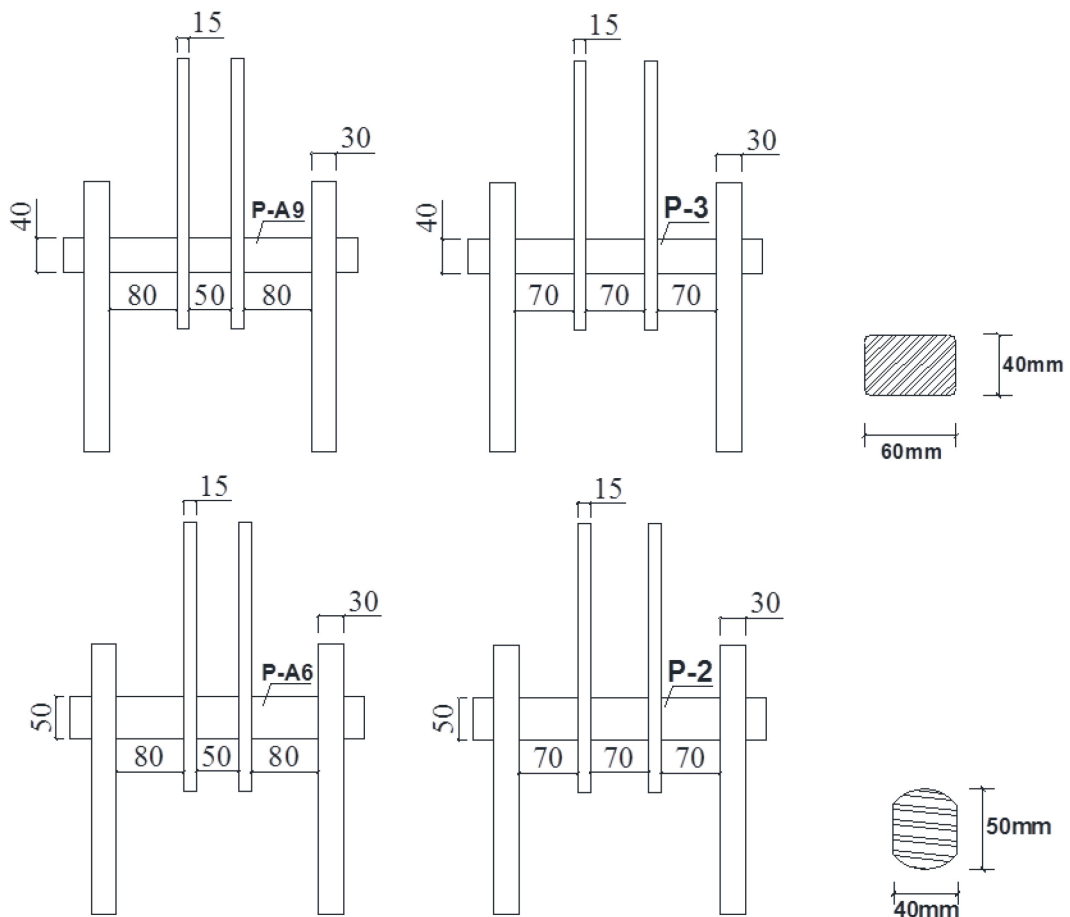


Figure 3.2: Pin Geometries used in experimental testing (Calado, 2010)

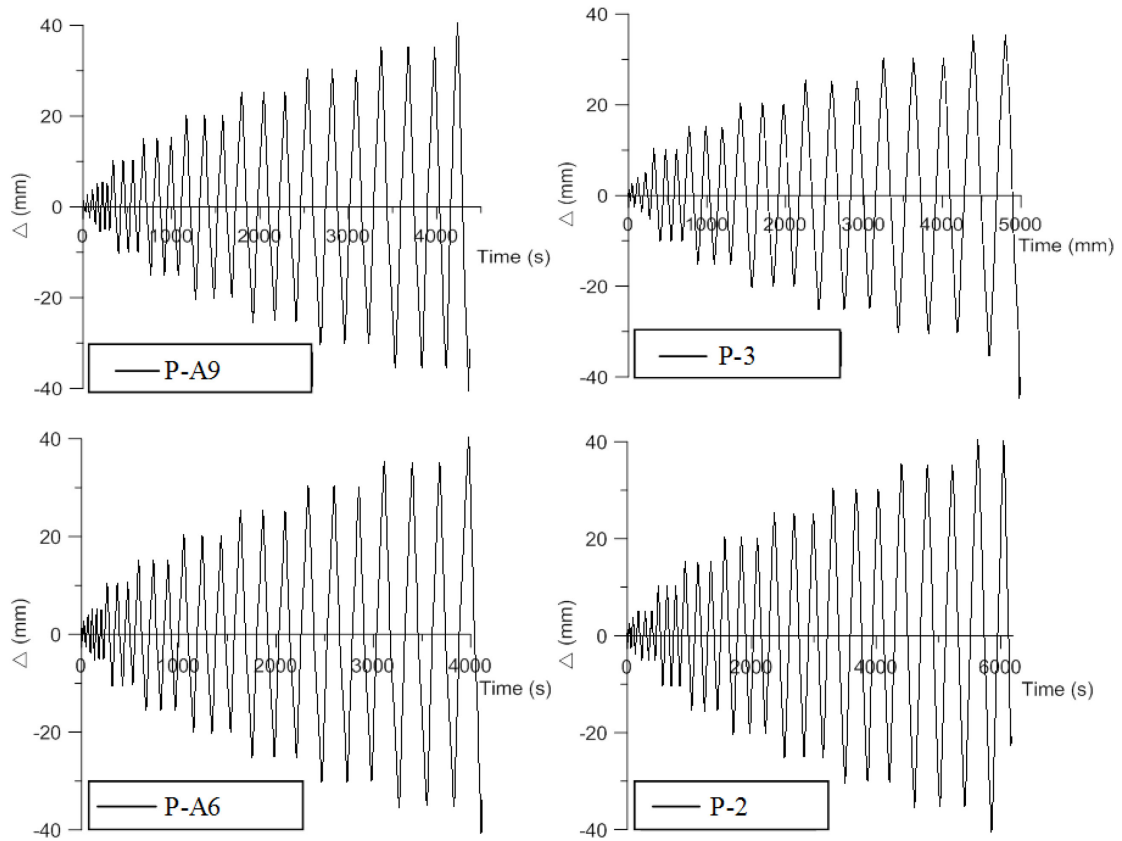


Figure 3.3: Loading protocols used in the experimental testing of the dissipative single-pin connections (Calado, 2010)

When comparing the geometry of the connection with the response of the pins, shown in Figure 3.5, and the number of cycles undergone before failure, it can be observed that the specimens P-3 and P-2 underwent one more cycle at the larger imposed displacement ($\Delta = 37mm$) than P-A9 and P-A6. This corresponds with the formulated conclusion that a larger distance between the inner plates contributes to an increased yielding capacity of the pin. It can also be observed that the specimen P-2 exhibited a greater deformation ($\Delta = 40mm$) under a force of 600kN, while the specimen P-3 yielded less (37mm) under a slightly larger force, 670kN. This demonstrates that the rectangular

pin deformed approximately 8% less than the pin with two circular faces, while it was able to carry a larger force (12% larger).

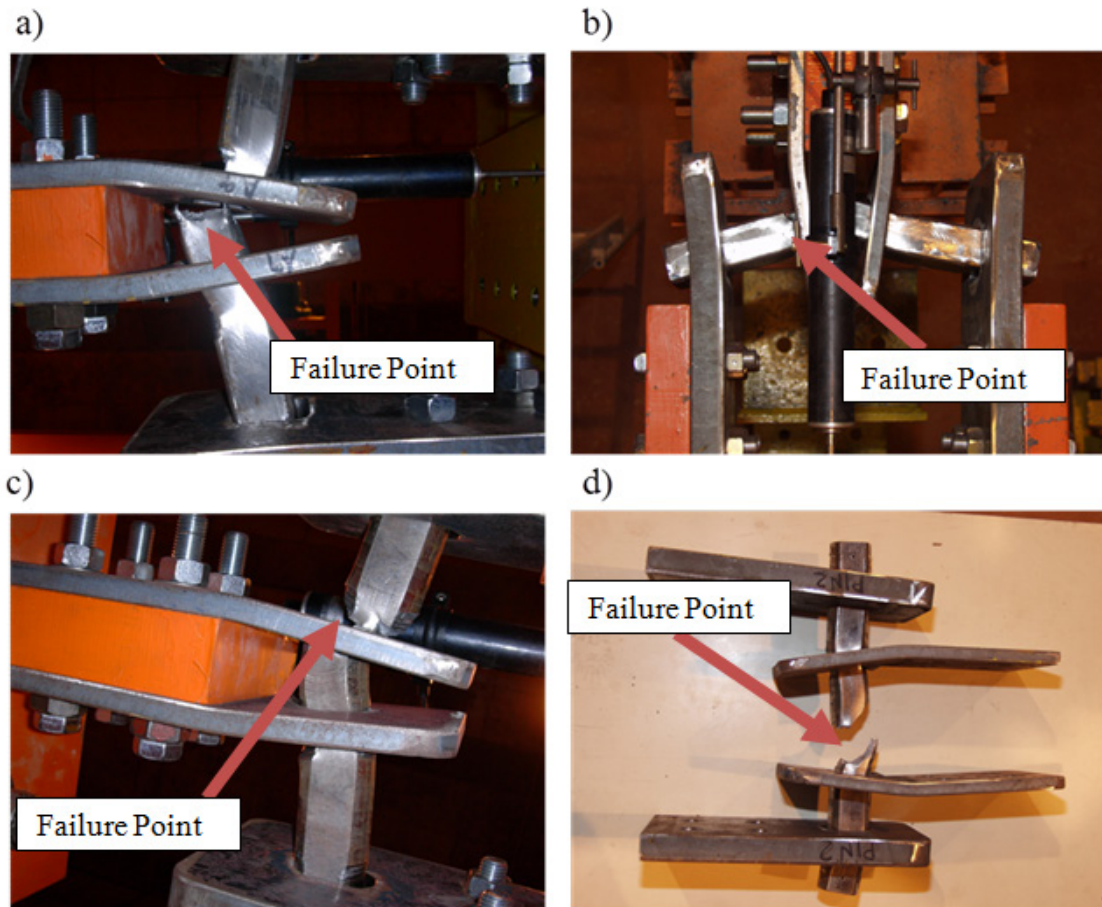


Figure 3.4: a) Failed specimen P-A9, b) Failed specimen P-3, c) Failed specimen P-A6, d) Failed specimen P-2, (Calado, 2010)

The final conclusions from the experimental tests are that a rectangular pin shape is able to dissipate a larger amount of energy under small amplitude cycles than the pin with two rounded faces, which performs better at larger amplitude cycles. This can be due to the positioning of the circular pin on its strong axis (Figure 3.2), but further experimental testing is required in order to confirm this observation. In addition, a pin

with rounded faces can resist larger forces due to reduced effects of torsion, while a rectangular pin poses a larger moment of inertia. This comparison can be seen in Figure 3.6, with regards to energy dissipated per cycle of specimens P-A6 and P-A9. Here in, $E/F_y\Delta_y$ is the ratio between the energy dissipated per cycle over the energy at yield ($F_y\Delta_y$). Once again, this conclusion must be verified with further experimental testing.

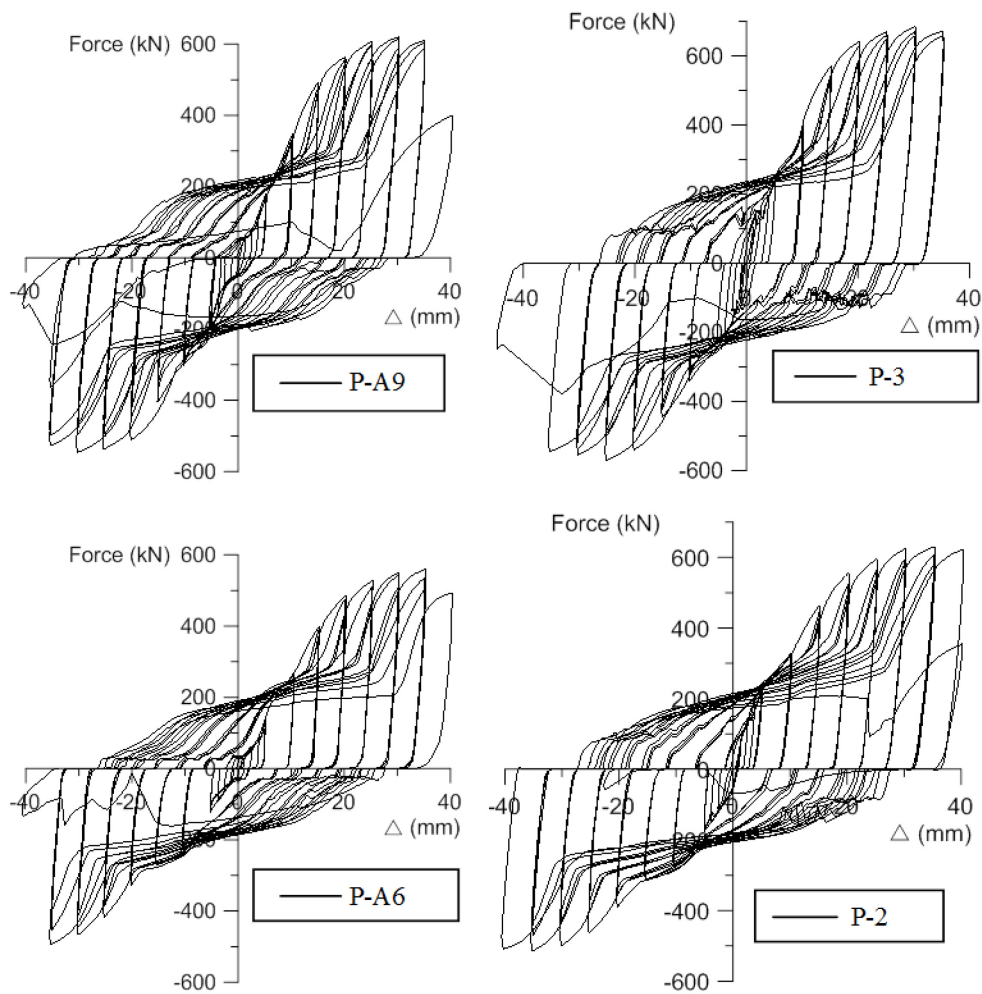


Figure 3.5: Hysteresis loops of single-pin connection responses obtained during the experimental tests under the ECCS displacement loading protocol (Calado, 2010)

Regarding the distance between the inner plates, it is concluded that the maximum energy is dissipated when a larger distance between these plates is provided. However, this configuration depends on the size and depth of the column's cross-section, which controls the length of the pin; therefore placing the inner plates at the maximum allowable distance will optimize the capacity of the connection.

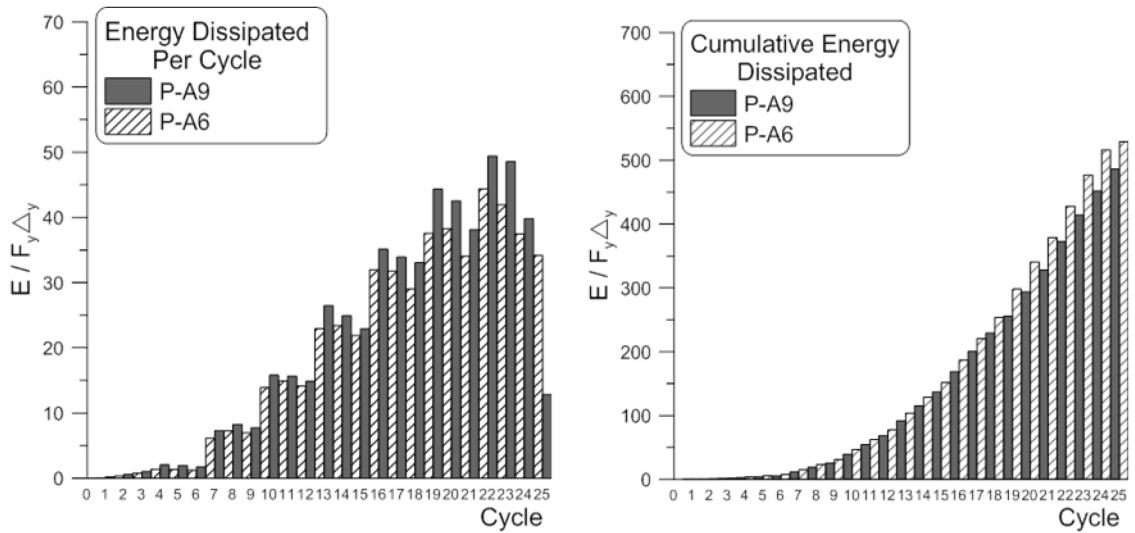


Figure 3.6: Energy dissipation comparison between specimens P-A6 and P-A9

3.2 Theoretical Study of the Dissipative Single-Pin Connection; Simple Beam Model

As illustrated in Figure 3.7, it was concluded from the obtained experimental test results (Calado, 2010) that the pin member behaves as a four point loaded beam and its behaviour could be devised in three distinct stages. The first stage defines the elastic pin's behaviour and it is found that the pin behaves as a simply supported beam. The second behavioural stage begins when yielding of extreme cross-section fibers is encountered and ends when the entire pin's cross-section is plastified. After the attainment of the plastic moment, some clamping is formed at the outer supports of the

pin, causing it to act as a beam with fixed supports. This clamping is due to the contact of the pin surface with the outer plate pin hole. As shown in Figure 3.7, the phenomenon of clamping begins at the stage where two plastic hinges form at the points of load application. During the experimental tests, some strain hardening (the third stage) was noticed before the failure of the pin member.

Therefore, by defining the force-displacement pair, at the boundary interval of the above mentioned behavioural stages, the tri-linear curve, shown in Figure 3.8, can be devised base on simple theoretical equations. Further on, the defined tri-linear curve should match the backbone curve of the hysteresis response of the single-pin connection under cyclic loading.

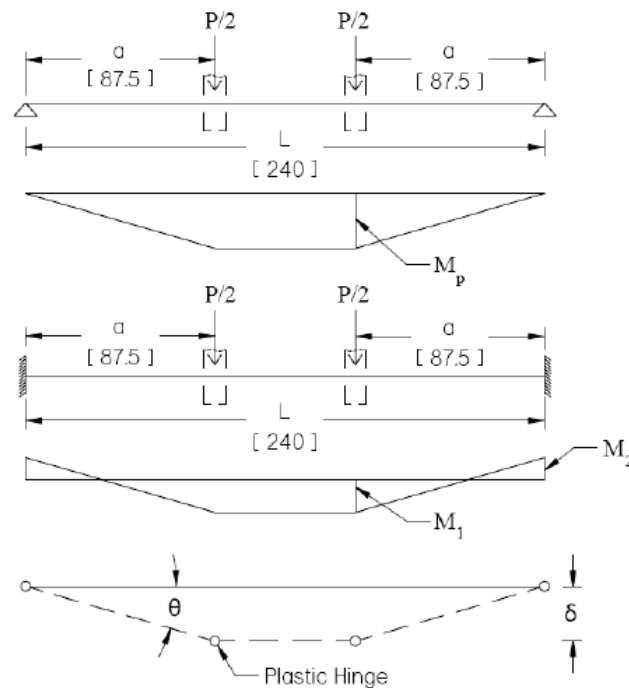


Figure 3.7: Proposed behaviour of the pin in a dissipative single-pin connection

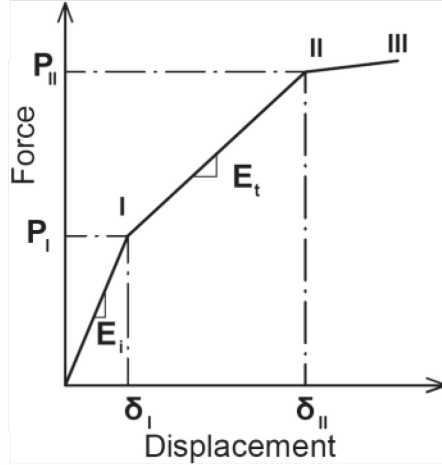


Figure 3.8: Tri-linear curve

The equations used to build the tri-linear curves are similar with those proposed by Plumier et al. (2005). However, some equations are slightly modified to improve the correlation with experimental test results. The first step in building the tri-linear response of the pin, is to define the segment regarding the elastic behaviour. When the yielding moment, $M_y = W_y F_y$, is reached, the pin starts to yield in bending under the uniform distributed load applied over the thickness of the inner plate, where W_y is the section modulus and F_y is the yield strength of the pin. The resultant of the uniform distributed force at yield is $P_y/2 = M_y/a$, where P_y is the load transferred from the brace by each one of the two inner plates. Hence, the true elastic behaviour of the pin would be until the yield moment, M_y , is attained. Thereafter, under the increased loading, the pin member encounters plastic behaviour. Since the corresponding displacement of the yield force is the yield displacement, it can be obtained by the following equation:

$$\delta_y = (M_y/6EI)aL(3 - 4a/L) \quad (3.1)$$

where EI is the flexural stiffness, L is the length of the pin, and a is the distance between the inner and outer plate. When considering the small deflection theory, the pin's

deflection at yield is $\delta_I = \varphi_I a$, where φ_I is the rotation at yield. By definition, $\varphi_I = \kappa_I l_p$, where κ_I is the curvature at yielding, computed as $\kappa_I = 3\varepsilon_I/h$, and l_p is the length of the plastic hinge, which may be approximated with the height, h , of the pin's cross-section. The strain corresponding to the static yield stress, ε_I , could be considered as two to five times the yield strain, ε_y , (Ziemian, 2010) and the dynamic yield stress is 10% larger. Thus, ε_I is expressed as: $\varepsilon_I = 1.1 \times 3\varepsilon_y$. It can be concluded that the boundary point of the elastic segment given in the tri-linear curve (Point 1, Figure 3.8) is defined by the following equations:

$$P_I = P_y = 2M_y/a \quad (3.2)$$

$$\delta_I = \delta_y = 2(1.1 \times 3\varepsilon_y)a \quad (3.3)$$

After the attainment of M_y and an increased loading ($P > P_y$), some clamping is developed at the pin's end supports and bending moment is generated at those points. It is noted that the pin is passing through the hole drilled in the outer plates, which act as the pin supports. By equating the external work, $P\delta/2 = P\varphi a/2$, with the internal work, $(M_1 + M_2)\varphi$, where M_1 and M_2 are the moments at the point of load application and the pin support respectively, the ultimate load of the beam can be approximated as: $P_{II} = P_u = 2(M_1 + M_2)/a$. The sum, $(M_1 + M_2)$, is approximated with two times the ultimate flexural capacity of the pin $2M_u = 2W_p F_u$, where F_u is the steel's ultimate strength, W_p is the plastic section modulus and M_u is the bending moment corresponding to the ultimate strength of steel, F_u .

Under the two-point loads $P_u/2$, the ultimate strain, ε_u , is estimated as being equal to, $\varepsilon_u = 1.1 \times 50\varepsilon_y = 0.1$, and the corresponding value of the ultimate plastic rotation, φ_u , becomes $\varphi_u = k_{II} l_p = 0.2$ radians, where $k_{II} = 2\varepsilon_u/h = 2(0.1)/h = 0.2/h$. Thus, from analyzing the pin's deformed shape, it is observed that the length of the plastic hinge, l_p ,

is larger than the dimension of the pin's cross-section, h , by approximately 15%. Therefore when estimating the corresponding ultimate pin's deflection, the numerical coefficient, 1.15, is applied and the value becomes: $\delta_{II} = 1.15 \times 0.2a$. In conclusion, the plastic force and deflection pair (Point II, Figure 3.8) that defines the tangent modulus of elasticity, can be defined by the following:

$$P_{II} = P_u = 2(M_1 + M_2)/a \sim 4M_u/a \quad (3.4)$$

$$\delta_{II} = \delta_u = 1.15 (0.2a) \quad (3.5)$$

The third slope of the tri-linear curve represents the strain hardening of material behaviour. This slope is estimated to be 2% for steel, and a displacement, δ_{lim} , of $0.4a$ was proposed based on experimental test results (Plumier et al., 2004). Therefore, the following equations would characterize the third point of the tri-linear curve:

$$P_{III} = P_{lim} = P_{II} + 0.02(\delta_{III} - \delta_{II}) \quad (3.6)$$

$$\delta_{III} = \delta_{lim} = 0.4a \quad (3.7)$$

Further experimental tests are required to establish the value of this point defined by the pair P_{III} and δ_{III} .

Equations 3.1 to 3.7 were applied to the case of the 60mmx40mm pin, used in the sample P-A9. The pin detail is shown in Figure 3.9, and the preliminary tri-linear curve is built in Figure 3.10. These results will be used further on to validate the OpenSees numerical model.

The 60mmx40mm rectangular pin has rounded corners and was placed to act on its weak axis in order to avoid out-of-plane bending. The inner plates are 15mm thick and the outer plates are 30mm thick. The steel properties of the pin used in the experimental test are $F_y=396 \text{ MPa}$, $F_u=558 \text{ MPa}$, and $E=206 \text{ GPa}$.

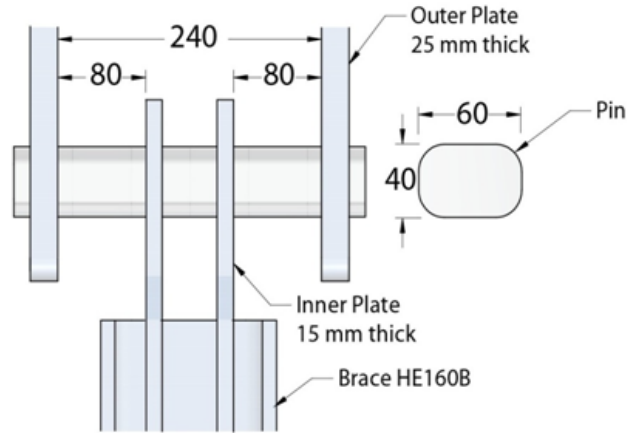


Figure 3.9: Dissipative single-pin connection configuration

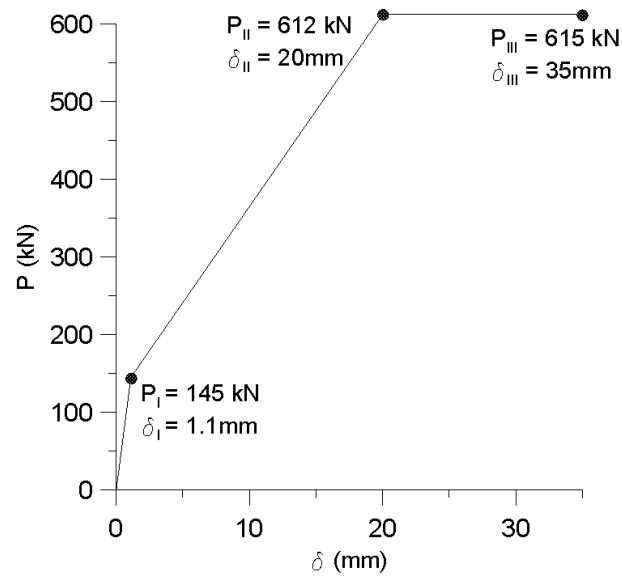


Figure 3.10: Tri-linear curve of the 40x60mm dissipative single-pin connection

3.3 OpenSees Beam Model

To validate the equations used to define the tri-linear curve, in this section the simple beam model is simulated in OpenSees framework software. The OpenSees beam model, shown in Figure 3.11, consists of eight nonlinear beam-column elements and four integration points per element. The cross-section used to describe the beam, which replicates the pin member, is made up of 60 fibers, 12 along the depth of the cross-section

and 5 along the width of the cross section. The length of the beam is the clear span between the outer plates, namely 240mm in the studied case. The material assigned to the beam model is *Steel02*, labeled Giuffr -Menegotto-Pinto material, with the same steel properties as per the experimental test: $F_y = 396\text{MPa}$, $F_u = 558\text{MPa}$ and $E = 206\text{MPa}$. In the OpenSees beam model, a strain hardening value of 0.02 is considered. In order to represent the behaviour of the pin, the 30 mm thick outer plates, acting as supports, are modelled as rigid links. To allow rotation between the beam member and the support (rigid link), a rotational spring, formed of *Pinching4* material, is added at each beam end.

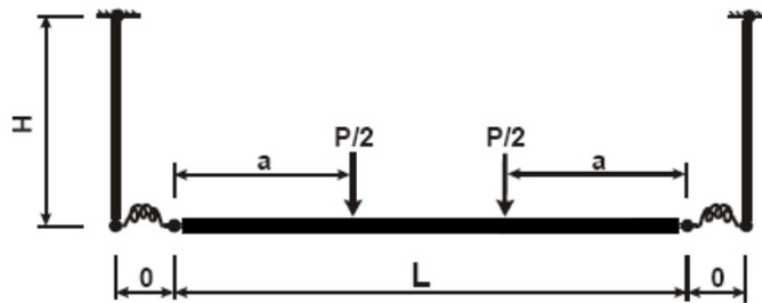


Figure 3.11: OpenSees beam model

The *Pinching4* material, explained further on, is used to simulate the deformation of the pin in the outer plate supports. This material is calibrated in order to represent the changes that occur in the pin's support, when the connection (pin member), is incrementally loaded. During the elastic behaviour, the pin's supports do not restrain its rotation and therefore no bending moment is observed. When the pin deformation in flexure becomes larger than that corresponding to the yield moment, M_y , the rotational springs begin to develop a higher stiffness in order to simulate the clamping effect, more

specifically, the bearing pressure is formed from contact between the outer plate pin hole and the pin.

Thus, to validate the theory previously mentioned, several tests are conducted with the OpenSees beam model. The first is to run the beam model, assuming a simply supported beam at all times, hence no clamping effect. This will then be compared to the model with a proposed stiffness for the addition of bearing pressure, which would be the case in practice. The purpose of testing the two cases is to propose a role for the outer plates. Due to a lack of experimental testing, the behaviour of the outer plates and their contribution to the connection cannot be completely justified. Although it was proposed that the pin behaves as a fixed beam once the plastic moment is attained, it can be seen, in Figure 3.12, that this is not entirely the case. The pin will continue to bend with the added resistance of the outer plates because, as shown, the outer plates will also exhibit some deformation. Therefore, it can be concluded that the pin is not entirely fixed at its ends, but rather acts as a semi-rigid connection.

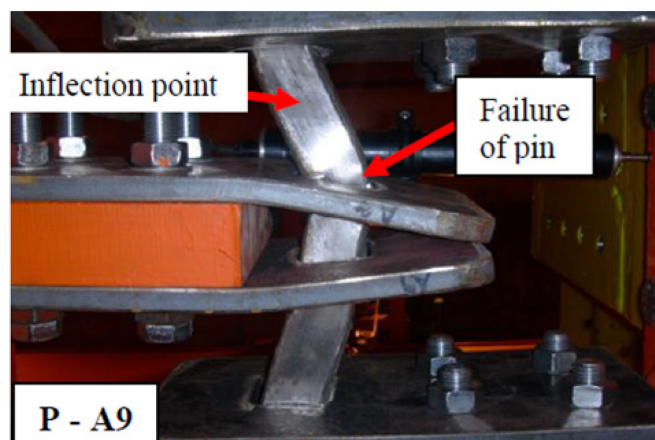


Figure 3.12: Deformation of the dissipative single-pin connection during experimental testing (Calado, 2010)

It was found that when the pin acts as a simply supported beam it displaces almost twice as much as the pin with semi-rigid connections. The proposed stiffness added to the rotational springs in the model is the rotational stiffness of the outer plate. The cross section of the outer plate used in the experimental tests is 160mmx30mm and the length used to calculate the rotational stiffness of the outer plate is the free length. The portion of the outer plate attached to the column does not contribute to the behaviour of the connection. The portion of the outer plates affecting the connection behaviour is from the inner edge of the column to the pin. The total height of the plates used is 440mm. If the section of the plate attached to the column and the length from the pin to the end of the plate is neglected the length is, $L_{\text{eff}} = 440 - 120 - 127.5 = 192.5\text{mm}$, as shown in Figure 3.13.

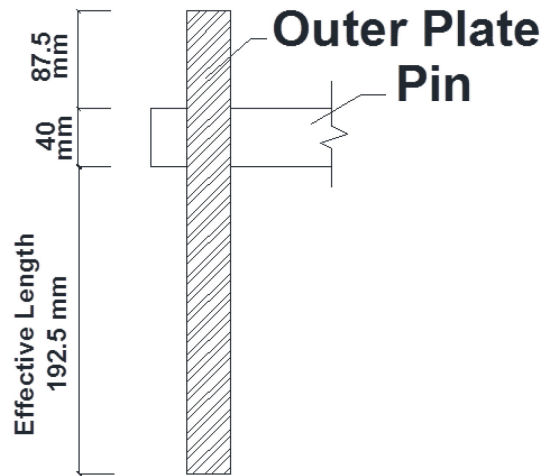


Figure 3.13: Effective length of the outer plate

The outer plate is considered to act as a cantilever beam, fixed at the column end and free at the pin end, therefore the rotational stiffness, $k_{rot} = 3EI/l^3$, of the outer plate would be 30.3kN/m . By employing the *Pinching4* material, the rotational spring at each

end of the pin would deform elastically until the pin reaches its plastic moment and would then deform with an added stiffness of $30.3kN/m$, replicating the contact between the outer plate pin hole and the pin. It is important to note that for the case of numerical modelling, the behaviour of the connection as a whole must be considered.

The proposed tri-linear curve, devised by the theoretical model in Section 3.2, and the behaviour of the semi-rigid model, are found to have a close correlation, as shown in Figure 3.14. In one curve both the yield and the plastic slopes are shown. This is an effective way to demonstrate that the theoretical values match the OpenSees beam model values. The tri-linear curve can consist of either the yield values or the plastic values when defining the elastic slope. For this research, the behaviour before the point of yield was considered elastic and after that point it was considered to be plastic. This is demonstrated in the second curve, where the first slope shows the elastic behavior, the second slope indicates the plastic behavior, and the third slope illustrates strain-hardening.

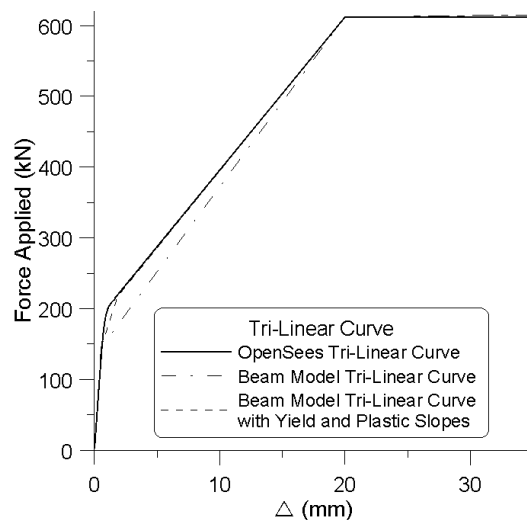


Figure 3.14: Comparison between the simple beam model and OpenSees tri-linear curves for the P-A9 sample

Further investigation was conducted with the OpenSees beam model. In order to observe the plastification of the fibers of the pin along its cross section, a strain diagram and a stress diagram were built and are shown in Figure 3.15. The maximum strain developed in the fibers is approximately $60\varepsilon_y$, where $\varepsilon_y = F_y/E = 396/206000 = 0.00192$. This strain is developed at a force $P_u = 612kN$, and the corresponding stress is $56MPa$, which is close to F_u . The stress and strain diagrams further validate the theoretical formulae previously devised. At the application of yield stress, only the first fibers are plastified. Similarly, when the plastic force is applied, all the fibers throughout the cross-section are plastified. In addition, at yield, the corresponding stress is $F_y = 396 MPa$.

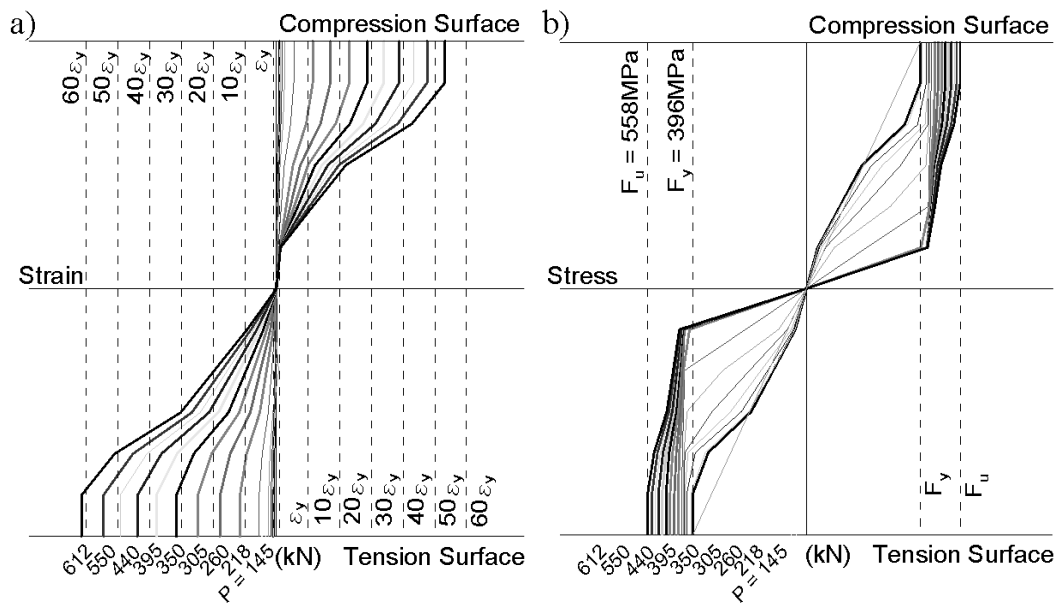


Figure 3.15: a) Strain diagram of OpenSees beam model replicating the P-A9 device, b) Stress diagram of OpenSees beam model at pin's mid-length replicating the P-A9 device behaviour

Another important component to consider when designing the pin is that its ultimate deformation influences the interstorey drift of the structure, which is limited by

the current NBCC code at $2.5\%h_s$, where h_s is the storey height. When a brace is equipped with dissipative single-pin connections at both ends, the diagonal line will elongate with two times the ultimate pin deformation, estimated at $2\delta_u = 2[1.15(0.2a)]$. The horizontal projection of the ultimate pin deformation is $\Delta = 2\delta_u/\cos\phi$, where ϕ is the angle between the brace member and a horizontal line. To ensure that the lateral drift is less than $2.5\%h_s$, the following equation must be satisfied: $2\delta_u/\cos\phi < 2.5\%h_s$. Thus, it is implied that the distance between the outer plate and the inner plate, a , should be in agreement with the following:

$$a < 0.054h_s \cos\phi \quad (3.8)$$

It can be concluded that the pin should be calibrated to satisfy both strength and deformability criteria. Regarding the strength criteria, the pin element should resist the axial force developed in the brace and be designed to yield before the brace reaches 60-70% of its compressive strength, C_r .

3.4 Numerical Modelling of Dissipative Single-Pin Connections

A numerical model of the single-pin connection is built in the following section. The model will be validated with the experimental results of the connection, tested in Lisbon, Portugal. This model can be integrated in the simulation of braced frames with dissipative connections.

3.4.1 Integrative Model for Use in Braced Frame Analysis

While the OpenSees beam model previously studied is an effective way to devise a preliminary design of the dissipative pin connection members and to determine the connection behaviour, a model must be built in order to integrate the connection in a

frame environment. The proposed method is to use a zero-length spring element, behaving in a diagonal translation, to which *Pinching4* material is assigned.

The *Pinching4* material defined in OpenSees represents a pinched force-deformation response. The pinching that is exhibited is the loss of resistance during unloading of the pin in tension and compression, right before reloading begins. In order to define the *Pinching4* material, the tri-linear curve, designed and validated in Section 3.2, is employed. The points of the tri-linear curve represent the skeleton or backbone curve of the pinching material, depicted in Figure 3.16 by the bold solid line.

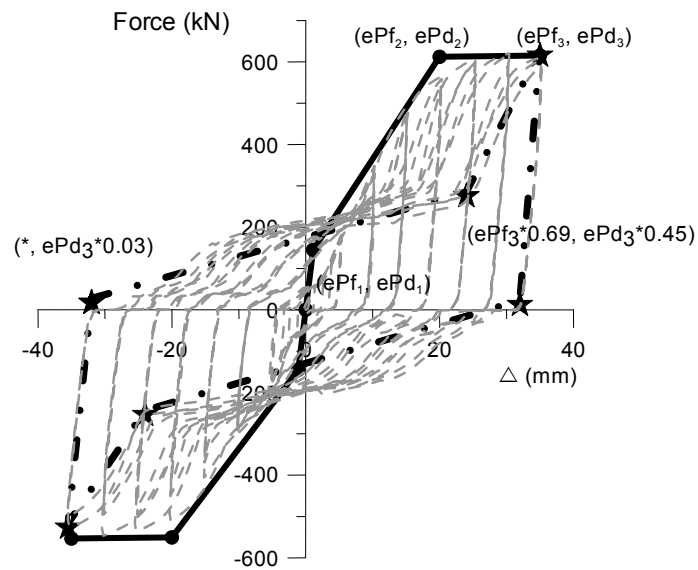


Figure 3.16: Pinching4 material definition

The skeleton curve can be defined in the positive range and the negative range. The next step is to define the pinched shape of the curve, which is the dash-dot line in Figure 3.16. This is done by specifying three floating point values in tension and three floating point values in compression. The first floating point value, both in tension and

compression, is defined by the ratio of the deformation at the point of reloading, in our case the plastic deformation, to the total hysteretic deformation demand. The second floating point value, again in both tension and compression, is the ratio of the force at the point of reloading, the load needed to achieve plastic deformation, to the force corresponding to the total hysteretic deformation demand. The plastic force is used as the reloading force because in the case of the single-pin connection, the pinching only begins when the plastic state is reached. In order to deform in the opposite direction, a force greater than or equal to the plastic force must be applied to the connection, enabling bending in the opposite direction. The third floating point value is a ratio of the strength developed upon unloading to the maximum strength developed in the monotonic loading stage, or in other words, the ratio of the total force developed to the maximum monotonic load the connection can withstand.

In order to test this proposal, an integrative OpenSees model was built. The model is a small excerpt of the connection that would be found in the braced frame model. It consists of a rigid link, which would be fixed to the column, with a zero-length rotational spring at its end, as shown in Figure 3.17. The spring would be subject to axial displacements along the x-direction in the case of this model, while in a frame environment the displacements would be parallel to the diagonal brace member.

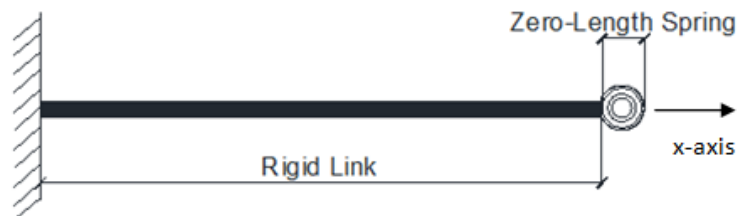


Figure 3.17: Integrative OpenSees model

3.4.2 Calibration of the Integrative Model

In order to calibrate the OpenSees model described in the previous section, the same displacement loading protocol applied during the experimental tests conducted in Lisbon, Portugal (Calado, 2010), is considered and both (experimental and simulated) hysteretic force-displacement loops are compared. Among the four specimens selected for analysis and shown in Figure 3.2, only the first two, P-A9 and P-3, are pertinent to this study.

As illustrated in Figure 3.3, the displacement loading applied to the P-A9 sample has 25 cycles with a rate of loading of 0.45mm/s and a maximum displacement, in the last cycle, of 40mm. The displacement loading protocol applied to the P-3 sample has 21 cycles, a rate of loading 0.33mm/s and a maximum displacement of 45mm. In both cases, three consecutive cycles reach the same displacement amplitude. The force-displacement hysteresis loops that characterize the behaviour of samples P-A9 and P-3 are shown in Figure 3.5. In both cases the failure of the pin occurred in compression at one of the two points of load application (Figure 3.4). Thus, in the case of specimen P-A9, when the distance between the outer plate and the inner plate is larger than the distance between the inner plates, the failure occurs in the longer pin segment at the external face of the inner plate. In the case of specimen P-3, the failure occurs in the middle segment at the internal face of the inner plate. For both specimens the same stiffness degradation occurred during reloading. Although both specimens attained the same deformation in bending, 35 mm, the corresponding ultimate tensile forces (615kN for P-A9 and 670kN for P-3) differ by 10%. On the other hand, for both specimens the capacity in tension is larger than that in compression by 12%. This difference in strength

is proposed to be due to out-of-plane bending of the outer plates which implies an increased distance between the pin's supports in the outer plate hole. In this case the outer plates deflect towards the exterior, as is shown in Figure 3.4b. For both specimens P-A9 and P-3, the response of the connection, as simulated in OpenSees, versus that resulted from experimental tests in Portugal, is shown in Figure 3.18. It is mentioned that it is possible to wrap fatigue material around the Steel02 material with the aim to accurately simulate the last cycle before rupture. This detail will be added in future work.

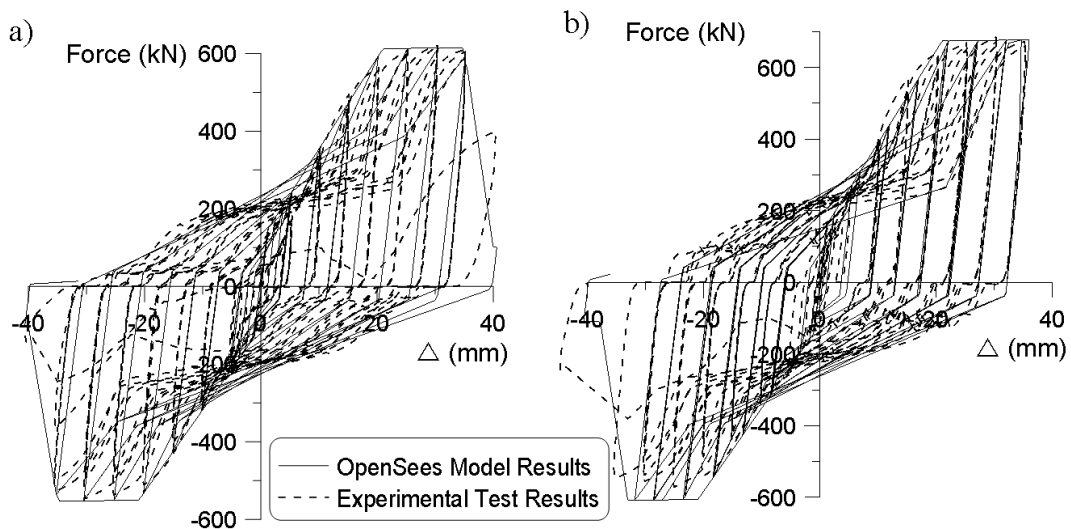


Figure 3.18: Hysteresis loops recorded from the OpenSees model vs. experimental test results: a) P- A9, b) P- 3

In order to validate the accuracy of the OpenSees model against the experimental results recorded for specimens P-A9 and P-3, the normalized energy dissipated per cycle and the normalized cumulative energy are compared, and shown in Figures 3.19 and 3.20. The hysteretic response of the specimen P-A9 during the last cycle, shows failure in compression after a tentative failure in tension before reloading. As illustrated in Figure 3.18a, the proposed computer model is not able to simulate this type of softening that

occurred during the last cycle and shows a large discrepancy in terms of energy dissipated. However, in the case of specimen P-3, a close correlation is observed (see Figure 3.18b). With regards to the cumulative energy dissipated by both samples, the P-3 specimen was subject to 21 cycles, while the P-A9 specimen underwent 25 cycles. Under similar conditions it is expected that the connection device with a larger distance between its inner plates possesses a larger dissipative energy capacity. In other words a larger distance between inner plates increases the load bearing capacity of the connection.

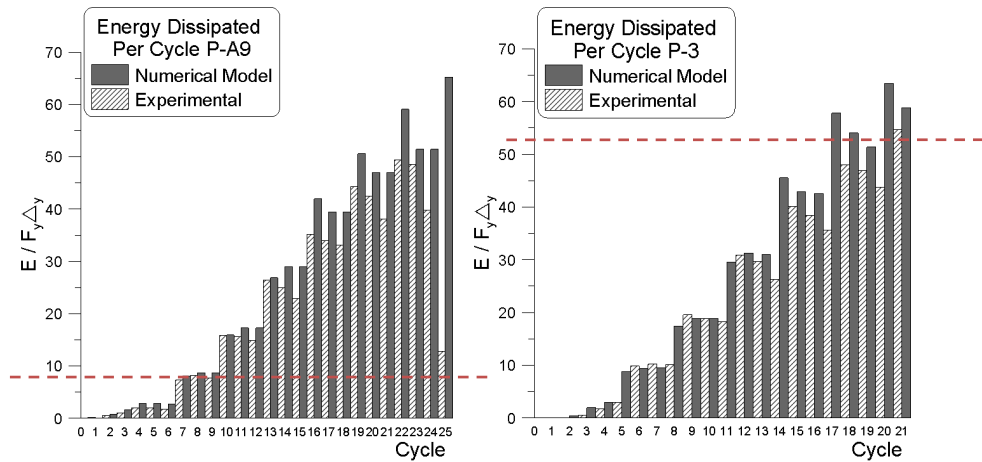


Figure 3.19: Energy dissipated per cycle for specimens P-A9 and P-3

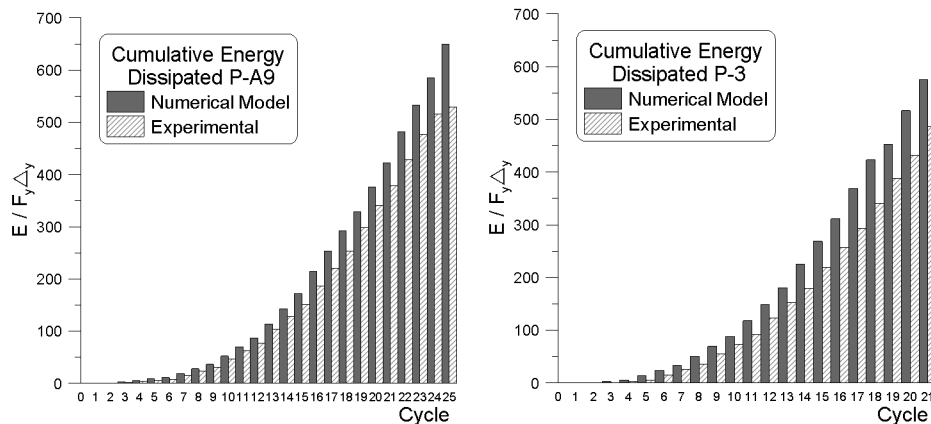


Figure 3.20: Cumulative energy dissipated for specimens P-A9 and P-3

3.5 Experimental Testing of a CBF Equipped with Dissipative Single-Pin

Connections

The behaviour of CBFs equipped with single-pin connections in an X-bracing configuration was tested at Politecnico di Milano, Italy (Plumier et al., 2005). As illustrated in Figure 3.21, the span and height of the frame tested are 3.4m and 3.0m, respectively. The column cross-section is a HE240B and the beam cross-section is a HE200B. For these cross-sections, the geometrical properties are obtained from the ARBED steel section property tables (ARBED, 1982). The beam is pin-connected to the column and both braces, made up of HE160B profiles, are equipped with dissipative single-pin connections at both ends. The pin configuration consists of two outer plates welded or bolted to the flange of the column member, two inner plates welded to the brace, and a pin running through the four plates, as shown in Figure 2.4. The selected test has a rectangular pin shape with rounded corners and a cross-section of 60mmx40mm. The frame described is subjected to two different types of loading, a quasi-static loading and a dynamic loading.

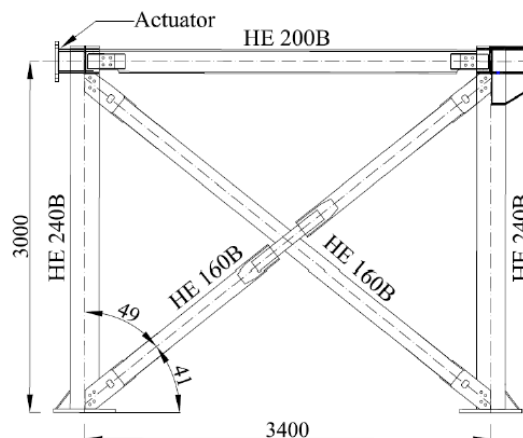


Figure 3.21: Milano experimental frame set-up (Plumier et al., 2004)

Experimental test results demonstrate that the single-pin connection is able to dissipate energy under both quasi-static displacement and seismic loads, while maintaining braces in elastic range. Thus, the introduction of dissipative connections in an X-braced frame allows braces to behave elastically and to avoid the drawbacks that characterize the response of a traditional braced frame. As long as braces are prevented from buckling, equal axial forces are developed in both braces while they act in tension or compression. The input energy, focused in the brace-to-column single-pin connections, causes the pin to yield first. To maintain the elastic behaviour of braces it is recommended to design the brace in compression to have the buckling strength larger than 130-140% of their connection capacity. The experimental test conducted in Europe paired a HE160B brace with a 60mmx40mm pin. The ultimate force of the connection, as previously calculated, is 612kN and the compressive strength of the brace, $C_r = 0.9AF_y(1 + \lambda^{2.68})^{-1/1.34}$, is 911kN, where A represents the area of the brace cross section and $\lambda = \frac{KL}{r} \sqrt{\left(\frac{F_y}{\pi^2 E}\right)}$. Therefore the connection will yield when 67% of the compressive strength of brace is reached.

Braces are restricted to behave in elastic range and the braced frame deformation is provided by the bending deflection of the pin as well as the elastic elongation of brace members. Thus, when the brace acts in tension, both pins deflect toward the brace and when the brace acts in compression, both pins deflect towards the columns. An example of the deformation in tension can be seen in Figure 3.22.

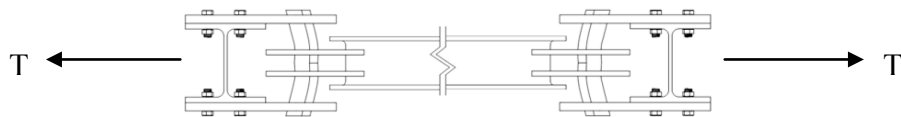


Figure 3.22: Brace equipped with connection and subjected to tensile forces

3.6 Numerical Modelling of the Experimentally Tested Braced Frame Equipped with Single-Pin Connections Using OpenSees

The tested one-storey braced frame in an X-braced configuration and equipped with single-pin connections (Castiglioni, 2010), as shown in Figure 3.23, is modelled in OpenSees. The beams and columns are modelled using one beam-with-hinge element per member and the length of the plastic hinge is set to be equal to the depth of the member. Each column cross-section is defined as a fiber section, with 5 fibers along the flange width and 6 fibers along the depth of the web. The columns are hinged at their base and pinned at the beam column connection. The beam section is also defined as a fiber cross-section with again 5 fibers in the flange and 6 fibers in the web. The beam is connected to the column with a zero-length rotational spring, C1. The x and y displacements of the beam end nodes are slaved to those of the column end nodes. The spring in between the two nodes is set to work in rotation and exhibits almost no stiffness. This allows the modelling of gusset plate connections found in traditional concentrically braced frames. As illustrated in Figure 3.23, each of the four brace segments are modelled with 8 nonlinear beam-column elements and 4 integration points per element. For the modelling of the X-bracing configuration, the tension brace is defined to work as one element using 16 sub-elements and the compression brace is designed as two half braces connected to the tension brace by very stiff rotational springs, C4. The purpose of choosing the nonlinear beam-column element for the braces is to ensure uniform distribution of plasticity along the brace length when buckling occurs. The initial camber set to each brace element is $L_{\text{brace}}/1000$ as recommended by Ziemian (2010) for a W-shape brace cross-section. The cross-section of each brace is defined with 5 fibers along the flange width

and 6 fibers along the depth of the web. A section aggregator is used to assign a torsional stiffness to each brace sub-element's cross-section. In order to connect the braces to the columns, four rigid links are used. These rigid links are defined as elastic beam-column elements and their model was discussed in section 3.4. The rigid links experience no deformation and therefore no plasticity is formed in them. Thus, the linear beam-column sufficed as an element choice. These rigid links represent the part of the brace connectors, the gusset plates or the outer plates, that are rigidly fastened to the column. The end node of the brace is connected to the end node of its respective rigid link. A zero-length spring is inserted between the two nodes. The properties of these springs, C2 and C3, are set for two different situations, one is to model a gusset plate, explained further in Chapter 4, and the other is to model the dissipative single-pin connection.

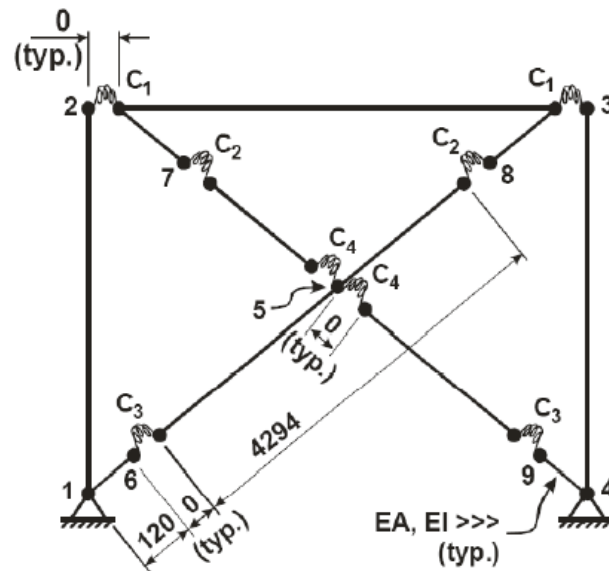


Figure 3.23: The OpenSees model of the experimentally tested CBF with single-pin connection devices

All of the aforementioned members were modelled with the *Steel02* Giuffrè-Menegotto-Pinto material. This material is represented by a force-deformation relationship and it exhibits some isotropic strain hardening in both tension and compression. The pin connection, represented by zero-length elements deforming in x and y translations, is modelled with the use of its tri-linear curve and the *Pinching4* material, as described in previous sections.

In order to replicate the braced frame response in OpenSees, the same quasi-static loading protocol under displacement control, defined in agreement with ECCS regulation and shown in Figure 3.24, is used. Herein, to see the influence of different loading protocols in the braced frame response, the AISC loading protocol was defined and employed in this study (see Figure 3.24).

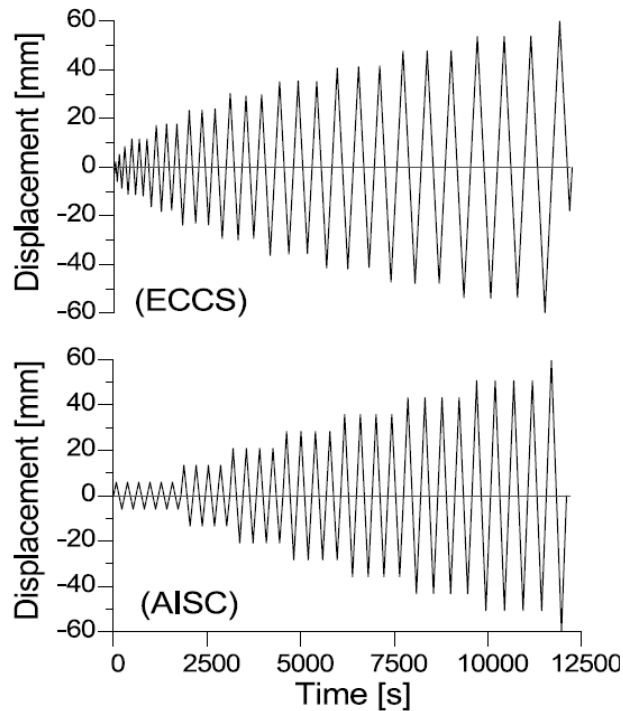


Figure 3.24: Loading protocols used for testing of the OpenSees braced frame models

The protocols consist of applying 30 incremental amplitude displacement cycles in several steps, with a maximum displacement of 2% storey height (60mm). However, the distribution of these time-series cycles differs for each of the two considered loading protocols. For example, following AISC regulation, the first 6 displacement cycles have amplitudes equal to the yielding displacement of the beam. Then, the displacement amplitudes of each group of 4 identical cycles is: $2.25\delta_y$; $3.5\delta_y$; $4.75\delta_y$; $6.0\delta_y$; $7.25\delta_y$; $8.5\delta_y$ and 1 cycle of $10.0\delta_y$. Related to the ECCS protocol, the 3rd cycle is $1.0\delta_y$ and it follows in groups of 3 identical cycles incremented with $1.0\delta_y$ from $2.0\delta_y$ to $9.0\delta_y$, and the last cycle is $10.0\delta_y$. In the first step, the ECCS loading protocol, used in the European testing is applied to the OpenSees model of the experimental frame. In Figure 3.26a, it is seen that the experimental frame's connection behaves slightly different in tension than in compression. This decrease in compression force is assumed to be caused by a difference in the deformation of the pin and the outer plates when subjected to tensile and compressive loads (Figure 3.25), although without additional experimental testing it would not be possible to decipher the behaviour difference in both instances; therefore the connection is assumed to behave symmetrically. On the tension side there is a significant match between the experimental results and the numerical model. The comparison of the single-pin is shown in Figure 3.26b and once again the tri-linear curve is validated.

For a comparative analysis in terms of braced frame response under lateral loading, the AISC loading protocol is applied to the experimental braced frame. As a result, the same overall frame displacement is achieved, but by a different path as explained above. The hysteresis loops of the braced frame response, in terms of lateral

force application versus lateral braced frame deformation as resulted from the OpenSees model, are illustrated in Figure 3.27. In comparison with the experimental response obtained under the ECCS loading protocol, the forces are slightly higher due to the increase in number of cycles at higher displacements, or in other words the AISC protocol has a higher deformation demand.

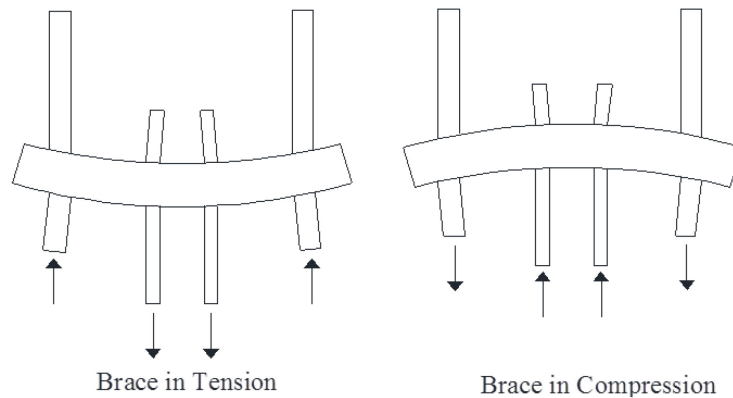


Figure 3.25: Deformation of dissipative single-pin connection when the brace is subjected to tensile and compressive forces

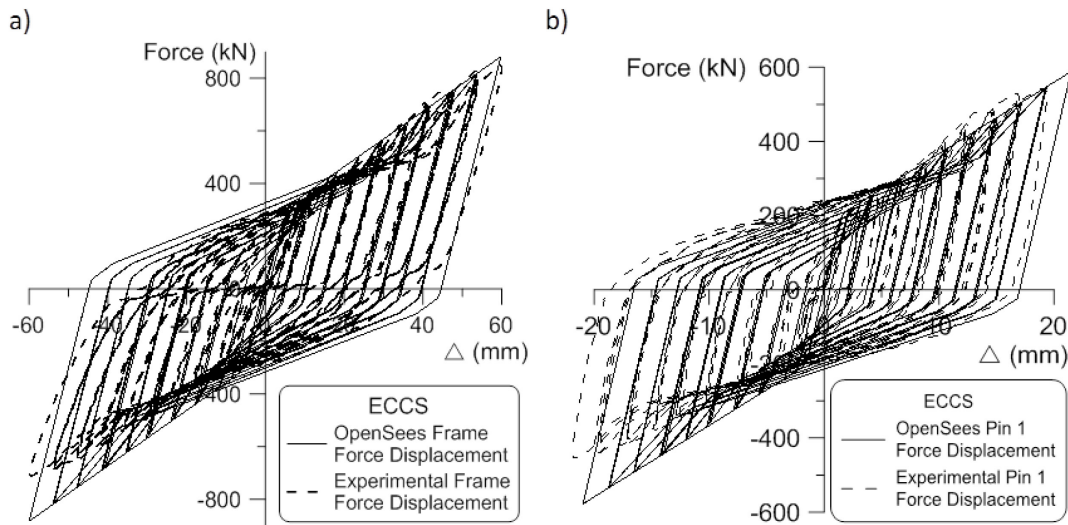


Figure 3.26: a) OpenSees frame response vs. experimental frame response (ECCS), b) OpenSees pin response vs. experimental pin response (ECCS)

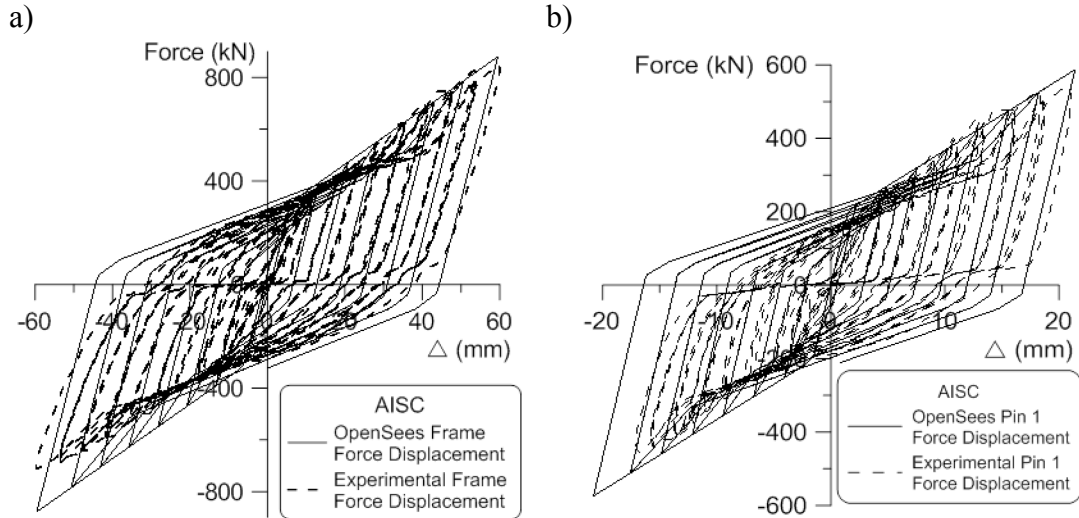


Figure 3.27: a) OpenSees frame response vs. experimental frame response (AISC), b) OpenSees pin response vs. experimental pin response (AISC)

In Figure 3.28, a comparative response in terms of cumulative dissipative energy between the experimental test results obtained under the ECCS loading protocol, the replicated OpenSees braced frame model response under the ECCS loading protocol, as well as under the AISC displacement loading protocol, is shown. As illustrated, the total cumulative dissipated energy computed with the OpenSees model (30 cycles), under both loading protocols equates the energy dissipated during the European experimental test and, in this respect, the OpenSees model of the braced frame equipped with single-pin connections is validated.

A comparison between the lateral response of a traditional CBF and a CBF with dissipative single-pin connections is also studied. The main purpose of promoting braced frames with dissipative connections, in place of traditional gusset plate connections, is the ductility criteria as well as the prevention of the soft storey mechanism formation, by restricting the braces to respond elastically while the seismic input energy is concentrated in the pins rather than in the braces. Meanwhile, braced frames with single-pin

connections are more flexible than the traditional CBFs, which means a reduction of the base shear force is exhibited. In Figure 3.29, the comparison of the base shear with respect to time, resulting from the experimental frame with and without single-pin connections, subjected to the ECCS loading protocol, is shown. For the same braced frame members, the traditional CBF develops a maximum base shear that corresponds to $R_d = 2$, $V = 2500kN$, and in the case of frame with the single-pin connections, it is expected that the developed base shear corresponds to $R_d = 3$, $V = 1900kN$. However, in general, the period of the braced frame with pin connections elongates by 1.5- 1.7 times the fundamental period of a traditional CBF. It is illustrated that the ductility of the structure is in fact improved in the CBF with single-pin connections.

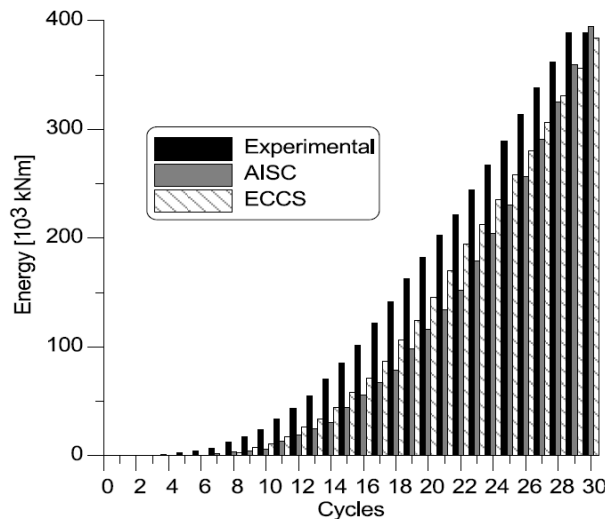


Figure 3.28: Comparison of cumulated energy dissipated during the experimental test using ECCS loading, the replicated computer model under the ECCS and AISC loading

Regarding the behaviour of the OpenSees braced frame model with single-pin connections, Figure 3.30 demonstrates that braces behave elastically, while the pins yield and dissipate energy. It can also be seen that the force passing through the brace is equal

to the force passing through its respective pins. The total deformation of the frame is 60mm, as imposed by the ECCS loading protocol. This horizontal drift is in accordance with the summation of the displacement of pin 1, 21.6mm, pin 3, 21.6mm, and the elastic deformation of the brace, 2mm, projected on the horizontal line, $(21.6 + 21.6 + 2)/\cos 41^\circ = 60\text{mm}$. As a comparison, Figure 3.31 demonstrates that the traditional CBF dissipates energy through the buckling and yielding of brace members.

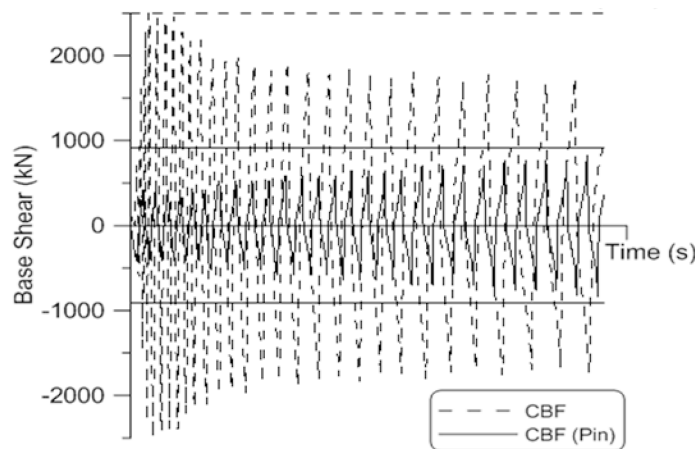


Figure 3.29: Time series of the base shear response of the modelled CBF with and without single-pin connections using OpenSees

It must also be noted that in the case of the X-braced frame tested at Politecnico di Milano, $a < [0.054h_s \cos \phi]$, where $0.054h_s \cos \phi \sim 122\text{mm}$ and the value used for a is 87.5mm, therefore the limit is satisfied.

The theoretical design of a dissipative pin connection has been validated with the experimental results and with the numerical modelling of the connection and the experimental frame equipped with the connection. It has also been concluded that low-

cyclic fatigue failure is not the typical failure mode for these tested devices (Tirca et al., 05/2012).

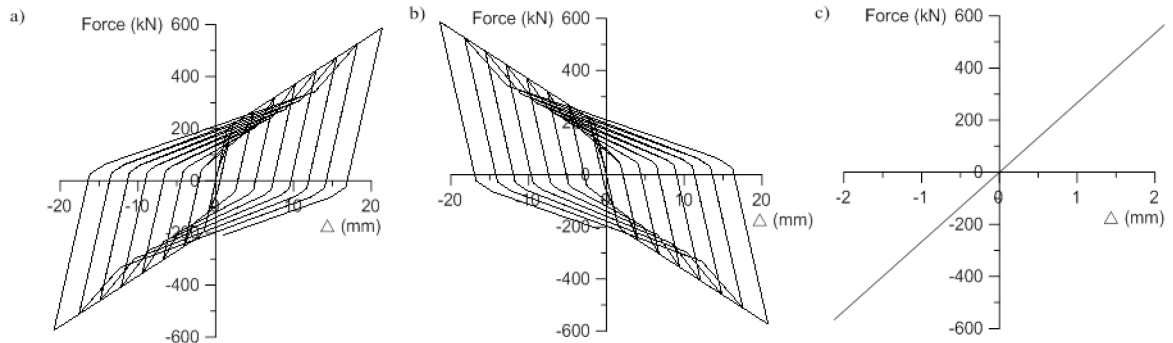


Figure 3.30: a) Bottom pin behaviour of tension brace (CBF with pins, ECCS), b) Top pin behaviour of tension brace (CBF with pins, ECCS), c) Tensile brace behaviour (CBF with pins, ECCS)

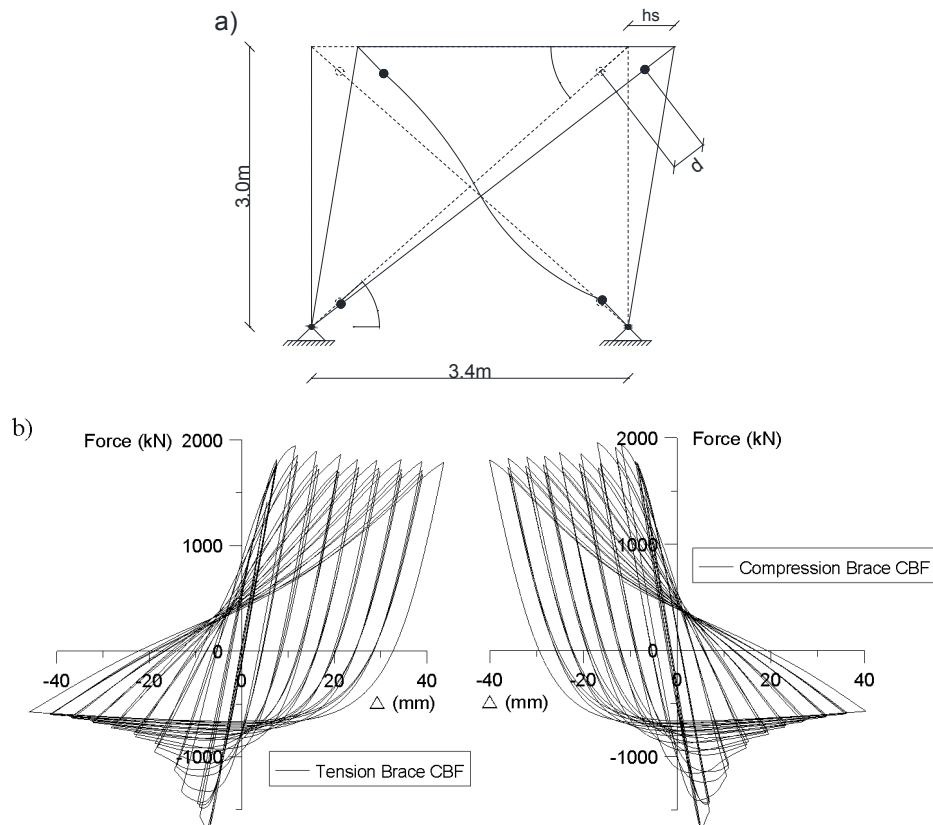


Figure 3.31: a) Braced Frame displacement, CBF (ECCS), b) Tension and compression brace displacement (ECCS)

Chapter 4. Seismic Analysis of Low-Rise Concentrically Braced Frames with Traditional Gusset Plate Connections Using OpenSees

In order to analyze the behaviour of a frame with dissipative single-pin connections, the same frame with gusset plate connections is studied. In this chapter, a single-storey and two-storey frame with gusset plate connections is designed and modelled using the OpenSees environment. In Chapter 5, the seismic response of CBFs subjected to several types of ground motions will be compared to that of the same braced frames with dissipative single-pin connections.

4.1 Design of One-Storey and Two-Storey Concentrically Braced Frames

There are two main components required in order to design CBFs with an X-bracing configuration. The first component consists of designing the gravity members followed by the design of a seismic force resisting system, using the NBCC 2010 and S16-2009 standards (NRCC, 2010 and CSA/S16, 2009). The building description and design will follow in the next subsections.

4.1.1 Building Description and Load Definitions

The single- and two-storey office buildings studied are located on a firm ground site in Victoria, B.C, Canada, and their plan view and computer model elevations are shown in Figure 4.1. In order to design the seismic force resisting system, the seismic load must be determined by using the following equations:

$$V = \frac{S(T_a)M_v I_E W}{R_d R_o} \quad (4.1)$$

Also, the minimum and maximum values of the static earthquake force must be satisfied:

$$V_{min} = \frac{S(2.0)M_v I_E W}{R_d R_o} \quad (4.2)$$

$$V_{max} = \frac{2}{3} \frac{S(0.2) I_E W}{R_d R_o} \quad (4.3)$$

The fundamental lateral period of the building, T_a , is determined by:

$$T_a = 0.025h_n \quad (4.4)$$

where h_n is the height of the building in meters. Therefore, the period for the single- and two-storey buildings are $T = 0.095s$ and $T = 0.19s$, respectively. It is stated that the dynamic period of the structure is approximately equal to twice the static period, $T_d = 2T_s$, therefore the periods become $T = 0.19s$ for the one-storey and $T = 0.38s$ for the two-storey structure. The design spectral response acceleration, $S(T_a)$, is determined by using the uniform hazard spectra of the region where the building is located. The specific spectral acceleration pairs for Victoria, B.C., are given in Appendix “C” of the NBCC 2010 for $T_a = 0.2s, 0.5s, 1.0s$ and $2.0s$ and the values are shown in Table 4.1. The spectral response acceleration, for the studied building period, is linearly interpolated from the uniform hazard spectrum (UHS), shown in Figure 4.2., and corresponds to the exceedance period of 2% in 50 years. The importance factor, I_E , for an office type building is $I_E = 1$. The ductility related force modification factor, R_d , is a factor inversely proportional to the static seismic force. This factor takes into account the capability of the structure to dissipate energy, and in turn, reduces the forces applied to the structure. In the same manner, the overstrength related force modification factor, R_o , reduces the seismic forces due to the portion of reserved strength in the members of the structure. The selected braced frame system for the single- and two-storey buildings is a limited ductility CBF system, with $R_d = 2.0$ and $R_o = 1.3$, as per the NBCC 2010. The higher

mode effects factor, M_v , amplifies the seismic load and takes into account the effects of higher modes. Effectively, for $T_1 \leq 1.0s$, the higher mode effects factor is $M_v = 1$.

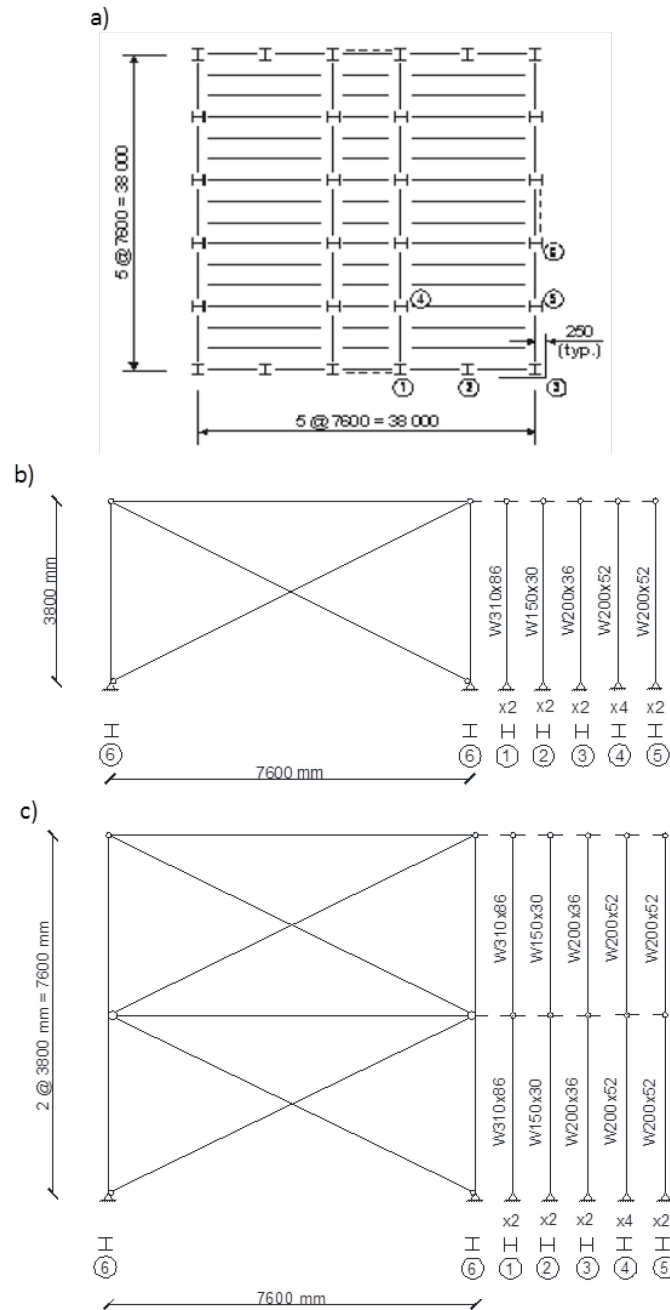


Figure 4.1: a) Plan view of studied buildings , b) CBF elevation of one-storey building model, c) CBF elevation of 2-storey building model

Table 4.1: Seismic design data for Victoria, B.C., Canada as per Appendix C, NBCC 2010

S (0.2)	S(0.5)	S(1.0)	S(2.0)
1.2	0.82	0.38	0.18

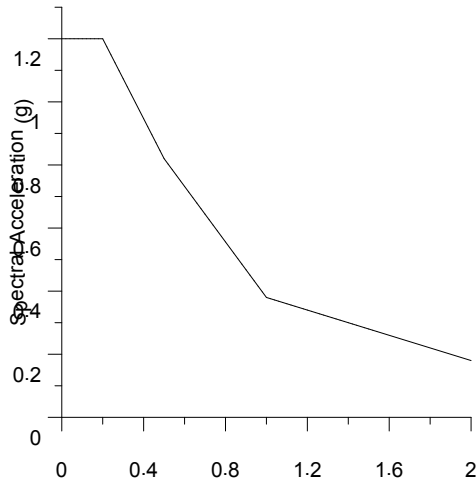


Figure 4.2: UHS for Victoria, B.C.

The distribution of lateral forces along the height of the building, F_x , is in agreement with equation 4.5, where w_x is the seismic weight of the floor x :

$$F_x = (V - F_t) \frac{w_x h_x}{\sum_{i=1}^n w_i h_i} \quad (4.5)$$

F_t is a portion of concentrated force at the top of the building, and cannot exceed 25% of the total seismic force. If the fundamental period of the building is less than 0.7 seconds, F_t is considered to be zero. This type of static load distribution follows a triangular pattern along the height of the building. It is noted that the seismic weight at roof level includes 25% of snow load, as per the NBCC 2010.

A summary of the dead loads and live loads applied at each floor level is given in Table 4.2.

Table 4.2: Load summary for 1-storey and 2-storey buildings

	Dead Load (DL) (kPa)	Live Load (LL) (kPa)	Snow Load (kPa)	Shear Force Load (kN)
Single-Storey (T=0.19s)				
<i>Roof Level</i>	3.4	-	1.48	875
Two-Storey (T=0.38s)				
<i>Roof Level</i>	3.4	-	1.48	1352
<i>Floor Level</i>	4.0	2.4	-	2830

4.1.2 SFRS Brace Selection

The X-braces of the limited ductility CBF system are designed to resist axial forces as per the following two load combinations:

$$DL + 0.5LL + E \quad (4.6)$$

$$1.25DL + 1.5LL \quad (4.7)$$

where E is the earthquake load, DL is the dead load, and LL is the live load. For the preliminary design of tension/compression brace members, the member forces should be equal to or lower than member resistance, which means: $C_f < C_r$ and $T_f < T_r$, where C_f and T_f are the factored compression and tension forces and C_r and T_r are the member resistance in compression and tension, respectively. The seismic force components, C_E and T_E , belonging to the combination given in Eq.(4.8), is computed as per the following equation:

$$C_E = T_E = \frac{V_{f,i}}{2\cos\theta_i} \quad (4.8)$$

where i represents the storey number, $V_{f,i}$ is the storey shear at the level i , and θ is the brace angle with respect to the beam. The properties of the selected HSS steel hollow box section are then used to verify that the compressive and tensile resistance of the

member is adequate to resist the previously determined factored loads. Thus, the expressions for C_r and T_r are:

$$C_r = 0.9 A F_y (1 + \lambda^{2n})^{-\frac{1}{n}} \quad (4.9)$$

$$T_r = 0.9 A F_y \quad (4.10)$$

where $\lambda = \frac{KL}{r} \sqrt{\left(\frac{F_y}{\pi^2 E}\right)}$ is the slenderness, A is the cross-sectional area of the member, and F_y is the yield stress of steel, $F_y = 350 \text{MPa}$. The slenderness ratio of the sections as well as the width-to-thickness ratios must be verified. When determining the brace slenderness of the X-bracing scheme, the support conditions of braces must be considered in order to determine the KL value. Thus, the effective length factor, K , is considered to be 0.5 (the compressive brace is supported at its mid-length by the tensile brace) and the length L of the brace is taken as the length between the location of the anticipated plastic hinges, at the ends of bracing members, attached by gusset plate connections. Although the S16-2009 standard allows, for the single- and two-storey LD type CBFs, to have a reduced KL/r value, in this study the KL/r ratio is considered less than 200 and the cross-section of the HSS braces is Class 1. In this study, for both the single- and two-storey frames, the slenderness ratio is less than 100, which sets the limit for the width-to-thickness ratio of the section as follows:

$$\frac{b-4t}{t} \leq \frac{330}{\sqrt{F_y}} \quad (4.11)$$

4.1.3 SFRS Beam and Column Design

The beams and columns of the seismic force resisting system are selected as W-shape cross-sections and Class 1.

With regards to the beams, a section able to withstand the maximum bending moment is chosen. The loads from the braces contributing to the bending moment of the beams are also taken into account. When choosing the sections for the beams the following interaction equations must be verified:

$$\frac{C_f}{C_r} + 0.85U_{1x} \frac{M_{fx}}{M_{rx}} \leq 1.0 \quad (4.12)$$

$$\frac{T_f}{T_r} + \frac{M_{fx}}{M_{rx}} \leq 1.0 \quad (4.13)$$

where C_f and T_f are the factored compressive and tensile forces; C_r and T_r are the member compressive and tensile resistance; and M_{fx} and M_{rx} are the factored bending moments and the moment resistance of in-plane bending. The width-to-thickness ratio limits of the beam W-shape section, which acts in flexural compression, must be met by the following equation for Class 1 of sections:

$$\frac{b}{t} \leq \frac{145}{\sqrt{F_y}} \quad (4.14)$$

For column design, both the dead and live load components are considered, as well as the projection of the probable compression, C_u , and tension resistance, T_u , of brace members. In the case of columns, the interaction equations 4.12 and 4.13 must be satisfied, as well as the width-to-thickness ratio that corresponds to Class 1 or Class 2 sections. Columns of the two-storey CBF system are considered continuous over the building height. A summary of the sections selected for the single- and two-storey CBFs is given in Table 4.3 and 4.4.

Table 4.3: Members selected for the single-storey CBF

Floor	Braces	Beams	Columns
1	HSS 127x6.4	W360x57	W310x74

Table 4.4: Members selected for the two-storey CBF

Floor	Braces	Beams	Columns
2	HSS 152x13	W460x52	W310x86
1	HSS 127x9.5	W360x51	W310x86

4.2 Modelling of the Single- and Two-Storey CBF Buildings in OpenSees

In order to perform a numerical analysis on the conventional concentrically braced frames, which will in turn be compared to the behaviour of the same frames with the dissipative single-pin connections, a model for both the single- and two-storey structures will be built using the OpenSees framework. Used for these purposes are the OpenSees Manual (Mazzoni et al., 2007) and the OpenSees software, version 2.2.0, (McKenna et al., 2009).

4.2.1 The OpenSees Framework

The OpenSees framework is an open source program developed at the University of California, Berkeley, by Frank McKenna et al. (2009). The framework uses the finite element method to simulate different applications in earthquake engineering. An open source program allows for the expansion of applications offered by the user of the proposed framework in terms of material nonlinearity definition, elements algorithms and so on.

In order to model, analyze and record the outputs of the models built in OpenSees, the TCL language is employed. The TCL language is a string-based scripting language which resembles the C programming language.

There are four main components pertaining to the process of analyzing in the framework, which can be found in Figure 4.3. The user input is pertinent to the “model-builder” application. This application constructs the objects of the model such as elements, sections, nodes, load patterns, time series, materials and other important factors needed to describe the model being analyzed. This information is then stored in the “domain”. The “analysis” application is the one which moves the model from time t_i to time $(t_i + dt)$, depending on the type of analysis requested by the user. While the analysis is processing, the “recorder” application monitors the parameters defined by the user in order to extract the data required. This data is stored in the “domain” as well, which gives access to both the “analysis” and “recorder” applications.

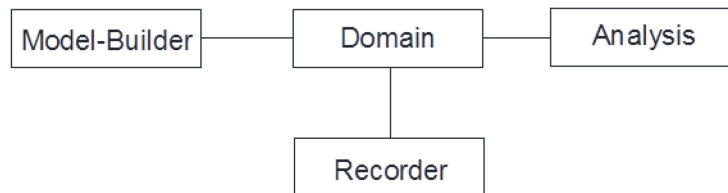


Figure 4.3: Overview of the OpenSees Framework (Mazzoni et al., 2007)

The modelling of the single- and two-storey frames in the OpenSees framework was adapted by Uriz and Mahin (2008) and will be detailed in the following sections.

4.2.2 Modelling of Beams and Columns

The beams and columns, previously designed in Section 4.1, are made up of the *Steel02* material. This material, better known as the Giuffré-Menegotto-Pinto material, is a steel material with isotropic strain hardening, which allows for the material to yield when strains develop, while keeping the cross-section centered about its neutral axis. The input parameters for this steel material are the elastic modulus, $E=200GPa$, the yield

strength, $F_y=350MPa$, and some parameters which control the transition from elastic to plastic, as well as some that define the isotropic strain hardening. The response of the *Steel02* material for different R parameters ($R=5$ and $R=20$) can be found in Figure 4.4.

The elements used to model the beams and columns are the beam with hinge elements. These elements are able to concentrate the plasticity of the element within the user defined plastic hinge sections, while the center of the elements behave elastically, as shown in Figure 4.5. The advantage of this element is that the user must only define the length of the plastic hinge at the end zone of the beam, while two integration points per plastic hinge, which are a pre-defined component of the element by the program, are able to represent the linear curvature distributions in an accurate fashion. Therefore, the information needed to define the elements is the member properties, the length of the plastic hinge, which is assumed to be the height of the cross section, and finally the cross-sectional properties of the member.

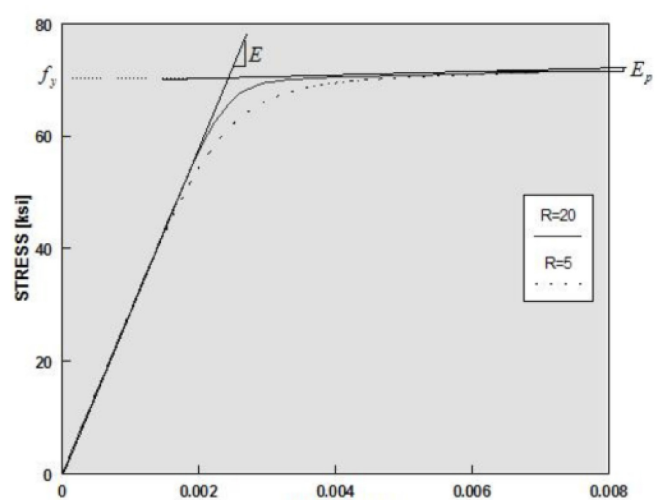


Figure 4.4: Response of the OpenSees *Steel02* material (Mazzoni et al., 2007)

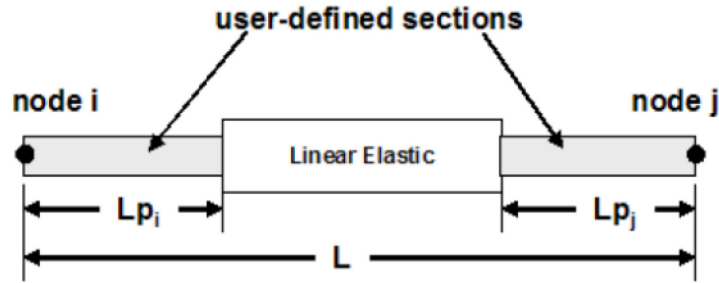


Figure 4.5: OpenSees beam with hinges elements (Mazzoni et al., 2007)

The cross-sectional definition of the beams and columns are composed of fibers. The fibers create a mesh like pattern and allow for the reading of stresses and strains along the cross sections of the members at any time during the loading process. Both the beams and columns are W-Sections and therefore the fibers were equally defined in both members. The cross-sections are composed of five fibers along the flanges and six fibers along the web, as shown in Figure 4.6.

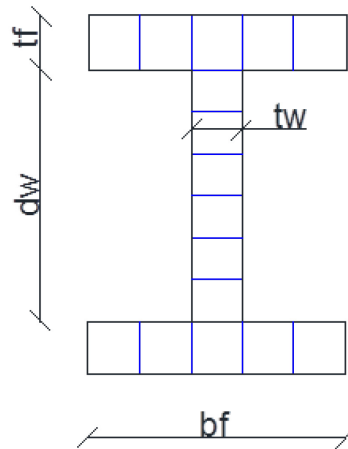


Figure 4.6: Discretization of the beam and column cross sections in OpenSees

As shown in Figure 4.7, the beams and columns are in a pinned configuration. The zero-length rotational springs, C1, are assigned to have no stiffness in the rotational

component, which in turn allows for the connection to be pinned and for the reading of the rotations at the beam ends.

There are two seismic force resisting systems in both principal directions (x and y). The building is symmetrical in both axes: x direction and y direction. Thus, half of the gravity columns are added to the model in order to simulate the stiffness of half of the building, while analyzing the seismic response in that particular direction. Gravity columns are modelled as pin-ended members in the same way as the columns belonging to the seismic force resisting system. In order to connect the gravity columns to the CBF system, rigid links are used. Columns of the 2-storey building are continuous over the total height of the building, as illustrated in Fig. 4.7.

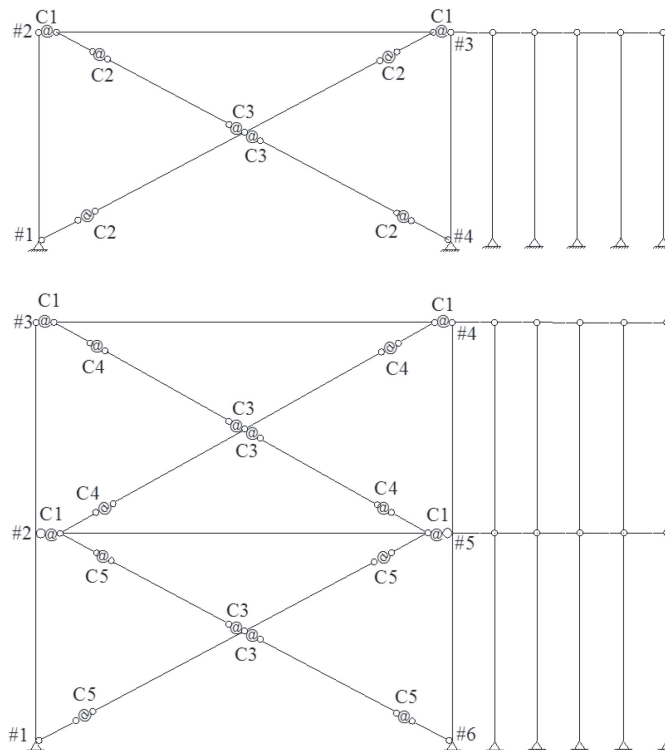


Figure 4.7: OpenSees model of the single- and two-storey structures

4.2.3 Modelling of Braces

The braces in both models are made up of eight non-linear beam column elements per half-length of the brace. The non-linear beam column is an element which ensures the distribution of plasticity along the whole length of the member, which is required for brace modelling. This element does not have pre-defined integration points, therefore four integration points per element were defined. Again, the material used to define these members is the *Steel02* material, as previously described in section 4.3.2. The camber of the brace, which accounts for the residual stresses that are not present in the brace model, is set to be $L/500$ per half brace, as proposed for HSS sections (Ziemian, 2010). In this study, the HSS brace cross section is formed from 216 fibers, as shown in Figure 4.8.

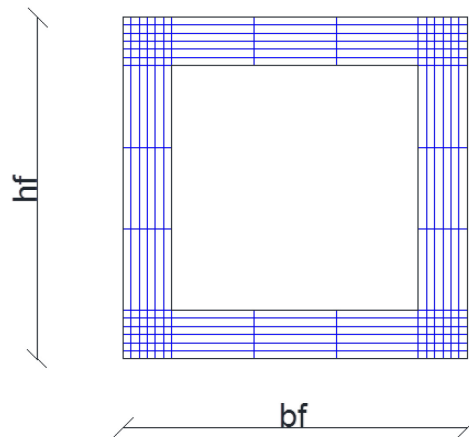


Figure 4.8: Discretization of the HSS brace cross-section

Each brace is equipped with a rigid link at both ends. This rigid link defines the portion of the brace-to-column connection, in this case the gusset plate, which is rigidly fastened to the column. Since this member is to behave rigidly and no deformation is to be recorded in the member, an elastic beam column element is used.

The compression brace is connected to the tension brace with two zero-length springs, C3 (Figure 4.7). These springs exhibit a rigid behaviour to imitate the type of connection between the two braces in practice.

4.2.4 Tridimensional Modelling of Gusset Plates

The zero-length connections, C2, C4, and C5 (Figure 4.7) are the rotational springs that act as the gusset plates, deforming in-plane and out-of plane. The values used to define the gusset plates are the flexural, torsional and out-of-plane strength of the plate depending on its size.

The first step to sizing the gusset plates is to determine the Whitmore width, b_w , (Whitmore 1952). As shown in Figure 4.9, the Whitmore width can be determined by drawing two lines, at an angle of 30 degrees from the two fastener lines.

When sizing the gusset plates, the compressive and tensile resistance of the plates must be greater than that of the brace, where the probable tensile resistance of a brace is $T_u = AR_y F_y$ and the probable compressive resistance is $C_u = 1.2AR_y F_y (1 + \lambda^{2n})^{-1/n}$. The equations for the tensile resistance of the gusset plate, Eq.(4.15), and the compressive resistance of the plate, Eq.(4.16), were formulated by Izvernari (2007) and are as follows:

$$T_g = \phi F_y b_w t_g \quad (4.15)$$

$$C_g = \phi A F_y (1 + \lambda^{2n})^{-1/n} \quad (4.16)$$

$$\lambda = \frac{KL_c}{t_g} \sqrt{\frac{12 F_y}{\pi^2 E}} \quad (4.17)$$

where L_c represents the critical length of the gusset plate and ϕ is a scale factor of 0.9. It was proposed by Thornton in 1984 that the three lines, L1, L2, and L3, found in Figure 4.9, can be considered as column strips of unit width. These columns represent the buckling strength of the gusset plate, based on their compressive resistance. Thornton

proposed that the longest of the three lines shall represent the critical length, but it was suggested by Cochran and Honeck (2004) that the average of the three lines represents the critical length. By equating the above formulae with the compressive and tensile resistances of the brace, the value for the thickness of the gusset plates, t_g , can be determined. The free length, $2t_g$, allows for plastic hinges to form in the gusset plate in the event of any out of plane buckling.

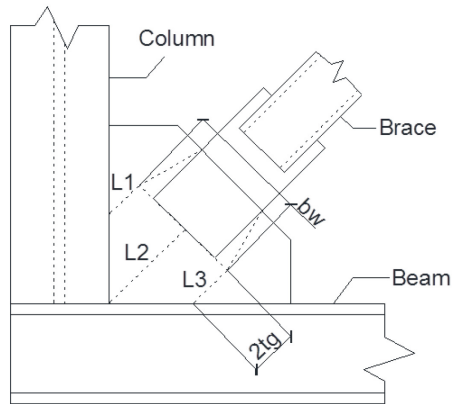


Figure 4.9: Sizing of the gusset plates (adapted from Izvernari, 2007)

The next step would be to determine the capacities of the gusset plates in flexure, tension, and out-of-plane buckling. To determine these capacities, the following equations were formulated by Izvernari (2007), the first being out-of-plane resistance, followed by torsional capacity and finally flexural capacity:

$$C_f = 1.5 \frac{EI}{2 t_g} \quad (4.18)$$

$$C_t = 1.5 \frac{GJ}{2 t_g} \quad (4.19)$$

$$M_p = \frac{1}{4} b_w t_g^2 F_y \quad (4.20)$$

where I is the flexural moment of inertia of the gusset plate and J is the torsional moment of inertia of the guest plate. The yield strength is that of steel, $F_y = 350MPa$, and again the thickness of the gusset plate and the Whitmore length are denoted by t_g and b_w , respectively. Therefore, a rotational spring, fixed in x and y translations as well as in rotation about the z-axis (out-of-plane bending) and given the properties above in flexure, torsion and out of plane buckling, will emulate a gusset plate connecting the braces to the beam/column.

4.2.5 Dynamic Analysis in OpenSees

In general the time step of ground motions is given at 0.02s, 0.01s, or 0.005s, while the integration time is 0.0005 seconds and must be smaller than the time step of the given record. The percentage of critical damping applied to all the members, except the braces, is 2%. The braces need not be damped due to the fact that they are the source of energy dissipation in the system. The Newton algorithm is used for analysis.

The dynamic characteristics for the single- and two-storey buildings are summarized in Table 4.5. Since the difference between the fundamental period resulted in OpenSees and that computed by using empirical equations differs by only 5%, the scaling of ground motions will be according to the period of the building determined in OpenSees.

Table 4.5: Seismic design and building characteristics for the CBF with gusset plate connections

Storey	Height [m]	W [kN]	T_a [s]	$S(T_a)$ [g]	V/frame [kN]	T_1 [s]	T_2 [s]	T_1/T_a
Equivalent static force procedure						OpenSees		
1	3.8	2845	0.19	(2/3)1.2=0.8	875	0.20	-	1.05
2	7.6	9190	0.38	(2/3)1.2=0.8	2830	0.42	0.20	1.05

4.3 Selection and Scaling of Ground Motions

The studied buildings are designed for Victoria, B.C. In order to carry out a seismic analysis, three sets of recorded ground motions are selected and scaled, totaling 21 seismic ground motions. The first set consists of historical crustal ground motions, the second set contains of historical subduction records and the third set is assigned to near-field records with pulse characteristic and forward directivity. Although Canada is not affected by near-field ground motions, they were selected to highlight their effect on the CBF response.

4.3.1 Selection of Ground Motions

The first set of ground motions used for design is the crustal group. It consists of seven recorded ground motions and the set was selected to match the dominant magnitude hypocentral scenarios of Victoria, B.C.: M6.5 at an epicentral distance of 30km and M7.2 at a epicentral distance of 70km (Atkinson, 2009). The seismic ground motions were selected from the the PEER Ground Motion Database Beta Version (2010). The number of selected records per group is in agreement with FEMA 356 (2000) and NBCC 2010, where it is mentioned that at least three different records are enough if the maximum response is selected, and seven records are required if “the average value of each response parameter shall be permitted to determine design acceptability” (FEMA356, 2000).

The set of subduction ground motions with a magnitude of M9.0, used to simulate the Cascadia subduction fault, consists of six recorded and one simulated ground motion. The study of building response to subduction ground motions is an important design step due to the proximity of Victoria to the subduction fault, which is estimated at

approximately 80km (Atkinson and Macias, 2008). Due to their similarities, the recorded ground motions employed in this study are from the Tohoku event, which occurred on March 11 of 2011, and were selected from the website: www.k-net.bosai.go.jp, while the artificial record for Victoria was simulated by Atkinson and Macias (2008).

The ground motions of the near-field group were recorded at a distance less than 10km from the source. However, near-field ground motions are not characteristic of the Victoria region. This group was selected to discuss the structure behaviour.

In Table 4.6, a list of all selected records and their characteristic are given. The characteristics such as: peak ground acceleration, PGA , and peak ground velocity, PGV , as well as the Trifunac duration, t_d , and the total earthquake duration, t , are given. The ratio of peak ground velocity to peak ground acceleration, PGV/PGA , has also proven to be an important factor in quantifying the frequency of the ground motions.

4.3.2 Scaling of Ground Motions

In order to analyze a specific structure when subjected to ground motions, the latter must be scaled in order to match the uniform hazard spectrum of the building location. There are no specific provisions in the NBCC 2010 code regarding ground motions scaling. However, it is mentioned that all selected ground motions should be scaled to match the UHS ordinate at the fundamental period, T_1 (ordinate $S(T_1)$) and to fit or be above the UHS at all points corresponding to the shorter period modes. More in detail, the ASCE/SEI 2007 provisions require that the mean of the 5% damped response spectra of a minimum of seven scaled ground motions should match or be above the UHS, illustrated in Figure 4.2, over the period of interest $0.2T - 1.5T$. Herein, the ASCE/SEI 2007 requirements are applied. It was found by researchers (Kalkan and

Chopra, 2011, and others) that during the inelastic behaviour, the stiffness of the structure degrades and the period of the building may elongate up to $1.5T_1$.

The method for scaling ground motions is based on the Reyes and Kalkan methodology (2011), which consists of minimizing the discrepancy between the scaled acceleration response spectrum of each record and the UHS over the specified period range ($0.2T_1-1.5T_1$).

The single- and two-storey buildings do not exhibit higher mode effects. Thus, for the single-storey building there are no higher modes and the period of interest ranges from T_1 to $1.5T_1$, which in this case study is between $T_1 = 0.20s$ and $1.5T_1 = 0.30s$. In the case of the two-storey building, the period of interest is proposed to be between T_2 and $1.5T_1$, more specifically, $0.2 - 1.11s$.

4.3.2.1 Ground Motion Scaling for the Single-Storey Building

It is stated in the Commentary J of the NBCC 2010, section 4.1.8.4.(6), 109., that "Although spectral accelerations at very short periods are typically about the same or slightly less than the $S_a(0.2)$, the design values of $S(T)$ for $T < 0.2s$ are specified to be the same as $S(0.2)$." This conservative assumption is due to the imprecision of identifying the period of structures with high stiffness. In order to address this drawback, the FEMA356 (2000) provisions are employed. In this light, it is proposed that from time 0 to time T_0 , the spectral acceleration ordinates increase linearly from $0.4S(0.2)$ to the $S(0.2)$ value where:

$$T_0 = 0.2 \times \frac{S(0.5)}{S(0.2)} \leq 0.10s \quad (4.21)$$

while,

$$0.4S(0.2) = 0.4 \times 1.2 = 0.48g \quad (4.22)$$

Table 4.6: Ground motion characteristics

NAME	EVENT	STATION	COMP	M _w	R (km)	PGA (g)	PGV (m/s)	$\frac{PGV}{PGA}$	t _d (s)	t (s)
CRUSTAL GROUND MOTIONS										
<i>C1</i>	Loma Prieta 1989*739	Anderson Dam	2500°	6.9	19.9	0.244	0.203	0.832	10.51	39.61
<i>C2</i>	Northridge 1994*954	Big Tujunga, Angeles N	3520°	6.7	19.1	0.325	0.127	0.391	9.44	29.99
<i>C3</i>	Northridge 1994*1077	Santa Monica City Hall	3600°	6.7	17.3	0.369	0.253	0.686	10.72	40.00
<i>C4</i>	Imperial Valley 1979 *164	Cerro Prieto	1470°	6.5	15.2	0.170	0.120	0.706	29.70	63.74
<i>C5</i>	Western Wash 1949	Olimpia, Test Lab.	860°	7.1	76.0	0.280	0.170	0.607	18.80	89.06
<i>C6</i>	Loma Prieta 1989 *736	APEEL9 – Crystal Springs Res	2770°	6.9	40.9	0.104	0.181	1.740	16.20	39.01
<i>C7</i>	San Fernando 1971 *78	Palmdale fire station	2100°	6.6	24.2	0.151	0.082	0.543	17.31	30.00
SUBDUCTION GROUND MOTIONS										
<i>S1</i>	Tohoku 2011	IWT007E	E-W	9.0	156	0.66	0.29	0.44	80.96	299.98
<i>S2</i>	Tohoku 2011	FKSH19N	N-S	9.0	201	0.61	0.40	0.66	89.07	299.98
<i>S3</i>	Tohoku 2011	IBRH16E	E-W	9.0	272	0.57	0.31	0.55	66.91	299.98
<i>S4</i>	Tohoku 2011	CHB001N	N-S	9.0	357	0.14	0.28	2.00	83.78	299.98
<i>S5</i>	Tohoku 2011	TKY027E	E-W	9.0	376	0.16	0.28	1.90	93.75	299.98
<i>S6</i>	Tohoku 2011	TKY026E	E-W	9.0	380	0.16	0.28	1.90	99.06	299.98
<i>S7</i>	Simulated Cascadia	VIC084E	E-W	9.0	84	0.10	0.28	2.80	38.06	262.01
NEAR-FIELD GROUND MOTIONS										
<i>N1</i>	Kobe 1995	JMA	90°	6.9	6.0	0.83	0.92	1.08	8.28	150.0
<i>N2</i>	Kobe 1995	Takatori	90°	6.9	2.0	0.61	1.27	2.08	9.94	40.96
<i>N3</i>	Northridge 1994	Rinaldi	228°	6.7	7.1	0.84	1.75	2.02	7.05	14.95
<i>N4</i>	Northridge 1994	Newhall	90°	6.7	7.1	0.58	1.18	2.03	5.92	40.00
<i>N5</i>	Northridge 1994	Sylmar CountyHosp.	90°	6.7	9.9	0.65	1.08	1.62	7.08	30.00
<i>N6</i>	Northridge 1994	Sylmar Converter	52°	6.7	6.4	0.60	1.22	2.03	11.99	60.00
<i>N7</i>	Nahanni, Canada 1985 *495	Site 1	10°	6.8	2.5	0.98	0.46	0.50	7.90	20.56

*) peer.berkeley.edu/peer_ground_motion_database

Therefore, for Victoria, the expression of T_0 is computed as $0.2S(0.5)/S(0.2) = 0.2 \times 0.82 / 1.2 = 0.137$ which is $> 0.1s$. Until further studies are conducted, it is proposed to limit T_0 to $0.1s$. A comparison of the UHS provided by the NBCC 2010 and the proposed UHS shape used to scale accelerograms employed in non-linear analysis is illustrated in Figure 4.10. Although this added slope does not affect the scaling of the selected ground motions, it is shown to confirm the assumption.

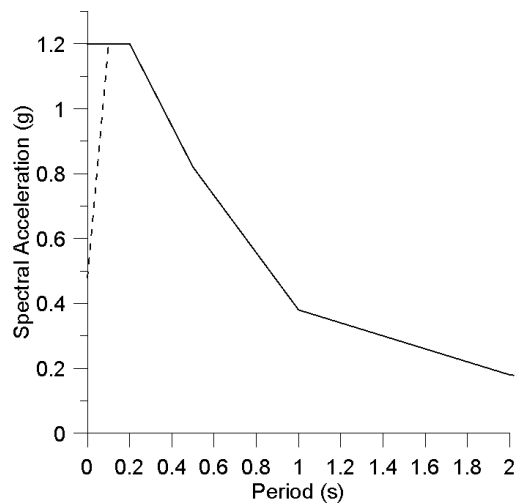


Figure 4.10: Victoria's UHS

For the single-storey building located in Victoria on soil class C, the mean of the minimum 7 scaled spectral accelerations should be equal to or above the UHS, over the period of interest $T_1 = 0.20s$ and $1.5T_1 = 0.30s$. As mentioned above, the method proposed by Reyes and Kalkan (2011) for ground motion scaling is employed.

As shown in Figure 4.11, the scale factors obtained are not influenced by the proposed slope in the high frequency range of the UHS. The single-storey structure has a period of $T=0.2s$, which is greater than the proposed zone between $T = 0$ and $T = 0.1s$. The scale factors used can be found in Table 4.7.

Table 4.7: Ground motions and their respective scale factors for the single-storey structure with gusset plate connections

NAME	Scale Factor $T_1-1.5T_1$	PGA (g)	PGV (m/s)	$\frac{PGV}{PGA}$
Crustal Ground Motions				
<i>C1</i>	2.00	0.490	0.410	0.840
<i>C2</i>	2.50	0.810	0.320	0.390
<i>C3</i>	2.20	0.810	0.560	0.690
<i>C4</i>	2.28	0.390	0.270	0.690
<i>C5</i>	2.00	0.560	0.340	0.610
<i>C6</i>	3.00	0.310	0.540	1.740
<i>C7</i>	3.00	0.450	0.250	0.560
Subduction Ground Motions				
<i>S1</i>	1.20	0.790	0.350	0.440
<i>S2</i>	0.80	0.490	0.320	0.660
<i>S3</i>	0.70	0.400	0.220	0.540
<i>S4</i>	3.30	0.460	0.920	2.000
<i>S5</i>	2.50	0.400	0.700	1.750
<i>S6</i>	2.20	0.350	0.620	1.750
<i>S7</i>	4.50	0.450	1.260	2.800
Near-Field Ground Motions				
<i>N1</i>	0.85	0.710	0.780	1.110
<i>N2</i>	0.75	0.460	0.950	2.080
<i>N3</i>	0.77	0.650	1.350	2.080
<i>N4</i>	0.70	0.410	0.830	2.030
<i>N5</i>	1.30	0.850	1.400	1.660
<i>N6</i>	1.25	0.750	1.530	2.030
<i>N7</i>	0.65	0.640	0.300	0.470

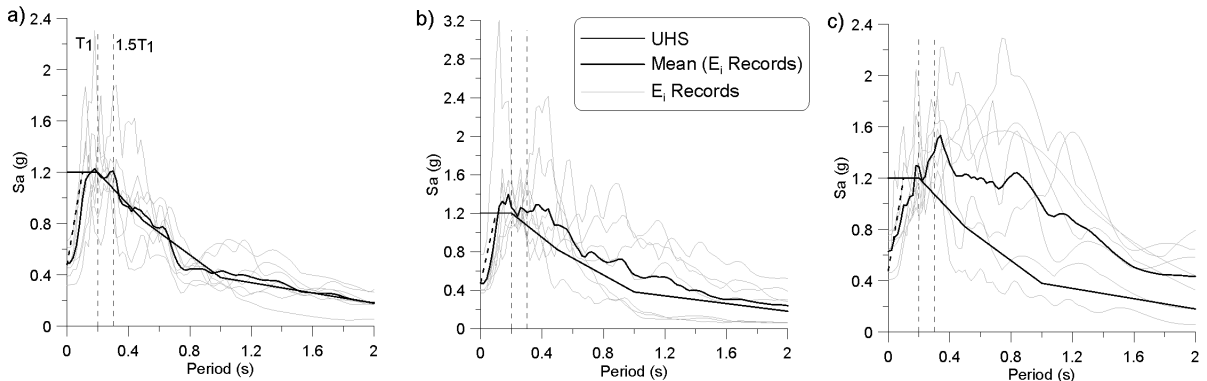


Figure 4.11: Scaled spectral acceleration for single-storey building - a) Crustal, b) Subduction, c) Near-Field

4.3.2.2 Ground Motion Scaling for the Two-Storey Building

The same analysis, stated in the previous subsection, is performed for the scaling factors of the two-storey structure. The crustal, near-field and subduction ground motions were scaled with respect to the original design spectra and the proposed equivalent design spectra. Similarly to the single-storey scaling, the scale factors remained the same and are found in Table 4.8. Figure 4.12 illustrates the scaled spectral acceleration for the two-storey building together with the mean and the UHS.

Table 4.8: Ground motions and their respective scale factors for the two-storey structure with gusset plate connections

NAME	Scale Factor $T_2-1.5T_1$	PGA (g)	PGV (m/s)	$\frac{PGV}{PGA}$
<i>Crustal Ground Motions</i>				
<i>C1</i>	1.85	0.450	0.380	0.840
<i>C2</i>	2.60	0.850	0.330	0.390
<i>C3</i>	1.70	0.630	0.430	0.690
<i>C4</i>	2.20	0.370	0.260	0.690
<i>C5</i>	2.20	0.620	0.370	0.610
<i>C6</i>	3.80	0.400	0.690	1.740
<i>C7</i>	3.80	0.570	0.310	0.560
<i>Subduction Ground Motions</i>				
<i>S1</i>	0.80	0.530	0.230	0.440
<i>S2</i>	0.70	0.430	0.280	0.660
<i>S3</i>	1.00	0.570	0.310	0.540
<i>S4</i>	2.90	0.410	0.810	2.000
<i>S5</i>	2.65	0.420	0.740	1.750
<i>S6</i>	2.70	0.430	0.760	1.750
<i>S7</i>	3.20	0.320	0.900	2.800
<i>Near-Field Ground Motions</i>				
<i>N1</i>	0.70	0.580	0.640	1.110
<i>N2</i>	0.75	0.460	0.950	2.080
<i>N3</i>	0.75	0.630	1.310	2.080
<i>N4</i>	0.85	0.490	1.000	2.030
<i>N5</i>	1.10	0.720	1.190	1.660
<i>N6</i>	1.00	0.600	1.220	2.030
<i>N7</i>	0.85	0.830	0.390	0.470

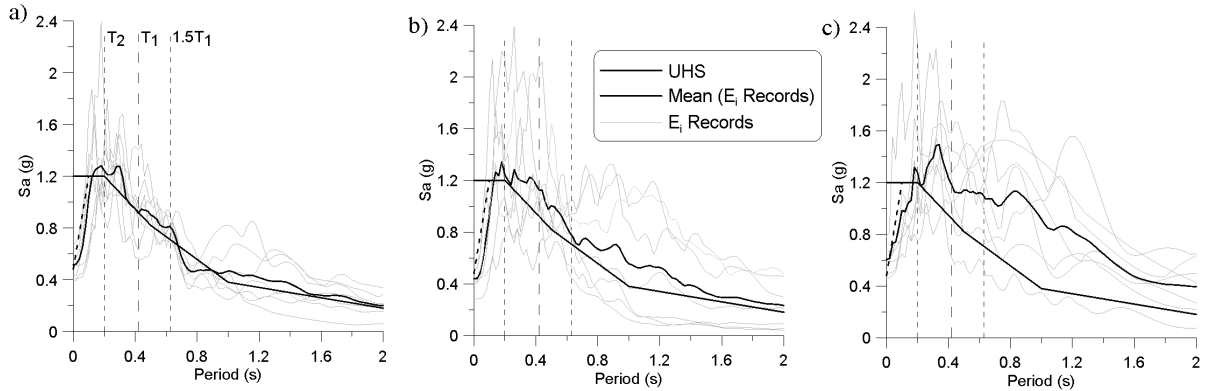


Figure 4.12: Scaled spectral acceleration for two-storey building - a) Crustal, b) Subduction, c) Near-Field

4.4 Seismic Response of Studied CBFs

4.4.1 Single-Storey CBF building

To analyze the behaviour of the single-storey CBF building, a total of six ground motions are selected among the 21 illustrated in Table 4.6, such as: C2 and C4; S1 and S3; and N1 and N3. Both records, C2 and C4, have similar peak ground velocities, as well as peak ground accelerations: *PGA* of C2 (0.33g) and *PGA* of the C4 record (0.28g). Meanwhile, C2 has a *PGV/PGA* ratio which is double that of the C4 record. In this discussion, the scaled ground motions are considered. For example, under the C2 ground motion, almost equal shear force ordinates are obtained in both tension and compression between the interval of 4.5s and 10s, as illustrated in Figure 4.13b. In this case, the *PGA* and *PGV* occurred at $t = 4.6s$ (Fig. 4.13a) and 4.65s, respectively (see Appendix A, Fig. A.2c), while the maximum shear force of 1361kN is reached in tension at 4.95s. After reloading, the first brace buckles in compression at $t = 5.02s$, as illustrated in Figure 4.13d. During the same cycle, the maximum shear force is reached in compression (1324kN) at $t = 5.05s$. After several cycles, a second peak is reached in the shear force diagram in tension (1355kN) at 9.97s. At this time step, the brace HSS 127x127x6.4 has

almost attained its tensile capacity, $T_r = 932kN$, as illustrated in Figure 4.13c. The maximum interstorey drift is $0.57\%h_s$. As per Table 4.5, the computed shear force, based on the equivalent static force procedure, is $875kN$. This value is lower than the base shear computed from the non-linear time-history analysis ($1361kN$), due to the location of the scaled spectral acceleration ordinate corresponding to T_1 , which is above the UHS (Figure 4.11b).

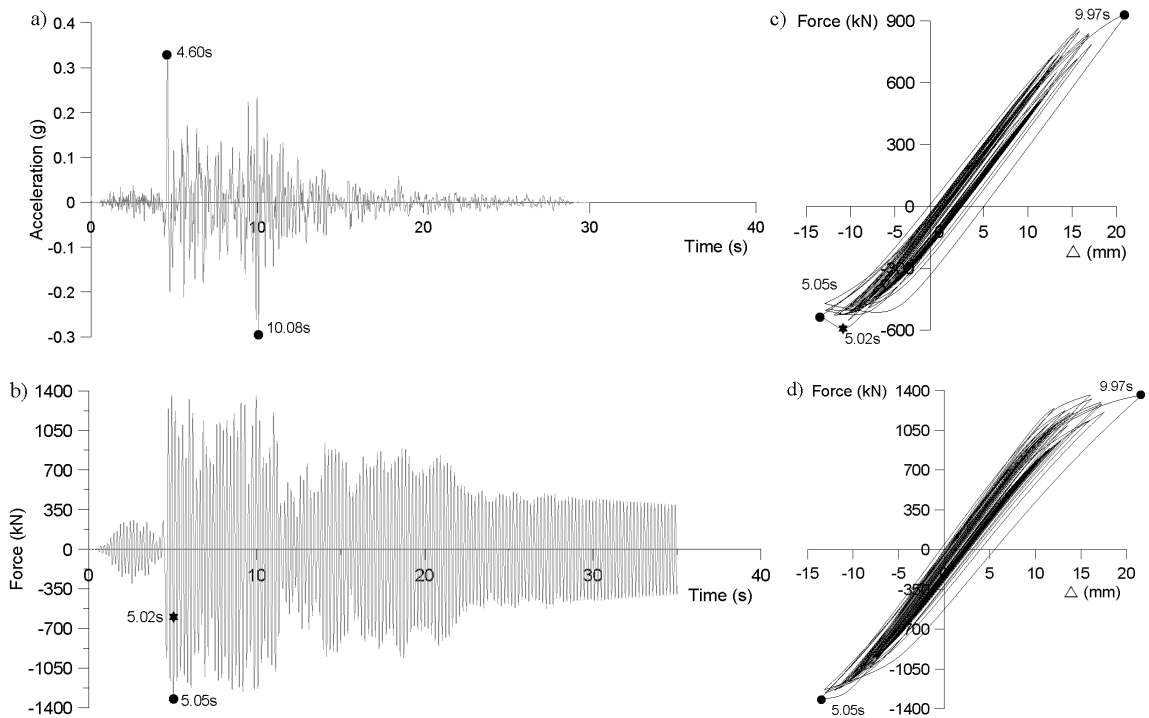


Figure 4.13: Time history response for C2 record - a) Accelerogram, b) Base shear, c) Response of brace from joint #1 to #3 (Figure 4.7), d) Single-storey frame response

Similarly, under the C4 ground motion, the maximum interstorey drift is $0.49\%h_s$, as illustrated in Figure 4.19, and the shear force computed from the non-linear time-history analysis is $1382kN$ at $t = 15.67s$ (Figure 4.14b). The brace reaches the maximum tensile force at a value slightly lower than T_r (Figure 4.14c) and buckles in compression

at $t = 12.75s$, a few cycles after the attainment of the PGA ($t = 6.70s$) and PGV ($t = 6.75s$), as illustrated in Figure 4.14a and Appendix A. As seen, the shear force is larger than the shear force computed based on the equivalent static force procedure.

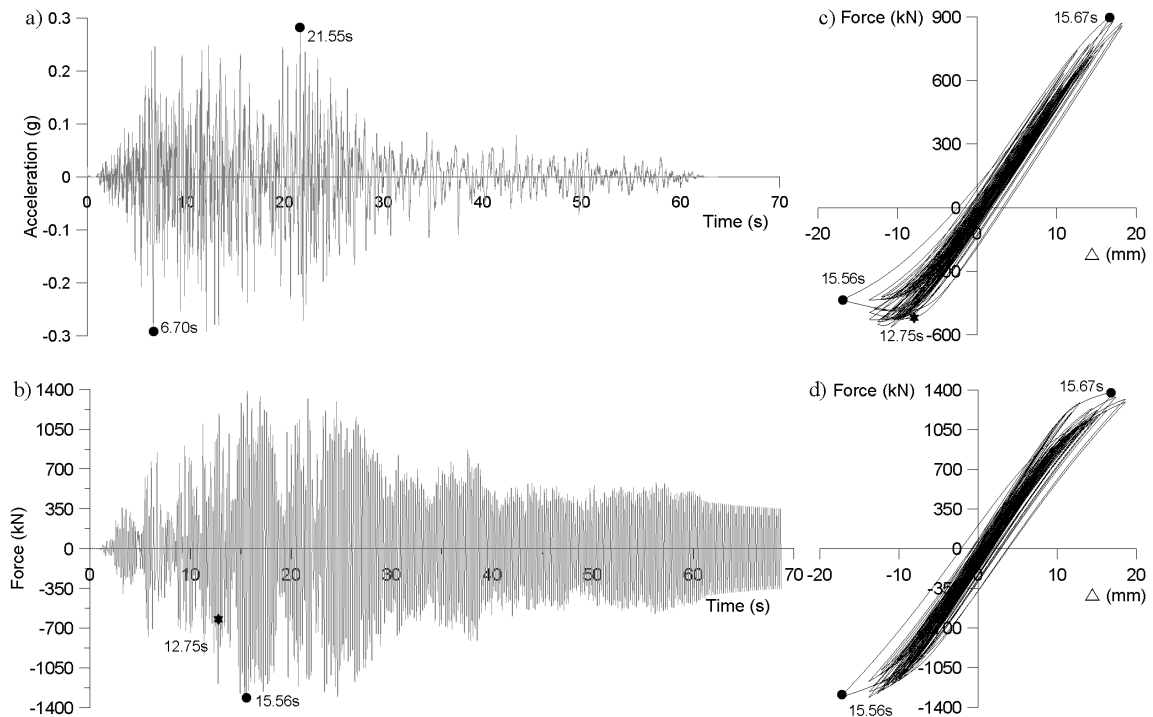


Figure 4.14: Time history response for C4 record - a) Accelerogram, b) Base shear, c) Response of brace from joint #1 to #3 (Figure 4.7), d) Single-storey frame response

The accelerogram time series of the selected subduction ground motions, S1 and S3, are illustrated in Figures 4.15a and 4.16a. The S1 record shows a maximum PGA of $0.40g$ at $t = 115.5s$ and S3 has a PGA value of $0.22g$ ($t = 114.86s$), which is approximately half of the PGA corresponding to S1. Under the S1 record, several cycles of maximum base shear, approximately $1300kN$, are experienced by the frame between $50s$ and $140s$, while under the ground motion S3, a similar base shear magnitude is developed over a smaller duration ($80s$ to $120s$). According to Figure 4.15b and 4.15c,

the brace buckles at $47.49s$ and reaches a maximum shear in compression of $1333kN$ at $t = 55.36s$. At the time step $t = 90.70s$, the brace reaches the tensile force of $923kN$, which is slightly smaller than $T_r = 932kN$, while the shear force is $1343kN$. The maximum interstorey drift is $0.56\%h_s$ which is similar to the interstorey drift obtained under crustal ground motions.

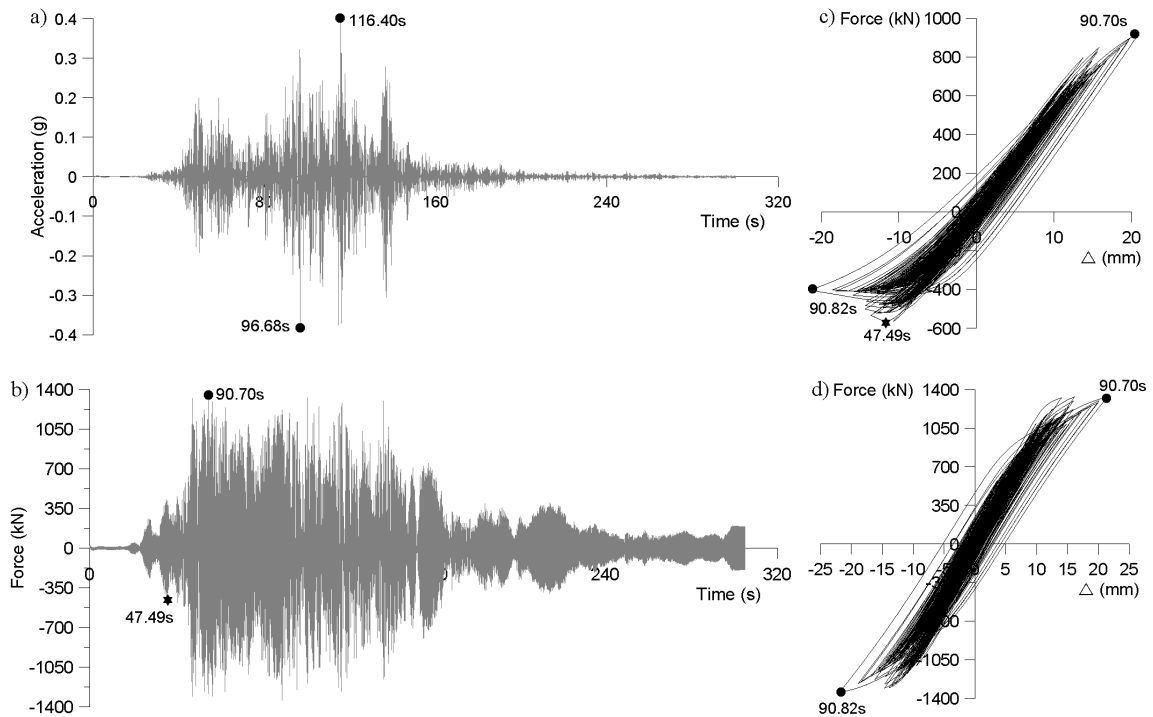


Figure 4.15: Time history response for S1 record - a) Accelerogram, b) Base shear, c) Response of brace from joint #1 to #3 (Figure 4.7), d) Single-storey frame response

Under the S3 ground motion, the brace buckles at $95.91s$ and the maximum shear attained in compression is $1003kN$ ($t = 95.93s$), which occurs before the PGA is reached. After the PGA is reached, at $114.86s$, a maximum tensile force is triggered in the brace ($931kN$) and is close to T_r . The maximum interstorey drift is $0.56\%h_s$.

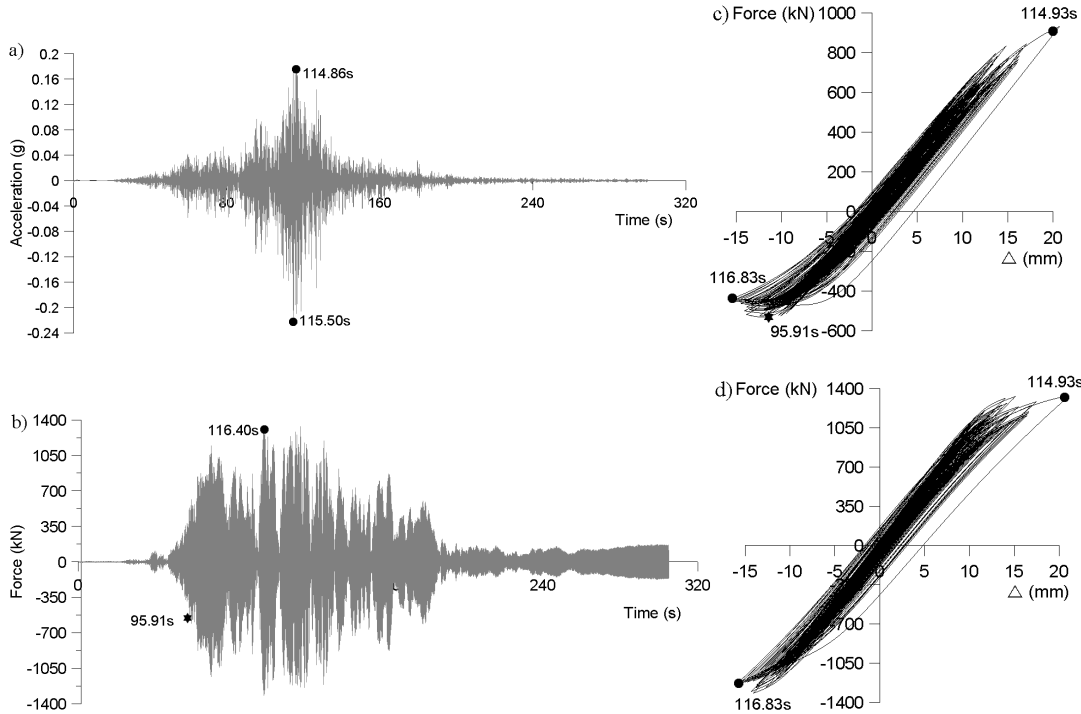


Figure 4.16: Time history response for S3 record - a) Accelerogram, b) Base shear, c) Response of brace from joint #1 to #3 (Figure 4.7), d) Single-storey frame response

Regarding near-field ground motions, the selected accelerograms are N1 and N3 and are illustrated in Figures 4.17 and 4.18. The maximum PGA ($0.42g$) occurs at the beginning of N1 ground motion at $t = 8.54s$, while for the N3 record, PGA ($0.66g$) occurs at $t = 2.69s$. These ground motions are characterized by large acceleration pulses and large incremented energy at the beginning of the ground motions. Under the N1 record the brace buckles at $t = 9.44s$ and reaches a maximum shear in compression of $1234kN$. However, the maximum shear force, $1365kN$, is reached in tension at $10.36s$. The tensile force developed in the brace is below the tensile strength, T_r . The interstorey drift is $0.41\%h_s$. Regarding the inelastic behaviour of the brace, it seems that only one cycle is experienced after the brace has buckled (Figure 4.17c). A similar behaviour is illustrated in Figure 4.18b, 4.18c, and 4.18d, when the single-storey CBF is subjected to the N3

record. The maximum base shear occurs in tension and has a magnitude of $1294kN$ at a time $t = 6.57s$, while the maximum interstorey drift is $0.35\%h_s$.

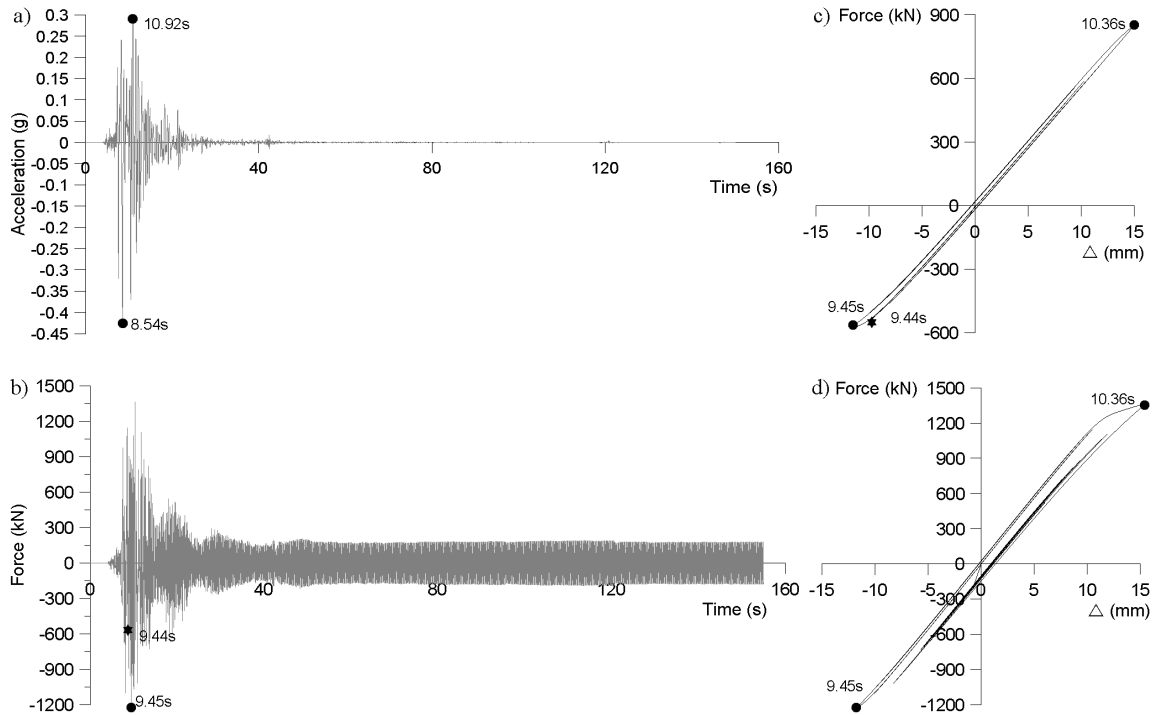


Figure 4.17: Time history response for N1 record - a) Accelerogram, b) Base shear, c) Response of brace from joint #1 to #3 (Figure 4.7), d) Single-storey frame response

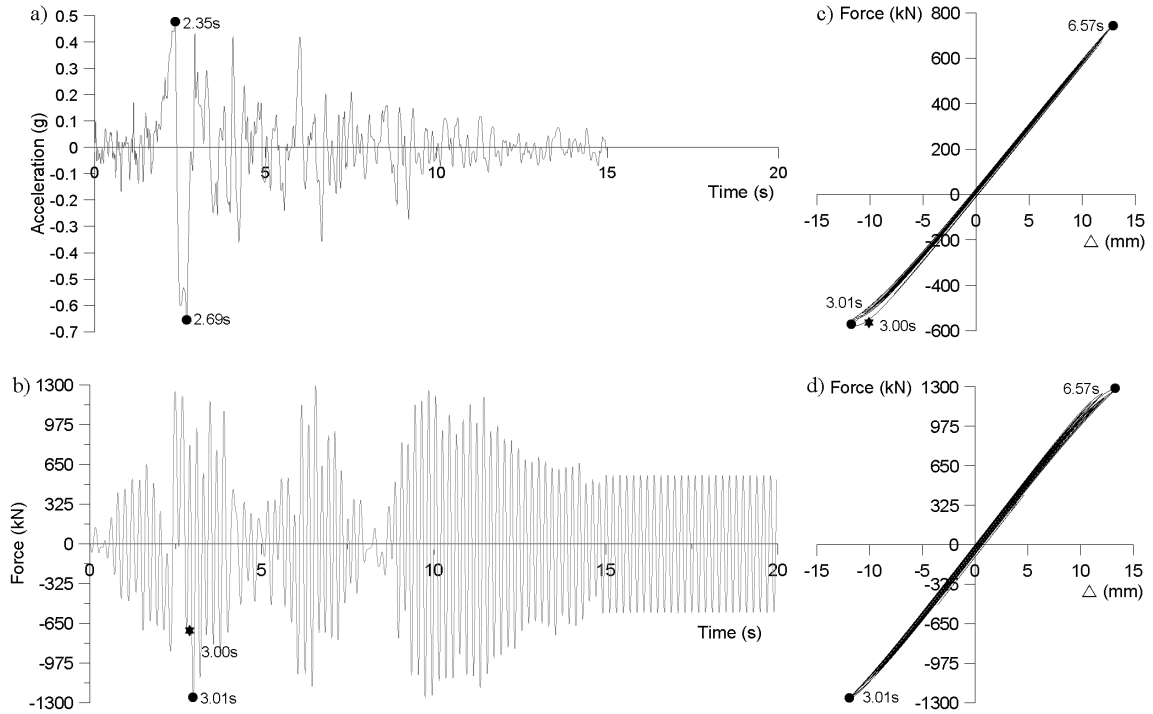


Figure 4.18: Time history response for N3 record - a) Accelerogram, b) Base shear, c) Response of brace from joint #1 to #3 (Figure 4.7), d) Single-storey frame response

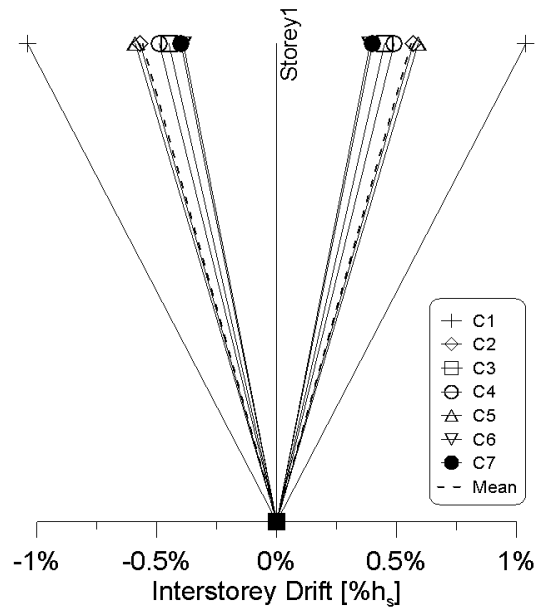


Figure 4.19: Interstorey drift - Crustal ground motions

4.4.2 Two-Storey CBF Building

To illustrate the seismic response of the two-storey CBF building, the four of the same ground motions are selected from the crustal and subduction ensembles: C2 and C4; and S1 and S3. In this discussion, the scaling factors, computed to match the proposed equivalent UHS and given in Table 4.8, are considered. For example, under the C2 ground motion, almost equal shear force ordinates are obtained, in both tension and compression, during the interval 4.5s to 10s, as illustrated in Figure 4.20b. The PGA occurs at $t = 4.6s$, while the second peak occurs at 10.08s (Fig. 4.20a). The maximum base shear force is 3298kN and occurs after the PGA was reached. The ground floor brace HSS 152x152x13 buckled at $t = 4.63s$ (Figure 4.21) and almost yields at $t = 4.97s$. Its tensile resistance is $T_r = 2104kN$ and the probable tensile resistance is $T_u = 1.1T_r/09 = 2572kN$. As illustrated in Figure 4.21, the HSS 152x152x13 brace reaches 2251kN in tension. The brace at the second floor is a HSS 127x127x9.5 and buckles almost simultaneously with the ground floor brace. After that, the brace behaves elastically in tension and reaches the maximum tensile force, T , at $t = 9.96s$ with a value of 1092kN < $T_r = 1335kN$. This value is reached a few seconds before the second acceleration peak occurs. The maximum base shear of 3298kN is larger than that computed from the equivalent static force procedure, which is 2830kN. It is noted that the spectral acceleration ordinate is above the UHS at $T_1 = 0.4s$ by 16%. The maximum interstorey drift occurs at the ground floor and is about 0.73% h_s , while the roof interstorey drift is 0.37% h_s , as illustrated in Figure 4.32. The ground floor brace deformation is below 25mm in both tension and compression, while the upper floor brace reaches a deformation below 15mm.

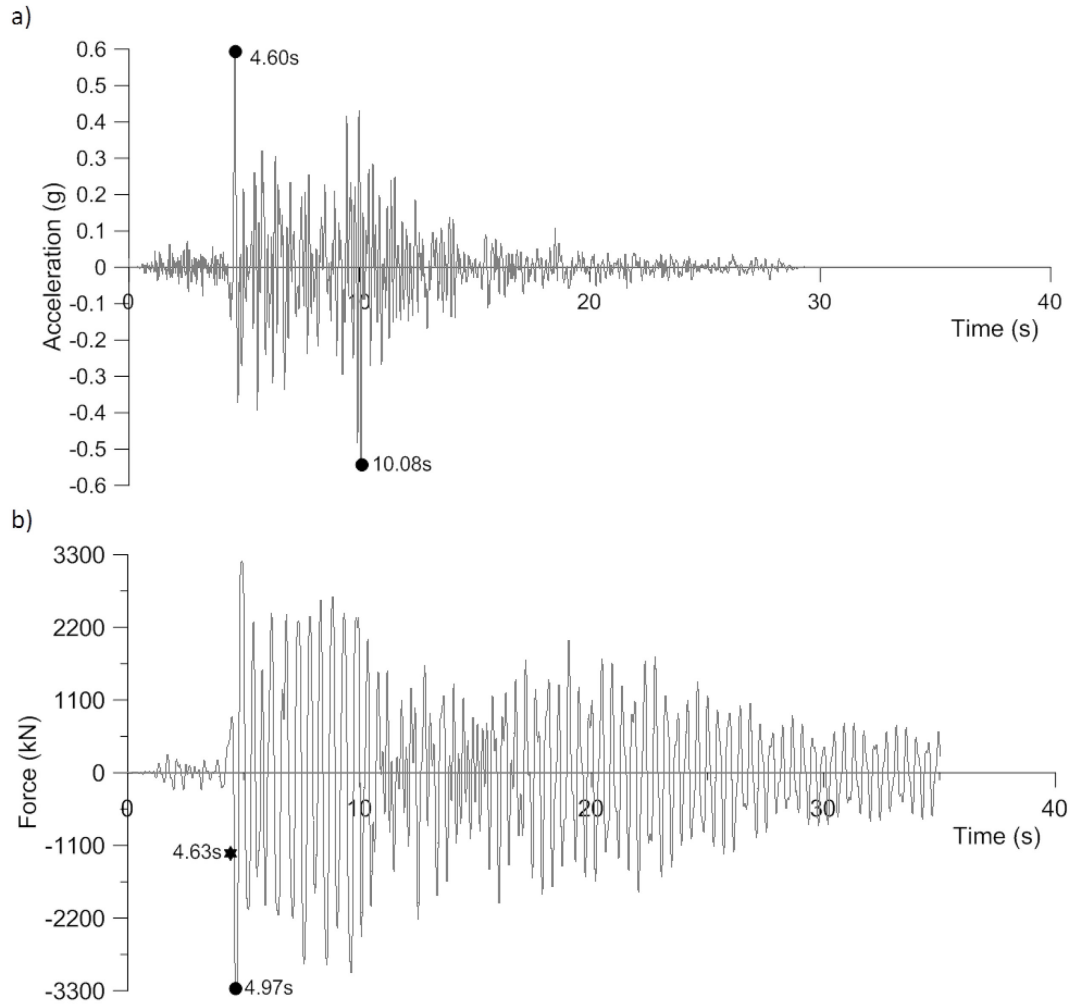


Figure 4.20: Time history response for C2 record - a) Accelerogram, b) Base shear

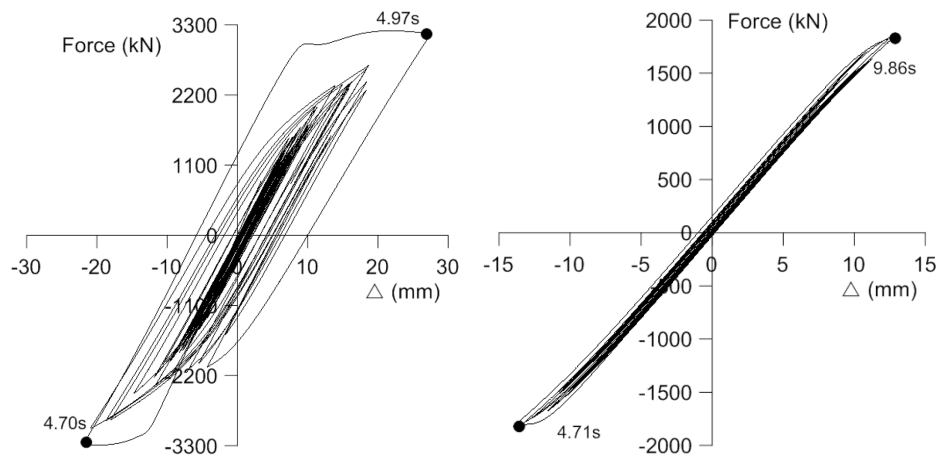


Figure 4.21: Hysteretic response for C2 record - a) Two-storey ground floor response, b) Two-storey second floor response

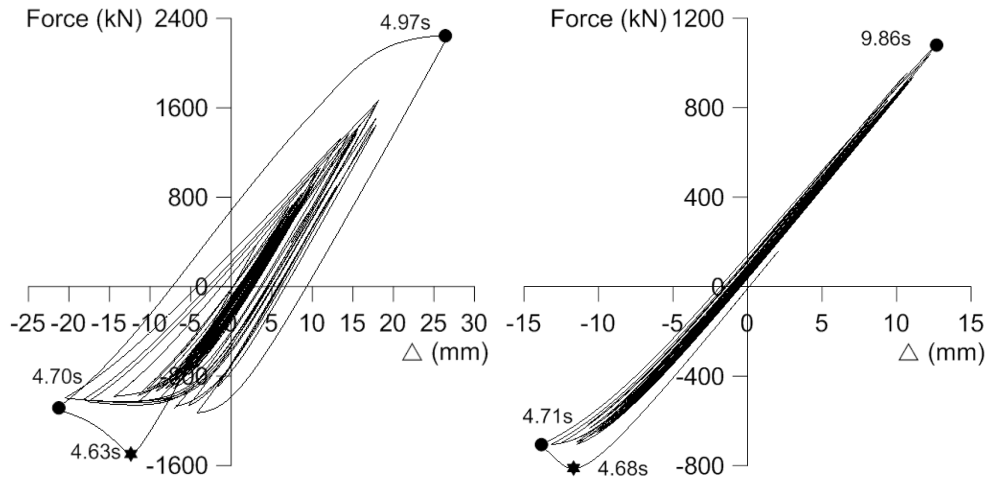


Figure 4.22: Hysteretic response for C2 record - a) Response of brace from joint #1 to #5 (Figure 4.7), b) Response of brace from joint #2 to #4 (Figure 4.7)

Regarding the C4 ground motion, the seismic response of the two-storey CBF is similar with that illustrated under the C2 ground motion. The maximum base shear occurs after the PGA and is $3285kN$. The first brace buckles in compression at $5.11s$ and occurs at the ground floor. The same brace yields in tension during the same cycle and the hysteresis loop reverses at $6.84s$. The largest amount of energy is dissipated during this cycle, while the maximum brace deformation in tension and compression is about $45mm$. The second floor brace buckles at $15.56s$ (Figure 4.25) before the second acceleration peak is reached and the maximum post-buckling strength occurs at $15.66s$ at the ground floor brace. The maximum interstorey drift occurs at the ground floor and is $1.03\%h_s$, while the roof interstorey drift is $0.42\%h_s$. As illustrated, a larger energy is dissipated at the ground floor level, especially under the C4 record, which imposed a larger deformation. The upper floor braces dissipate a small amount of energy when compared to the ground floor braces.

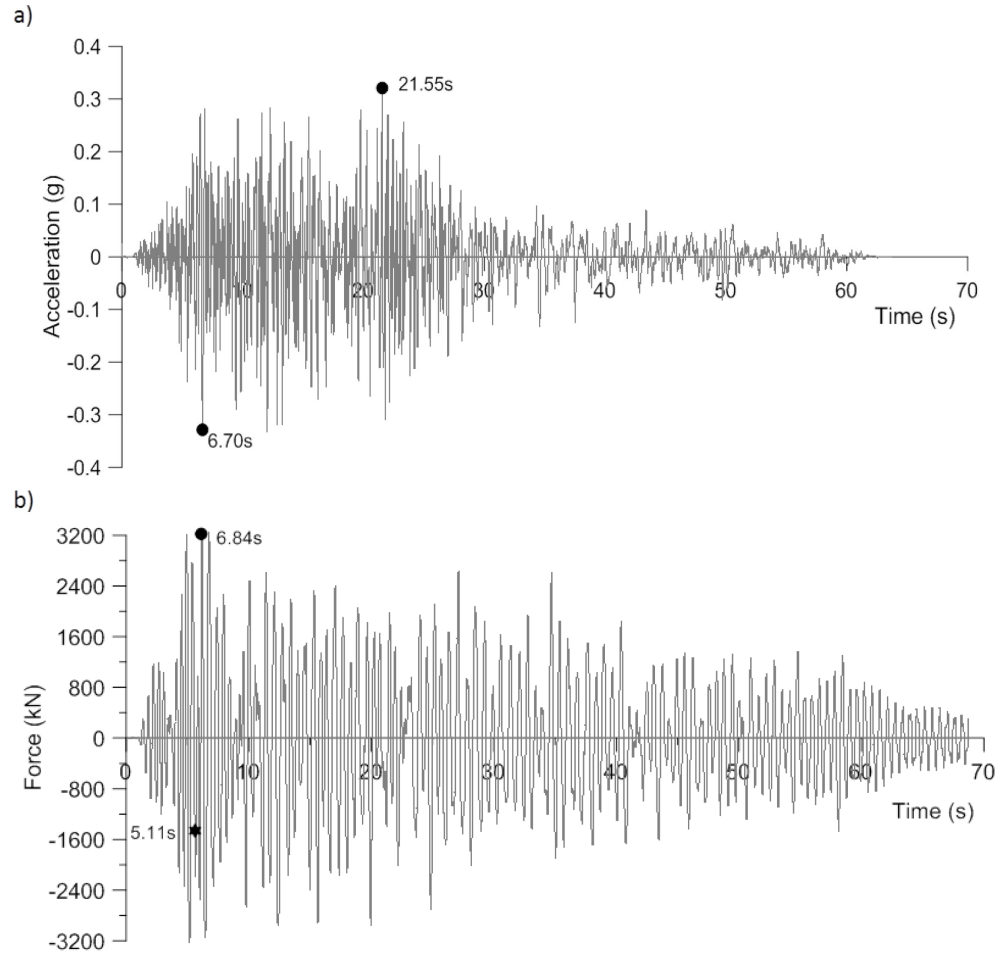


Figure 4.23: Time history response for C4 record - a) Accelerogram, b) Base shear

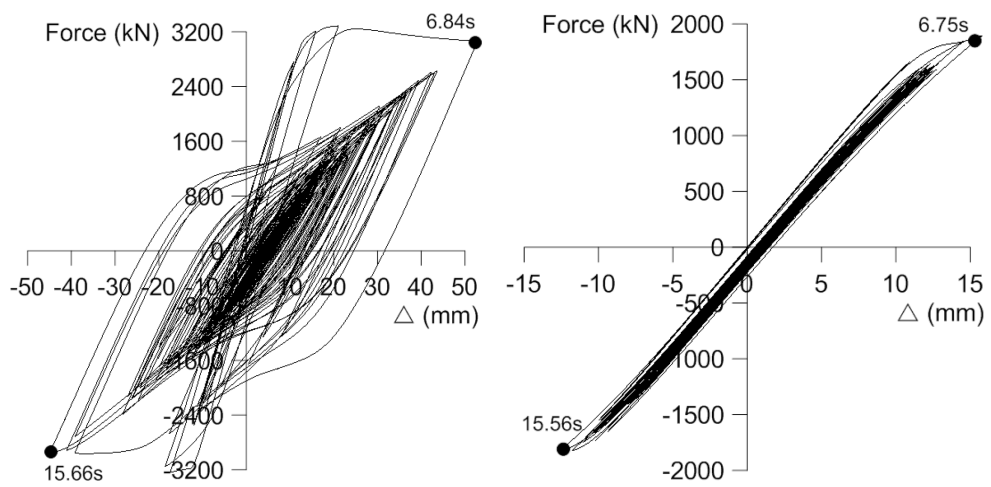


Figure 4.24: Hysteretic response for C4 record - a) Two-storey ground floor response, b) Two-storey second floor response record

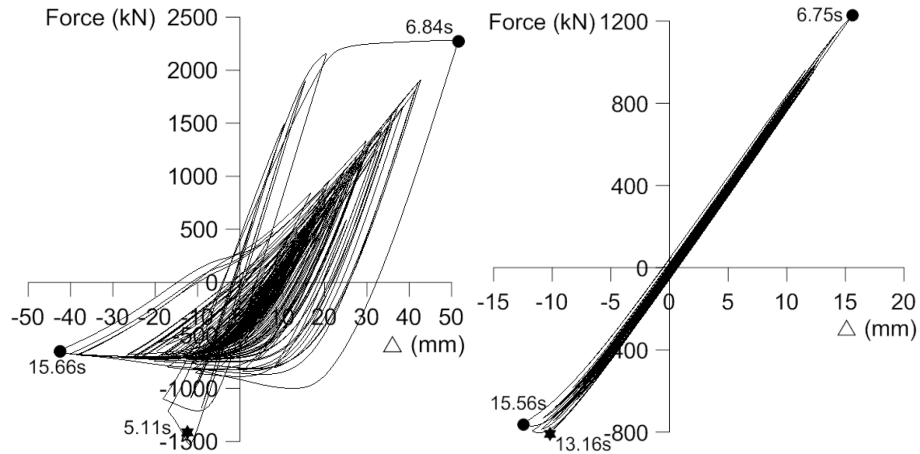


Figure 4.25: Hysteretic response for C4 record - a) Response of brace from joint #1 to #5 (Figure 4.7), b) Response of brace from joint #2 to #4 (Figure 4.7)

The behaviour under the S1 subduction ground motion is similar with the seismic response under the C4 record. The ground floor brace dissipates most of the energy, while the upper floor braces, although they buckle in compression, dissipate a small amount of energy. The ground floor brace is able to deform under S1, approximately 40mm in both tension and compression, while the maximum interstorey drift is $1.02\%h_s$. Under both S1 and S3 ground motions the developed base shear is approximately $3200kN$. However, the S3 ground motion imposes larger deformations at the upper floor than at the lower floor. The ground floor brace buckles first at $t = 69.85s$. The upper floor brace buckles at a later time, $t = 94.95s$, before the PGA is reached ($114.86s$), as illustrated in Figure 4.29b. The maximum base shear value occurs at $t = 118.88s$, when the upper brace in tension yields and the ground floor brace has almost reached the yielding point. The upper floor brace deforms more (about 40mm in both tension and compression), while the ground floor brace deforms less. The maximum interstorey drift occurs at the top floor and is about $1.10\%h_s$, while the interstorey drift of the ground floor is $0.67\%h_s$.

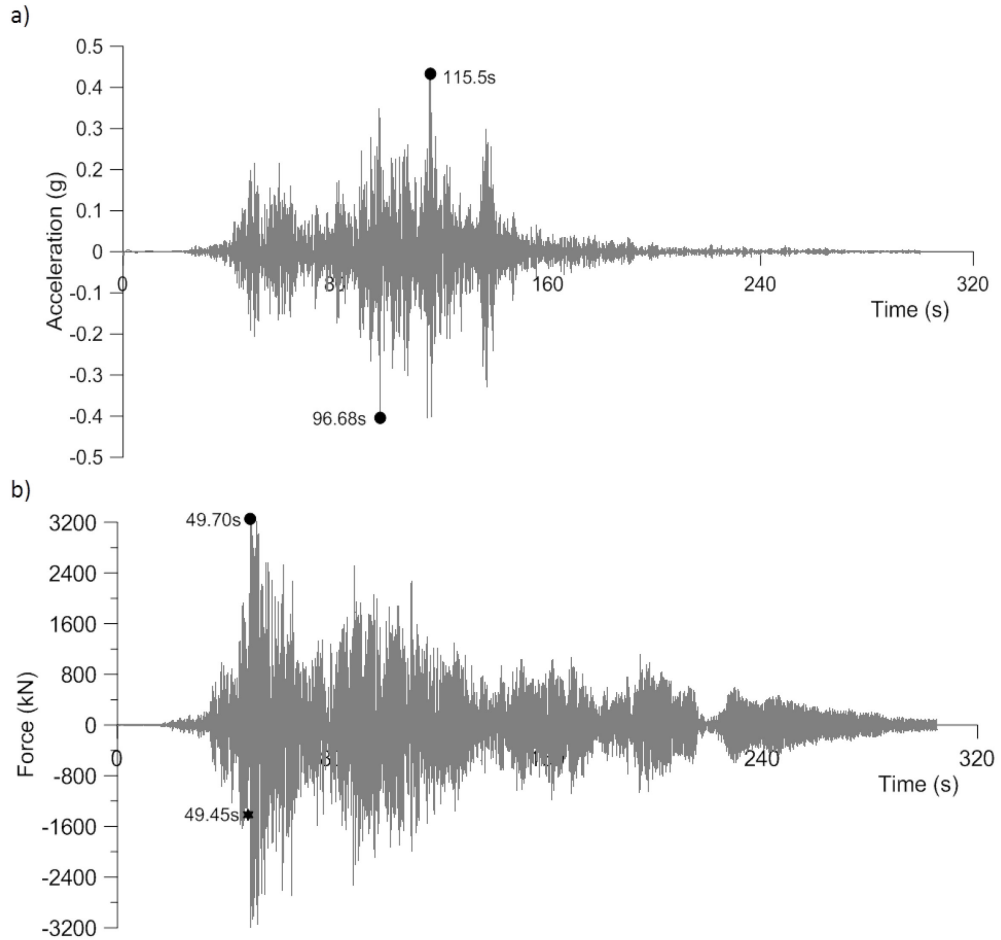


Figure 4.26: Time history response for S1 record - a) Accelerogram, b) Base shear

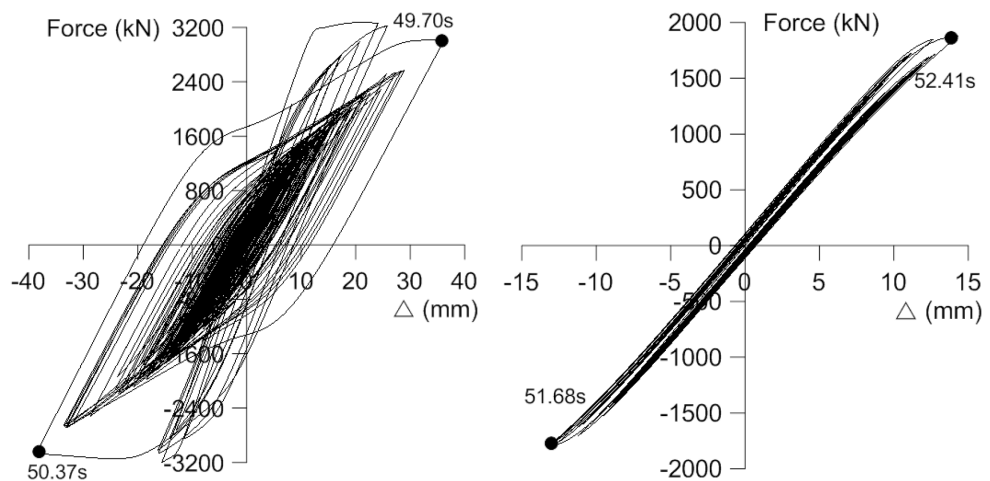


Figure 4.27: Hysteretic response for S1 record - a) Two-storey ground floor response, b) Two-storey second floor response

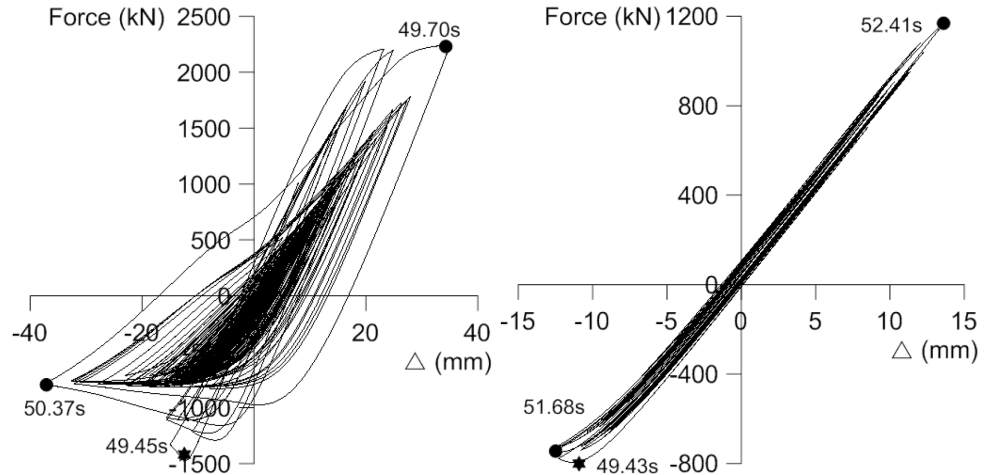


Figure 4.28: Hysteretic response for S1 record - a) Response of brace from joint #1 to #5 (Figure 4.7), b) Response of brace from joint #2 to #4 (Figure 4.7)

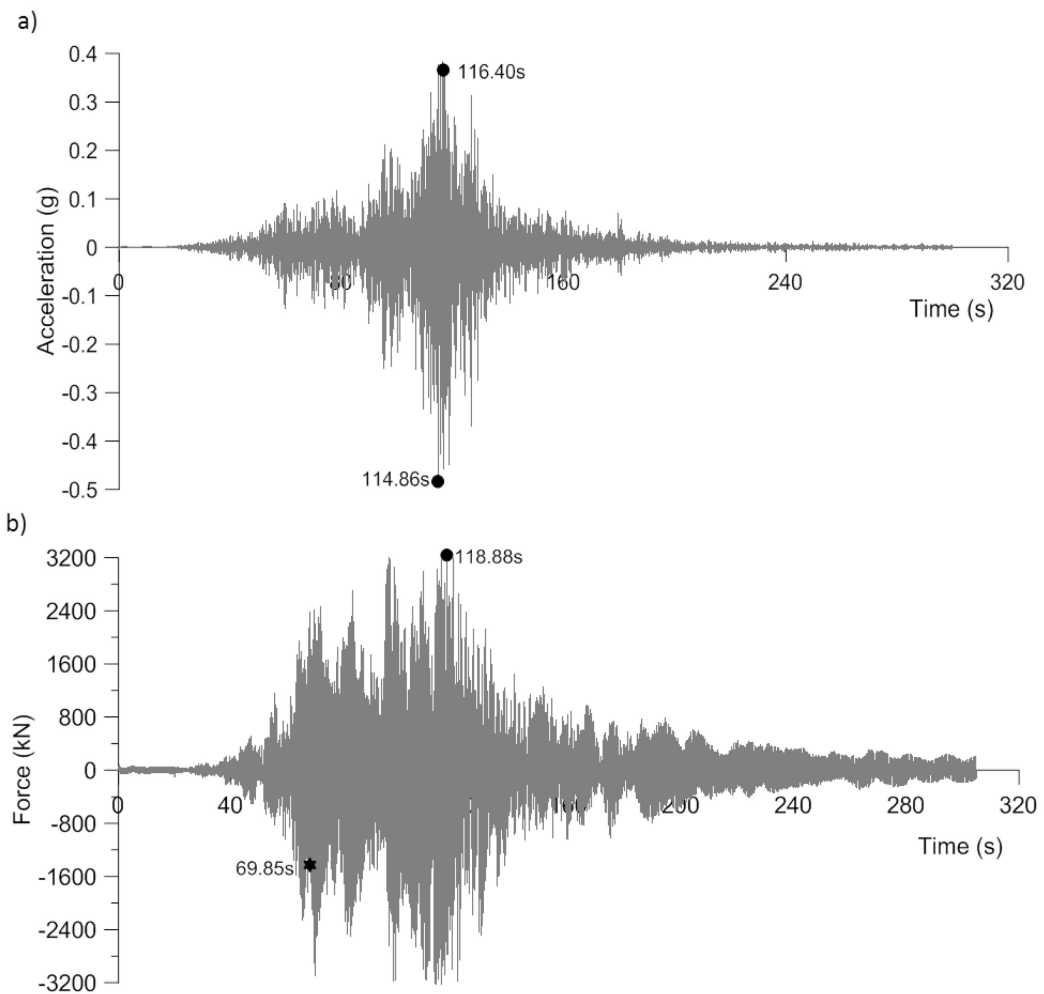


Figure 4.29: Time history response for S3 record - a) Accelerogram, b) Base shear

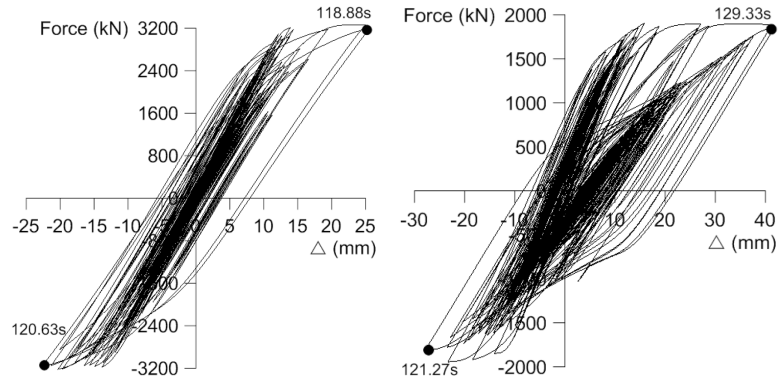


Figure 4.30: Hysteretic response for S3 record - a) Two-storey ground floor response, b) Two-storey second floor response

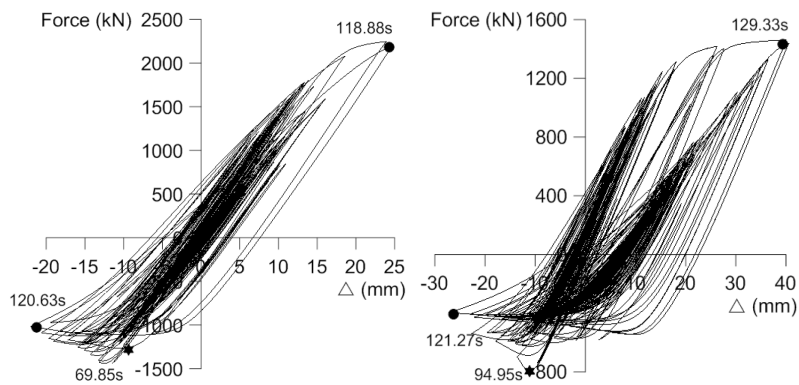


Figure 4.31: Hysteretic response for S3 record - a) Response of brace from joint #1 to #5 (Figure 4.7), b) Response of brace from joint #2 to #4 (Figure 4.7)

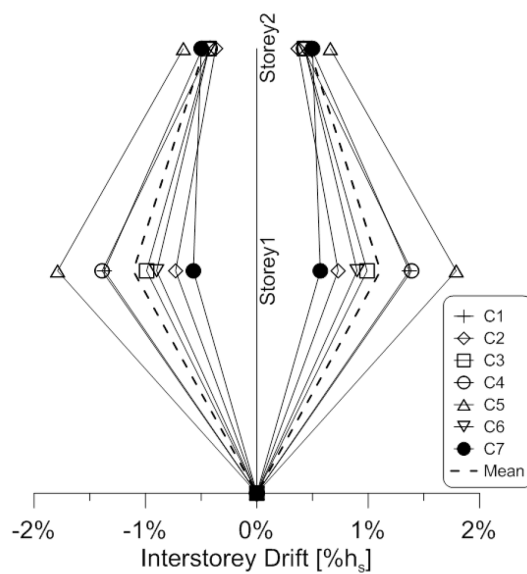


Figure 4.32: Interstorey drift - Crustal ground motions

Chapter 5. Seismic Analysis of Low-Rise Structures Equipped with Dissipative Single- Pin Connections Using OpenSees

5.1 Design of the Dissipative Single-Pin Connections

The same single- and two-storey CBF systems, studied in section 4.1, will be equipped with dissipative single-pin brace-to-column connections with the aim to study their seismic response. In this chapter, the connection will be designed for both frames and the frames equipped with the devices will then be subjected to the same ground motions selected in section 4.3. Comparative studies will be carried out for the frames with and without dissipative single-pin connections.

5.1.1 Design of the Connection for the Single-Storey Structure

The members of the designed single-storey limited ductility CBF are given in Table 4.3. The members size remains the same while the changes are applied at the level of the brace-to-column connections. The design philosophy is to size the brace-to-column connections to yield first and to dissipate the seismic input energy, while the brace member (HSS 127x6.4 in this example) behaves in elastic range. To assure that this assumption is respected, it is recommended that the pin yields at 60-80% of the compressive strength, C_r , of the brace. In this particular case, for the HSS 127x6.4 section, $C_r=525kN$. A suitable pin for the brace would have an ultimate strength between $P_u=315kN$ and $P_u=420kN$; therefore a pin of the size 35x50mm is proposed. Although in the experimental tests depicted in Chapter 3, it was shown that the pin was located on its weak axis, in the following numerical examples, the pin is located on its strong axis. However, further experimental tests are required to limit the applications of the pin to its weak axis.

The first step in the connection design is to determine the distance between the inner plates in accordance with the brace and columns being used, followed by the thickness of the inner and outer plates. The tri-linear curve will then be built using the connection dimensions.

The column used in the single-storey frame is a W310x86 section. This implies that the pin length will be 310mm. With regards to the distance between the outer plates, the limitation given by equation 3.8 and the building geometry is $a < 183.6mm$. Considering the size of the brace and the limitation, the proposed distance, a , is 112.5mm.

The inner and outer plates are designed to behave very rigidly in order to minimize their deformation while the pin yields. They are treated as a cantilever beam, as shown in Figure 5.1, subjected to axial, shear and moment forces stemming from the pin. It is proposed to design the outer plates with a stiffness equivalent to double that of the pin being used and for the inner plates to possess 1.5 times the stiffness of the pin. Therefore, for the case of a 35x50mm pin, the inner and outer plates would have a thickness of 15mm and 19mm respectively, and the width of the plates is 250mm.

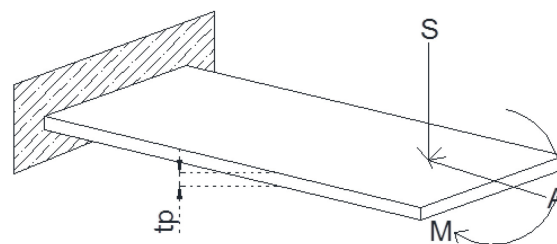


Figure 5.1: Design of the inner and outer plates

By using equations 3.2 through 3.7, the pin's tri-linear curve is built and can be found in Figure 5.2a.

A numerical model was built for the connection in order to validate the tri-linear curve devised from the theoretical method. As shown in Figure 3.8, P_I , P_{II} , and P_{III} were applied to the 35x50mm pin and the comparison between the theoretical and numerical responses of the connection can be seen in Figure 5.2b. Finally, in order to validate both models, the stress and strain curves were built for the connection, shown in Figure 5.3, where it can be seen that the yield values correspond to the theoretical and numerical study.

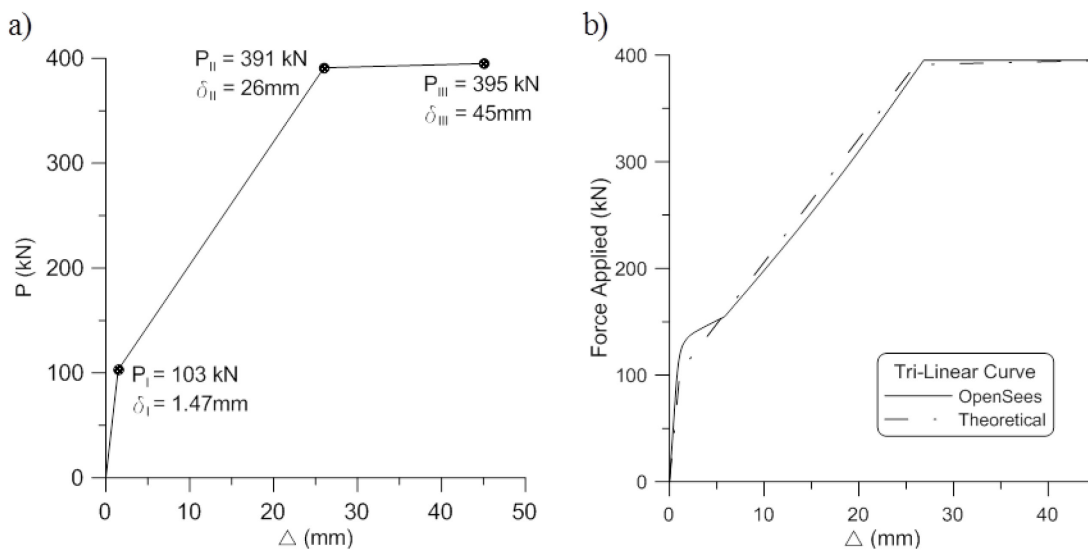


Figure 5.2: Pin design for the single-storey CBF- a) Theoretical tri-linear curve of the 35x50mm pin , b) OpenSees tri-linear curve comparison

As a result of the above, the final pin design for the single-storey structure will be as shown in Figure 5.4.

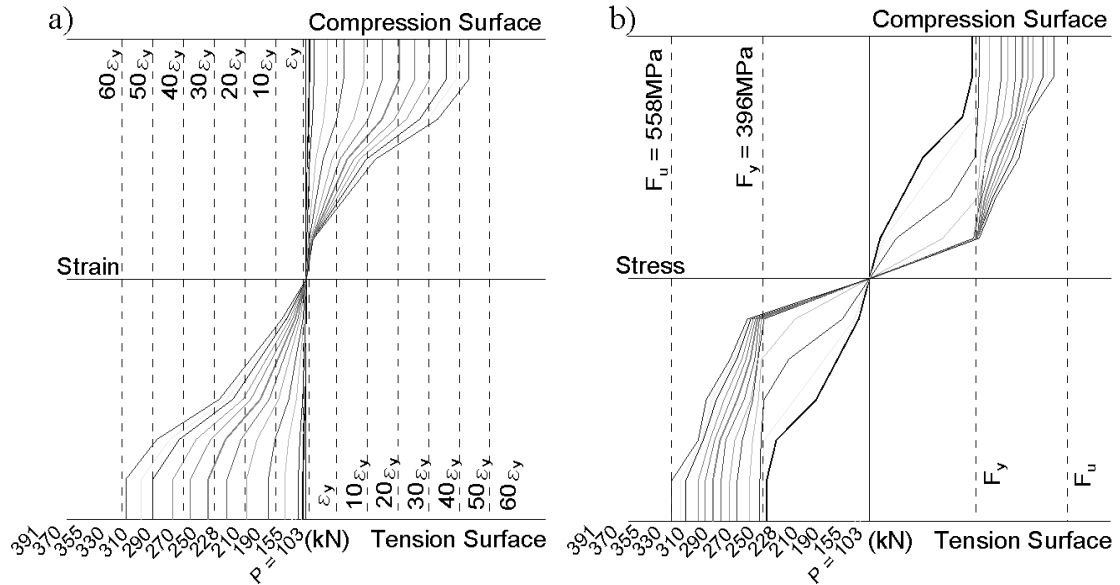


Figure 5.3: a) Strain curve along the height of the cross-section of the 35x50mm pin connection, b) Stress curve along the height of the cross-section of the 35x50mm pin connection

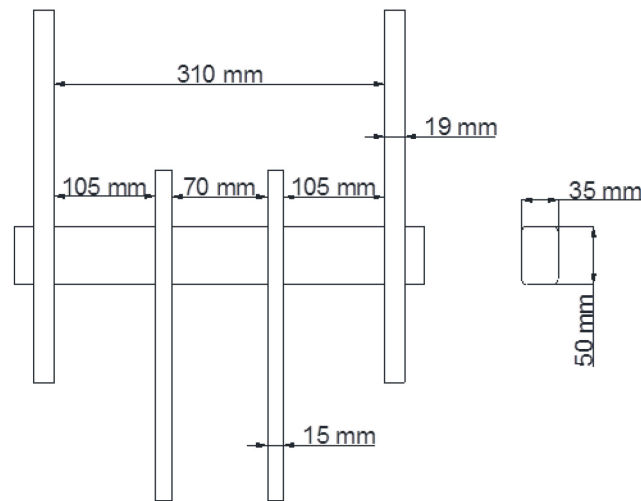


Figure 5.4: Characteristics of the dissipative single-pin connection for the single-storey frame

5.1.2 Design of the Connections for the Two-Storey Structure

Regarding the two-storey structure, the braces are HSS152x13 for the first storey and HSS127x9.5 for the second storey. The compressive resistance, C_r , of the braces are

$C_r = 1277kN$ and $C_r = 652kN$, for the first and second storey respectively. For the first storey a 45x60mm pin was proposed and its compressive resistance is 70% that of its respective brace. A 30x55mm pin was chosen for the second storey and it also exhibits 70% of its brace's compressive resistance.

The column used in the two-storey frame is a W310x86 section. This implies that the pin length will, again, be 310mm. With regards to the distance between the outer plates, the limitation given by equation 3.8 and the building geometry required a proposed limit of $a < 183.6 \text{ mm}$, as it was for the single-storey due to the fact that the building geometry is the same. Considering the size of the brace and the limitation, the proposed distance, a , is 100mm for the first storey and 112.5mm for the second storey.

As previously explained, the required stiffness for the inner plates is 1.5 times that of the pin and for the outer plates it is 2 times that of the pin. For the first storey the inner plates were designed with a thickness of 19mm and the outer plates with a thickness of 22mm . The inner and outer plates for the second storey connection have a thickness of 15mm and 19mm respectively. The width of all plates for the first storey is 280mm and that of the plates belonging to the second storey connection is 250mm .

With equations 3.2 through 3.7, the pin tri-linear curves are built, as shown in Figure 5.5a and 5.5c. A comparison between the theoretical and numerical response of the connections can be seen in Figure 5.5b and 5.5d. Shown in Figure 5.6 are the stress and strain diagrams of the pins, where the stress and strain are taken at the mid-span of the pin.

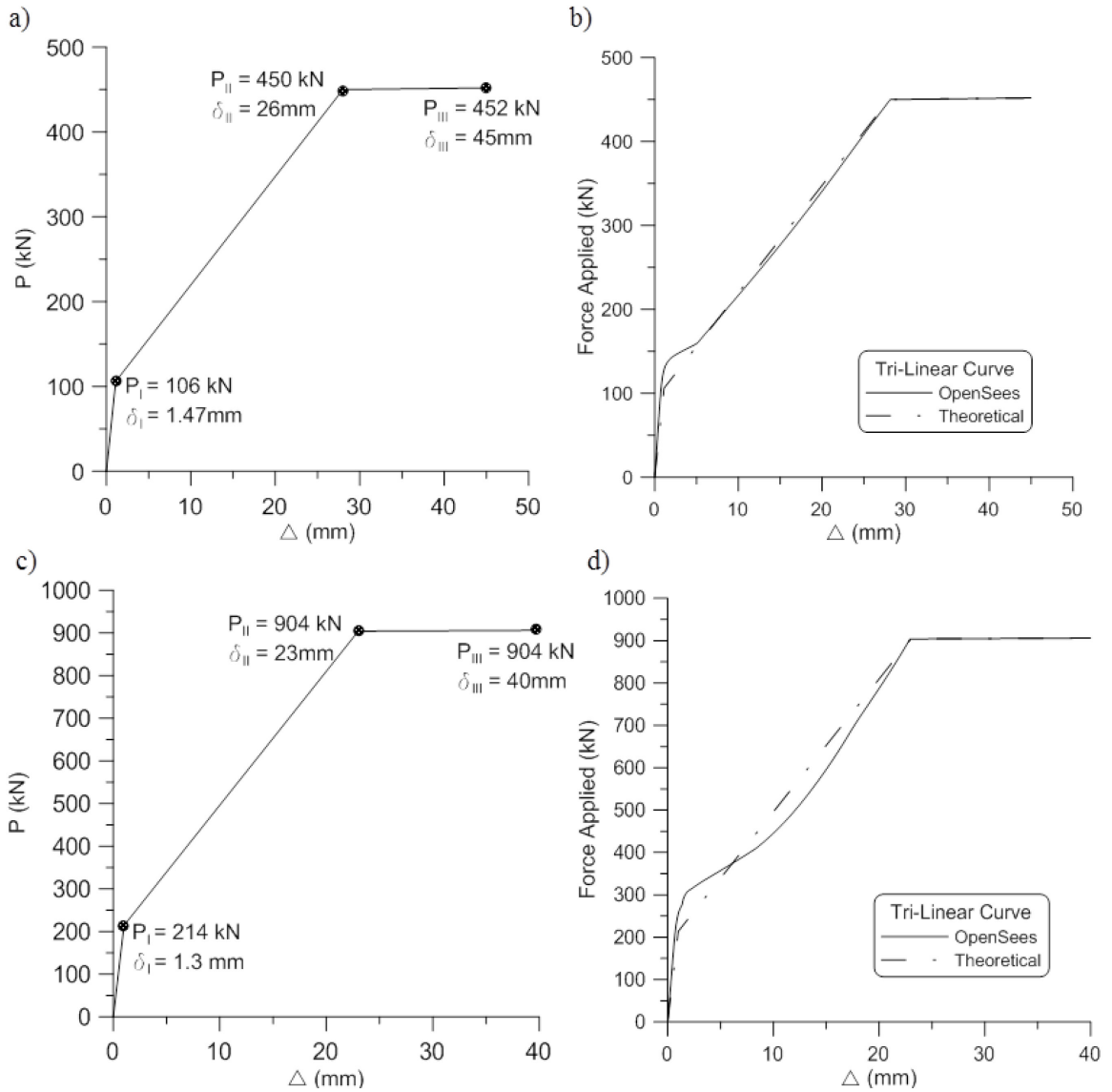


Figure 5.5: Pin design for the two-storey CBF: a) Theoretical tri-linear curve of pin 30x55mm pin, b) OpenSees tri-linear curve comparison for 30x55mm pin, c) Theoretical tri-linear curve of pin 45x60mm pin, d) OpenSees tri-linear curve comparison of 45x60mm

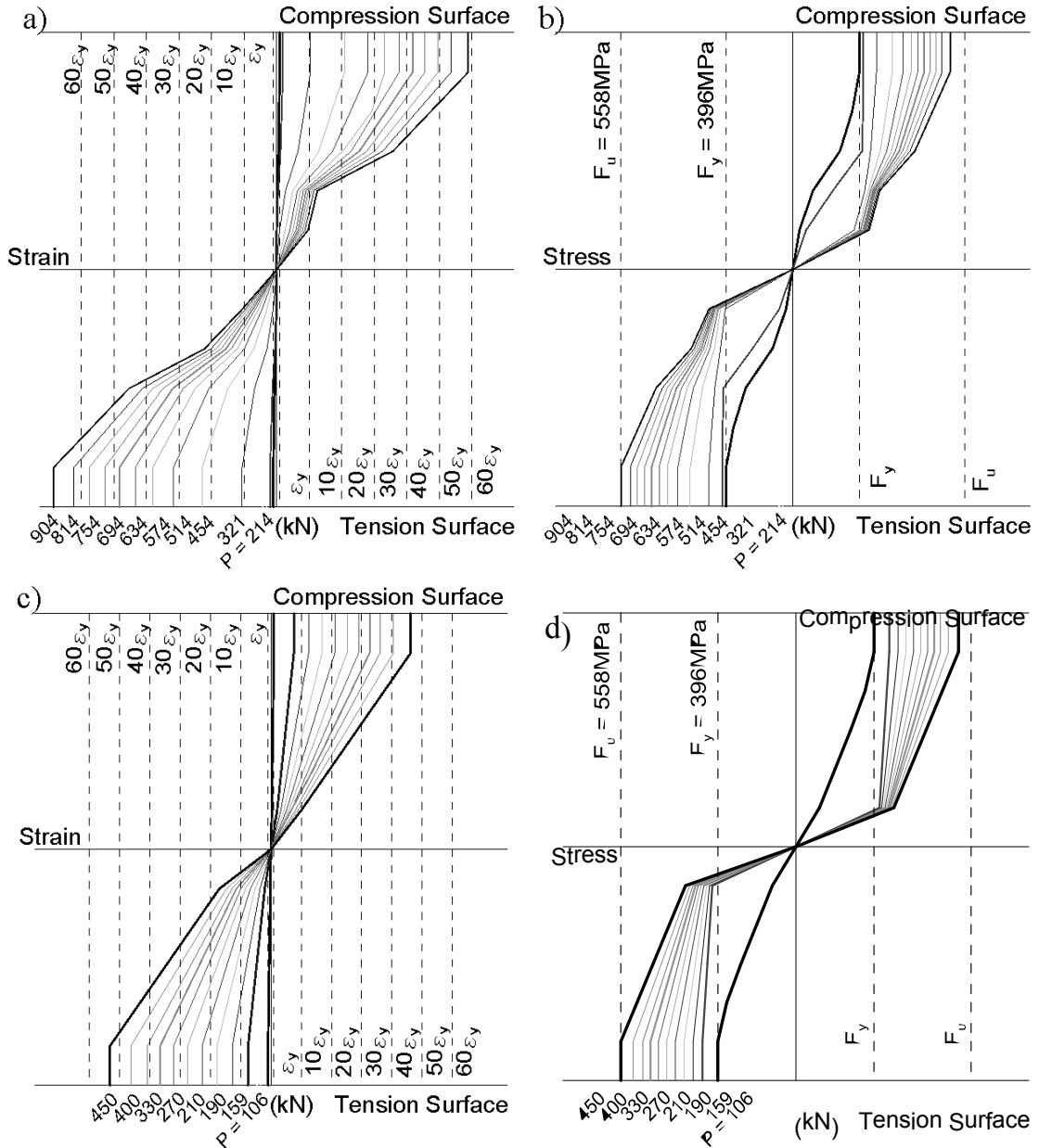


Figure 5.6: a) Strain curve along the height of the cross-section (45x60), b) Stress curve along the height of the cross-section (45x60), c) Strain curve along the height of the cross-section (30x55), d) Stress curve along the height of the cross-section (30x55)

As a result of the above, the final pin design for the single-storey structure will be as shown in Figure 5.7.

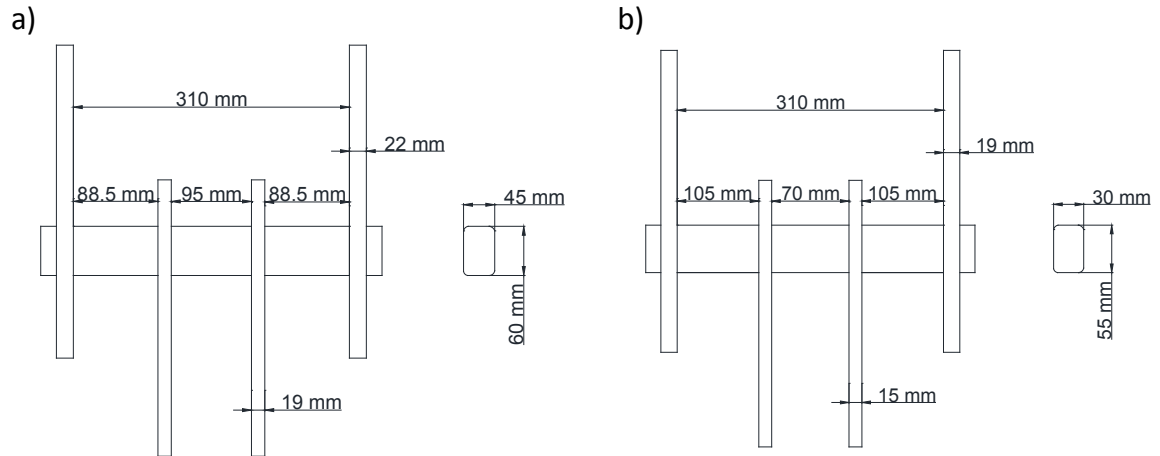


Figure 5.7: a) Pin geometry for the 45x60mm pin connection, b) Pin geometry for the 30x55mm pin connection

Following this study of the dissipative connections for the single- and two-storey structure, the connections will be integrated into the braced frames using the method described in section 3.4. An axial spring made up of *Pinching4* material will replace the gusset plate brace-to-frame connections in both structural models. The pinching material will have the properties of the connections determined above.

For the frames equipped with the single-pin connections, the periods of the structures were determined by OpenSees and can be found in Table 5.1. T_a was determined by approximating, $T_l = 1.05T_a$. The rest of the characteristics of the structures remain the same due to the only change being the gusset plate connections are replaced by the single-pin dissipative connections.

5.2 Scaling and Simulation of Ground Motions

The same group of ground motions, studied for the traditional concentrically brace frames, will be applied to the frames equipped with single-pin dissipative connections. The ground motions must be re-scaled to meet the requirements of the new

period of the buildings. Due to a lower stiffness provided by the dissipative single-pin connections, the periods of the single- and two-storey structure are elongated.

Table 5.1: Seismic design and building characteristics for the CBF equipped with single-pin connections

Storey	Height [m]	W [kN]	T_a [s]	$S(T_a)$ [g]	V/frame $R_d=2$ [kN]	V/frame $R_d=3$ [kN]	T_1 [s]	T_2 [s]	T_1/T_a
Equivalent static force procedure							OpenSees		
1	3.8	2845	0.33	(2/3)1.2=0.8	875	583	0.35	-	1.05
2	7.6	9190	0.70	(2/3)1.2=0.8	2152	1435	0.74	0.34	1.05

5.2.1 Scaling of Ground Motions for the Single-Storey Structure with Dissipative Single-Pin Connections

When the dissipative single-pin connections are introduced into the single-storey structure, the fundamental period computed in OpenSees elongates from $T = 0.20s$ to $T = 0.35s$, which is approximately 1.75 times longer. This introduces a new period of interest for the ground motion scaling of the single-storey building, from $T_1 = 0.35s$ to $1.5T_1 = 0.525s$.

The three sets of ground motions, crustal, subduction, and near-field, will be applied to the single-storey structure with dissipative connections using the method described in section 4.3. Table 5.2 indicates the new scale factors for the ground motions.

Regarding the computed scale factors obtained to match the spectral acceleration ordinates with those of the UHS over the period of interest, they are not influenced by the slope added in the short period range (Figure 5.8).

Table 5.2: Ground motions and their respective scale factors for the single-storey structure with single-pin connections

NAME	Scale Factor $T_1-1.5T_1$	PGA (g)	PGV (m/s)	$\frac{PGV}{PGA}$
Crustal Ground Motions				
<i>C1</i>	1.80	0.440	0.370	0.830
<i>C2</i>	2.60	0.850	0.330	0.390
<i>C3</i>	2.10	0.770	0.530	0.690
<i>C4</i>	2.20	0.370	0.260	0.710
<i>C5</i>	1.80	0.500	0.310	0.610
<i>C6</i>	3.80	0.400	0.670	1.680
<i>C7</i>	3.80	0.570	0.310	0.540
Subduction Ground Motions				
<i>S1</i>	0.80	0.530	0.230	0.440
<i>S2</i>	0.40	0.240	0.160	0.660
<i>S3</i>	0.90	0.510	0.280	0.540
<i>S4</i>	3.10	0.430	0.870	2.000
<i>S5</i>	2.20	0.350	0.620	1.750
<i>S6</i>	2.40	0.380	0.670	1.750
<i>S7</i>	3.20	0.320	0.900	2.800
Near-Field Ground Motions				
<i>N1</i>	0.40	0.330	0.370	1.110
<i>N2</i>	0.70	0.430	0.890	2.080
<i>N3</i>	0.50	0.420	0.880	2.080
<i>N4</i>	0.90	0.520	1.060	2.030
<i>N5</i>	0.70	0.460	0.760	1.660
<i>N6</i>	0.80	0.480	0.980	2.030
<i>N7</i>	1.10	1.080	0.510	0.470

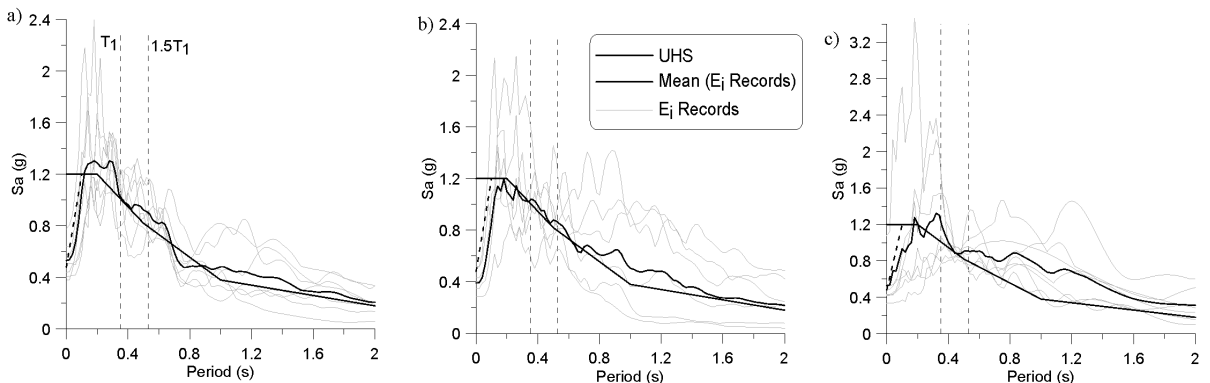


Figure 5.8: Scaled spectral acceleration for single-storey building - a) Crustal, b) Subduction, c) Near-Field

5.2.2 Scaling of Ground Motions for the Two-Storey Structure with Dissipative Single-Pin Connections

The two-storey structure will be subjected to the crustal and subduction ground motion groups. When the dissipative single-pin connections are introduced into the structure, the fundamental period elongates from $0.42s$ to $0.74s$. Once again, the period of the structure with the dissipative connections is 1.76 times longer than that with conventional shear connections. The period of the second mode, T_2 , elongates from $0.2s$ to $0.34s$, which is approximately 1.7 times longer. The new period range of interest for the two-storey CBF with dissipative single-pin connections therefore becomes: $T_2 = 0.34s$ to $1.5T_1 = 1.11s$. In Table 5.3, the scale factor for this period of interest can be found.

Table 5.3: Ground motions and their respective scale factors for the two-storey structure with single-pin connections

NAME	Scale Factor $T_2-1.5T_1$	PGA (g)	PGV (m/s)	$\frac{PGV}{PGA}$
<i>Crustal Ground Motions</i>				
<i>C1</i>	3.20	0.780	0.650	0.830
<i>C2</i>	3.20	1.040	0.410	0.390
<i>C3</i>	2.50	0.920	0.630	0.690
<i>C4</i>	2.50	0.430	0.300	0.710
<i>C5</i>	3.20	0.900	0.540	0.610
<i>C6</i>	3.30	0.340	0.600	1.740
<i>C7</i>	2.70	0.410	0.220	0.540
<i>Subduction Ground Motions</i>				
<i>S1</i>	1.00	0.660	0.290	0.440
<i>S2</i>	0.70	0.430	0.280	0.660
<i>S3</i>	1.20	0.680	0.370	0.540
<i>S4</i>	2.30	0.320	0.640	2.000
<i>S5</i>	2.40	0.380	0.670	1.750
<i>S6</i>	2.40	0.380	0.670	1.750
<i>S7</i>	3.00	0.300	0.840	2.800

The scaling results for the two-storey structure do not show a difference in the scale factors. The reason for this can be better understood in the graphical representations found in Figure 5.11, comparing the two averages with respect to the UHS and the proposed UHS. This minimal difference in scale factors is due to the fact that the proposed UHS differs from the original UHS between the periods of 0 seconds to 1.0 seconds, therefore any range of periods greater than 1.0 seconds will be scaled equally for both the original and proposed UHS. Another observation made is that the scale factors for the two-storey building are greater than those of the single-storey building when the dissipative single-pin connections are introduced. As shown in Figure 5.9, for a bigger scale factor there is a drop in the mean of the acceleration response spectra, which causes the scale factors to increase in order to bring the average above the design spectra. This causes the scale factors to be greater for the two-storey structure, despite the fact that the structure is more ductile.

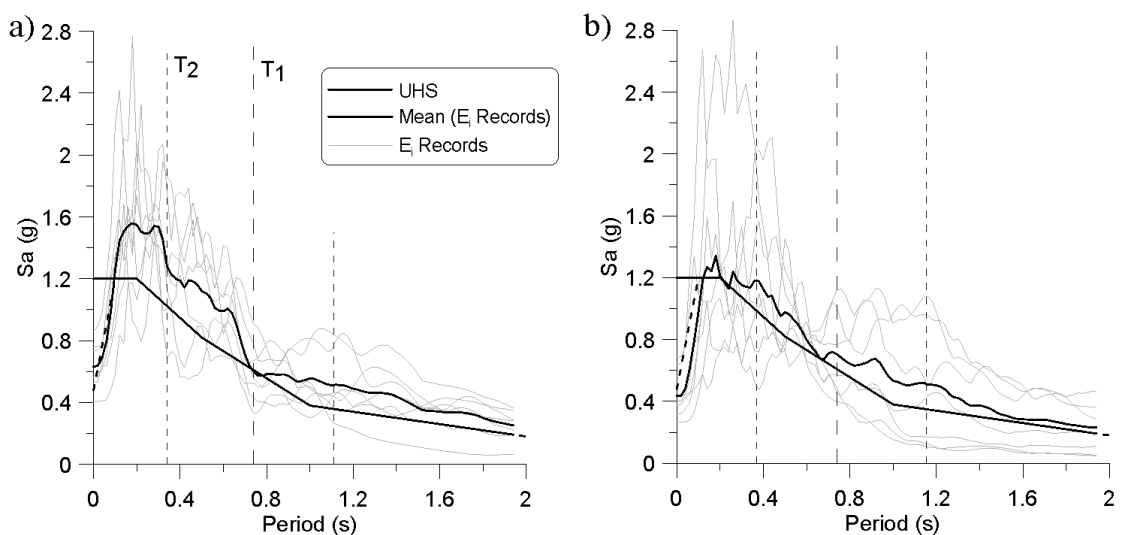


Figure 5.9: Scaled spectral acceleration for two-storey building - a) Crustal, b) Subduction, c) Near-Field

5.3 Seismic Response of Studied CBFs with Single-Pin Connections

5.3.1 Single-Storey CBF Building with Single-Pin Connections

To emphasize on the behaviour of CBFs equipped with dissipative single-pin connections, two crustal, two subduction and two near-field scaled ground motions were selected for the following study. Thus, among the 7 crustal records, C2 and C4 were chosen. In the case of C2 (Figure 5.10a) the PGA is reached at the beginning of ground motion, while in the case of C4 (Figure 5.13a) it is towards the end of the ground motion, which implies differences in behaviour. The time-history shear force is shown in Figure 5.10b for the C2 record and 5.13b for the C4 record. In both cases, the pin yields at the beginning of the ground motion, while the period was elongated. The spectral ordinate was reduced to that corresponding to $1.5T_1$, which means lowered base shear demand. Thus, under the C2 and C4 records the pin start yielding at $t = 4.61s$ and $t = 3.63s$ respectively, before the PGA time step was reached. As illustrated in Figure 5.12, the pin was displaced 6 mm at yielding in both directions of oscillation (brace in tension and compression). When the brace yields in tension, the deformation of the attached pins is as illustrated in Figure 3.22. Thus, the pin of joint #1 (Figure 4.7) shows a positive force and displacement, while the pin located in joint #3 shows a positive displacement and a negative force. The lateral deformation of the single-storey CBF with pins is in the same range as that illustrated for the CBF without pins, as well as the interstorey drift. The difference is given by the magnitude of base shear, which is about four times lower in the case of pins. However, the CBF with pins is more ductile than traditional LD-CBF. Based on the equivalent static force procedure, for $R_d = 3$ and the fundamental period 0.2s, the base shear is $583kN$ (Table 5.1). However for the elongated period, $T_1 = 1.5T_1 =$

0.3s, the same base shear of 583kN is required. As resulted from the OpenSees output, the fundamental period of the single-storey CBF with pins is 0.35s. It seems that under C2, the pins experienced a large yielding cycle that corresponds to the time when the PGA was reached.

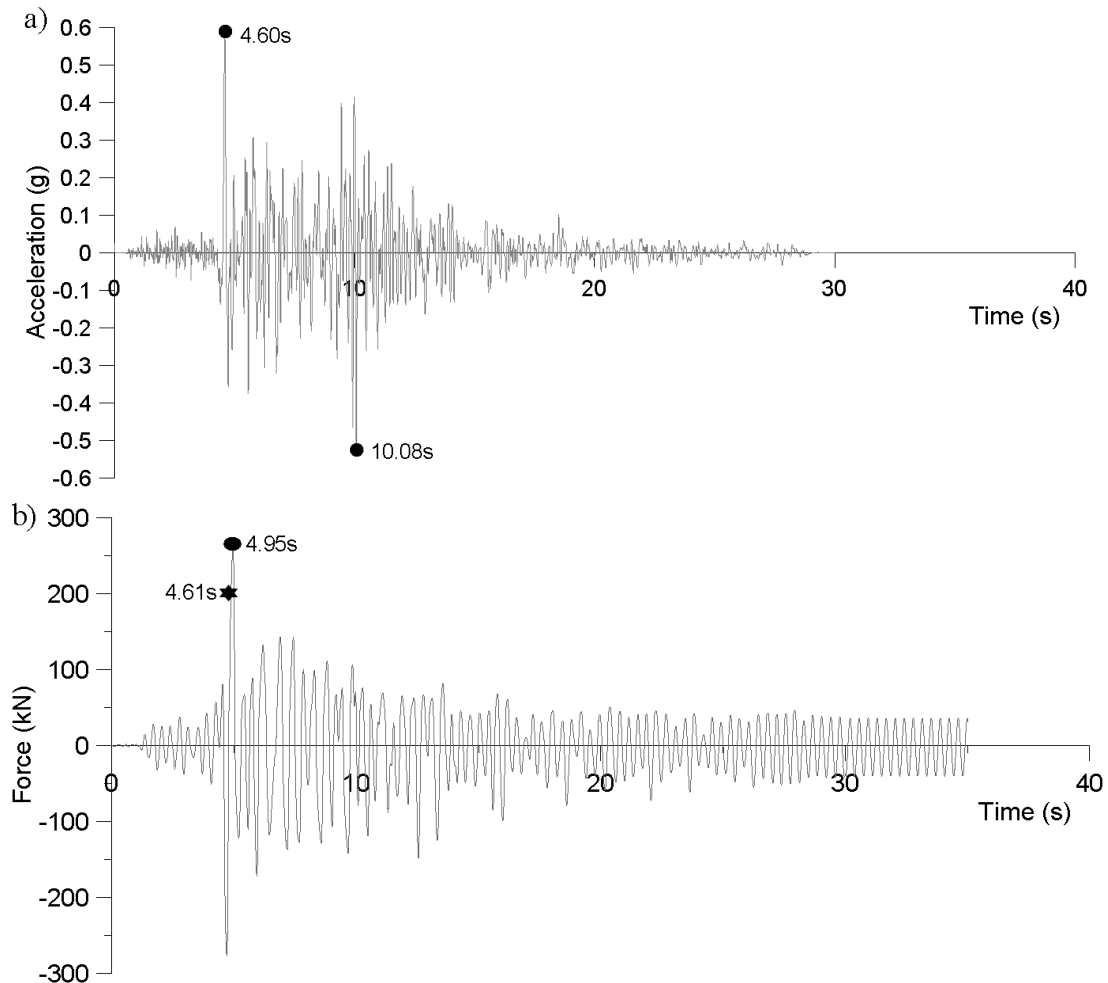


Figure 5.10: Time history response for C2 record - a) Accelerogram, b) Base shear

After that, the CBF with pins exhibited plastic deformations corresponding to post-yielding stiffness. The maximum base shear developed under C2 is about 300kN and under C4 is 400kN. The hysteresis response of the CBF with pins under the C2 and C4

records is shown in Figures 5.11 and 5.14, and the response of the pin members is shown in Figures 5.12 and 5.15. Meanwhile, under the C2 record, the lateral displacement demand is less than for C4 (6.7mm versus 13.8mm per pin). As per the hysteresis rule implemented and shown in the tri-linear curve of the 35x50mm pin (Figure 5.2), the pin is able to carry larger lateral forces if larger deformations are imposed. For example, when the pin deforms around 13.8mm under the C4 record it responds with a $216kN$ force.

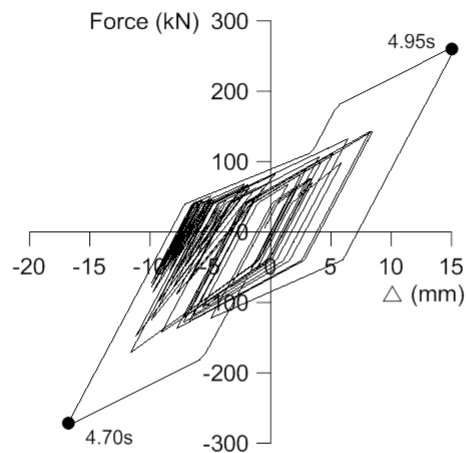


Figure 5.11: Single-storey frame response for C2 record

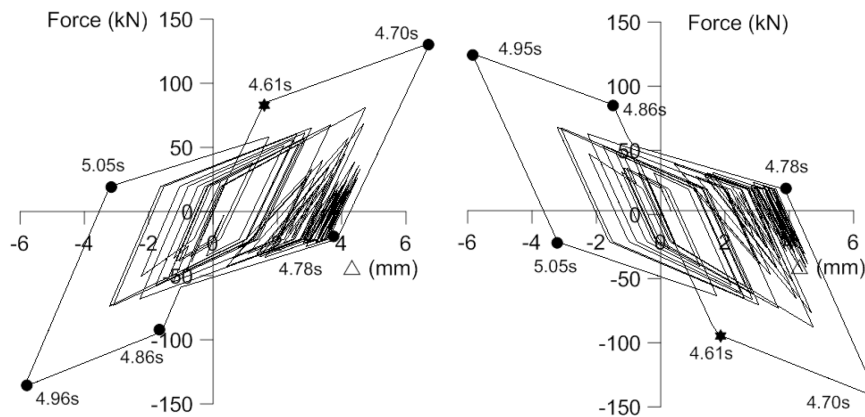


Figure 5.12: Hysteretic response of pin devices belonging to brace from joint #1 to #3 (Figure 4.7) for C2 record

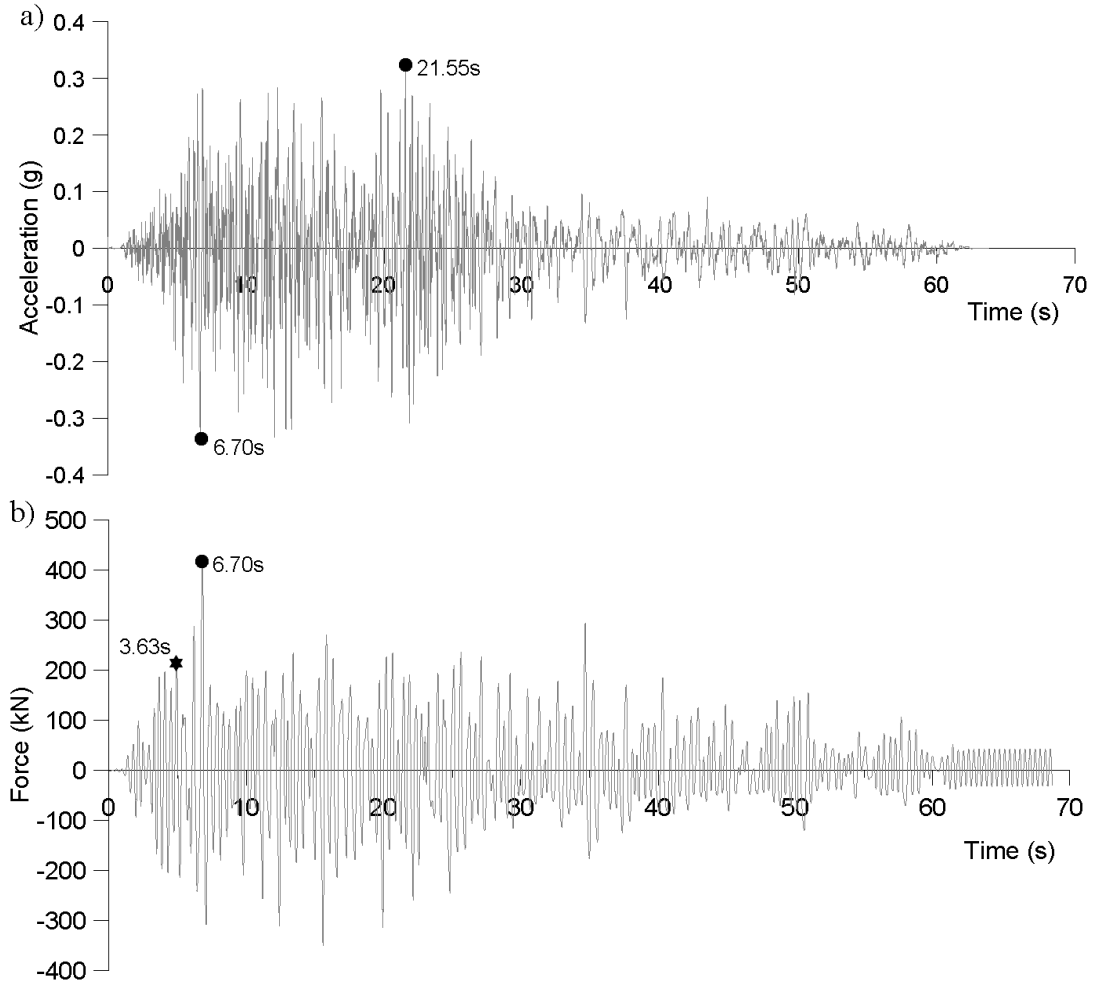


Figure 5.13: Time history response for C4 record - a) Accelerogram, b) Base shear

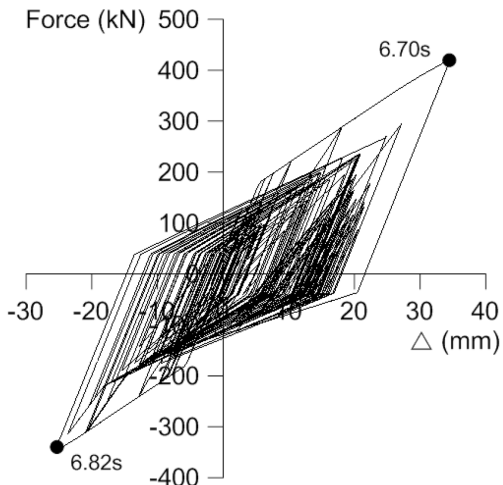


Figure 5.14: Single-storey frame response for C4 record

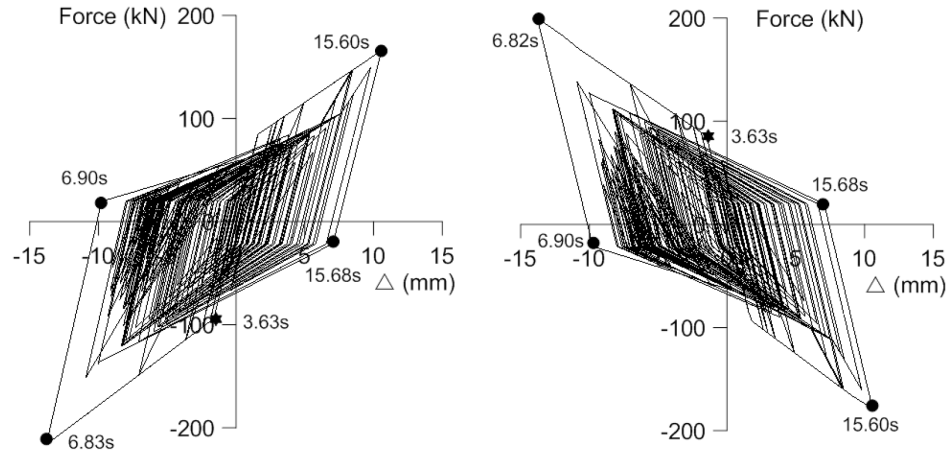


Figure 5.15: Hysteretic response of pin devices belonging to brace from joint #1 to #3 (Figure 4.7) for C4 record

Two subduction ground motions S1 and S3 were selected and show a maximum PGA of about $0.3g$ at $t = 100s$, as illustrated in Figures 5.16a and 5.19a. Meanwhile, the S1 accelerogram seems to allow the building to behave symmetrically in both tension and compression (Figures 5.18, 5.19), while the S3 record demands larger deformations on one side than the other (Figures 5.20, 5.21). As a consequence, the seismic response in terms of hysteresis force-displacement loops, under the S1 record, is more symmetrical than under the S3 record. When the single-storey CBF with pin devices is subjected to the S1 record, several cycles of maximum base shear of $350kN$ are experienced by the frame in the interval of $50s$ to $115s$, while under the ground motion S3, a similar base shear magnitude was developed over a smaller duration interval, $114s$ to $117s$. As illustrated in Figure 5.28, the interstorey drift recorded under S1 and S3 is approximately $0.75h_s$, while the maximum deformation of the pin device is about $8mm$ (Figure 5.18 and 5.21).

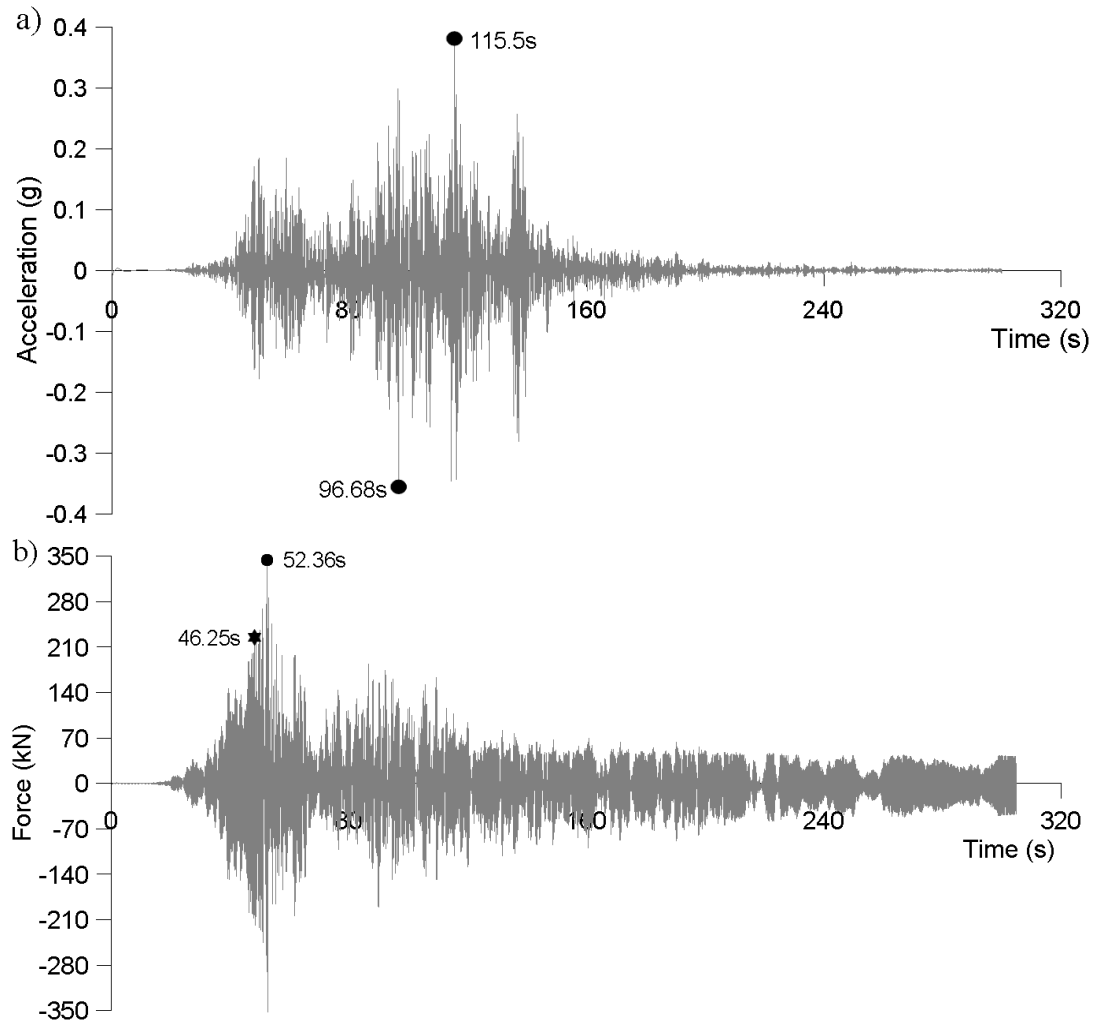


Figure 5.16: Time history response for S1 record - a) Accelerogram, b) Base shear

The high frequency content of subduction ground motions does not impose larger deformations. Although the spectral ordinate corresponding to the fundamental period, $0.35s$, is $0.72g$ for S1 and $1.7g$ for S3, the spectral ordinates drop below the UHS for a period larger than $0.43s$ and $0.48s$ respectively (Figure 5.9).

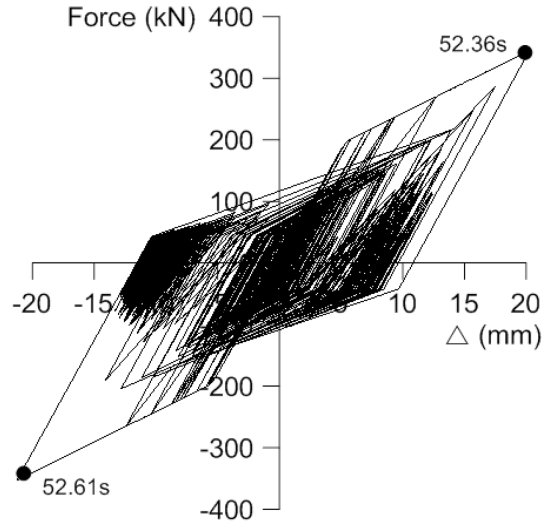


Figure 5.17: Single-storey frame response for S1 record

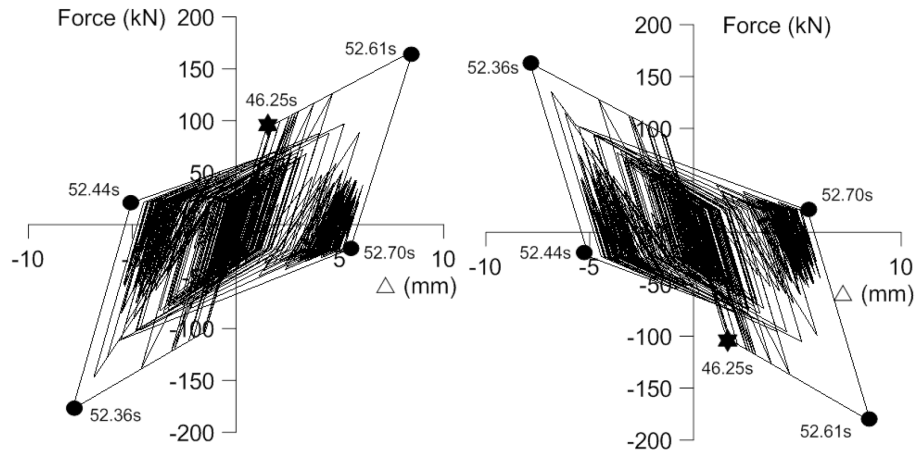


Figure 5.18: Hysteretic response of pin devices belonging to brace from joint #1 to #3 (Figure 4.7) for S1 record

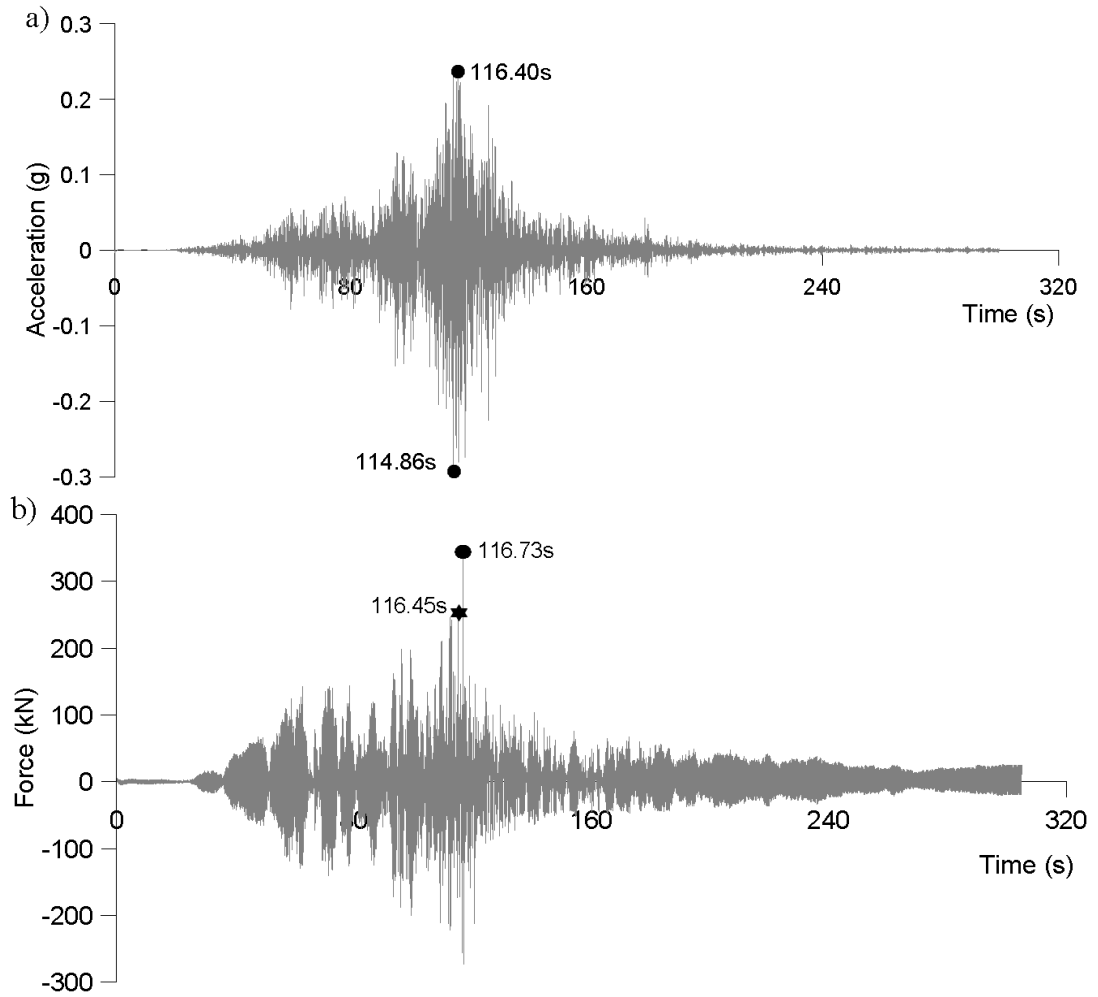


Figure 5.19: Time history response for S3 record - a) Accelerogram, b) Base shear

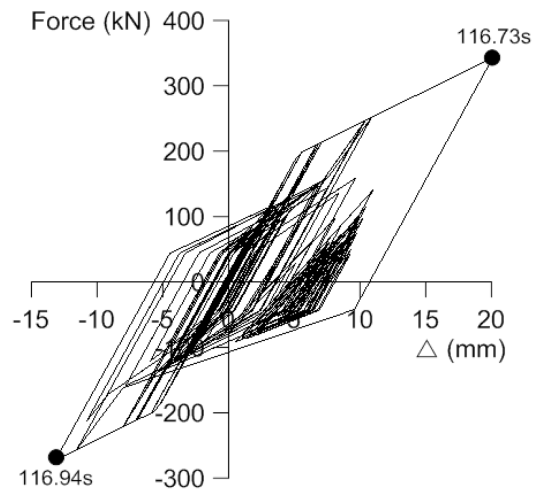


Figure 5.20: Single-storey frame response for S3 record

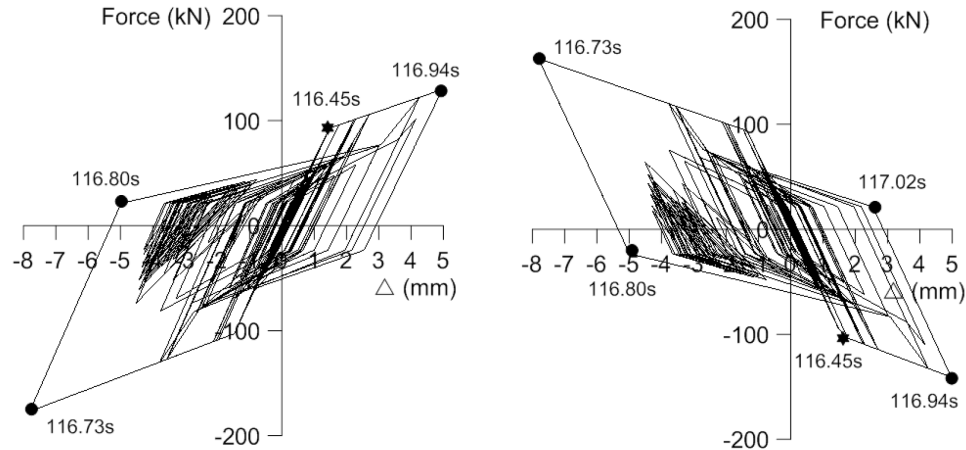


Figure 5.21: Hysteretic response of pin devices belonging to brace from joint #1 to #3 (Figure 4.7) for S3 record

Regarding near-field ground motions, the selected accelerograms correspond to N1 and N3 records as illustrated in Figures 5.22a and 5.25a. The maximum PGA occurs at the beginning of the near-field records N1 and N3 at $\sim t = 2.0s$ and $t = 8.0s$, respectively when a larger acceleration pulse is developed. The maximum base shear is about $750kN$ to $800kN$ and is reached at the beginning of ground motions, as illustrated in Figures 5.22b and 5.25b. The maximum deformation of the pin is $35mm$ which corresponds to the ultimate deformation of the $35 \times 50mm$ pin (P_{III} , δ_{III} in the tri-linear curve). The maximum interstorey drift is $2.3\%h_s$ under N1 and $2.2\%h_s$ under N3. In both cases the spectral ordinates show an almost constant value of $\sim 0.9g$ in the interval $0.35s - 0.53s$ which is slightly above the proposed equivalent UHS.

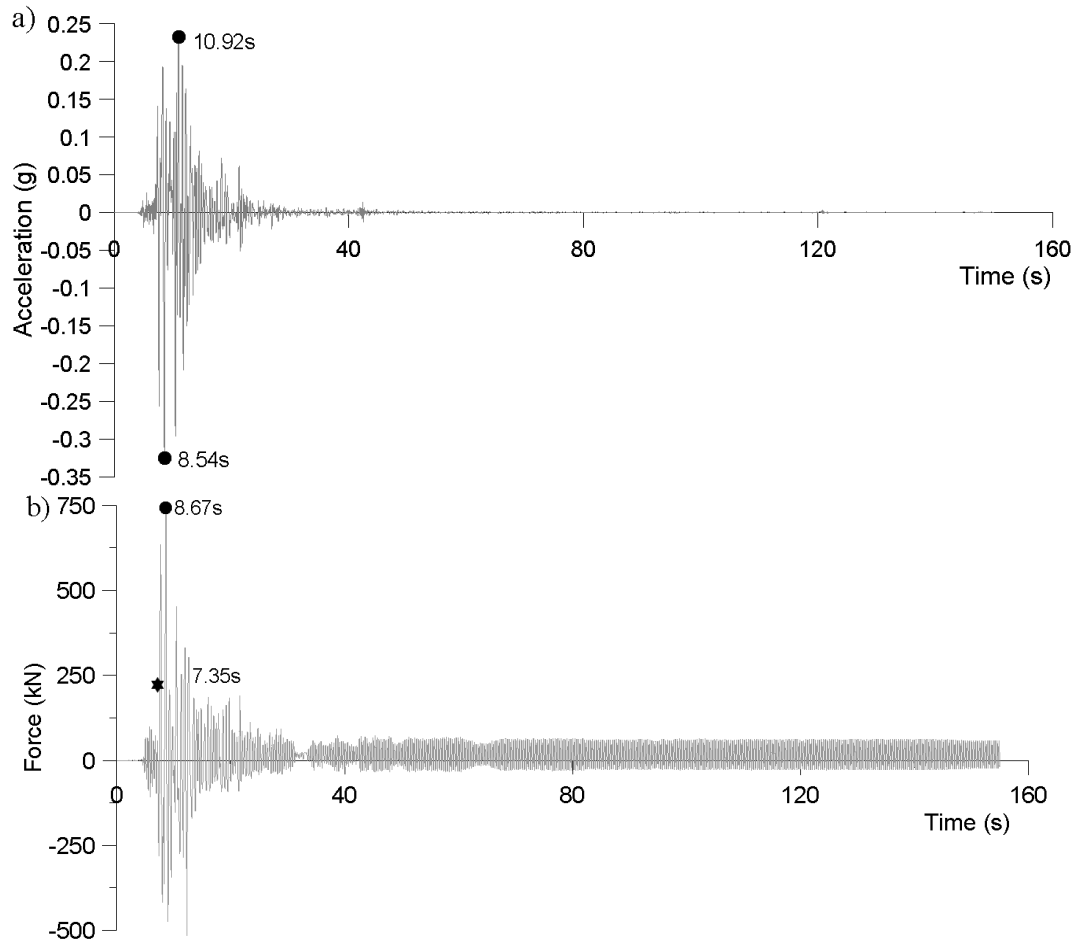


Figure 5.22: Time history response for N1 record - a) Accelerogram, b) Base shear

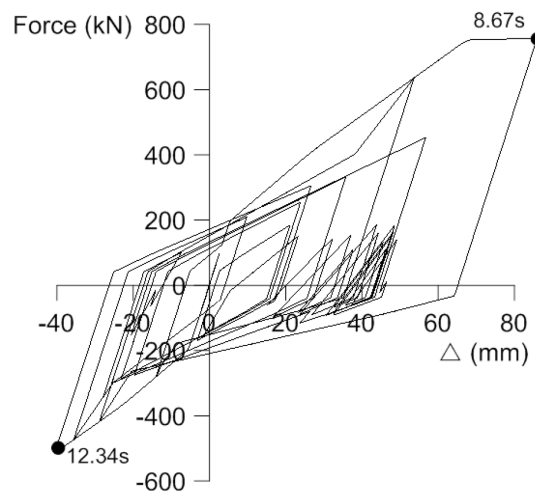


Figure 5.23: Single-storey frame response for N1 record

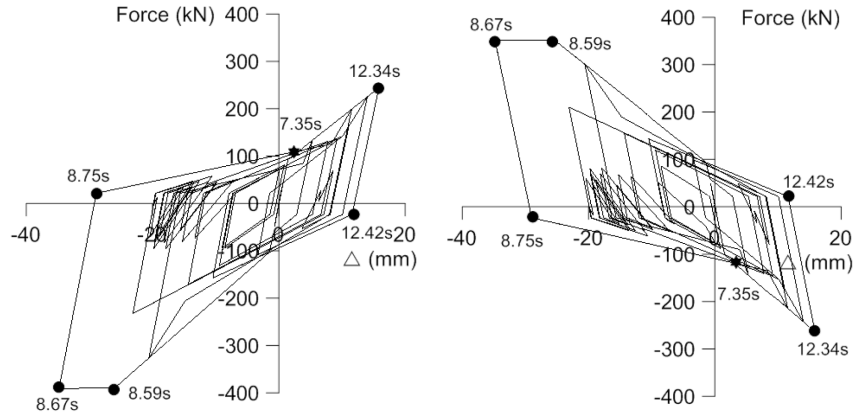


Figure 5.24: Hysteretic response of pin devices belonging to brace from joint #1 to #3 (Figure 4.7) for N1 record

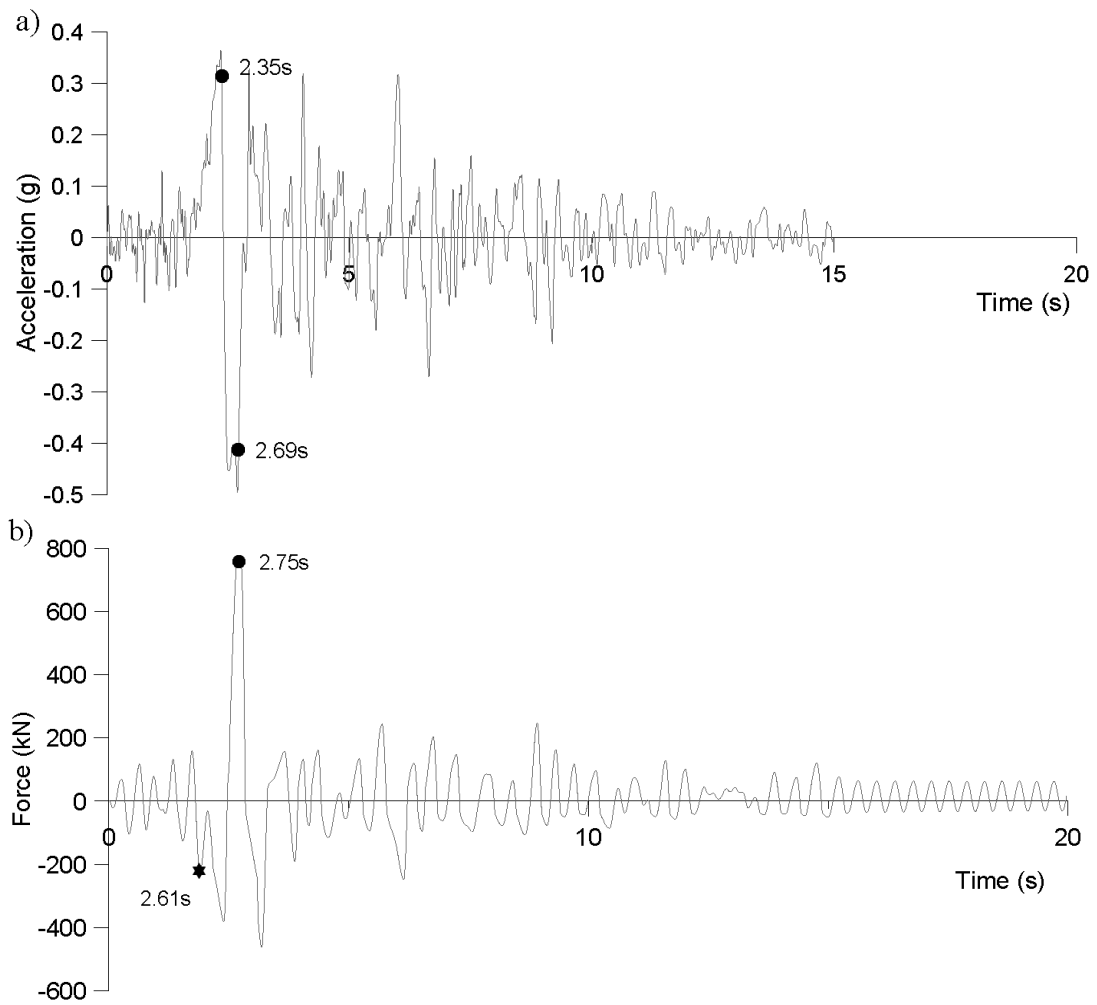


Figure 5.25: Time history response for N3 record - a) Accelerogram, b) Base shear

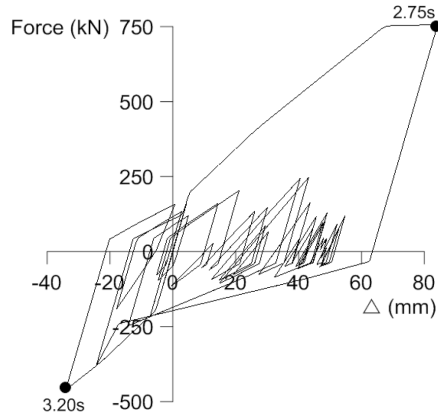


Figure 5.26: Single-storey frame response for N3 record

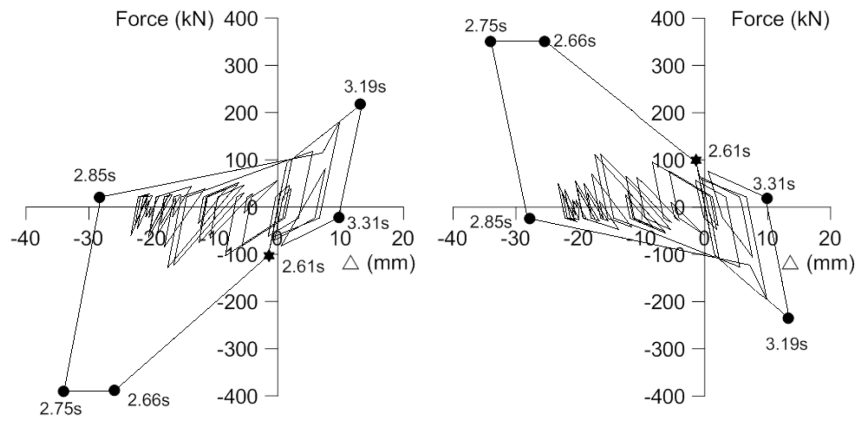


Figure 5.27: Hysteretic response of pin devices belonging to brace from joint #1 to #3 (Figure 4.7) for N3 record

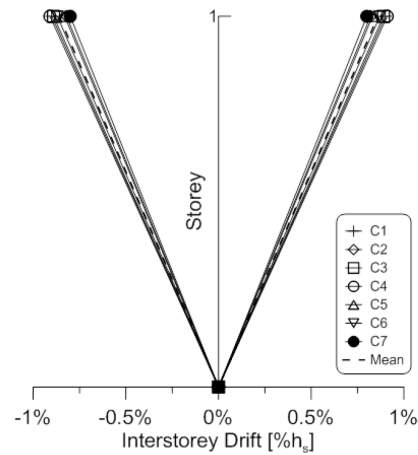


Figure 5.28: Interstorey drift - Crustal ground motions

The CBF displacement ductility is measured as Δ/Δ_y , where Δ is the maximum interstorey drift and Δ_y the interstorey drift at yield. Figure 5.29 illustrates the computed Δ/Δ_y ratio resulting under the crustal ground motions. It is shown that Δ/Δ_y is about 5 times larger for a CBF with pins than for LD-CBFs.

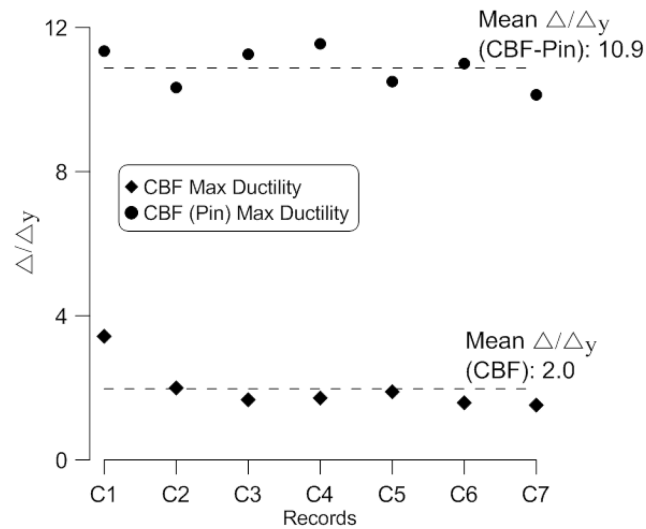


Figure 5.29: Displacement ductility comparisons for single-storey CBF with and without dissipative single-pin connection under crustal ground motions

5.3.2 Two-Storey CBF Building with Single-Pin Connections

To emphasize on the behaviour of two-storey CBFs equipped with dissipative single-pin connections, the seismic response is illustrated under the following ground motions: C2 and C4; S1 and S3 and N1 and N3.

Under the C2 records the ground floor pin 40x60mm yields at $t = 4.42s$ and the 2nd floor pin 30x55mm at $t = 4.45s$. Under the C4 record, the ground floor pin yields at $t = 3.32s$ after the yielding of the 2nd floor pin that occurs at $t = 2.28s$. In both cases the yielding of pins occurs before the PGA time step is reached. As illustrated in Figure 5.32, under the C2 ground motion the ground floor pins displace 14.5mm, while exhibiting a

force of about $572kN$ and the 2nd floor pins experience 20.6mm deformation, under a force of $3336kN$ (Figure 5.34). The maximum base shear of $1183kN$ is reached immediately after the PGA is recorded. It was previously mentioned that base shear resulting from the equivalent static force procedure, for $T_1 = 0.75s$ and $R_d = 2$, is $2152kN$. For $1.5T_1 = 1.125s$, this value becomes $942kN$ which is slightly lower than that computed from the dynamic procedure. Regarding the base shear response under the C4 record (Figure 5.35) the maximum value is $1542kN$.

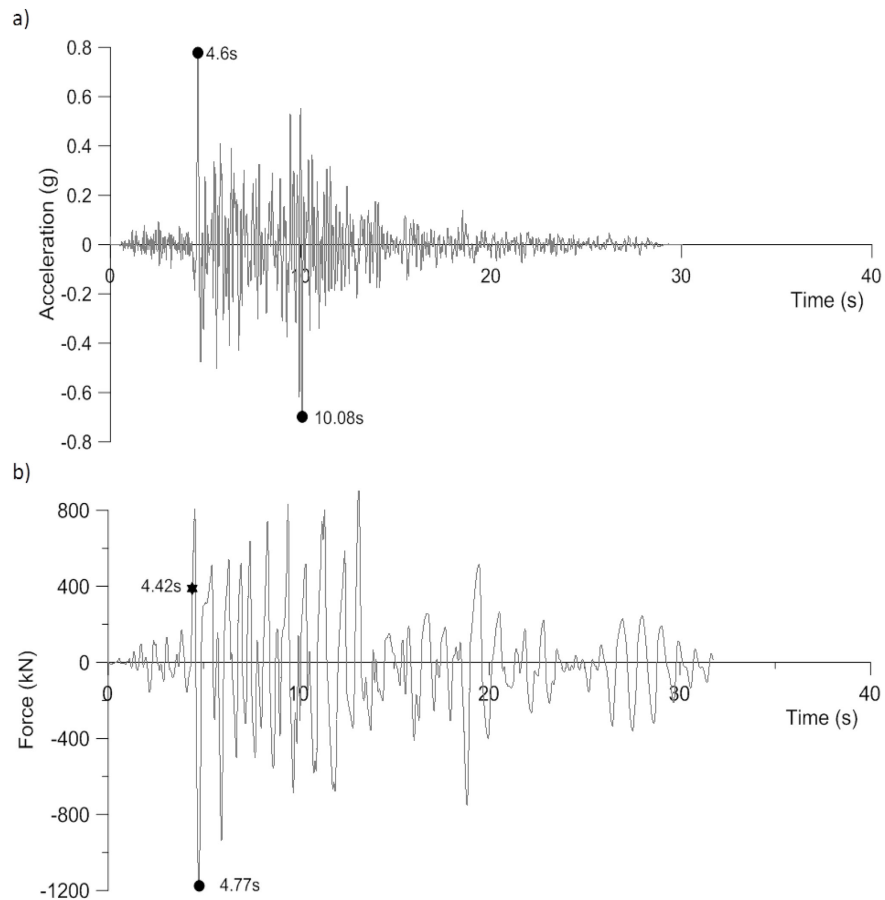


Figure 5.30: Two-storey CBF with pin devices: a) Accelerogram C2, b) Base shear time history response for C2 record

As illustrated in Figure 5.37, the ground floor pins experienced 17.7mm deformation under a force of 662kN, while the 2nd floor pins deformed 23.8mm under a force of 418kN. Under C2 the interstorey drift is 1.00% h_s and under C2 the interstorey drift is 1.43% h_s , as illustrated in Figure 5.54, with a slightly larger value at the top floor than at the ground floor level. The interstorey drift recorded at the ground floor level is similar between the CBF with pins versus the traditional LD-CBF. However, the interstorey drift at roof level is smaller for the LD-CBF than for the CBF with pins. The main difference between the CBF with and without pins is the fundamental period, which is about 70 – 80% larger in the case of CBFs with pins. The base shear developed for the CBFs with pins is almost half than the base shear developed for the LD-CBF structures. The spectral acceleration ordinates are above the UHS over the period of interest 0.34s – 1.125s.

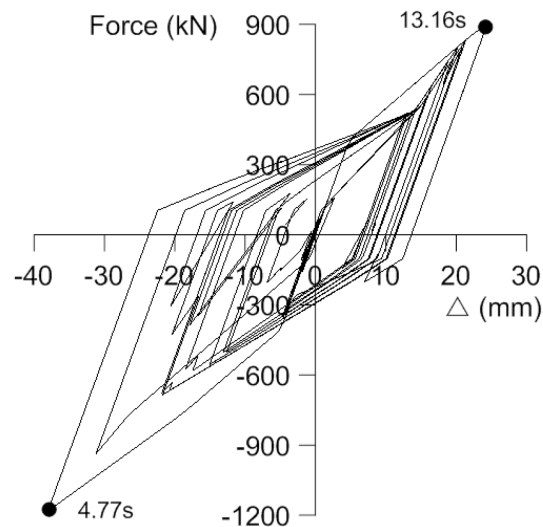


Figure 5.31: Two-storey CBF with pin devices: CBF response of ground floor for C2 record

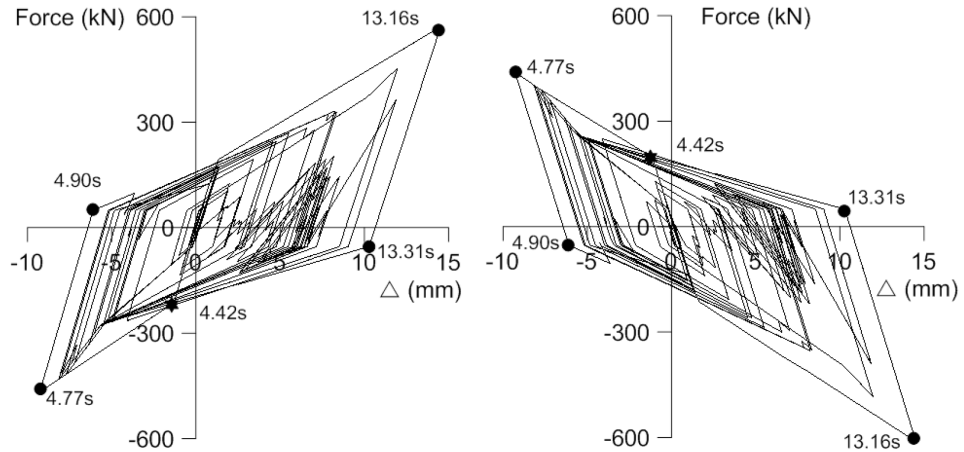


Figure 5.32: Two-storey CBF with pin devices: Hysteretic response of pin devices located at ground floor and belonging to brace from joint #1 to #5 (Figure 4.7) for C2 record

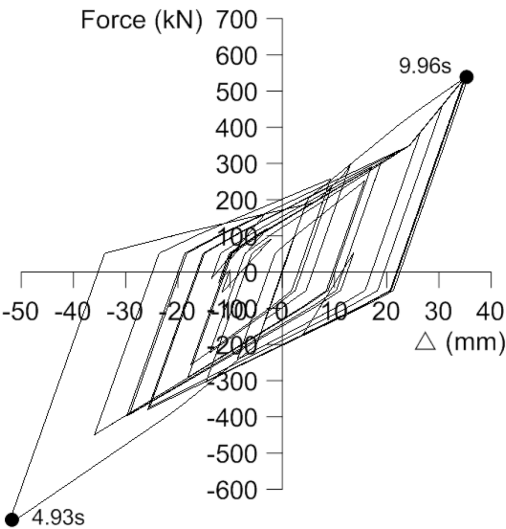


Figure 5.33: Two-storey CBF with pin devices: CBF response of second floor for C2 record

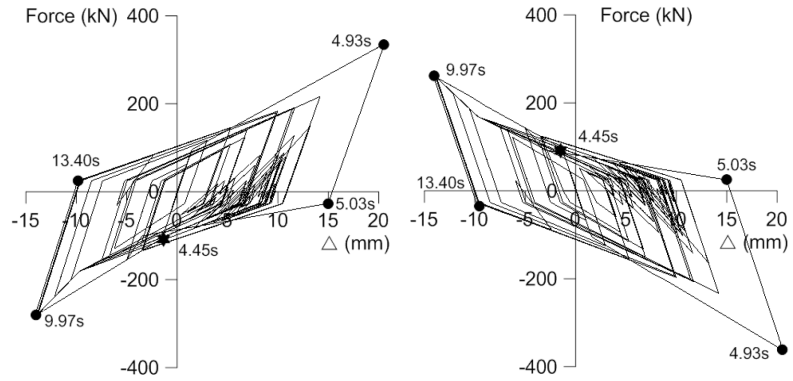


Figure 5.34: Two-storey CBF with pin devices: Hysteretic response of pin devices located at the 2nd floor and belonging to brace from joint #2 to #4 (Figure 4.7) for C2 record

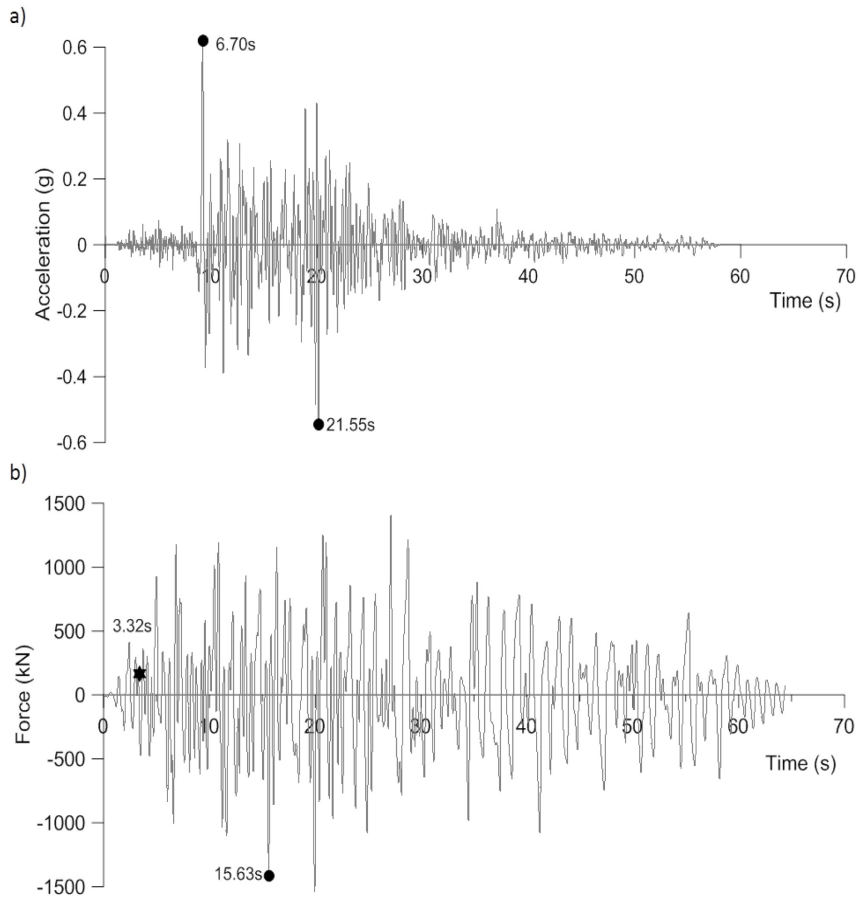


Figure 5.35: Two-storey CBF with pin devices: a) Accelerogram C4, b) Base shear time history response for C4 record

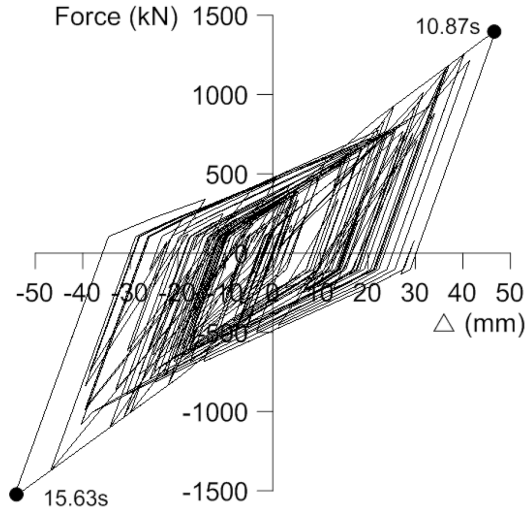


Figure 5.36: Two-storey CBF with pin devices: CBF response of ground floor for C4 record

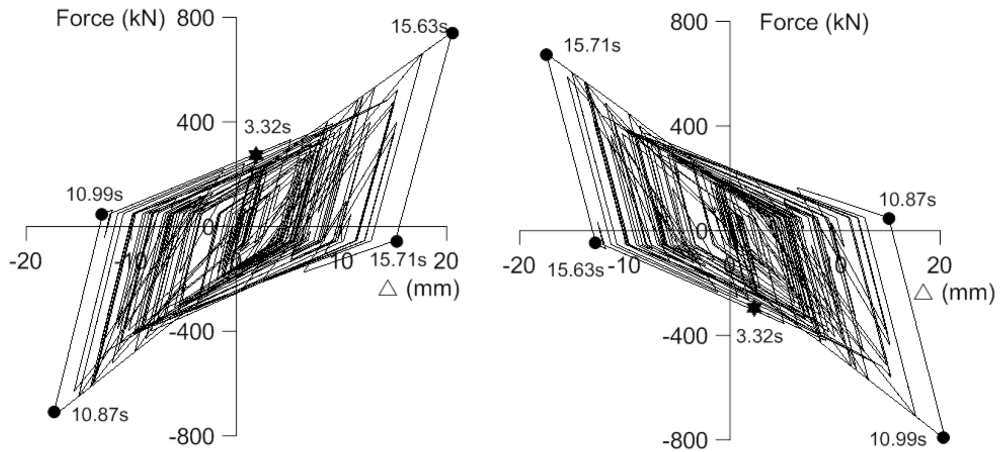


Figure 5.37: Two-storey CBF with pin devices: Hysteretic response of pin devices located at ground floor and belonging to brace from joint #1 to #5 (Figure 4.7) for C4 record

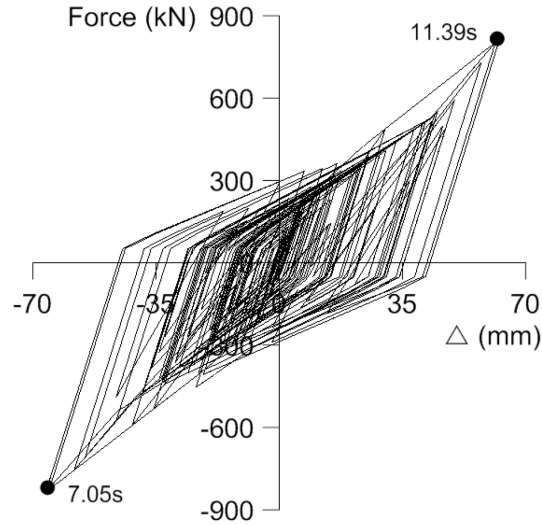


Figure 5.38: Two-storey CBF with pin devices: CBF response of 2nd floor for C4 record

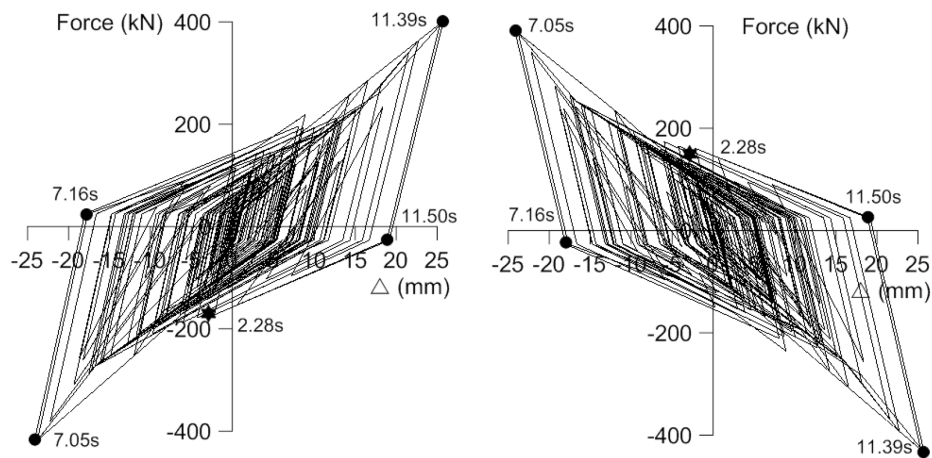


Figure 5.39: Two-storey CBF with pin devices Hysteretic response of pin devices located at 2nd floor and belonging to brace from joint #2 to #4 (Figure 4.7) for C4 record

Both selected subduction ground motions, S1 and S3, show a maximum PGA of about $0.3g$ at $t = 100s$, as illustrated in Figures 5.40a and 5.45a. Meanwhile, the S1 accelerogram seems to allow the building to behave symmetrically in both tension and compression (Figures 5.41, 5.43), while the S3 record demands larger deformations on one side than the other (Figures 5.46, 5.47). As a consequence, the seismic response in term of hysteresis force-displacement loops, under the S1 record, is more symmetrical than

under the S3 record. When the two-storey CBF with pin devices is subjected to the S1 record, the maximum base shear of 600kN occurs at 52.84s . At the same time, $t = 52.84\text{s}$, a maximum deformation of the ground floor pins is recorded (7mm). Under the ground motion S3, the base shear is larger, 780kN , while the pins' deformation is also slightly larger (8mm). The pins' deformation at the 2nd floor level is similar in both cases ($\sim 9\text{mm}$). The interstorey drift recorded under the S1 and S3 records is approximately $0.4\%h_s$. The high frequency content of subduction ground motions does not impose larger deformations, and therefore reduced base shear values are recorded, although the spectral ordinates corresponding to the period of interest are above the UHS.

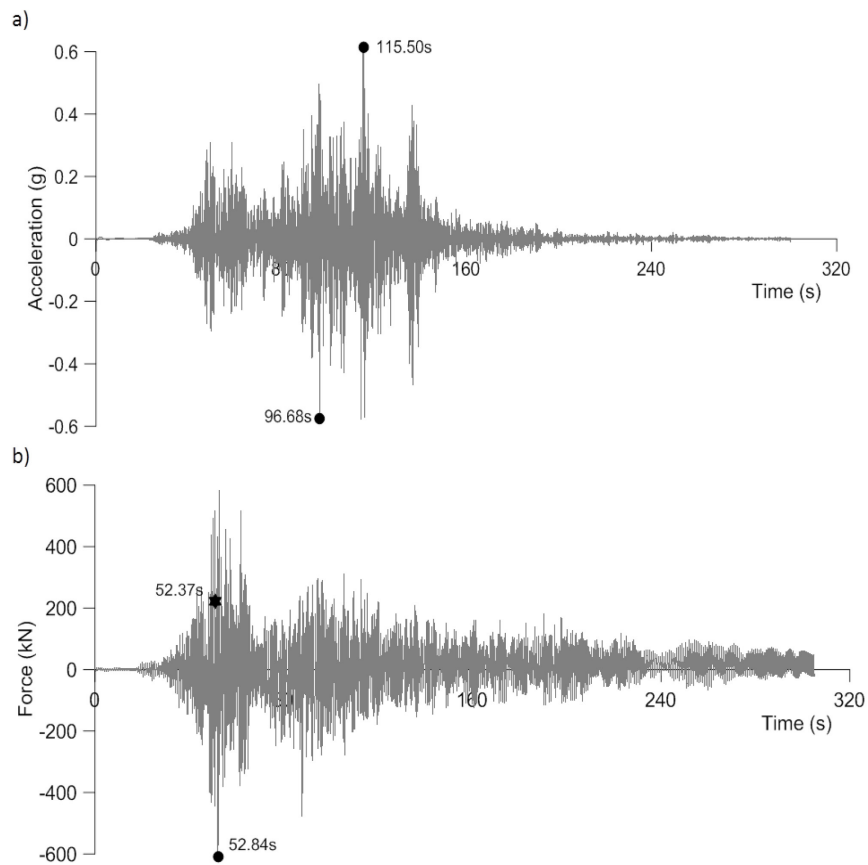


Figure 5.40: Two-storey CBF with pin devices: a) Accelerogram S1, b) Base shear time history response for S1 record

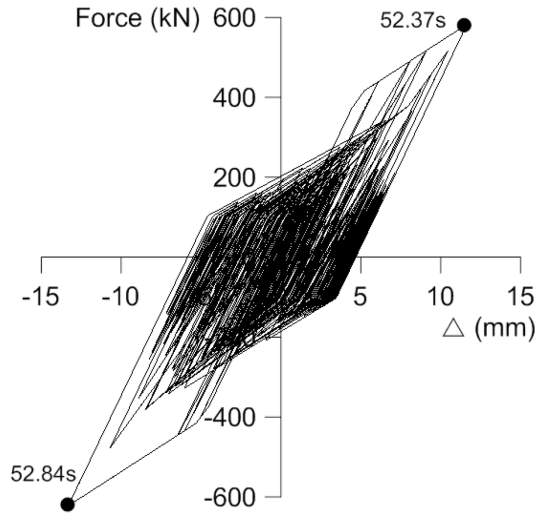


Figure 5.41: Two-storey CBF with pin devices: CBF response of ground floor for S1 record

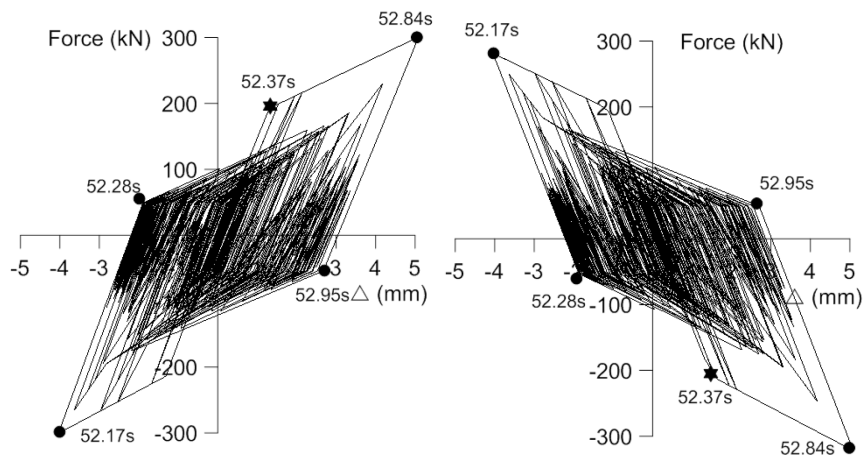


Figure 5.42: Two-storey CBF with pin devices: Hysteretic response of pin devices located at ground floor and belonging to brace from joint #1 to #5 (Figure 4.7) for S1 record

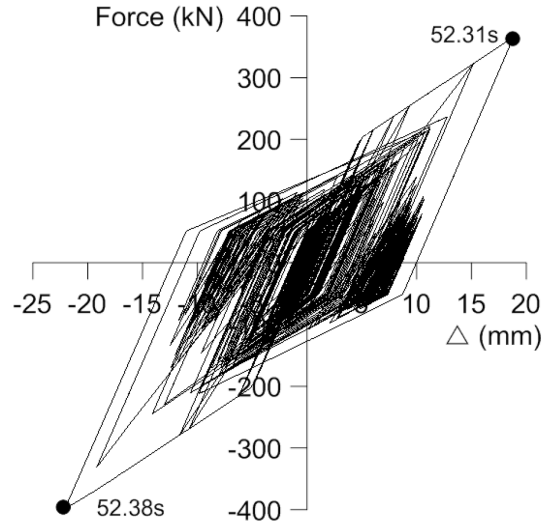


Figure 5.43: Two-storey CBF with pin devices: CBF response of 2nd for S1 record

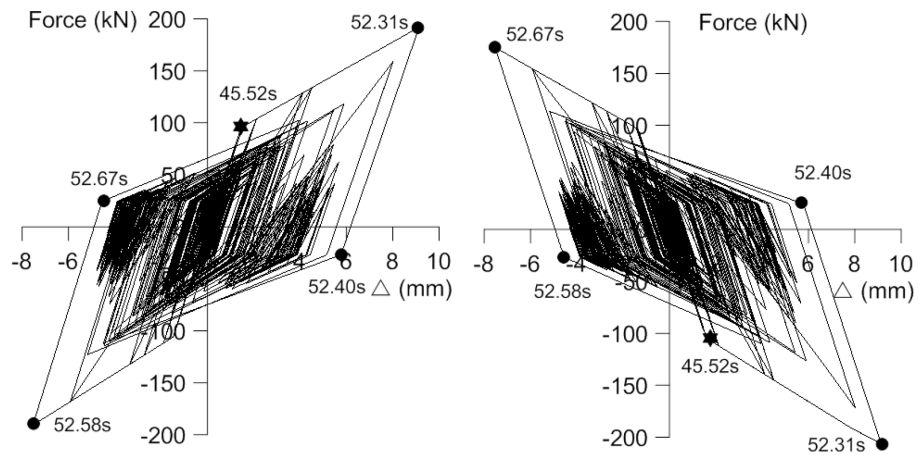


Figure 5.44: Two-storey CBF with pin devices: Hysteretic response of pin devices located at 2nd floor and belonging to brace from joint #2 to #4 (Figure 4.7) for S1 record

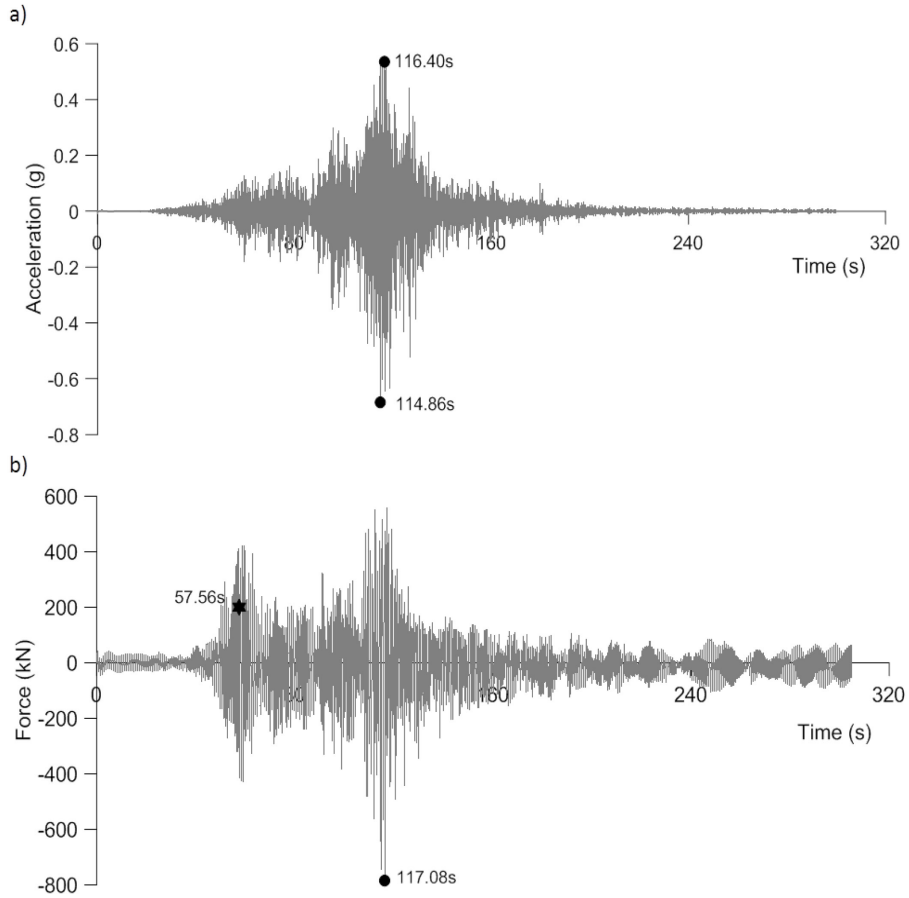


Figure 5.45: Two-storey CBF with pin devices: a) Accelerogram S3, b) Base shear time history response for S3 record

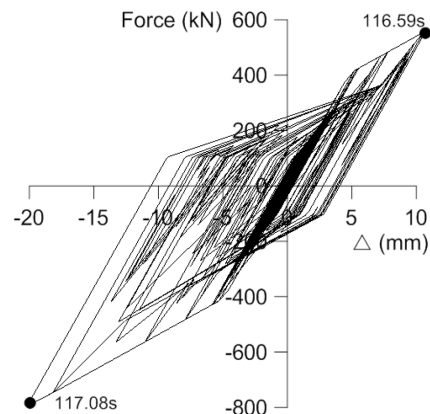


Figure 5.46: Two-storey CBF with pin devices: Two-storey frame response of ground floor for S3 record

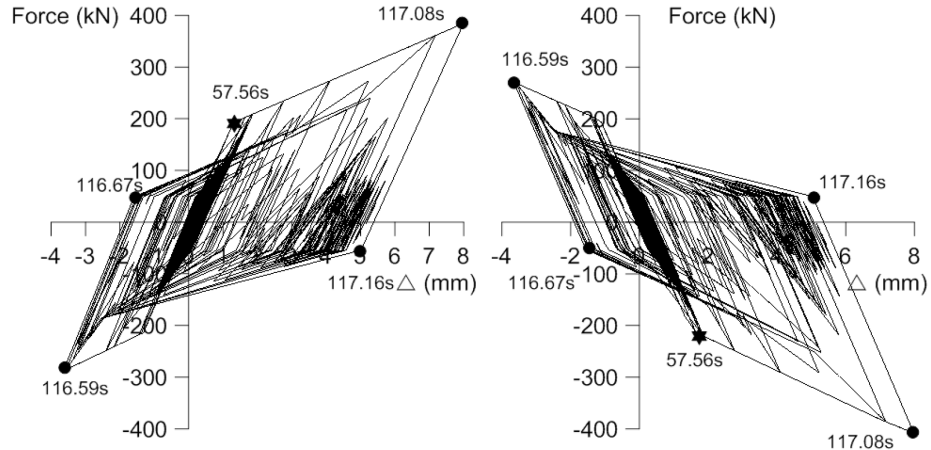


Figure 5.47: Two-storey CBF with pin devices: Hysteretic response of pin devices located at ground floor and belonging to brace from joint #1 to #5 (Figure 4.7) for S3 record

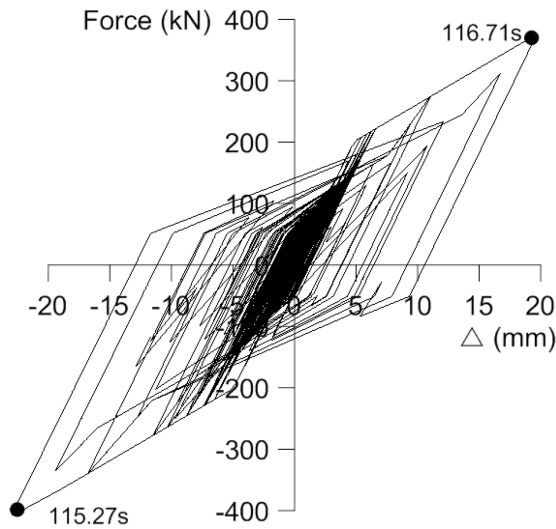


Figure 5.48: Two-storey CBF with pin devices: CBF response of 2nd floor for S3 record

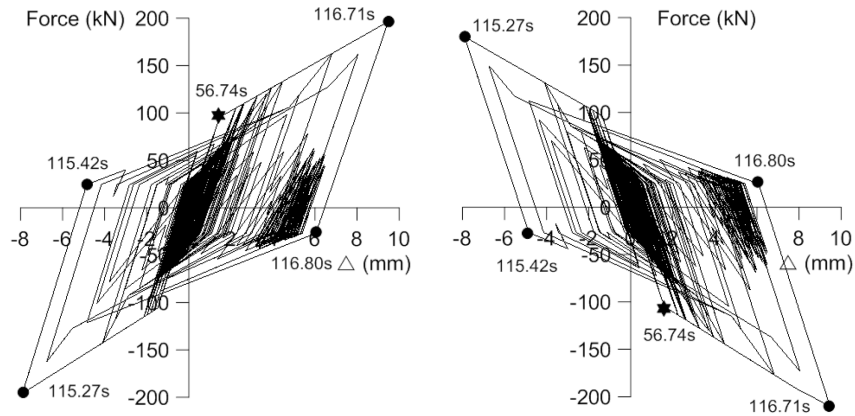


Figure 5.49: Two-storey CBF with pin devices: Hysteretic response of pin devices located at 2nd floor and belonging to brace from joint #2 to #4 (Figure 4.7) for S3 record

Regarding near-field ground motions, the selected accelerograms correspond to N1 and N3 records, as illustrated in Figures 5.50 and 5.52. The maximum PGA occurs at the beginning of near-field N1 and N3 records at $\sim t = 2.0s$ and $t = 8.0s$, respectively when a larger acceleration pulse is developed. The two-storey CBF with pins was not able to carry the larger acceleration pulse and failure was encountered before the PGA was attained, as illustrated in Figures 5.51 and 5.53.

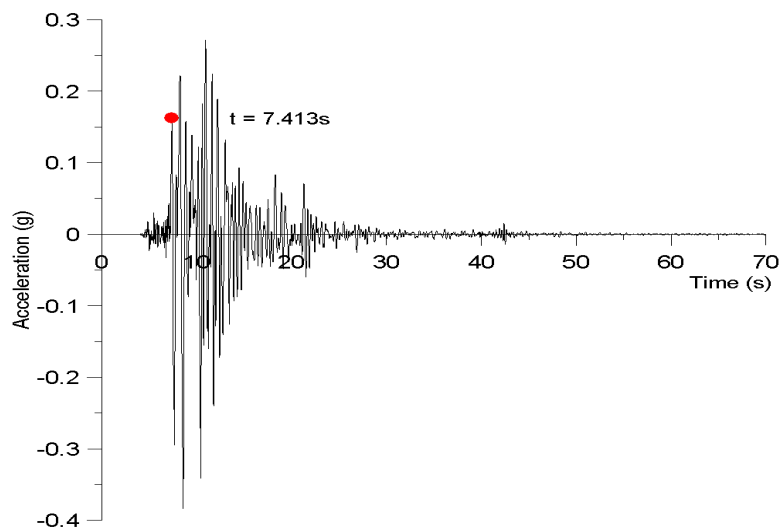


Figure 5.50: Acceleration time history for N1 record

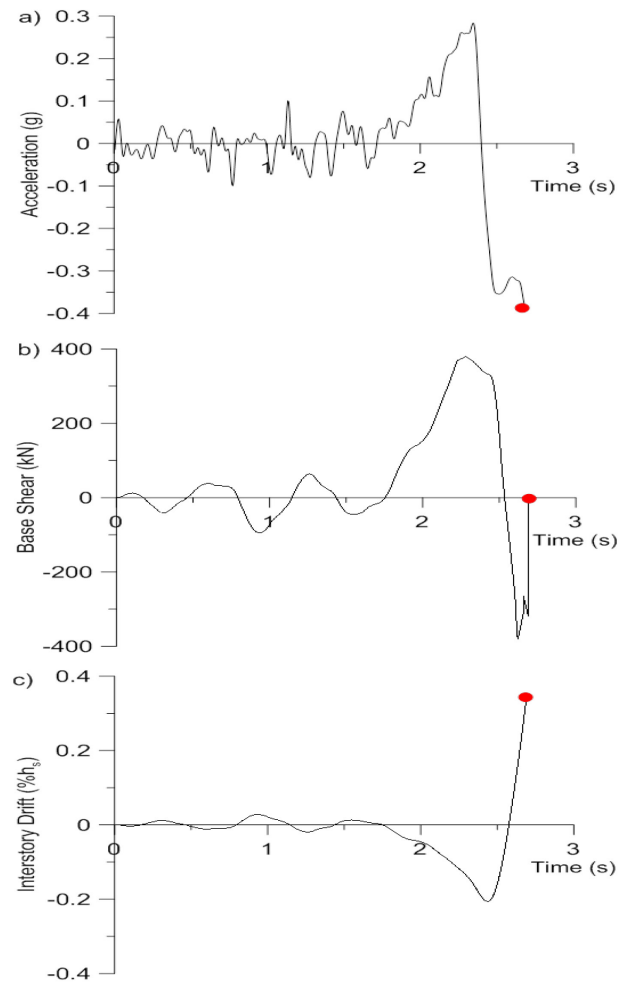


Figure 5.51: Time history responses for N1 record - a) Acceleration, b) Base shear, c) Interstorey drift

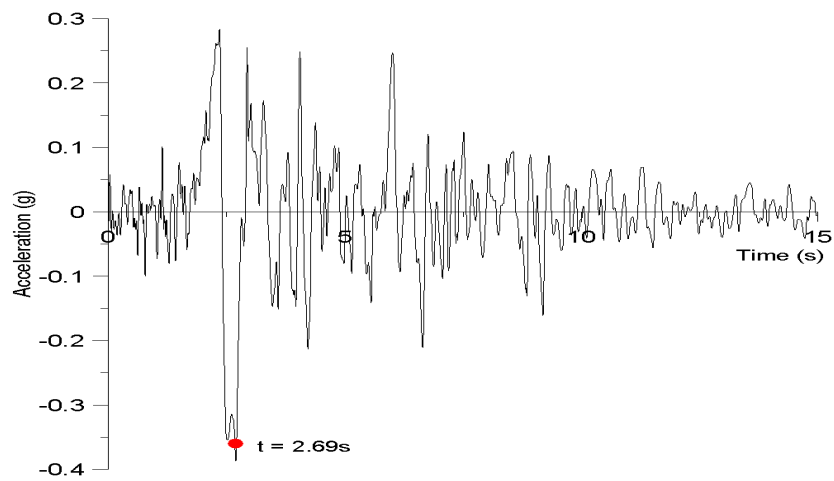


Figure 5.52: Acceleration time history for N1 record

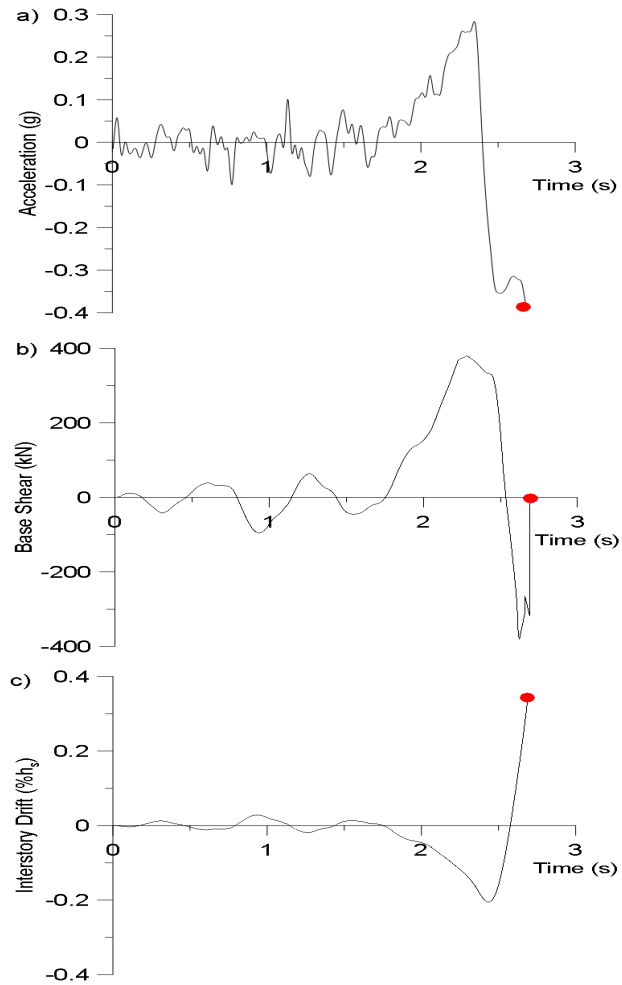


Figure 5.53: Time history responses for N3 record - a) Acceleration, b) Base shear, c) Interstorey drift

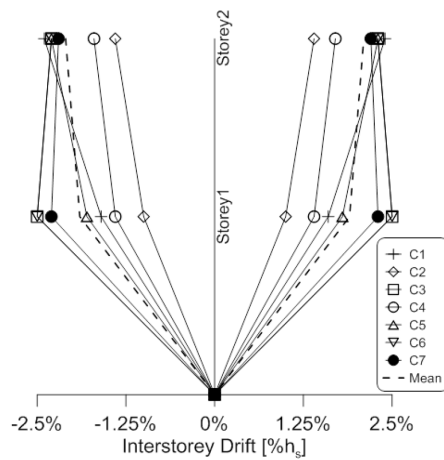


Figure 5.54: Interstorey drift - Crustal ground motions

Figure 5.55 illustrates the computed Δ/Δ_y ratio resulted under the crustal ground motions. It is shown that Δ/Δ_y is about 6 times larger for CBF with pins than for LD-CBFs. It seems that this difference increases by increasing the number of storeys.

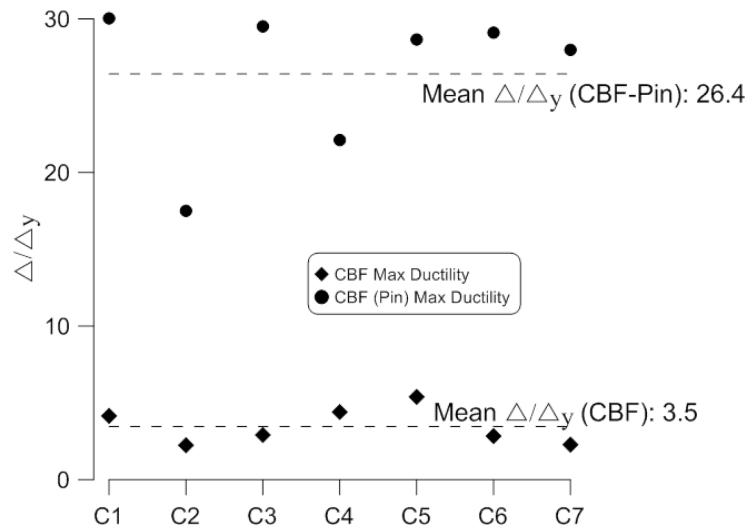


Figure 5.55: Displacement ductility comparisons of two-storey frame with and without dissipative single-pin connection

5.3.3 Residual Deformations

The seismic design philosophy emphasizes promoting ductile structural systems able to perform in non-linear range during earthquakes, while maintaining their structural integrity. The seismic response of the structure is generally assessed based on the amount of energy dissipated and the maximum deformation. By analyzing the time-history deformations under earthquake loading, residual deformations were observed at the end of ground motions. The magnitude of residual deformation can be amplified due to the P-delta effect and collapse, due to dynamic instability, may occur. However, these residual deformations do exist for most traditional earthquake resistant systems. Regarding the assessment of residual deformations of CBFs equipped with pin devices, the parameter

defined as the maximum interstorey residual deformation over the maximum interstorey drift (IRD/ID) is illustrated herein. This parameter proposed by Christopoulos and Pampanian (2004), is computed for the single- and the two-storey CBFs equipped with pin devices under the selected ground motions: C2, C4; S1, S3 and N1, N3. Figure 5.56 illustrates the maximum interstorey residual deformations, the maximum interstorey drift and the ratio IRD/ID , for the single-storey CBF system with pin devices under the aforementioned ground motions. As observed, the maximum deformation response occurred under the near-field records, while under the C2, C4, S1 and S3 ground motions, the ratio IRD/ID is < 0.6 . Regarding the deformation response of the two-storey CBF with pins, under the C2, C4, S1 and S3 ground motions, the seismic response in terms of IRD/ID ratio is < 0.6 as well, with maximum demand at the ground floor level, as illustrated in Figure 5.57.

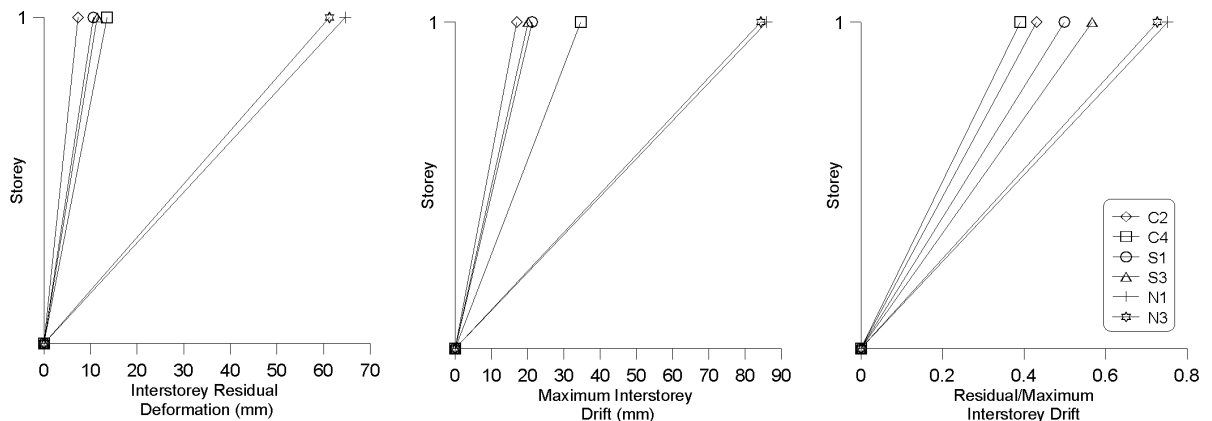


Figure 5.56: Single-storey CBF with pin devices: a) Interstorey residual deformation under the studies ground motions, b) Maximum interstorey drift under the studies ground motions, c) Ratio of the interstorey residual deformation to the maximum interstorey drift

As reported by Christopoulos and Pampanian (2004), the computed IRD/ID ratio values for CBFs with pin devices illustrated in Figures 5.56 – 5.57 are within acceptable limits.

In the same study it was noted that residual deformations are a function of post yielding stiffness and hysteretic formulation. Therefore, the targeted residual deformation may be a parameter that should be considered in the preliminary design of the pin member.

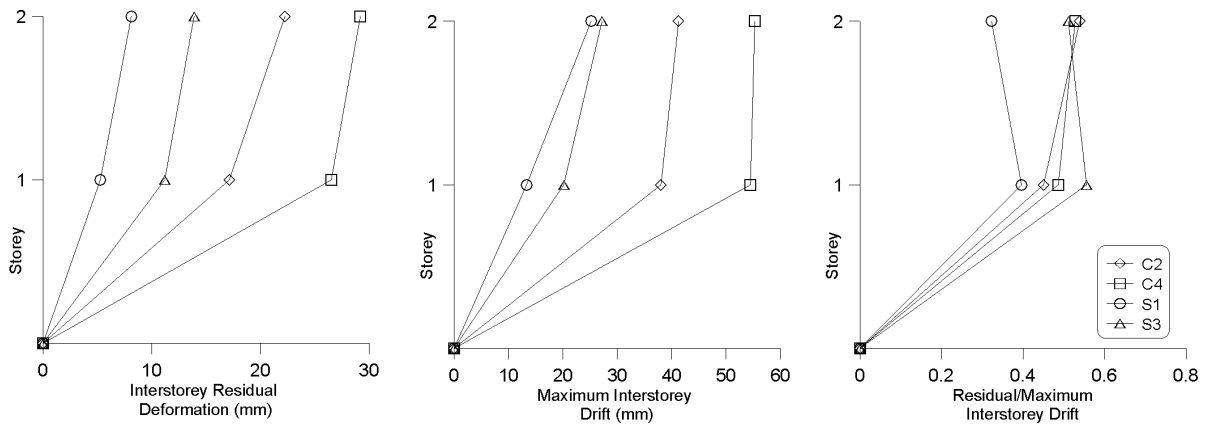


Figure 5.57: Two-storey structure - a) Interstorey residual deformation under the studies ground motions, b) Maximum interstorey drift under the studies ground motions, c) Ratio of the interstorey residual deformation to the maximum interstorey drift

5.4 Limitations of the Dissipative Single Pin Connection

5.4.1 Limitations with Respect to Pin Size

As for every type of connection, there are certain limitations restricting their use. In the case of dissipative single-pin connection, the size of the pin should be considered as being limited. In previous sections a single- and two-storey CBF structure were analyzed whereby the storey shear did not surpass a certain magnitude. When structures comprised of more stories will be studied, the storey shears will increase, causing the pin size to increase as well. The structural members of a building are limited in size and therefore the dissipative single-pin connections must also be limited in size. The question arises concerning size limitation and a design solution once the limitation is reached.

A 4- and 8-storey building were designed in both Victoria, B.C., and Montreal, QC (Figure 4.1). These two frames enable the study of connection size in different seismic regions as well as encountering limitations in connection sizes. Table 5.4 gives a design summary in order to determine the pin size of all the braced frames studied in this section. It is observed that in the case of the structures residing in the Montreal region, the demanded pin sizes are relatively small. In the case of the 4- and 8-storey structures belonging to the Victoria region, the demanded pin sizes begin to increase. After studying the design of these various structures in the two regions, it is proposed to begin considering an alternative possibility for connection design when a storey shear of magnitude 2500kN or greater is required to be developed in the structure.

An interesting alternative design would be to devise the same connection, but with two pins of equal size acting together rather than one pin. This would allow for two smaller pin sizes and would only elongate the connection size rather than increase the thicknesses of all the connection components. With a dissipative double pin connection, the two pins would undergo the same magnitude of displacement meanwhile the axial force from the brace would be divided in 2 pins, therefore having two pins of smaller cross section.

With the limitation of a storey shear less than 2500kN, it can be seen in Figure 5.27 that in the case of the 4-storey frame in the Victoria region, the first two storeys would be candidates for a double pin dissipative connections. The same would be true for the first four storeys of the eight storey structure of the Victoria region as well.

For the 4-storey frame, under the same design conditions, two pins able to resist a combined force between 1158kN and 1543kN would be required for its first storey;

therefore each pin would have to have an ultimate strength between the values of 579kN and 771kN. In the same light, for the second storey, two pins, each able to resist between 415kN and 554kN, are required. The same analysis can be done for the lower 4 storeys of the 8-storey building and the resulting alternative design is found in Table 5.5.

Table 5.4: Pin design for 4- and 8-storey structures in Montreal and Victoria regions

Fl.	Floor Shear (kN)	Braces (HSS)	C_r (kN)	Columns	d (mm)	a (mm)	60%-80%Cr (kN)	Pin
VICTORIA								
4	1225	152x8.0	953.5	W310X79	306	108	573-763	40X60
3	2207	178x9.5	1385.8			95.5	831-1109	50X60
2	2862	178x9.5	1385.8	W310X179	333	109	831-1109	55X60
1	3190	203x9.5	1929.3			101.5	1158-1543	60X70
8	836	152x8.0	953.5	W200X71	216	58	573-763	35X45
7	1390	178x9.5	1385.8			45.5	831-1109	40X50
6	1866	178x13.0	1921.1	W250X115	269	84.5	1153-1537	50X70
5	2262	178x13.0	1921.1			84.5	1153-1537	50X70
4	2579	178x13.0	2259.1	WWF350X176	350	125	1355-1807	70X80
3	2817	203x13.0	2259.1			115	1355-1807	70X70
2	2975	203x13.0	2259.1	WWF450X274	450	165	1355-1807	70X90
1	3054	178x13.0	1921.1			170	1153-1537	70X80
MONTREAL								
4	554	114X8.0	483	W310X74	310	127.5	290-386	40X45
3	975	127X9.5	724.1			125	434-579	40X55
2	1255	127X9.5	724.1	W310X129	318	129	434-579	40X55
1	1395	152X8.0	953.5			119	573-763	40X60
8	289	114X8.0	483	W200X71	216	80.5	290-386	35X40
7	474	127X8.0	629.5			78	378-504	40X40
6	632	127X8.0	629.5	W250X115	269	104.5	378-504	40X50
5	763	127X9.5	724.1			104.5	434-579	40X50
4	869	127X9.5	724.1	W310X179	333	136.5	434-579	40X60
3	948	127X9.5	724.1			136.5	434-579	40X60
2	1000	127X9.5	724.1	WWF350X238	350	145	434-579	40X70
1	1027	127X9.5	724.1			145	434-579	40X70

The possibility of dissipative multi-pin connections is also available and may be devised for high-rise structures when size limitation becomes an issue.

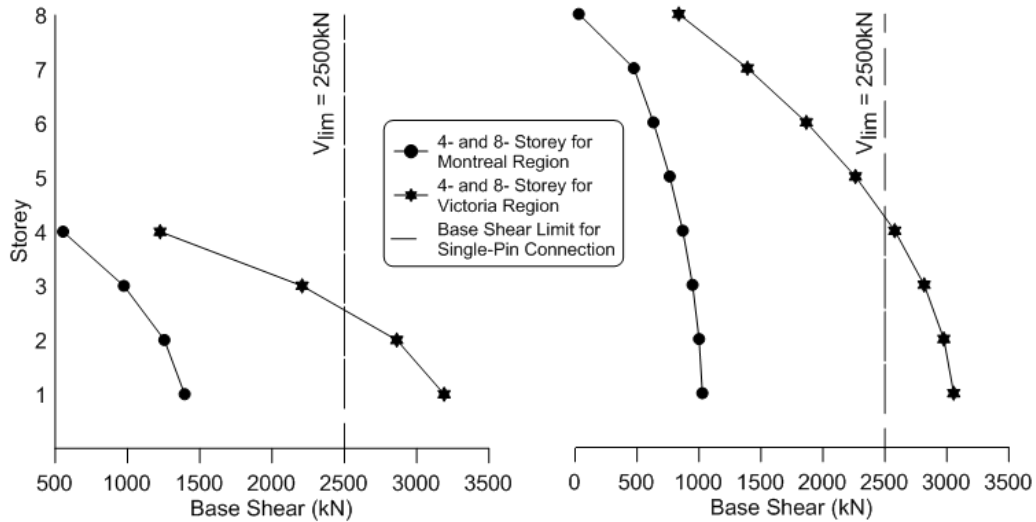


Figure 5.58: Montreal and Victoria region storey shear for a 4-, and 8-storey structure with respect to storey shear limitation for single and double pin dissipative connections

Table 5.5: Alternative design for the 4- and 8-storey structure in the Victoria region

Fl.	Floor Shear (kN)	Braces (HSS)	Cr (kN)	Columns	d (mm)	a (mm)	60%-80%Cr (kN)	Pin
VICTORIA								
4	1225	152x8.0	953.5	W310X79	306	108	573-763	40X60
3	2207	178x9.5	1385.8			95.5	831-1109	50X60
2	2862	178x9.5	1385.8	W310X179	333	109	831-1109	2x[40X50]
1	3190	203x9.5	1929.3			101.5	1158-1543	2x[40X60]
8	836	152x8.0	953.5	W200X71	216	58	573-763	35X45
7	1390	178x9.5	1385.8			45.5	831-1109	40X50
6	1866	178x13.0	1921.1	W250X115	269	84.5	1153-1537	50X70
5	2262	178x13.0	1921.1			84.5	1153-1537	50X70
4	2579	178x13.0	2259.1	WWF350X176	350	125	1355-1807	2x[40X50]
3	2817	203x13.0	2259.1			115	1355-1807	2x[40X50]
2	2975	203x13.0	2259.1	WWF450X274	450	165	1355-1807	2x[40X60]
1	3054	178x13.0	1921.1			170	1153-1537	2x[40X60]

5.4.2 Limitations with Respect to Wind Loads

In regions where seismic activity is the dominant lateral load with respect to structures, it is the main design criteria for the dissipative pin connections, although the wind load is not to be disregarded. It is important to ensure that the magnitude of the wind load on the structure does not force the pin connections to work in the plastic range. Their strength must be uncompromised in order for their optimum behavior when subjected to seismic loads.

In order to prevent the yielding of the connections under wind loads, when the pin design has been completed, its elastic strength must be cross checked with the magnitude of wind load applied to its specific floor. Using the NBCC 2010 provisions wind load is calculated by using the following:

$$p = I_w q C_e C_g C_p \quad (5.1)$$

where I_w is the importance factor of the building, and q is the reference velocity pressure in accordance to the region where the structure is being built. The coefficients, C_e , C_g , and C_p , pertain to exposure, gust and external pressure, respectively. Once the effective width has been determined the wind load per floor may be determined. The axial force in the brace from the floor wind load, W_f , can then be determined as $W_f/2\cos\theta$. This load, transferred in the brace member, must be less than the elastic capacity of the connection to ensure that the strength of the connection will not be compromised:

$$P_I = 2M_y/a \geq W_f/2\cos\theta \quad (5.2)$$

Therefore ultimately:

$$W_f \leq \frac{4 M_y \cos\theta}{a} \quad (5.3)$$

The single-storey structure with single-pin dissipative connections designed in section 5.1.1 is equipped with a 35 x 50mm pin with an elastic capacity of, $M_y \cdot \cos\theta/a=103\text{kN}$. The floor wind load for this structure, calculated using equations 5.1 and 5.2 is, $W_f = 71.89\text{kN}$. Therefore, since $W_f \leq P_I$ the dissipative pin will not yield under the wind load.

Chapter 6. Conclusion and Future Work

6.1 Conclusion

In this research, the behaviour of low-rise CBFs equipped with dissipative brace-to-column connection devices, labelled dissipative single-pin connections, are underlined. The evaluation of this structural system, designed to respond in elastic range, while the single-pin devices experience yielding in flexure under seismic loads, is carried out in three levels as follows:

- The pin element is studied by using the theoretical simple beam model and the OpenSees beam model under monotonic loading;
- The single-pin connection is analyzed using the OpenSees beam model under cyclic quasi-static displacement loading. The proposed OpenSees model is calibrated against experimental test results;
- The braced frame with pin-devices is analyzed by using the OpenSees model under cyclic quasi-static displacement loading. The proposed OpenSees model is calibrated against experimental test results;

To assess the behaviour of CBFs with single-pin devices, a comparative study conducted on a single- and two-storey office building in Victoria, B.C., was carried and the seismic response was evaluated against traditional LD-CBFs under 21 ground motions. All computations were carried out in the OpenSees framework.

From the aforementioned analyses, it can be concluded:

- The theoretical simple beam model can be used for preliminary design applications;

- The dissipative energy capacity of single-pin connection device increases if larger distance between the inner plates is provided;
- From experimental tests conducted at the level of the single-pin device in Portugal, it was concluded that low-cyclic fatigue failure is not the typical failure mode of these devices. However, in this study, the low-cycle fatigue failure mode was not simulated in OpenSees and the cycle encountering failure is not accurately simulated in the computer model;
- The CBF with the single-pin brace-to-column connection sample use in the experimental tests (Castiglioni, 2010) was simulated in OpenSees and was calibrated against the test results;

By analysing the acceleration spectra of the 21 selected ground motions, an increase is observed in the spectral ordinate from $0.4S(0.2)$ to $S(0.2)$ in the interval from $0 - T_o$, where T_o is defined in the ASCE regulation and the FEMA 356 (2000) provisions, while symbolising the period when the spectral ordinate reaches its maximum value. Therefore, in order to avoid the conservative UHS, during the short period range, $0 - T_o$, the spectral acceleration ordinates, $0.4S(0.2) - S(0.2)$, are proposed to increase linearly. It was observed, however, that this reduction has no effect on the seismic response of the single- and two-storey building with and without single pin-connections.

The single-pin connections are designed to yield at 60-70% of the buckling strength of braces, in turn constraining the braces to respond in elastic range. In this respect, the following design methodology for CBFs with single-pin connections is proposed: i) for regular systems, design the member sizes of LD-CBFs based on the equivalent static force procedure; ii) build the tri-linear curve of the pin devices based on

the buckling strength of braces; iii) simulate the OpenSees model and assess the seismic response in terms of force and deformation. The CBF with single-pin devices experiences a larger period and less shear force demand than the CBF system. Although, there is no weight reduction in the CBF structure with devices, the foundation costs decrease due to the development of lower base shear.

The CBF with single-pin devices experiences residual deformations in acceptable limits. The ratio of maximum residual interstorey deformation over the maximum interstorey drift is less than 0.6. In order to obtain lower residual deformations, a limitation should be imposed in the design of the single-pin connection device.

A CBF structure with single-pin devices prevents braces from buckling and it eliminates the uncertainty of modelling the plastic zone of the brace. When considering the single-pin connection as a calibrated device, the modelling in plastic range can be accurately controlled.

The CBF with pin devices is sensitive to the frequency content of ground motions. Thus, ground motions with dominant short periods impose less deformation and less shear forces, while ground motions with dominant larger periods and pulse characteristics, like the near-field ground motions, demand large deformation and forces. Until further experimental tests are conducted, it is not recommended to select CBF with single-pin connections in seismic areas subjected to near-field ground motions.

Overall, the braced frame system with dissipative connections is an efficient earthquake resistant structure. Its efficiency consists of a reduced structural cost and feasibility of pin replacement after seismic events. The single-pin brace-to-column connections are able to behave in a ductile manner and are capable of dissipating almost

the same energy as a brace behaving in tension or compression. For middle-rise buildings located in high risk seismic areas, the double-pin brace-to-column connections are recommended instead of single-pin devices.

6.2 Future Work

The following work is proposed in order to further the advancement of research of the dissipative single-pin connections:

- Experimental testing of different pin dimensions is required in order to determine the formation of plastic hinges in the pin and to improve the design method which determines the displacement of the pin under different point loads. It is important to study the behavior of the pin located on its strong axis versus its weak axis.
- Experimental testing of the dissipative single-pin connection with different outer plate dimensions in order to clarify the effect of outer plate bending on the connections as a whole and the effect of bearing stress on the deformation of the pin.
- Numerical modeling with fatigue material at the level of braces and at the level of the dissipative single-pin connections in order to simulate the low-cyclic fatigue that may be encountered in the brace and connection response.

Further studies required in order to reduce residual deformation:

- if residual deformations are found to be too large, limits have to be considered as a design factor for the single-pin connection;
- if maximum deformation is reduced, the residual deformation will reduce as well;

Performance targets may be set at the preliminary design level. Residual deformations could also be reduced by adding a self-centering system in parallel with the single-pin connections.

REFERENCES

- Adams, J., Atkinson, G. *Development of the seismic hazard maps for the proposed 2005 edition of the National Building Code of Canada*. Can J Civil Eng 2003;30:255–71.
- Aguero, A., Izvernari, C. and Tremblay, R. 2006. *Modelling of the Seismic Response of Concentrically Braced Steel Steel Frames using the OpenSees Analysis Environment*. International Journal of Advanced Steel Construction, 2, 3, (pp 242-274).
- AISC. 2005. ANSI/AISC 341-05, *Seismic Provisions for Structural Steel Buildings* (Draft September 10, 2004). American Institute of Steel Construction. Chicago, IL.
- ARBED: Rolling Program Structural Shapes. 1982. Luxembourg.
- Atkinson, G. 2009. *Earthquake time histories compatible with the 2005 National building code of Canada uniform hazard spectrum*. Can J Civil Eng; 36(6):991–1000.
- Atkinson, G., Macias, M. 2009. *Predicted ground motions for great interface earthquakes in the Cascadia subduction zone*. Bull Seismol Soc Am; 99(3):1552–78.
- Baker JW. 2011. *The conditional mean spectrum: tool for ground motion selection*. J Struct Eng, ASCE;137(3):322–31.
- Calado, L. "Lisbon experimental Test Results." Email to Luica Tirca. 2010.
- Calado, L., Ferreira, J., Feligioni, S. 2004. Report 2: *Characterization of Dissipative Connections for Concentric Bracing Systems in Steel Frames in Seismic Areas*. Instituto Superior Tecnico. Lisbon, Portugal.
- CAN/CSA. 2009. Canadian Standard Association. CSA/ S16-2009: *Design of Steel Structures*. Toronto, Ontario.

Castiglioni, C. "Milano experimental Test Results." Email to Luica Tirca. 2010.

Castiglioni, C., Brescianini, J., Crespi, A., Dell'Anna, S., Lazzarotto, L. 2004. Final Report 2: *Two Innovations for Earthquake Resistant Design*. Politecnico di Milano. Milano, Italy.

Chen L. 2011. *Innovative bracing system for earthquake resistant concentrically braced frame structures*. Master Thesis. Civil Engineering. Department of Building, Civil and Environmental Engineering. Concordia University. Montreal, QC. April.

Christopoulos, C., Pampanin, S. 2004. *Towards performance based seismic design of mode structures with explicit consideration of residual deformations*. ISET Journal of Earthquake Technology. Paper no. 440, Vol. 41, No. 1, (pp.53-57).

Constantinou, M.C., and Symans, M.D. 1993. *Seismic response of structures with supplemental damping*. The Structural Design of tall buildings, 2, (pp. 77- 92).

Desjardins, E., and Légeron, F. 2010. *Method to Reduce Seismic Demand on Connections of Concentrically Braced Systems*. 2nd International Structures Specialty Conference, CSCE, Winnipeg, Manitoba.

ECCS. 1986. ECCS – TWG 1.3. *Seismic Design Recommended Testing Procedure for Assessing the Behaviour of Structural Steel Elements under Cyclic Loads*. European Convention for Constructional Steelwork, Technical Committee - Structural safety and loading. Brussels, Belgium.

EN 1993-1-9-2005: European Committee for Standardization – CEN. Eurocode 3: *Design of steel structures*. Part 1.9: Fatigue. Brussels.

EN 1998-1-2005. European Committee for Standardization – CEN. Eurocode 8: *Design of structures for earthquake resistance*. Brussels.

Federal Emergency Management Agency. 2000. FEMA 356: *Prestandard and commentary for the seismic rehabilitation of buildings*. Building Seismic Safety Council of the National Institute of Building Sciences; Washington, D.C.

Federal Emergency Management Agency. 2003. FEMA 450: *NEHRP recommended provisions and commentary for seismic regulations for new buildings and other structures*. Building Seismic Safety Council of the National Institute of Building Sciences; Washington, D.C.

Gray, M.G., Christopoulos, C., and Packer, J. A. 2010. *Cast steel yielding fuse for concentrically braced frames*. Proc. 9th U.S. Nat. & 10th Can. Conf. on Earthquake Eng. Toronto, ON. Paper No. 595.

Ibarra, L. F., Medina, R. A., Krawinkler, H. 2005. *Hysteretic Models That Incorporate Strength and Stiffness Deterioration*. Earthquake Engineering and Structural Dynamics, Vol. 34, (pp. 1489-1511).

Izvernari, C. 2007. *The seismic behaviour of steel braces with large sections*. Master Thesis. Génie Civil. Département des Génies Civil, Géologique et des Mines. École Polytechnique de Montréal, Canada. Avril.

Kalkan, E., Kunnath, SK. 2007. *Effective cyclic energy as a measure of seismic demand*. J Earthquake Eng, ASCE; 11(5).

Kalkan, E., Chopra, AK. 2010. *Practical guidelines to select and scale earthquake records for nonlinear response history analysis of structures*. USGS open file report no. 2010-1068. 126p.

Kalkan, E., Chopra, AK. 2011. *Modal-pushover-based ground motion scaling procedure*. J Struct Eng, ASCE;137(3):298–310.

Kassis, D. and Tremblay, R. 2008. *Brace fuse system for cost-effective design of low-rise steel buildings*. Proc. CSCE 2008 Annual Conference, Quebec, QC, Paper No. 248.

Mazzoni, S., McKenna, F., Scott, M.H. and Fenves, G.L. et al. 2007. *OpenSees comand language manual*. Pacific Eathquake Engineering Research Center, University of California, Berkeley.

McKenna, F., Scott, M.H. and Fenves, G.L. et al. 2009. *Open system for earth-quake engineering simulation*. OpenSees software version 2.2.0.

NRCC. 2010. *National Building Code of Canada 2010*. 13th ed., National Research Council of Canada, Ottawa, ON.

Pacific Earthquake Engineering Research Center (PEER), University of California, Berkeley, CA. (<http://opensees.berkeley.edu/index.html>)

Plumier, A., Doneux, C., Castiglioni, C., Brescianini, J., Crespi, A., Dell'Anna, S., Lazzarotto, L., Calado, L., Ferreira, L., Feligioni, S., Bursi, O., Ferrario, F., Somnavilla, M., Vayas, I., Thanopoulos, P., and Demarco, T. 2004, *Two innovations for earthquake resistant design*. European Commission, Techni-cal Steel Research, Report EUR 22044 EN, ISBN 92-79-01694-6.

Plumier, A., Castiglioni, C., Vayas, I., Calado, L. 2005. *Behaviour of seismic resistant braced frame with innovative dissipative connections*. EUROSteel Conf., Maastricht, The Netherlands.

Reyes., J.C., Kalkan, E. 2011. *Required Number of Records for ASCE/SEI 7 Ground Motion Scaling Procedure*. <http://pubs.usgs.gov/of/2011/1083/of2011-1083.pdf>.

Rezai, M., Prion, H., Tremblay, R., Bouatay, N., and Timler, P. 2000. *Seismic Performance of Brace Fuse Elements for Concentrically Steel Braced Frames*. F. Mazzolani and R. Tremblay (eds.), Proc. STESSA 2000 Conf., Montréal, Canada, (pp. 39-46).

"SOFiSTiK". SOFiSTiK. <http://www.sofistik.com/sofistik/> (November 21, 2011)

Thanopoulos, P. 2006. Behaviour of seismic resistant steel frames with energy absorbing devices. Master Thesis. Structural Engineering. Department of Structural Engineering. National Technical University of Athens. Athens, Greece. November.

Tremblay, R. 2002. *Inelastic Seismic Response of Steel Bracing Members*. Journal of Constructional Steel Research, 58, (pp. 665-701).

Tremblay, R. and Bouatay, N. 2002. *Loading Protocols for the Seismic Testing of Ductile Bracing Members in Concentrically Braced Steel Frames*. Proc. 12th European Conf. on Earthquake Eng., London, UK, Paper No. 480.

Tremblay, R. and Castonguay, P. 2010. *Seismic Performance of Concentrically Braced Steel Frames of the Conventional Construction Category*. GRS Project/Report SR10-03. Structural Engineering. Dept. of Civil, Geological and Mining Engineering. École Polytechnique de Montréal, Canada. February.

Tremblay, R., St-Onge, E., Rogers, C., Morrison, T., Legeron, F., Desjardins, E., Tirca, L., Gray, M., Christopoulos, C., and Packer, J. 2011. *Overview of ductile seismic brace fuse systems in Canada*. EUROSteel conference, Buda-pest, (pp. 939-945).

Tirca, L., Caprarelli, C., Danila, N. 2011. *Behaviour of a Low Rise Concentrically Braced Frame Building with and without Dissipative Pin Connections*. Proc. CSCE Annual Conf., Ottawa, ON, 14 17 June 2011.

Tirca, L., Caprarelli, C., and Danila, N. 01/2012. *Seismic simulation and design of low-rise CBF buildings with and without dissipative connections using Open-Sees*. STESSA conference, Santiago, Chile, (pp. 365-371).

Tirca, L., Caprarelli, C., Danila, N., Calado, L. 05/2012. *Modelling and Design of Dissipative Connections for Brace-to-Column Joints*. 7th International Workshop on Connections in Steel Structures. Timișoara, Romania.

Uriz, P., Mahin, S.A. 2008. *Toward Earthquake-Resistant Design of Concentrically Braced Steel-Frame Structures*. Pacific Earthquake Engineering Research Center. University of California, Berkeley. San-Francisco, California.

Vayas, I., Thanopoulos, P. 2005. *Innovative Dissipative (INERD) Pin Connections for Seismic Resistant Braced Frames*. International Journal of Steel Structures, Vol. 5.

Ziemian, R. 2010. *Guide to Stability Design Criteria for Metal Structures*. publisher J. Wiley & Sons.

APPENDIX A - Selected Records

In this appendix the characteristics of the ground motions mentioned in Table 4.6 will be shown. Thus, the plotted figures are: acceleration time history, velocity time history, acceleration spectra and velocity spectra.

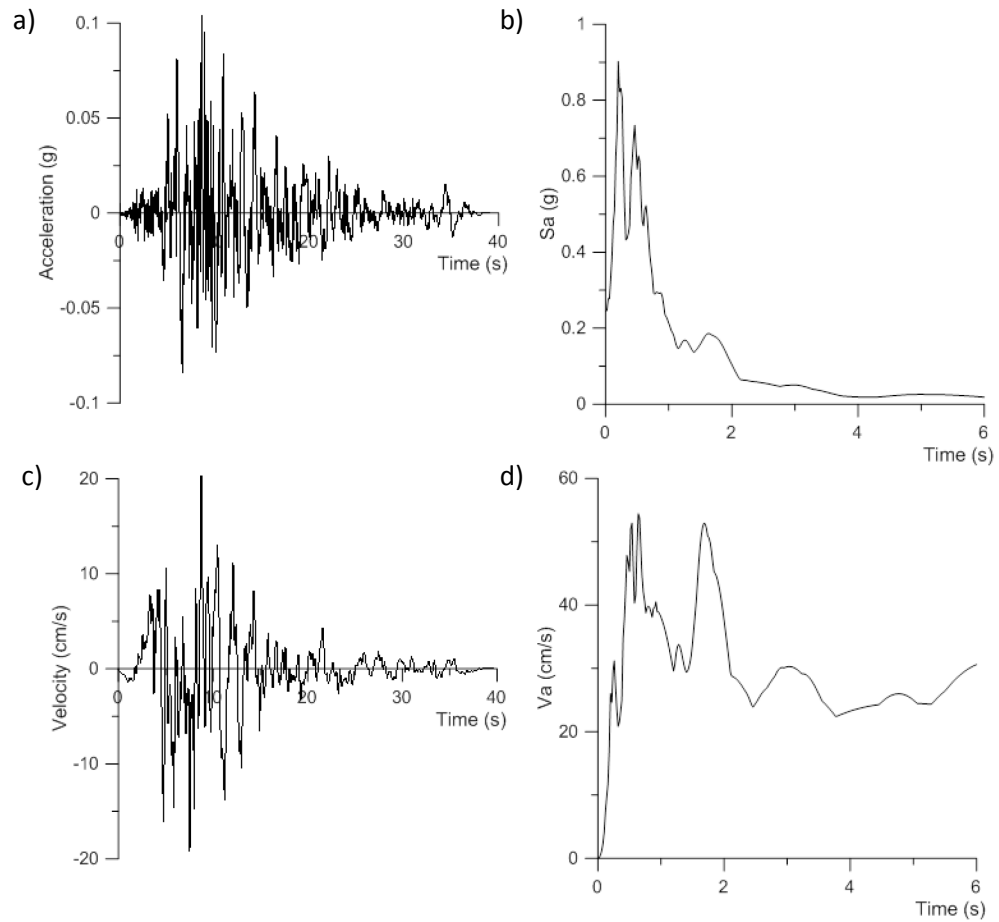


Figure A.1: C1 record - a) Acceleration time history, b) Spectral acceleration, c) Velocity time history, d) Spectral velocity

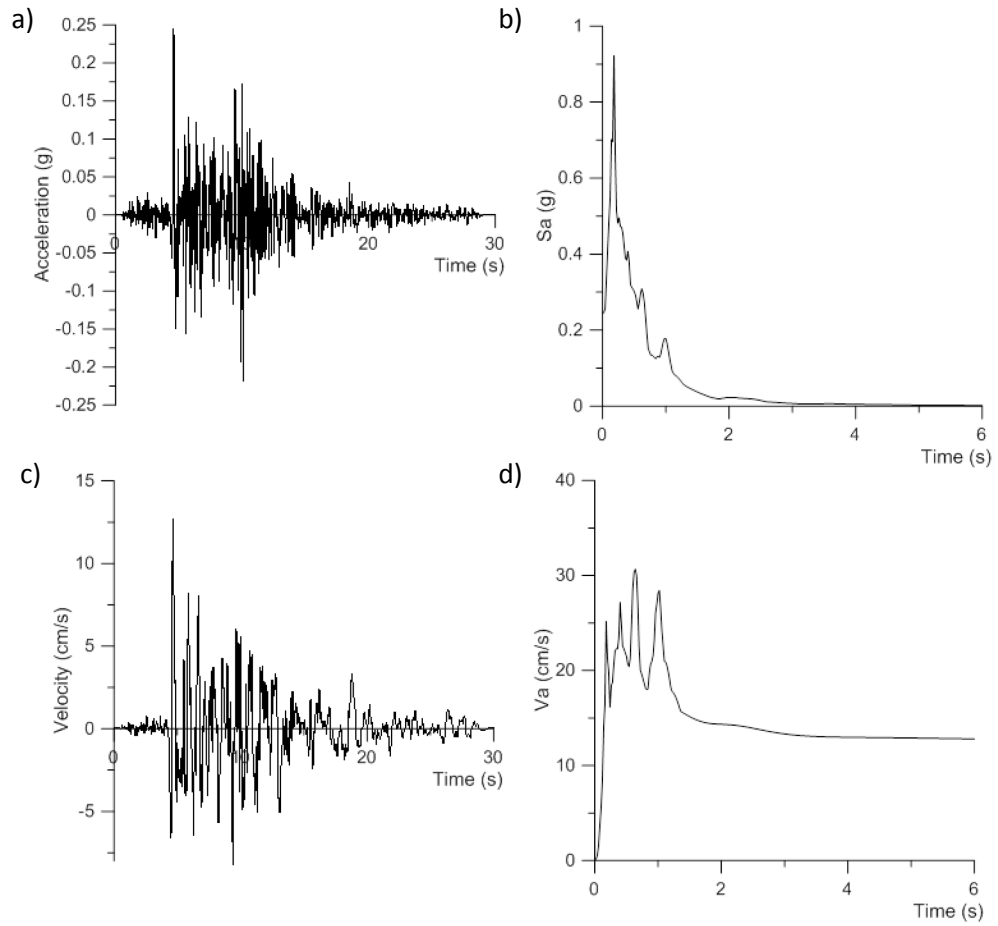


Figure A.2: C2 record - a) Acceleration time history, b) Spectral acceleration, c) Velocity time history, d) Spectral velocity

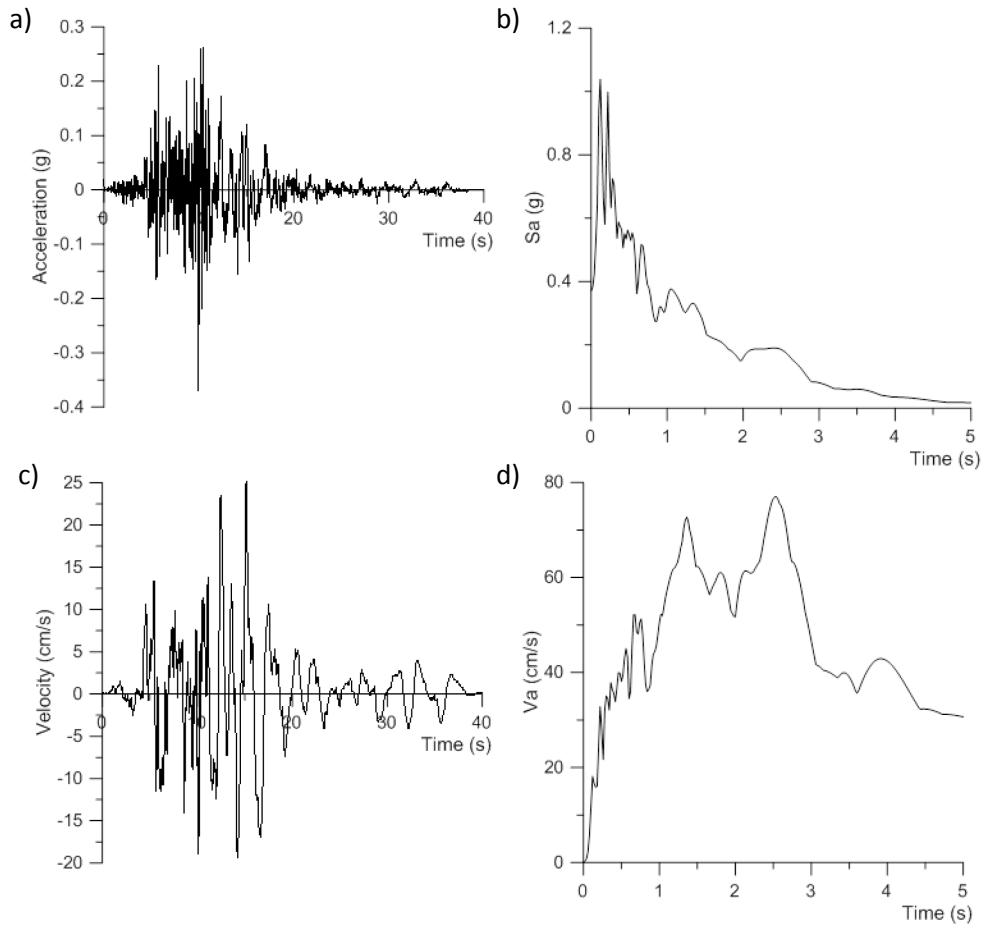


Figure A.3: C3 record - a) Acceleration time history, b) Spectral acceleration, c) Velocity time history, d) Spectral velocity

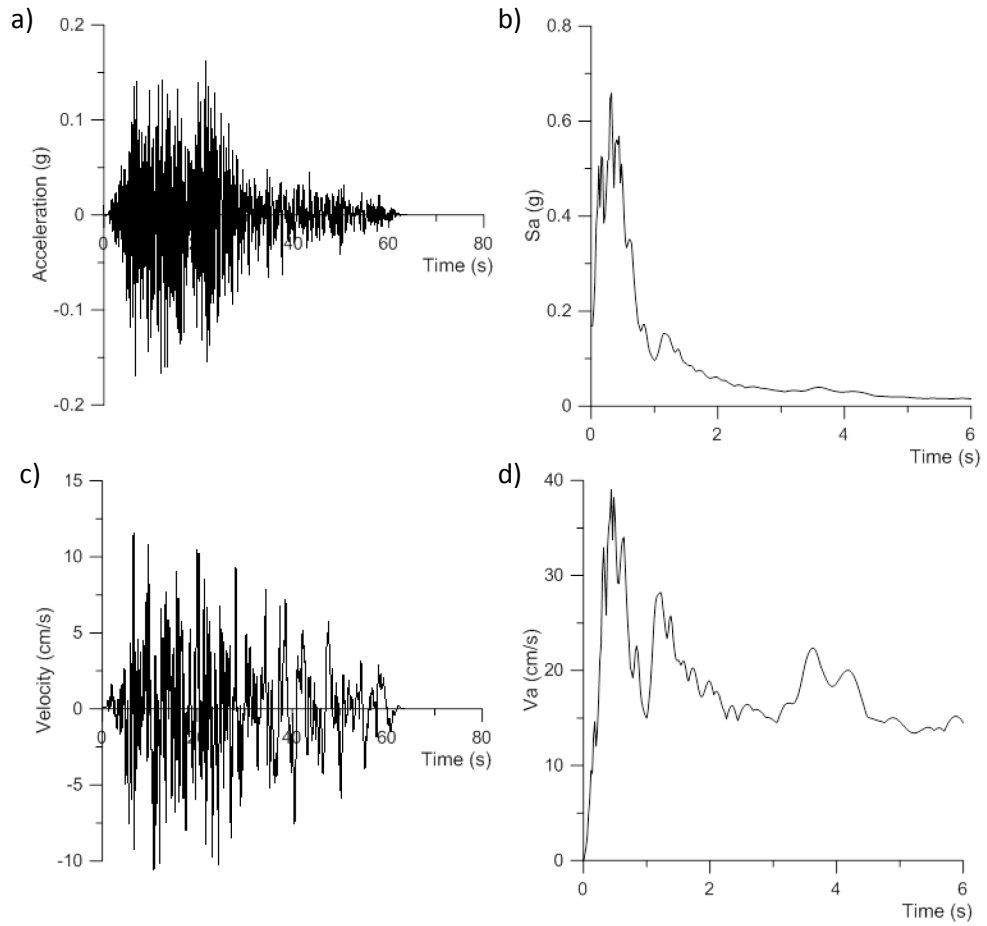


Figure A.4: C4 record - a) Acceleration time history, b) Spectral acceleration, c) Velocity time history, d) Spectral velocity

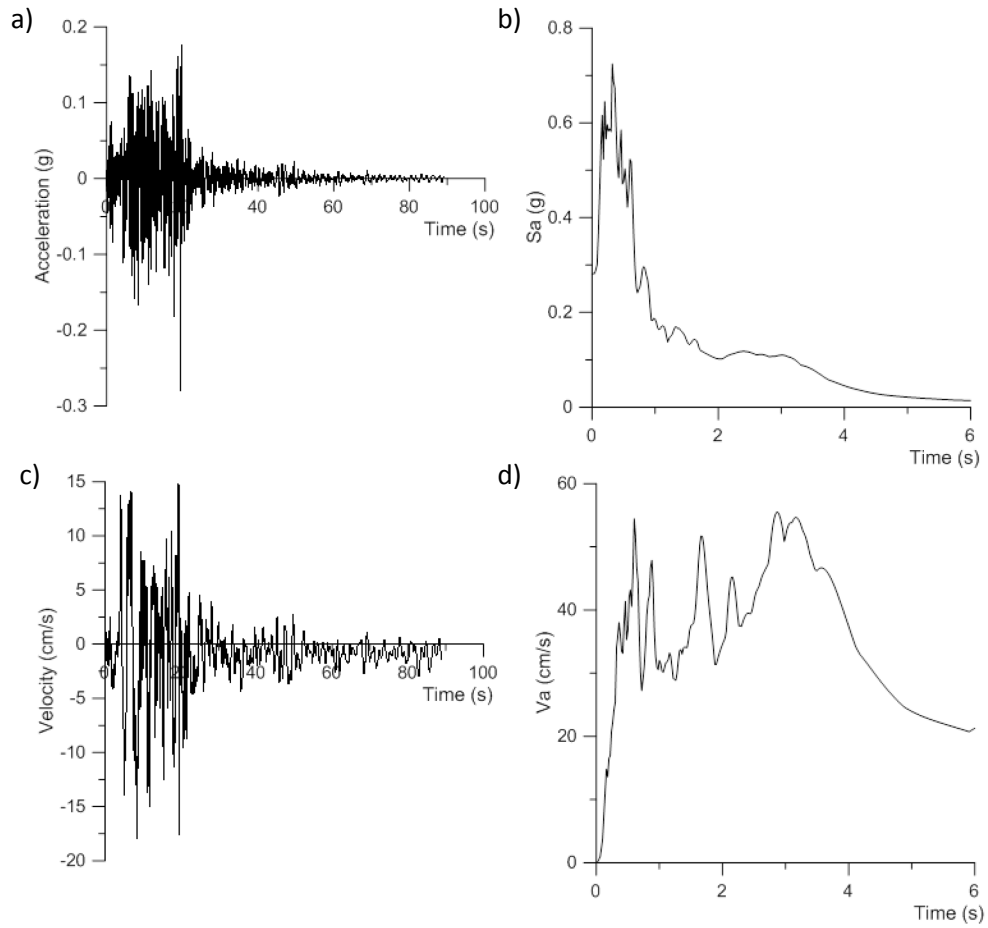


Figure A.5: C5 record - a) Acceleration time history, b) Spectral acceleration, c) Velocity time history, d) Spectral velocity

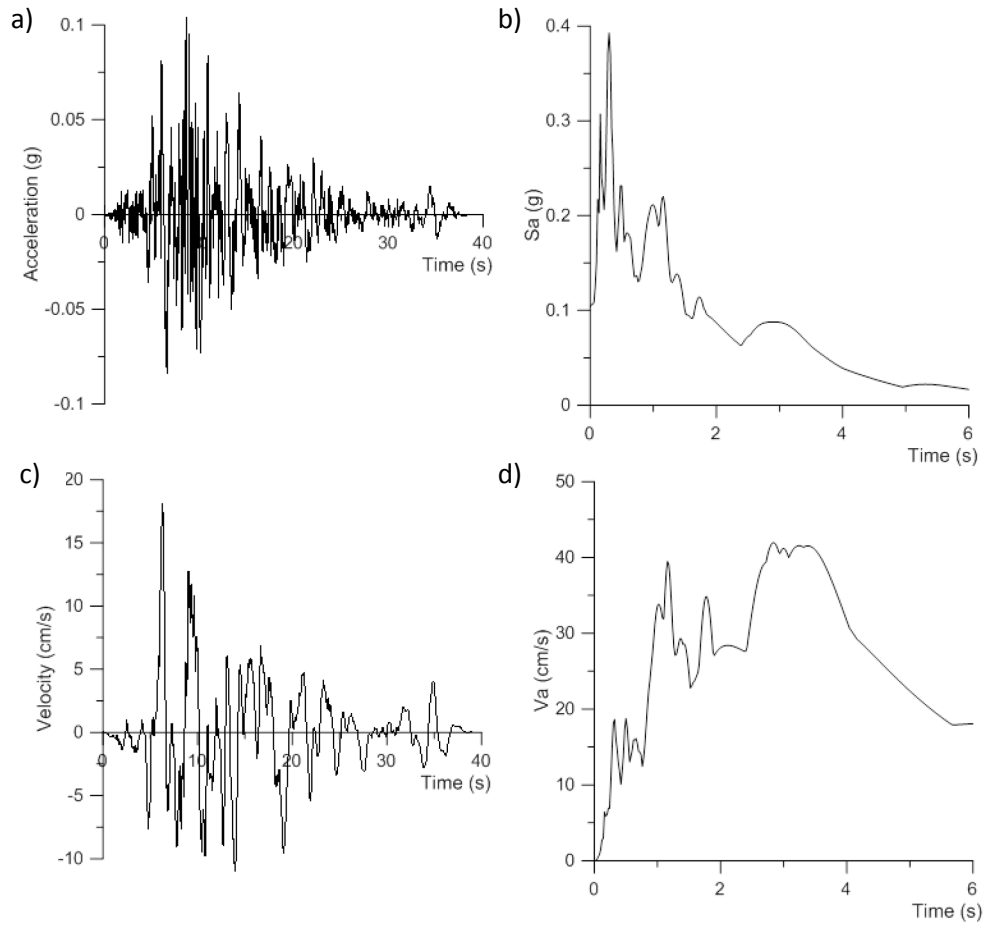


Figure A.6: C6 record - a) Acceleration time history, b) Spectral acceleration, c) Velocity time history, d) Spectral velocity

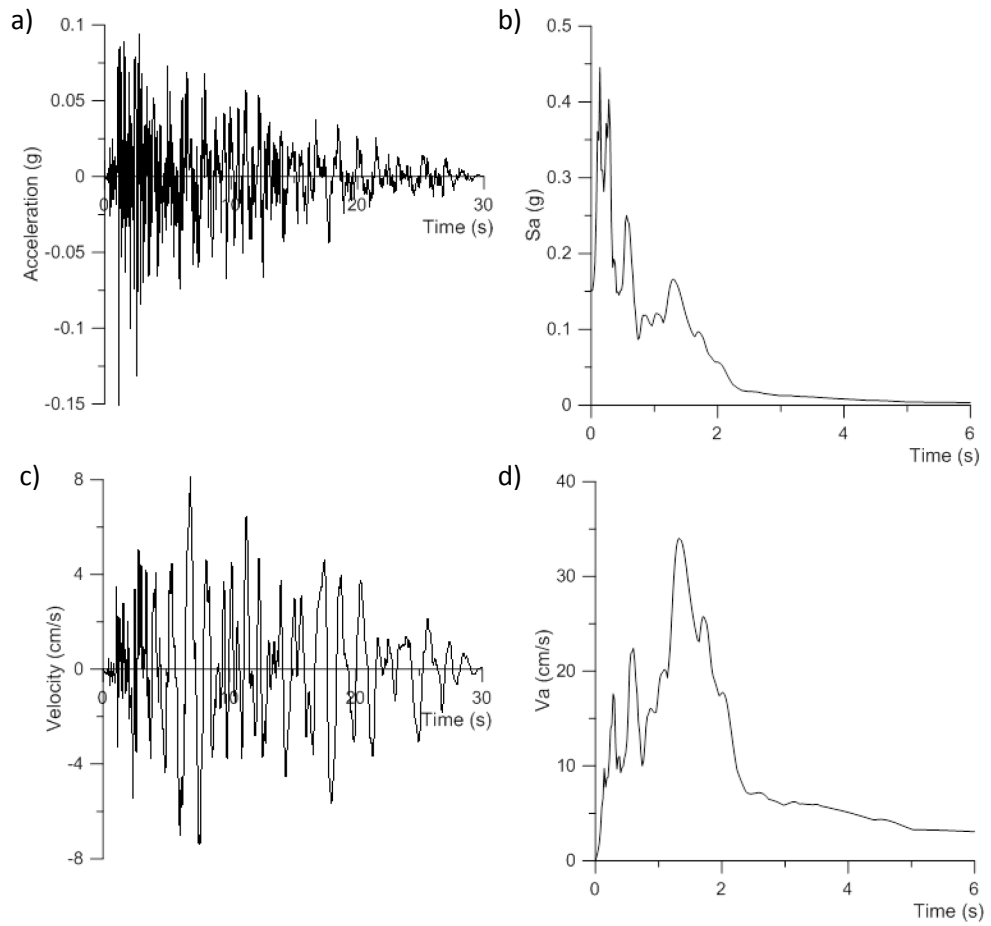


Figure A.7: C7 record - a) Acceleration time history, b) Spectral acceleration, c) Velocity time history, d) Spectral velocity

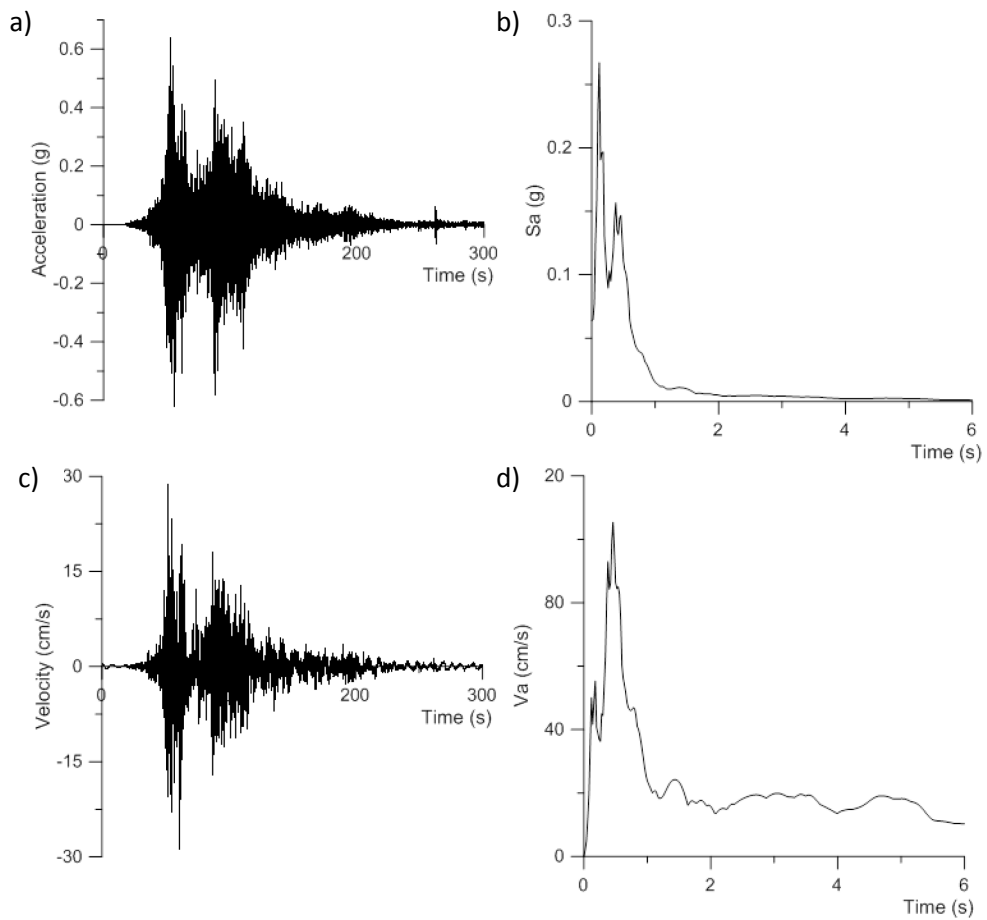


Figure A.8: S1 record - a) Acceleration time history, b) Spectral acceleration, c) Velocity time history, d) Spectral velocity

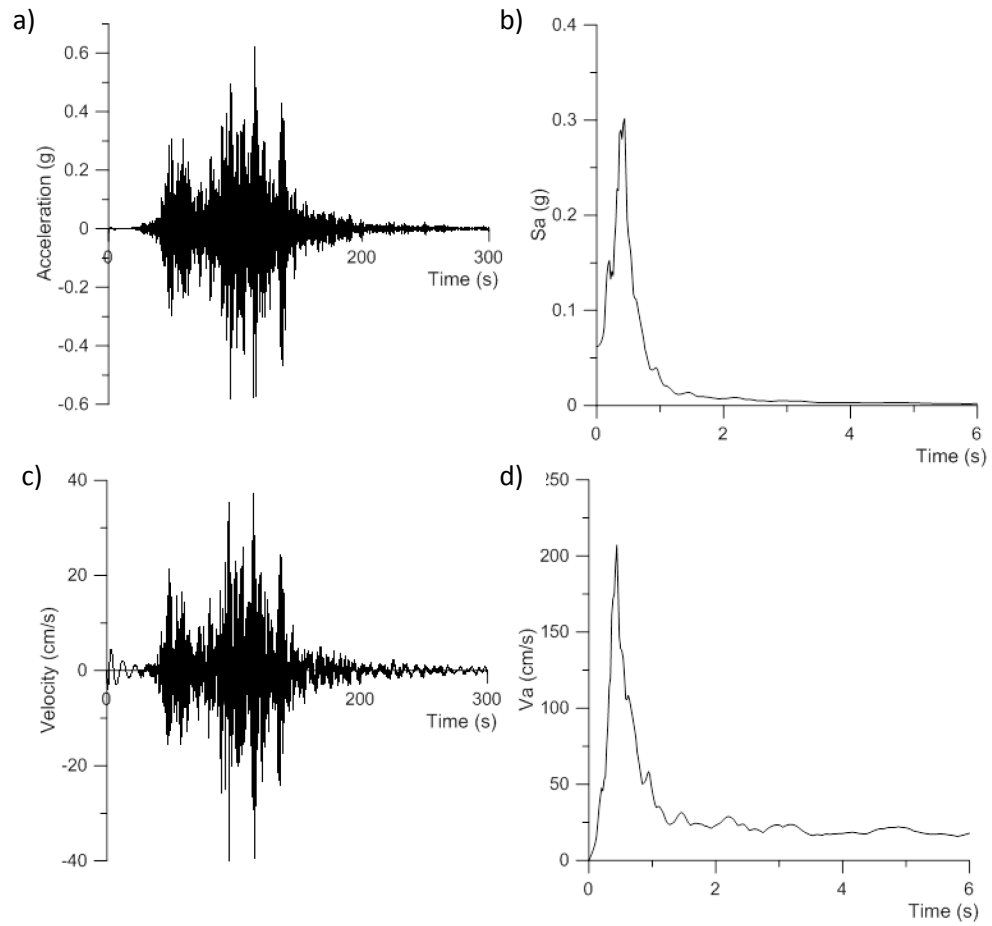


Figure A.9: S2 record - a) Acceleration time history, b) Spectral acceleration, c) Velocity time history, d) Spectral velocity

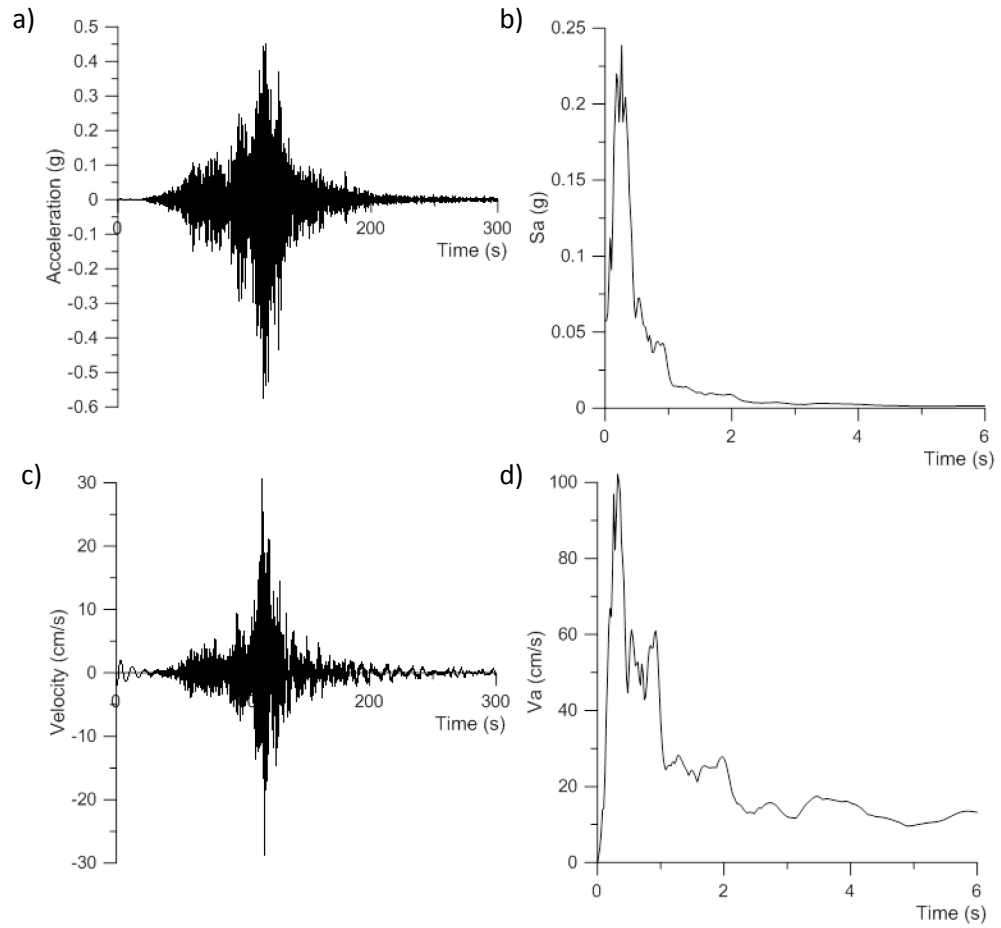


Figure A.10: S3 record - a) Acceleration time history, b) Spectral acceleration, c) Velocity time history, d) Spectral velocity

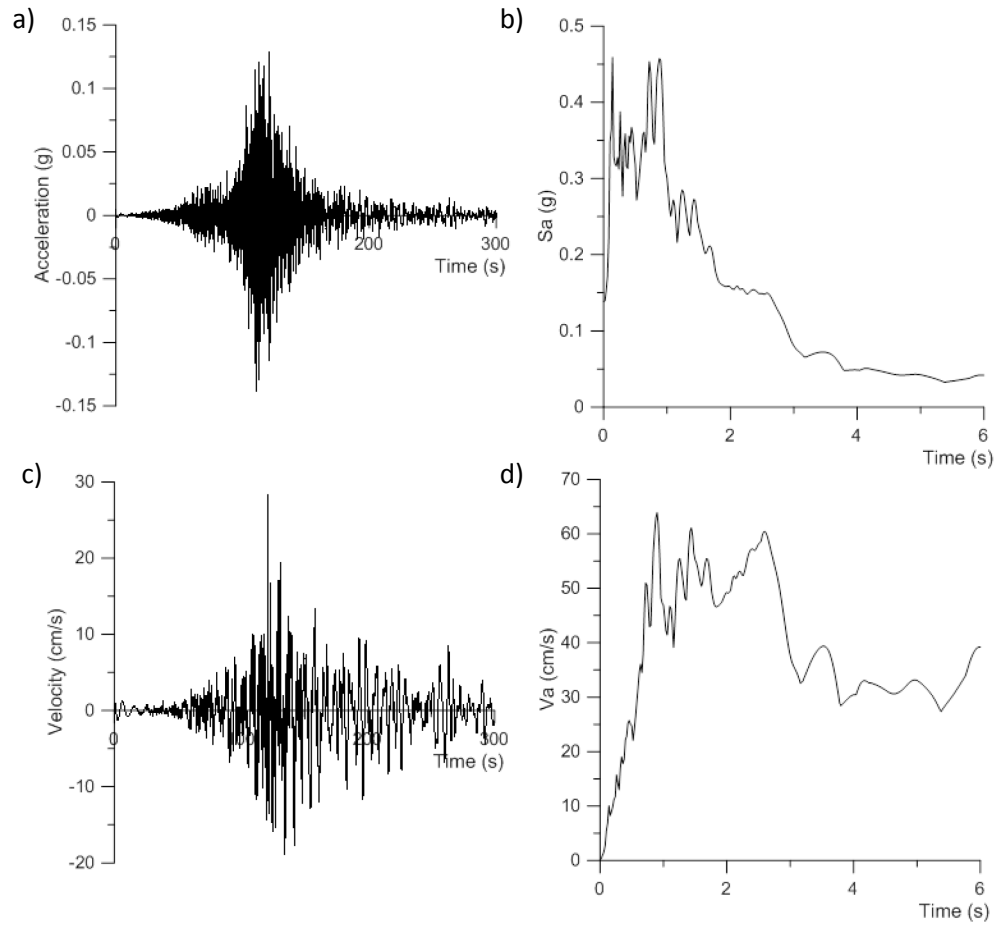


Figure A.11: S4 record - a) Acceleration time history, b) Spectral acceleration, c) Velocity time history, d) Spectral velocity

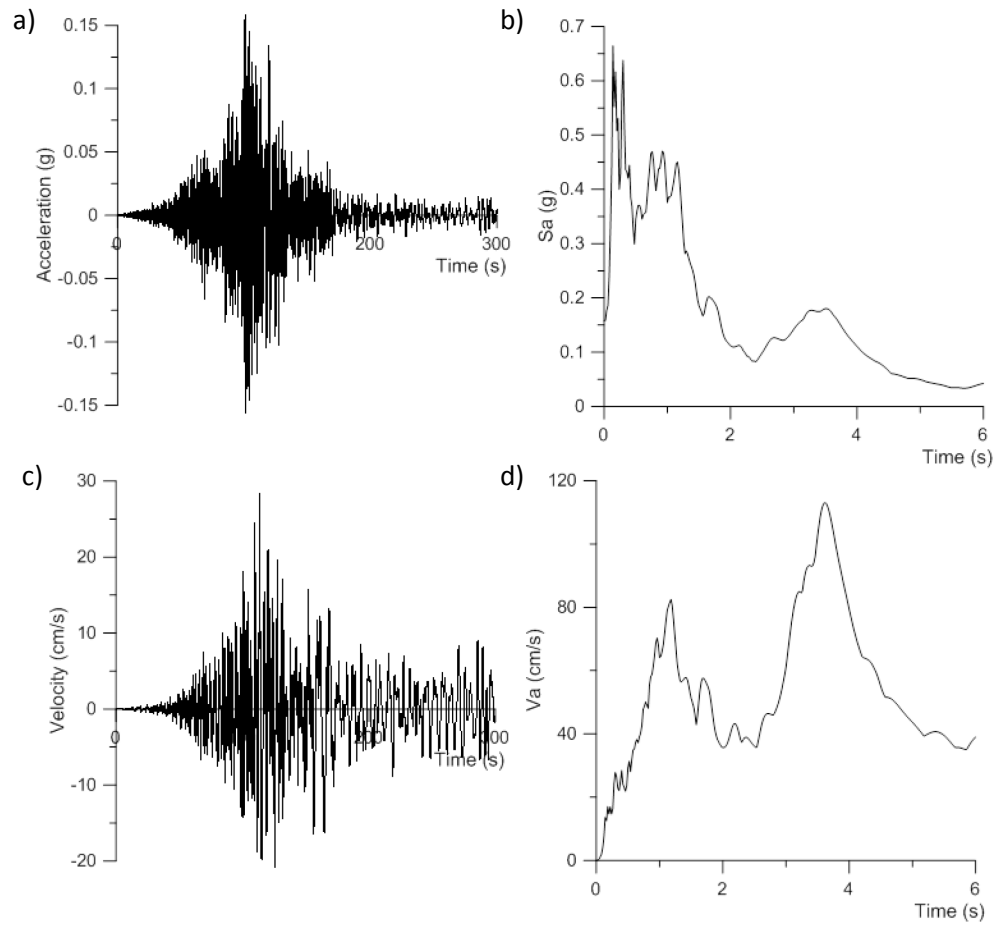


Figure A.12: S5 record - a) Acceleration time history, b) Spectral acceleration, c) Velocity time history, d) Spectral velocity

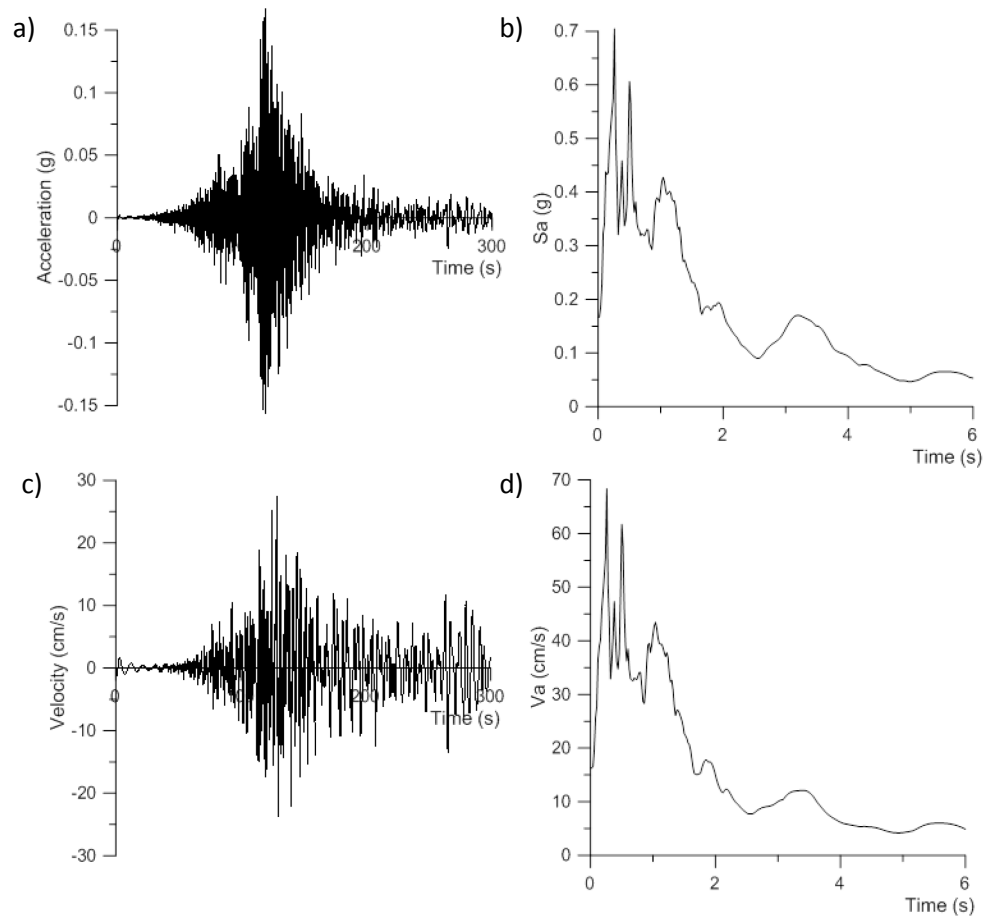


Figure A.13: S6 record - a) Acceleration time history, b) Spectral acceleration, c) Velocity time history, d) Spectral velocity

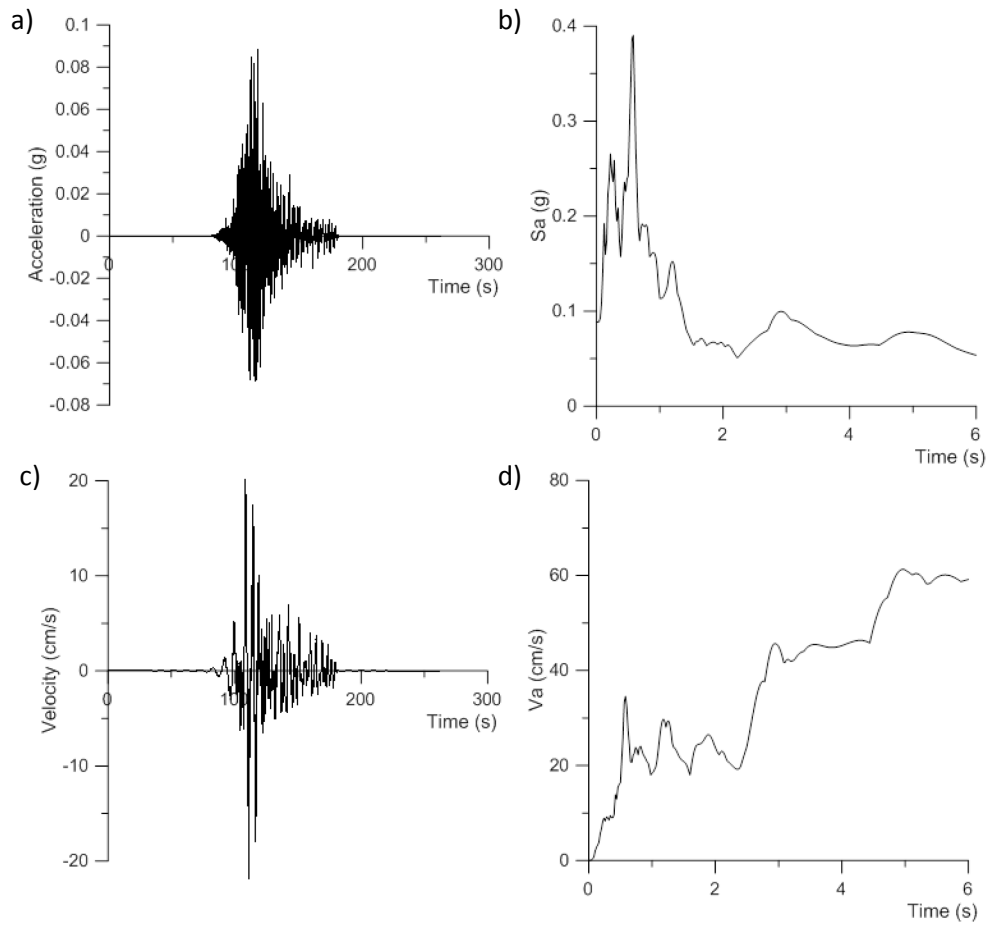


Figure A.14: S7 record - a) Acceleration time history, b) Spectral acceleration, c) Velocity time history, d) Spectral velocity

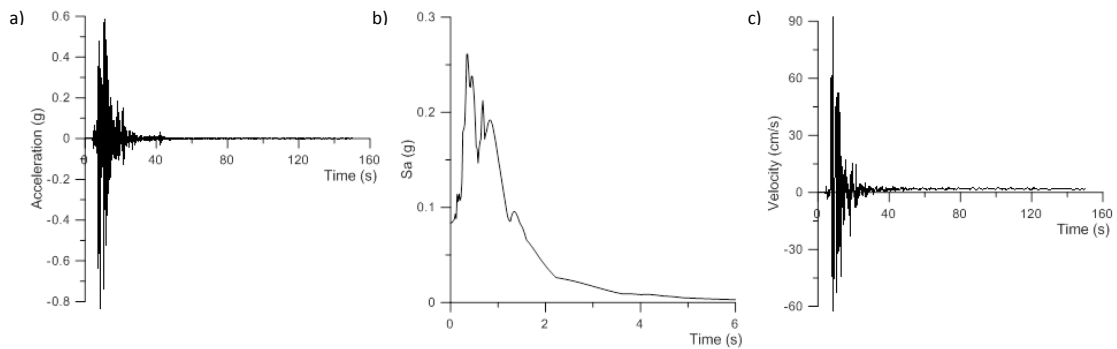


Figure A.15: N1 record - a) Acceleration time history, b) Spectral acceleration, c) Velocity time history

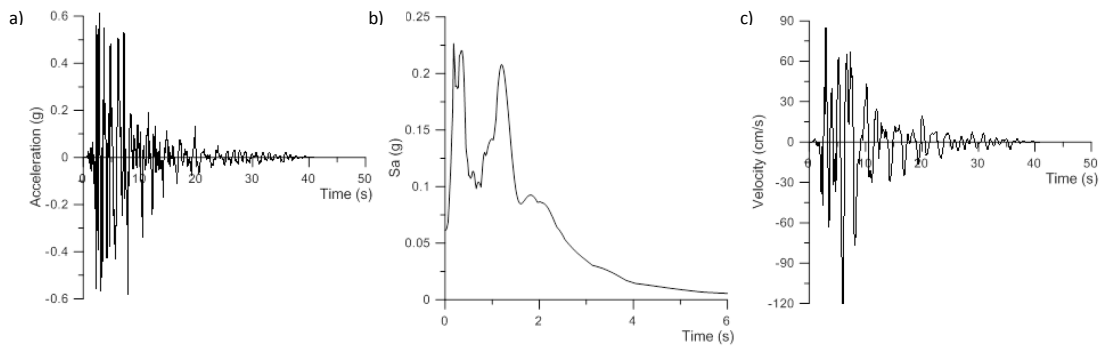


Figure A.16: N2 record - a) Acceleration time history, b) Spectral acceleration, c) Velocity time history

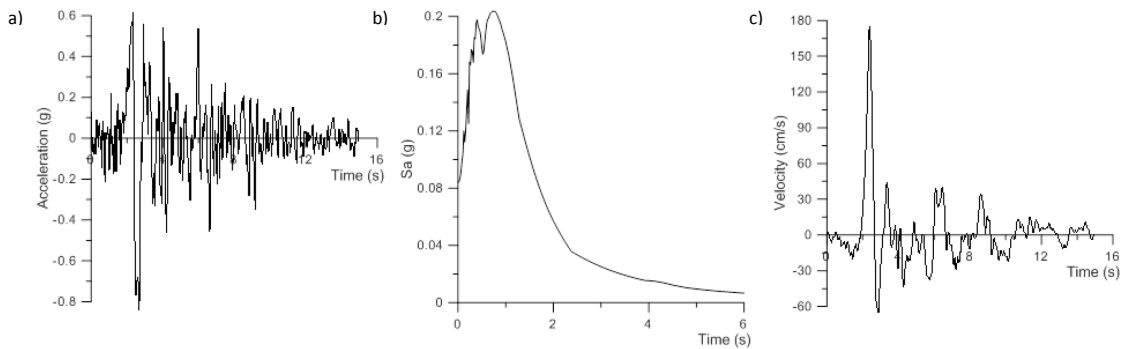


Figure A.17: N3 record - a) Acceleration time history, b) Spectral acceleration, c) Velocity time history

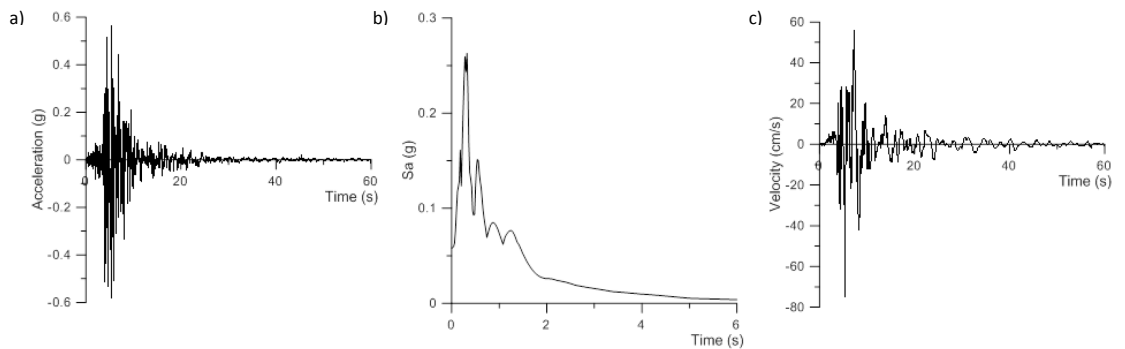


Figure A.18: N4 record - a) Acceleration time history, b) Spectral acceleration, c) Velocity time history

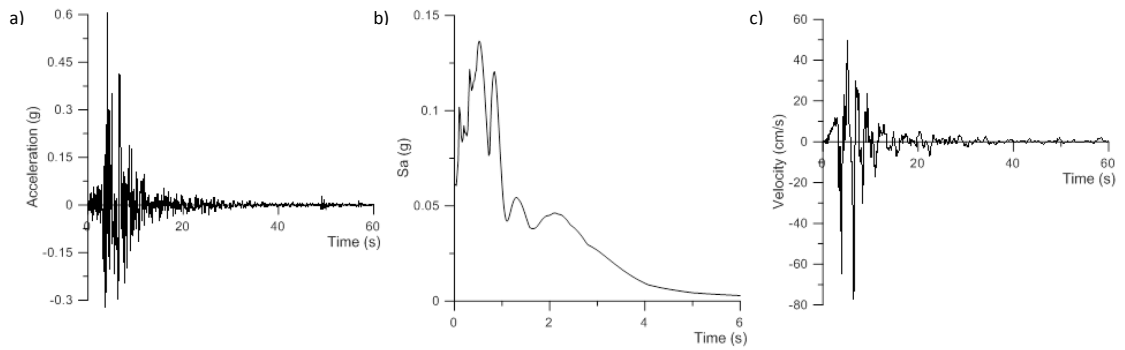


Figure A.19: N5 record - a) Acceleration time history, b) Spectral acceleration, c) Velocity time history

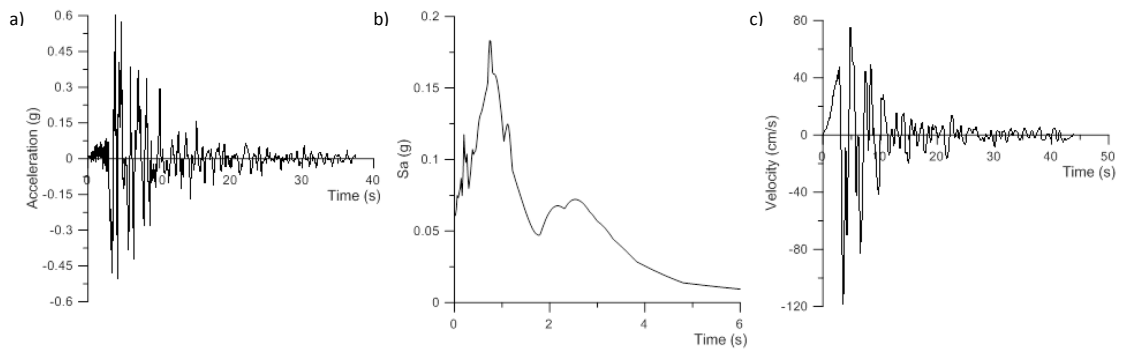


Figure A.20: N6 record - a) Acceleration time history, b) Spectral acceleration, c) Velocity time history

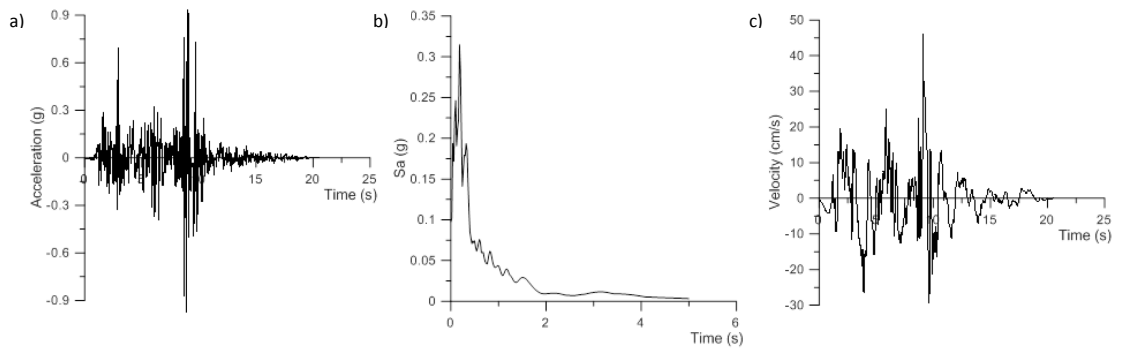


Figure A.21: N7 record - a) Acceleration time history, b) Spectral acceleration, c) Velocity time history

** Please refer to Table 4.6 for ground motion characteristics*